Mixture preparation and Injection Strategy in Direct Injection Spark Ignition Engines



Safwan Hanis bin Mohd Murad

St-Hilda's College

University of Oxford

A thesis submitted in partial fulfilment of the requirements for the degree of Doctor of Philosophy

Hilary 2018

Acknowledgements

I would like to thank:

Professor Richard Stone; for his supervision and endless enthusiasm, for his expert technical guidance and problem resolving throughout the project in his research group at the University of Oxford, and also for the continuous encouragement and believe in my work.

The Higher Education Ministry of Malaysia, Universiti Teknikal Melaka Malaysia, The Department of Engineering Science and not forgetting my college, St-Hilda's College for generous financial support throughout my studies.

Professor Martin Davy; for his interest in my work since and many helpful discussions along the way.

Former and current fellow students Dr Joseph Camm, Dr Felix Leach, Dr Nathan Hinton, Riyaz Ismail, Nick Papaioannou, Johannes Mutzke, Louis Nicholson, Blane Scott and Leo Fang of the Combustion and Engines research group, Dr Kun Liang and Dr Ian Berryman of the Cryogenics research group, Dr Christopher Willman of the Department of Physics, and academic visitor Dr Zhifu Zhou of Xi'an Jiao Tong University, China; for sharing the office and lab space with me for four years, and for the daily intellectual discussions that was always intriguing.

Professor Ben Williams; for sharing his knowledge in optics as well as experience in the optical engine operation. Members of the Workshop, Maintenance, Electronics and IT teams at the Department of Engineering Science, for helping to fabricate the components for the spray chamber, and for working to keep my experiments and simulations running.

My wife, Aimi Izzaty; for her never-ending support, for her believe in me finishing this very challenging journey, and for mostly giving the unconditional love to our children, Isma Hanis and Ilyas Hanis. My father, Dr.Mohd Murad, and mother, Abidah Ahmad; for being the proudest parents in the world and for always encouraging me to new heights. My parents-in-law Professor Zolkepli Buang and Faridah Puteh for being there through my difficulties.

Mixture Preparation and Injection Strategy in Direct Injection Spark Ignition Engines

Safwan Hanis Mohd Murad DPhil
St-Hilda's College, University of Oxford Department of Engineering Science

A thesis submitted in partial fulfilment of the requirements for the degree of Doctor of Philosophy, Hilary term 2018

ABSTRACT

Gasoline Direct Injection Spark Ignition (DISI) engines are becoming more popular than Port Fuel Injection (PFI). However, DISI engines can emit high levels of particulate matter which may be very harmful to humans. A popular method known to reduce particulates is to use oxygenated fuels such as the M15 (15% methanol by volume) gasoline which is currently widely used in China. However, the literature indicates that oxygenates might instigate more particulates rather than reducing them.

Model M15 gasoline fuels have been created from pure fuel components, to give independent control of volatility, the heavy end content and the aromatic content, in order to understand the effect of the fuel properties on DISI fuel spray behaviour and the subsequent particulate number emissions. Each fuel was used at a range of fuel temperatures in a spray rig and in a motored optical engine, to cover the full range from non-flashing sprays through to flare flashing sprays.

Spray behaviour is characterised here in terms of the saturation pressure ratio – the ratio of fuel saturation pressure to the in-cylinder pressure. Model fuels have been used in this work so as to be able to tailor their saturation pressure variation with temperature. The saturation pressure has been calculated using non-ideal Vapour-Liquid-Equilibrium (VLE) models based on the UNIFAC approach. The saturation pressure-temperature has been validated over a range of temperatures using an RVP type of apparatus. In-cylinder pressure was measured so as to know the in-cylinder pressure during injection, as there are substantial variations during the cycle; especially when the engine is boosted

Spray development has been characterised by Mie scattering images with a semi-quantitative analysis, along with the use of a presence probability analysis. The particulate matter emissions produced from the GDI engine have been measured using a Cambustion DMS500 particle sizer which can measure particles in the range of 5-1000 nm. The legally compliant CPC analysers has been replicated by using a using a filter defined by a Wiebe function. The particulate measurement experiments show that fuel volatility has a beneficial impact on reducing particulate matter emissions, even if flash boiling does not occur. Flash boiling did not necessarily reduce the particulate number, but it did reduce the mean particulate size which can lead to a lower total mass.

Spray impingement has been identified as a major factor that may influence the particulate number and mass. Using a single jet injector, a spray impingement experiment on a piston surface was devised using the spray rig. Thin Film Gauges (TFGs) were placed on the piston surface to measure the temperature change that will reflect heat flux when subjected to single injection. Two pure fuels as well as model fuels were tested at cold to superheated temperatures. A finite difference model was used for the heat flux calculation, which enables calculation of the total heat energy exchange on the piston surface during spray impingement. Detailed analysis shows that the presence of lighter fuel components will determine the spray structure of a mixture. This in turn determines the effectiveness of the spray cooling on the piston surface. At flashing conditions, the heat flow magnitude becomes similar for all model fuels as a result of having similar T90 values and this is attributed to the lighter components evaporating before they reach the piston surface.

Table of Contents

1. Research Motivation 1
   1.1. Evolution of internal combustion engines 7
      1.1.1. Spray Guided Direct Injection (SGDI) 10
   1.2. Particulate Matter 14
      1.2.1. Particulate matter from internal combustion engines 14
      1.2.2. Health Issues 17
      1.2.3. Latest P_M emissions regulations on GDI engines 21
      1.2.4. Factors influencing P_M emissions in GDI engine 25
   1.3. Chapter summary 38
2. Experimental Facilities and Analysis Tools 39
   2.1. Introduction 39
   2.2. Single cylinder optical engine 41
      2.2.1. Optical engine build combinations 46
      2.2.2. Engine operating conditions and components durability 49
      2.2.3. Engine controls and data acquisition system 51
   2.3. Optical Spray Rig 54
      2.3.1. Spray rig setup and controls for spray characterization experiment 54
      2.3.2. Spray impingement experiment setup on the spray rig 59
   2.4. Vapour pressure measurement apparatus 71
      2.4.1. Working principal 72
   2.5. High speed camera 73
   2.6. DMS 500 Mk II Fast Particulate Spectrometer 75
      2.6.1. Working principal 75
      2.6.2. Digital filtering 76
      2.6.3. Total particulate mass calculation 77
   2.7. Spray image analysis tool (IMSPRAY) 79
      2.7.1. Program description 79
      2.7.2. Image thresholding 82
      2.7.3. Spray image measurement standard (SAE J2715) 85
      2.7.3.1. Spray penetration measurement 85
      2.7.3.2. Spray angle measurement 86
      2.7.4. Spray repeatability measurement technique 87
   2.8. Chapter summary 89

3. Fuels, Fuels Modelling and Data Validation 90
3.1. Introduction 90
3.2. Oxygenated gasoline fuels 91
3.3. Methanol gasoline usage in China 92
3.3.1. Methanol gasoline blending characteristics 94
3.3.1.1. Physical properties 95
3.4. Evaporation modelling 98
3.4.1. Raoult's Law & UNIFAC 98
3.5. Gasoline model fuels 101
3.5.1. Oxygenated gasoline mixtures without aromatics (Light-end fuels) 103
3.5.2. Oxygenated gasoline mixtures with aromatics (heavy-end fuels) 104
3.5.3. Establishing the saturation pressure ratio (Engine & Spray rig) 105
3.6. Vapour pressure validation results 107
3.6.1. Pure fuels 107
3.6.2. Mixtures 109
3.7. Chapter summary 110
4. Spray Characterization Experiments and Results 112
4.1. Introduction 112
4.2. Test conditions 113
4.3. Spray axial penetration measurements of light end mixtures 115
4.4. Spray angle measurements of light end mixtures 126
4.5. Spray geometry comparison between light and heavy mixtures 129
4.6. Spray repeatability test of the heavy fuel mixture at various fuel temperatures 131
4.7. Injector tip temperature measurement for multiple injections 133
4.8. Chapter summary 134
5. Single Cylinder Optical Engine Experiments and Results 136
5.1. Introduction 136
5.2. Pressure ratio investigation using in-cylinder pressure measurements during motoring 137
5.2.1. Naturally aspirated 137
5.2.2. Forced induction 138
5.3. Engine motoring spray imaging results 140
5.3.1. Integrated spray intensity comparison between light-end and heavy-end mixtures 146
5.4. Combustion imaging of non-flashing and flashing fuel condition 148

5.5. Particulate matter results 151
5.5.1. Unfiltered vs Filtered (Wiebe Function) particulate matter data comparisons 151
5.5.2. Particulate number and mass of heavy mixtures at various injection timings... 158
5.5.3. Performance comparison of quartz against metal engine components..... 161
5.5.4. Lambda sweep of two distinctly different in-cylinder pressure ratio (R_P) fuels, injection timings of 310° and 340°BTDC. 164
5.5.5. Chapter summary 168
6. Single Jet Spray Impingement Experiments, Results, and Validation 170
6.1. Introduction 170
6.2. Experimental test conditions 171
6.3. High speed imaging results 173
6.3.1. 2D Piston surface heat map results 182
6.3.2. 1D and 2D finite difference method calculation validation 188
6.3.3. Comparison of latent heat of evaporation of the pure fuels and mixtures used for the spray impingement experiments. 189
6.4. Piston surface heat flux results 193
6.4.1. Heat flux calculation of piston surface temperature 193
6.4.2. Total energy exchange calculation during impingement period 194
7. Conclusions and Further Work 209
7.1. Conclusions 209
7.1.1. Oxygenated gasoline mixtures modelling and validation 210
7.1.2. Establishment of saturation pressure ratio for flash boiling stage identification 210
7.1.3. Importance of spray characterisation of model fuels on spray rig 210
7.1.4. The impact of in-cylinder pressure on fuel evaporation 211
7.1.5. Particulate matter correlation towards different spray characteristics 212
7.1.6. Spray impingement characteristics of the model fuels 213
7.2. Future work 216
7.2.1. Methanol gasoline blends 216
7.2.2. Flash boiling spray characterisation standard 216
7.2.3. Flash boiling correlation towards P_M emissions on boosted engine 217
7.2.4. Inclusion of sub 23 nm P_M legislation size distribution 217
7.2.5. Papers published, submitted, and in preparation 219
8. References 220

Nomenclature

AFR	Air Fuel Ratio
ASOI	After Start of Injection
ASVP	Air Saturated Vapour Pressure
ATDC	After Top Dead Centre
BMEP	Break Mean Effective Pressure
BOV	Blending Octane Value
BTDC	Before Top Dead Centre
c	Specific Heat
CAD	Crank Angle Degree
CARB	California Air Resource Board
CI	Compression Ignition
CMD	Count Mean Diameter
CNG	Compressed Natural Gas
COV	Coefficient of Variance
CPCs	Condensation Particulate Counters
CWD	Cold Weather Drivability
DBE	Double Bond Equivalent
DMS	Differential Mobility Spectrometer
d_p	Particle Mass Diameter
DPF	Diesel Particulate Filter
dt	Time step
DVPE	Dry Vapoure Pressure Equivalent
dx	Step change in x-direction
dz	Step change in z-direction
EEA	European Environment Agency
EPA	Environment Protection Agency
ETBE	Ethyl-Tertiary-Butyl Ether
ETCS	Engine Timing Control System
EU	European Union
EVC	Exhaust Valve Closing
EVO	Exhaust Valve Opening
F	Fuel Temperature
FBP	Final Boiling Point
GDI	Gasoline Direct Injection
HC	Hydrocarbon
x	Molar Fraction
α	Thermal Diffusivity
ρ	Material Density
δ	Total Thermal Depth Penetration
γ	Activity Coefficient
HWD	Hot Weather Drivability
ICE	Internal Combustion Engine
IVC	Intake Valve Closing
IVO	Intake Valve Opening
k	Thermal Conductivity
ln P	Natural Logarithm of Vapour Pressure
N	Particulate Number
NEDC	New European Drive Cycle
OBD	On-Board Diagnostic
P	Piston Surface Temperature
PAH	Polycyclic Aromatic Hydrocarbon
P_{amb}	Ambient Pressure
P_{cyl}	In-cylinder Pressure
PFI	Port Fuel Injection
PM	Particulate Mass
P_M	Particulate Matter
$PM_{2.5}$	sub 2.5 μm particulate size
PMP	Particle Measurement Programme
PN	Particulate Number
PR	Pressure Ratio
R	Gas Constant
RON	Research Octane Number
RVP	Reid Vapour Pressure
SGDI	Spray Guided Direct Injection
SI	Spark Ignition
SOF	Soluble Organic Fraction
T50	Temperature at which 50% of fuel has evaporated
T90	Temperature at which 90% of fuel has evaporated
TC	Thermometer
TFG	Thin Film Guage
T_{sat}	Saturation Temperature
TWC	Three Way Catalyst
UNIFAC	UNIversal Functional Activity Coefficient
VFEC	Vacuum Flash Evaporation Cooling
WHO	World Health Organization
WLTP	Worldwide Light Duty Test Procedure
ΔH_v	Latent Heat of Evaporation
σg	Geometric Standard Deviation
Γ_k	Group Residual Activity Coefficient

1. Research Motivation

Particulate matter emissions from internal combustion engines are one of many big challenges for vehicle manufacturers to overcome. Environmental and health enforcers require the automotive industry to comply with new stringent emission requirements. It is reported that in Europe, over 90% of the population is estimated to be exposed to levels of particulate pollution that represents a risk to health, and about a third of all European citizens are exposed to levels of particulate pollution above EU permitted levels of air quality in Europe in 2014 (EEA, 2016).

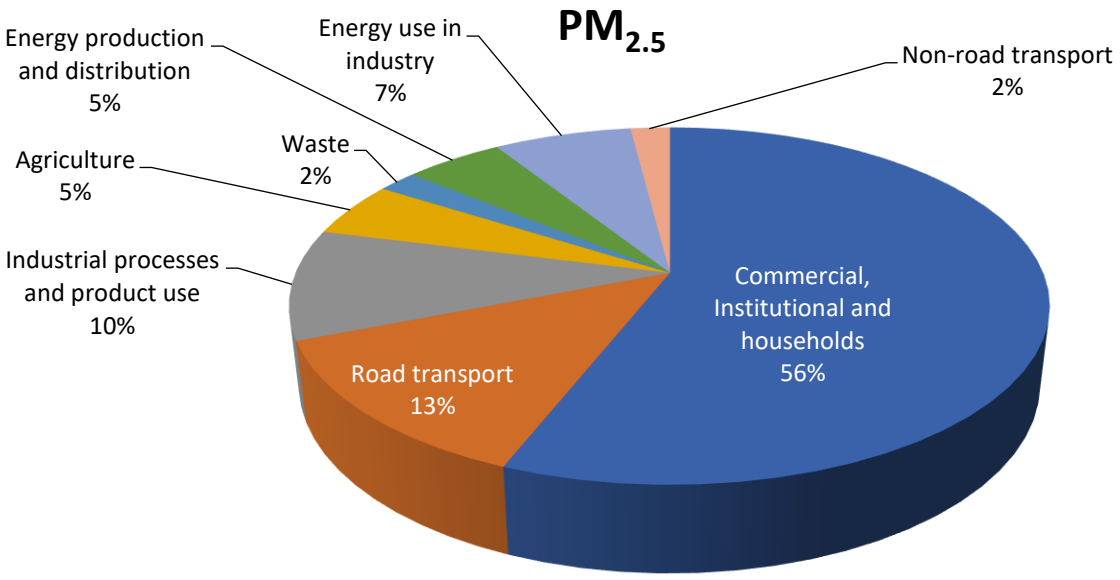


Figure 1.1: $PM_{2.5}$ emissions in the EU-28: share by sector group in 2014 (EEA 2016)

Figure 1.1 illustrates that transportation sector contributes 13% towards the production of fine particulates ($PM_{2.5}$ particulate matter below 2.5μm) with the stereotype assumption that diesel engines are the main source. However, most particulate matter can also come from the tyres, road surface and brakes. On the other hand, there is new evidence that suggests that vehicles using gasoline direct injection (GDI) engines can emit significantly high levels of particulate matter and some struggle to achieve the limit set by

the latest legislations, be it by quantifying mass or number. Figure 1.2 shows the compilation of particulate mass emissions recorded over the New European Drive Cycle (NEDC) from various gasoline powered vehicles with different injection systems. In this compiled literature, the recorded Particulate Mass (PM) data clearly shows that some of the GDI engines only barely meet the regulation requirements and perform poorly against Port Fuel Injection (PFI) engines. However, these GDI engines would not have had their operation optimized for meeting particulate matter legislation, as it is only with Euro 6 that this legislation has been applied to GDI engines. The Euro 6 calibrated vehicle clearly shows that it managed to achieve below the PM Euro 6c/6d limit. However, it is nowhere near the level produced by the older and increasingly less popular PFI system.

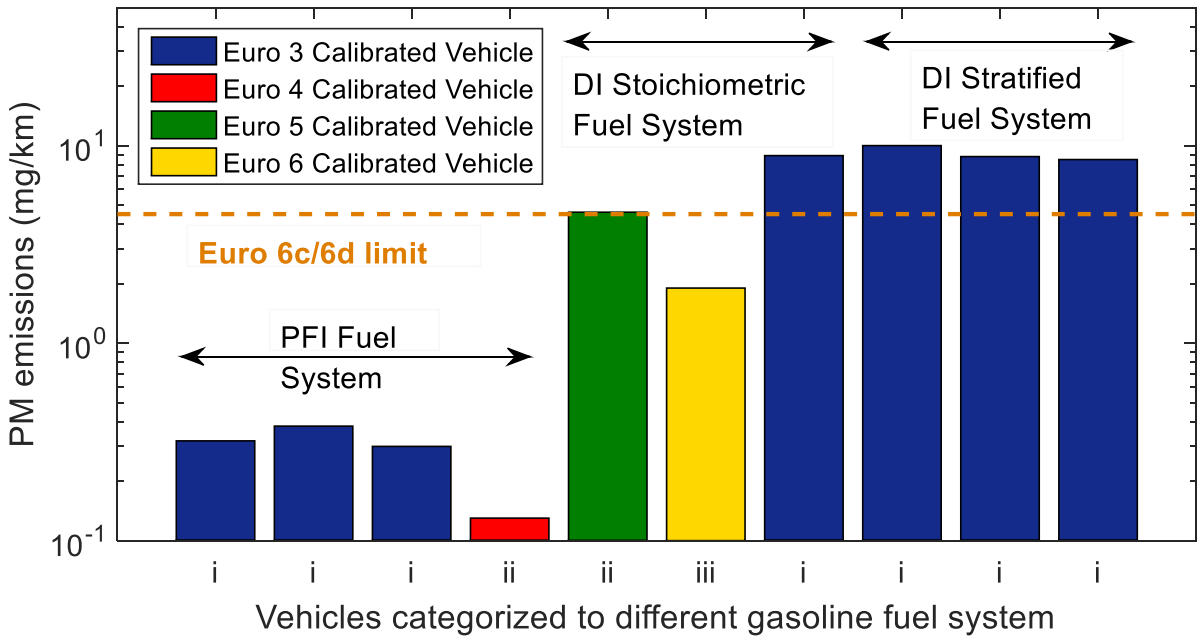


Figure 1.2: Reported PM emissions from gasoline powered vehicles of different fuel systems tested over NEDC. (i): (Ntziachristos *et al.* 2004), (ii): (Braisher *et al.* 2010), (iii): (Bielaczyc *et al.* 2017)

Apart from PM, gasoline vehicles are also tested for solid particles emissions number which is normally termed as Particulate Number (PN). The problem with DI engines is

highlighted even further when looking at the comparison of PN emissions of various gasoline vehicles in Figure 1.3. These vehicle emissions data comprise of PN emissions from gasoline engine calibrated from the oldest Euro 4 up to the latest Euro 6 settings. As can be seen, the majority of the DI engine emitted more than the Euro 6c/6d PN limit of $4.5x10^{11}$ #/km even with latest engine calibration. To make things worse, the new drive cycle, the Worldwide Harmonized Light Duty Test Procedure (WLTP) is known to have much harsher driving conditions and is to replace the outdated NEDC. This will be described later in this chapter.

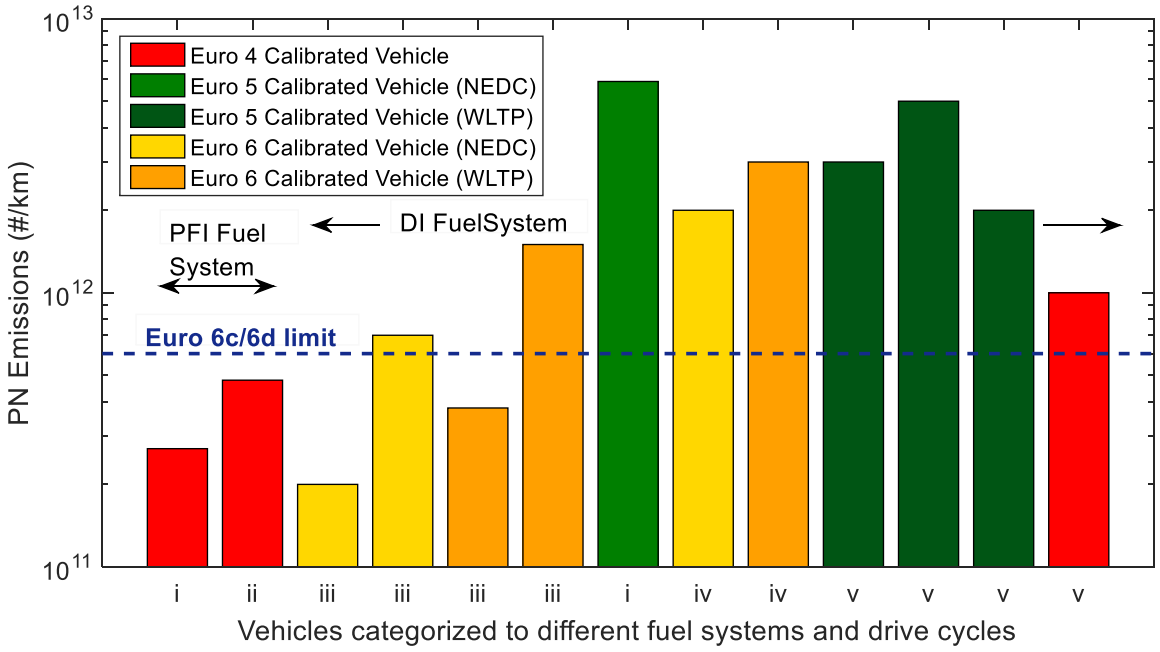


Figure 1.3: Reported PN emissions from various gasoline powered vehicles of different fuel systems tested over NEDC and WLTP. (i): (Braisher *et al.* 2010), (ii): (Bosteels *et al.* 2006), (iii): (Schoenhaber *et al.* 2017), (iv): (Bielaczyc *et al.* 2017), (v): (Czerwinski *et al.* 2017)

Though many engine manufacturers are looking into hardware innovation in engine components to reduce particulate emissions, there is also work on the effect of fuel formulation and fuel mixing strategies. For example, the use of alcohol fuels in previous

research works has given mixed results with regards to the development of particulate emissions. Vuk & Vander Griend (2013) tested various gasoline mixtures such as Indolene, E10 (gasoline with 10% ethanol by volume), E30 and E50 on GDI powered vehicles and found significant reduction in PN and PM even with the lowest additional amount of ethanol. Other work on alcohol fuels was conducted by Karavalakis *et al*. (2015), whereby gasoline mixtures using ethanol (E10, E15 and E20) and iso-butanol (Bu16, Bu24 and Bu32) were tested on GDI vehicles for PN and PM over the American Federal Test Procedure (FTP). It was found that overall, there were reductions in magnitude for both PM and PN measurements as the alcohol blend level was increased. On the other hand, (Chen et al. 2012a) tested various ethanol gasoline mixture of E0 up to E85 on a single cylinder research engine and found that PN and PM values were higher as the percentage of ethanol was increased. This was however, tested only at stoichiometric and steady state engine conditions.

Despite being in the same class of chemical compounds, primary alcohols, ethanol, iso-butanol and methanol when blended into gasoline give different outcomes as far as particulate matter is concerned. This is evident from the research work of (Price *et al*. 2007a) where E85, M30 (gasoline with 30% methanol by volume) and unleaded gasoline were tested under steady state stoichiometric conditions. From this report, the E85 fuel produced the lowest PN value followed by unleaded gasoline and finally M30 was the worst performer. However, the distribution of the particulate size from the M30 was reported to be mostly in the nucleation region. Another recent finding by Leach (2014) was that the use of M15 fuel in a highly boosted GDI engine produced very high levels of PN emissions. It has to be noted that Leach tested the M15 fuel on an SGDI based engine while varying injection timing as well as engine loads. This in turn, contradicts with some of the results published by Liang *et al*. (2013) and Geng *et al*. (2015) that showed reduction in particulate

matter, particularly for the M15 fuel compared to normal gasoline. In the works of Liang *et al*. (2013), the NEDC test showed the results of both GDI and PFI engines producing better PN and PM when using M15 as compared to gasoline. However, there were no details of what type of DI injector or specifically noted at which point in the NEDC cycle that PM or PN was significantly produced. Geng *et al*. (2015) on the other hand, only used a PFI engine and tested at steady state condition at different loads at constant engine speed. This variation of methods used for the test might have led to the discrepancies when testing the M15.

Due to these discrepancies in particulate emissions, this research will explore in detail, the mixture preparation of gasoline alcohol mixtures in GDI engines. This involves spray development, flash boiling effects, in-cylinder varying conditions, piston impingement and various fuel mixtures evaporation performance. When alcohol is mixed into gasoline, the calorific value of the mixture would be reduced but at the same time, the latent heat of evaporation is increased. This can be seen in Table 1.1, whereby the stoichiometric air-fuel ratio is seen to have reduced by a third while enthalpy of evaporation increases by more than double the original as more ethanol is added to the gasoline.

Table 1.1: Air fuel ratio, molecular weight and enthalpy of evaporation of various gasoline ethanol mixtures. Adapted from (Kar *et al*. 2008)

Fuel	Stoichiometric gravimetric air-fuel ratio	Molar Mass (kg/kmol)	Enthalpy of evaporation (kJ/kg)
ULG	14.5	86	298
E10	13.9	79	379
E30	12.8	68	431
E50	11.7	59.7	517
E85	9.8	49.4	792

The basic idea behind the development of particulates is the inability of the fuel to atomize, evaporate and mix efficiently. All of which will be related to the thermophysical characteristics of the fuel used. As a result of this, combustion occurs with the presence of diffusion flames that produce sooty combustion consisting of fine particulates Vuk & Vander Griend (2013). This can be a problem with the emerging trend of boosted GDI engines. Due to the high operating Brake Mean Efficiency Pressure (BMEP) of some boosted engines, more fuel mass needs to be injected to achieve a stoichiometric condition which can cause an increase in injection period (depending on injection pressure). It is hypothesised that due to this, spray impingement which is inevitable, would intensely cool down the piston or wall surface temperatures and lead to creating a liquid pool. Fuel volatility can be the key factor to prevent these issues by creating a homogeneous mixture that can help the fuel to atomize better. In order to study the effect of volatility on the performance of gasoline alcohol fuel mixtures, numerous fuels compositions have been devised and studied in the current research.

For the research here, a gasoline methanol mixture, e.g. M15 is emphasized rather than other alcohols. The popularity of this mixture is on the rise, especially in China, owing to the abundance of methanol that is derived from coal and natural gas. As more engine manufacturers from Europe are entering the Chinese market, due its ever-growing economy, many are concerned that this fuel might become more main-stream there in the future. Other than that, China is also planning to impose similar emissions regulations as the EU which will affect many manufacturers of GDI powered vehicle. The details of this development are discussed further later in Chapter 3, Section 3.3.

1.1. Evolution of internal combustion engines

For decades, the internal combustion engine (ICE) has been the main propulsion tool in vehicles. Even with the comeback of electric vehicle in the market, this does not deter the popularity of the ICE at all, be it with gasoline or diesel. Manufacturers still consider the ICE to have great potential and are thus maintaining their research commitments towards it. The development of the ICE has not stopped, and manufacturers are introducing new technologies to make it more reliable, environmental friendly, fuel efficient and powerful.

For years there have only been two really dominant types of ICE available in the market. The first is the spark ignition (SI) engine (commonly known as a gasoline engine), whereby combustion in the chamber happens only with the assistance of high voltage current supplied by a spark plug. The other being the Diesel engine, (also known as compression ignition (CI) engine), which initiates combustion solely from the result of air and fuel mixture being compressed to a temperature that will self-ignite the fuel.

Both engines have their advantages and disadvantages. Gasoline engines have the reputation of being the cleaner engine with very minimal amount of soot and particulates produced when in operation, but are less efficient (due to running at lower compression ratios so as to prevent combustion knock) Kasseris & Heywood (2012). In an SI engine, Port Fuel Injection (PFI) system is the more common one, with fuel is injected before the intake valves and mixed with air very early, even before the intake stroke. When the intake valves open, the back flow of hot gases from the previous cycle can enter the intake port and help vaporize the fuel. All these factors give a wide window of opportunity for the mixture to become almost homogeneous. A homogeneous mixture prevents wall wetting (be it the cylinder or piston surfaces) that can cause diffusion flames as a result of slow evaporation of the fuel. However, there are limitations with the PFI system that is preventing the gasoline

engine from achieving better fuel efficiency (Alkidas & El Tahry 2003), namely: (i) very poor throttle load control that produces high pumping losses at part-load operating conditions, (ii) much reduced compression ratio due to high chances of engine knocking at low speed high load conditions, and (iii) stoichiometric operating condition for the requirement of the Three Way Catalyst (TWC) to control high emissions of HC and NO. All three of which contribute to a higher fuel consumption for the PFI engine.

Diesel engines on the other hand, have a higher thermal efficiency than gasoline engines by adopting higher compression ratios, but produce more soot and particulates due to the manner in which they operate, that is, injecting fuel very late into the compression stroke to begin combustion after a delay of about 1 ms. At this stage, fuel impingement, wall wetting and the possibility of having unburned hydrocarbons as well as soot are almost inevitable Ko & Arai (2002). To solve this problem and meet emissions regulations, the Diesel Particulate Filter (DPF) is being used in Diesel engines whereby PN is seen to have reduced by up to three orders of magnitudes while PM is decreased by two orders of magnitude Whitaker *et al*. (2011).

The shortcomings of both engine types led to the development of a new architecture for SI engines which adapts the CI engine method of direct fuel injection. With the advancement of new technologies from injector manufacturers, it is now possible to make significant improvements by the introduction of gasoline direct injection (GDI) systems. In a GDI engine, the highly pressurized gasoline fuel is injected directly into the cylinder, contrasting to the PFI engine where gasoline fuel is injected into the intake runner just before the intake valves. Figure 1.4 compares GDI and PFI engines. GDI engines have two modes for mixture preparation: fuel stratification or homogeneous operation.

The GDI engine can then switch to either operating condition as the engine electronic control unit can identify the speed and engine load demand. By having this advantage, the engine could be operated at a stratified lean operating condition at part load to minimize the use of fuel. The gasoline fuel is injected into the combustion chamber late during the compression stroke with an approximately stoichiometric mixture close to the spark plug. The ignitable mixture is only needed in a certain area of the combustion chamber while the rest of the volume can be much weaker. In contrast to stratification, the homogeneous operating condition is when fuel is injected into the chamber during the intake stroke. Unlike PFI engines, the fuel evaporates in the cylinder, cooling the charge and leading to an increase in volumetric efficiency and improved resistance to knock Eichlseder *et al*. (2000) & Price *et al*. (2007). The compression ratio of the engine can therefore be raised by 1 or 2 ratios for a given quantity of fuel.

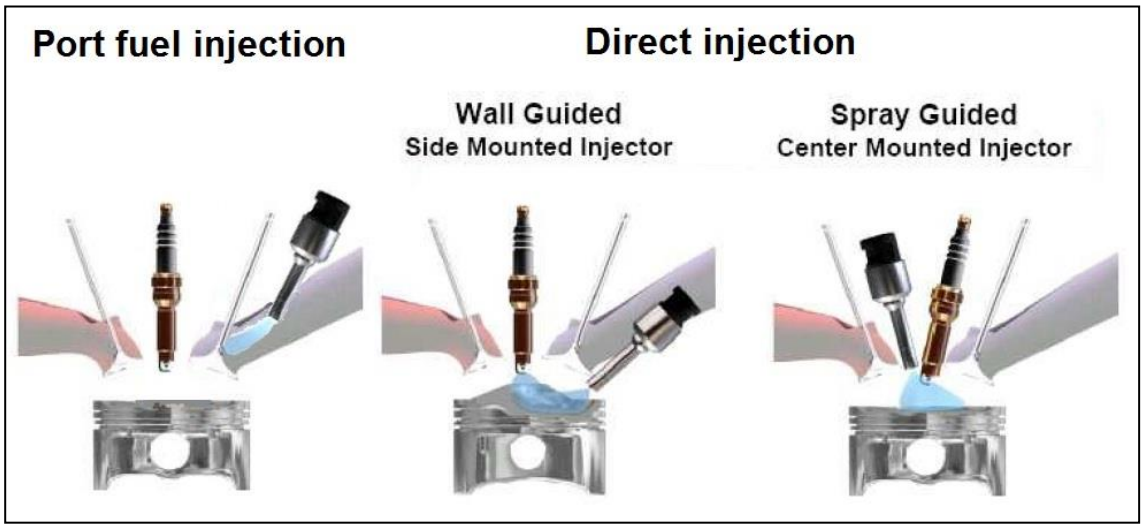


Figure 1.4: A comparison of Port Fuel Injection (PFI) with Direct Injection (DI), showing: a side-mounted injector with a wall guided combustion system, and a centrally mounted spray guided injector; adapted from (Wirth *et al*. 2004)

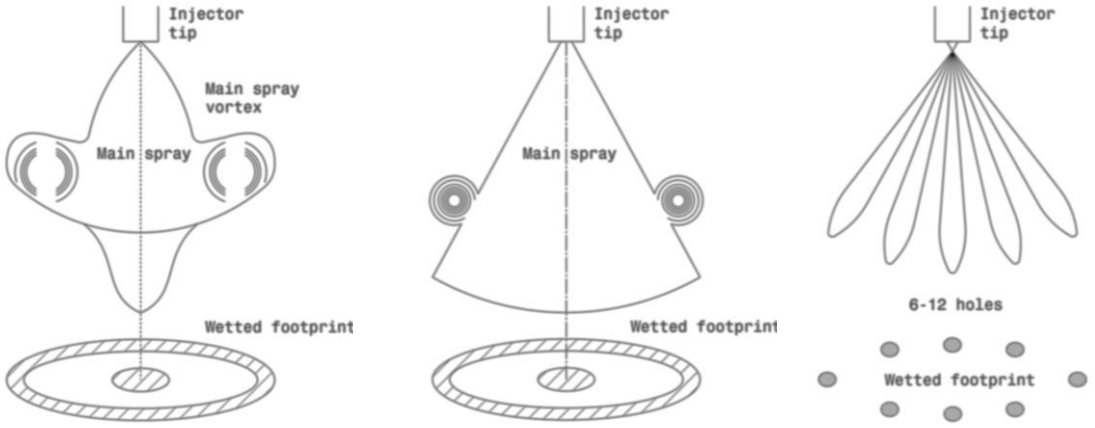
There are two key variations on how direct injection is applied in the GDI engine, namely: wall guided direct injection and spray guided direct injection (SGDI) as shown in Figure 1.4. Wall guided direct injection engines are commonly found in the "first generation" GDI engines. These injection systems can easily produce stable combustion due to the interaction of the spray shape with the fixed piston geometry. However, these mechanisms lead to the creation of liquid film on the piston surface and pool fires, with diffusion combustion that results in high emissions levels, particularly particulates Vanderwege *et al*. (2003).

Apart from that, the SGDI system enables even further reduction in fuel consumption to wall/air-guided system by having improved combustion efficiency and phasing as a result of the ability to provide the air-fuel mixture much later in compression stroke. SGDI is therefore currently being used by many manufacturers as an injection system but running with only homogeneous operating conditions to minimise fuel impinging onto the piston. Although running at stoichiometric, the homogeneous operating condition is stable at all load and speed requirements. The other reason for avoiding stratified operation system in SGDI engines is to meet the challenging emissions limit that have been enacted in 2017. Despite the challenges, SGDI currently is still believed to be the most promising technology to be utilized in the gasoline ICE. This research will also focus solely in homogeneous operations of GDI engines.

1.1.1. Spray Guided Direct Injection (SGDI)

SGDI is an injection mechanism that utilizes the fuel spray dynamics for controlling the mixture preparation. SGDI was developed with the main intention to minimize the impingement of fuel onto the cylinder wall or piston head by controlling the physical

dynamics of the spray Honda *et al*. (2004). With early injection, a nominally homogeneous mixture is generated, but with later injection or split injection it is also possible to have control over mixture stratification. It has to be noted that some of the earlier developments of SGDI focused a lot on improving the stratification operation, particularly to move away from the dependence on piston position for injection in the case of wall-guided DI.



(i) (ii) (iii)

Figure 1.5: GDI injector classification by nozzle design; (i) Swirl injector, (ii) Outward opening injector, (iii) Multi-hole injector. Adapted from (Hung *et al*. 2008)

There are three types of injectors normally used in SGDI engines: the Swirl Injector, Multi-Hole and Outwardly-Opening Injector as shown in Figure 1.5. Most manufacturers also adopt a central mounted injector position in order to achieve more stable combustion over a wide range of operating conditions as reported by Morikawa & Kaneko (2005). Centrally mounted SGDI, also known as "narrow spacing", normally has only a narrow gap between the injector tip and the spark plug. This enables some of the plumes to be injected directly towards the spark plug, and for the fuel to arrive in a shorter period of time Shigeo Yamamoto (2009). Therefore, in order to achieve high stability and low emission combustion, the mixture must be formed rapidly by promoting fuel diffusion, vaporization and air-entrainment immediately after injection (for the case of the stratified mode).

Detailed research on the centrally positioned SGDI system can be found in a report by Katashiba *et al*. (2006). Schwarz *et al*. (2006) reported reduced wall heat losses and incomplete combustion from SGDI engine as compared to wall-guided engines of similar engine specifications when tested. With the realization of the Euro 5 (PM, PN limit introduction), most engine manufacturers shifted their focus from the stratified mode to the purely homogeneous mode. This can be seen in the report from Dardiotis & Martini (2012) whereby on average, GDI engines running on a homogeneous mode produce less PN compared to a stratified mode. Figure 1.2 illustrated the same findings. Although running a stratified mode gives higher efficiency, it also requires different after treatment systems which comprises of a Lean NO_x trap and an oxidation catalyst which can be more complex and costly. To make matters worse, there is a possibility that the Gasoline Particulate Filter (GPF) could be made mandatory by regulatory bodies to control particulate emissions from GDI engines. Due to this, running homogeneous is currently the preferred configuration by many manufacturers. A recent study by Demuynck *et al*. (2017) tested a Euro 6 calibrated vehicle retrofitted with a GPF combined with a TWC showed significant reduction in PN but not so much on PM.

Although direct injection technology has gone through a series of evolutions to the SGDI system, it is still far from being perfect. The SGDI system has its own challenges. One of them is the tendency of producing a significantly different spray pattern whenever the spray collapses which defies its original purpose. The spray can collapse when there is flash boiling. Flash boiling sprays are nothing new and have been studied thoroughly for decades. However, for the case of the SGDI system, this phenomenon is often overlooked due to the complexity of the process. In order for flash boiling to occur, the fuel injected must be above its saturation temperature which on a vehicle, can only be achieved by means of controlling the fuel temperature, fuel volatility or chamber pressure. All of which are

very difficult to standardize and control during applications. The flash boiling phenomena will be discussed further in section 1.2.4.2.

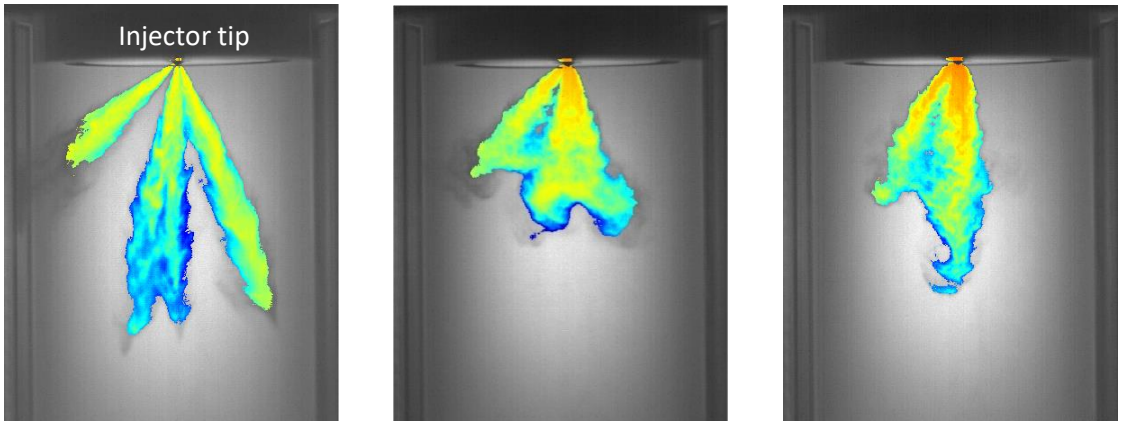


Figure 1.6: Typical example of spray geometry transformation due to flash-boiling phenomena of a fuel spray from an SGDI multi-hole injector imaged in a spray rig. Fuel used: n-pentane. P_{cyl} = atmospheric; Tsat = 36.1°C

An example of collapsed spray phenomena due to flash-boiling has been reported by Aleiferis & Van Romunde (2013) in their research where a multi-hole injector was used. Collapsed spray images were captured mostly at superheated temperatures and when different single component fuels were tested. The pattern of the n-pentane fuel spray at temperature of 120°C in the report showed little resemblance to its original lower temperature spray geometry. A similar test was conducted in the preliminary stages of this research using a spray rig and the spray collapse is shown in Figure 1.6. This collapsed spray behaviour is hypothesized to have caused particulates emission problems; the flash boiling phenomenon alters many original spray characteristics such as the: penetration rate, spray angles, liquid droplet diameter as well as evaporation performance. There is also a possibility that this makes the spray penetrate deeper into the combustion chamber, impinging on the piston crown to create pool fires or cause a departure from mixture homogeneity. This hypothesis will be studied in this research despite the contradiction of

findings from the research work of Xu *et al*. (2013) that recommends the use of flash boiling to improve spray atomization in GDI engines.

1.2. Particulate Matter

1.2.1. Particulate matter from internal combustion engines

There are basically two types of particulate matter (P_M); the ones being emitted into the atmosphere are known as primary particulates and the other are formed in the atmosphere and are known as secondary particulates. Partial or primary particulate comes from anthropogenic sources that include fuel combustion in thermal power generation, incineration, domestic heating for households and fuel combustion for vehicles (EEA Report 2014) (EPA United States Environmental Protection Agency 2004). It is well known to date that the ICE does exhaust P_M quite substantially. However, diesel engines have historically been the one being more thoroughly scrutinized and deemed less environmentally friendly due to the significant amount of visible soot that can be emitted. In contrast, gasoline engines running on carburettor or PFI were the cleaner engine.

Exhaust particles are made of highly agglomerated solid carbonaceous materials, ash, and volatile organic and sulphur compounds. The occasional occurrence of a high concentration of fuel in the combustion chamber causes the formation of a locally rich region that when involved in the combustion process, produces solid carbon which is only partial oxidized. Other components can escape oxidization and appear as volatile or soluble organic fraction (SOF) in the exhaust (Kittelson 1998). Farrar-Khan *et al.*, (1992) found that the SOF contains polycyclic aromatic compounds also containing oxygen, nitrogen and sulphur. Though this research on P_M was for a diesel engine, these particle characteristics are similar for the gasoline engine. This was evident from the works of Barone *et al*. (2012), where

samples of particulate matter emissions were imaged using Transmission Electron Microscopy (TEM) and compared. The soot agglomerate had fractal-like morphology that is similar to diesel particulate matter.

For gasoline engines, it is suspected that diffusion combustion and rich inhomogeneities are the key contributing factors for generating soot and other P_M. Diffusion combustion in a GDI engine occurs with the burning of a liquid film when fuel impinges on combustion chamber surfaces Aikawa *et al*. (2010).

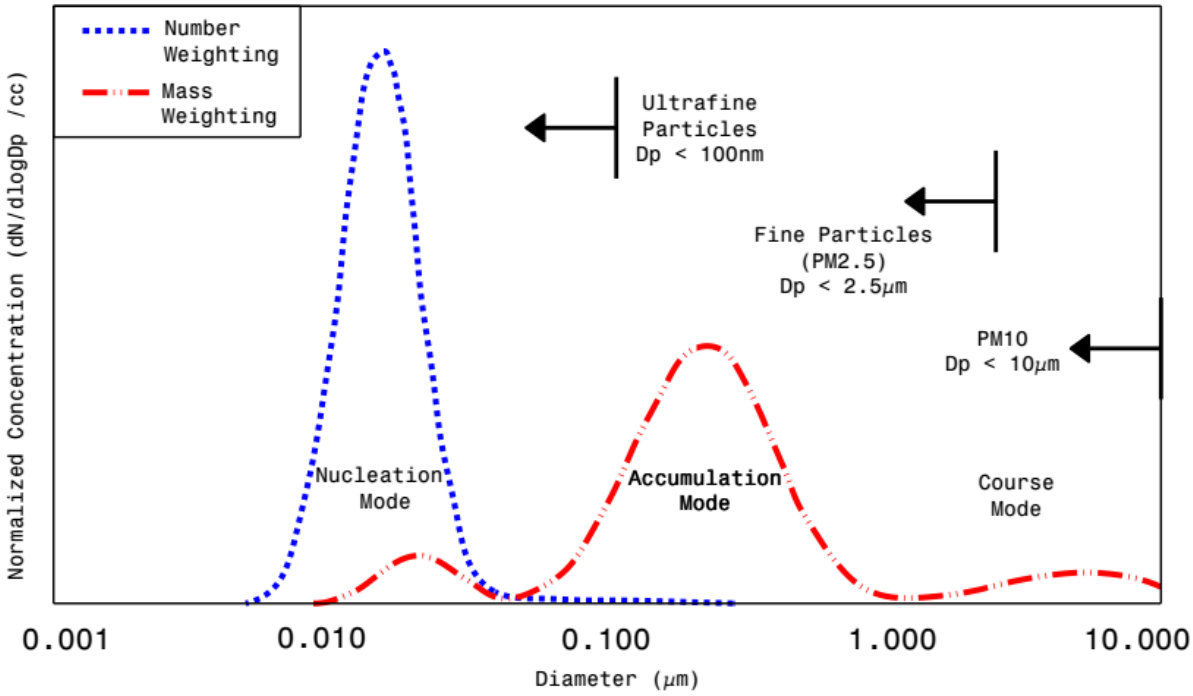


Figure 1.7: Typical engine exhaust size P_M distribution for mass and number weightings. Adapted from (Kittelson 1998)

Figure 1.7, adapted from Kittelson (1998), shows an example of lognormal P_M distribution from an ICE exhaust. Note that this type particulate distribution is normally found in a Diesel engine but, a similar pattern of particulates from GDI engine was also found in various works such as Leach (2014). Nucleation mode particulates consists of

volatiles components such as unburned hydrocarbon, sulphate, soot and metal ash. This mode is made of a gas species that nucleate into new particles, and can contain up to 90% of particle number emission even though only representing 1-20% of the mass. Measurement of the nucleation mode depends highly on the dilution ratio and cooling of the exhaust. It is notoriously difficult to measure the nucleation mode in a consistent and reliable way as described by Zervas-Renault (2004). Repeatability can be a problem given that this mode has a very high number of small particulates. Much of the blame for this can be pointed to the volatile components and the highly non-linear nature of nucleation.

Accumulation mode (semi-volatiles or solid) on the other hand, is composed of soot, organic compounds, sulphate, ash and its agglomerates. This mode is normally only affected by saturation to some extent, as this decides the capture or release of volatile compounds. As a result of this, the accumulation mode is more likely to represent the genuine emission than the nucleation mode. On another note, the accumulation mode (also known as $PM_{2.5}$) would be of more interest in this research because particulates in this region are the ones produced very much by GDI engines and deemed to cause health problems Dergham *et al*. (2015) Kim *et al*. (2015). There are however, discrepancies in the findings on particle size characterisation in the literature.

Leach (2014) in his work, described the nucleation mode particles as characterized by having diametric size less than approximately 20 nm while the accumulation mode particles generally lie in the size range of 40-200 nm. This size range is shared also by the works of Czerwinski *et al*. (2017) when testing GDI engines. Natti *et al*. (2013) defined the nucleation mode as particles with diameter of less than 40 nm with peak mean diameter at 25 nm while the accumulation mode was defined as particles larger than 50 nm. In the works by (Barone *et al*. 2012b), it was found that particulates samples taken from GDI engine produced agglomerate primary particles (accumulation mode) in the range of 7-60 nm.

These discrepancies are a concern because at the moment, most Condensation Particulate Counters (CPCs) used by many researchers are specifically designed to measure only solid particles of diameter > 23 nm; as required by the EU legislation. Due to this, sub-23 nm particles are not regulated and could actually be polluting the environment. If an engine is fitted with a particulate filter, then particulates below the 50 nm are effectively removed Taylor *et al*. (2012). Regulating solid particles above 23 nm for an engine with a particulate filter is essentially regulating all particles, but this is not the case for engines without a particulate filter. As described by Kittelson (2016), gasoline engines be it PFI or GDI that are running fuels such as Compressed Natural Gas (CNG), Liquified Natural Gas (LNG) or Dimethyl Ether (DME) are known to emit solid particles smaller than 23 nm.

Due to this finding, it is only correct that this research work considers both modes when any particulate measurements are made, the data will be analysed in two ways; particulate data which emulates the CPC as per EU regulations (size > 23 nm; 50% count efficiency), and raw data (which includes the entire size range).

While all ultrafine particulates are known to be dangerous to human health, the sub-23 nm particles are thought to have deeper impact on human respiratory functions. (Oberdörster *et al*. 2005) reports that the 5 nm particle has a 30% deposition efficiency in the alveolar region, while the 20 nm particle has the highest deposition efficiency of 50%.

1.2.2. Health Issues

Air pollution, as defined by Kim *et al*. (2013), is the introduction of diverse pollutants into the atmosphere that cause harm to humans, other living organisms and the natural environment. It is estimated that around 2 million deaths were estimated to occur globally each year as a consequence of air pollution. Among these deaths, about 0.2 million are caused by fine $PM_{2.5}$ (Silva *et al*. 2013). The World Health Organization (WHO)

characterize P_M to consist of a heterogeneous mixture of solid and liquid particles suspended in air that varies continuously in size and chemical composition in space and time (World Health Organization 2013). It was stated that the chemical constituents of P_M are very diverse and it includes nitrates, sulfates, organic compound (e.g., Polycyclic aromatic hydrocarbons), metals (e.g., iron, nickel, copper) and organic carbon.

Over the years, air pollution has always been associated with vehicles utilizing the ICE. This is probably due to their presence in high numbers as well as they are sometimes seen emitting visible emissions. However, it is a different case when it comes to P_M, whereby its sources can be explained as either direct emission into the air or as conversion of gaseous precursors released from both anthropogenic sources and natural sources, Atkinson *et al*. (2010). Even though combustion from fossil fuels is one example of an anthropogenic source, there are also other sources which include industrial and agricultural activities, erosion of pavement by road traffic, and abrasion of brakes and tyres de Kok *et al*. (2006). As for naturally emitted P_M, the sources can be from volcanoes, forest fires, dust storms and even sea spray (European Environment Agency 2012). Due to this, it is very difficult to distinguish and characterise particles from ICE whenever measurements are taken in open surroundings rather than in an engine test cell or on a chassis dynamometer.

Fine particles, as a result of having really small size, tend to be suspended in the air for a long period of time, with a caveat that the ambient atmosphere remains dry Johansson *et al*. (2007). It has also been reported that the time period for particle suspension can be up to weeks or even months. Other than that, these fine particles can be transported for up to thousands of kilometres from the original source due to changes in wind patterns which in turn cause fluctuations in P_M concentrations.

The biggest obvious method to how P_M can be damaging towards human health is of course through the respiratory system. They can be harmful to other organs of the human body such as eyes or skin but harming organs in the respiratory system can be life-threatening. The human respiratory system's main purpose is for breathing air which provides oxygen to the body. Therefore, it is imperative that nothing other than air travels into the lungs.

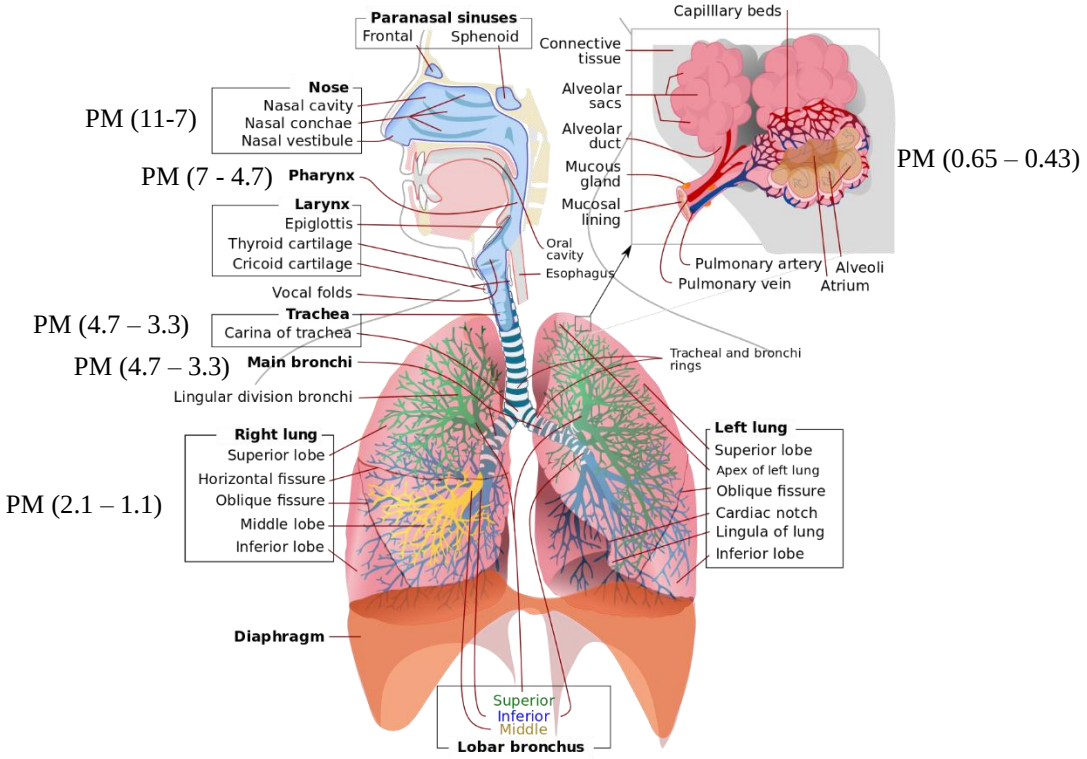


Figure 1.8: Deposition potential for particulates of varying size. Adapted from (Löndahl et al. 2010)

Through nasal-breathing, the cilia and mucus acts as a very effective filter for most coarse mode particulates, those exceeding 10µm in diameter. Initially most of the fractions of this P_M size would get trapped at the trachea or in the bronchi and eventually cause a build-up. The human body will react to eliminate these intrusions through sneezing or coughing Kim *et al*. (2015). Up to now, particles that have the most impact on human health have been recognized to be those with diameter < 10 µm. Particles of this size can penetrate

within the respiratory track from the nasal passage to the alveoli, deep within the lungs Löndahl *et al*. (2007). Particles of the size 5 µm to 10 µm are most likely to get deposited in the tracheobronchial tree, while those of 1 µm to 5 µm are likely to be deposited in the respiratory bronchioles and the alveoli where gas exchange occurs Löndahl *et al*. (2006). Figure 1.8 shows the human respiratory system diagram showing varying deposition for different particulate sizes. As a consequence, there will be a reduction in lung efficiency. Continuous exposure to these particulates has been identified as the cause of several health problems such as the exacerbation of chronic respiratory illness, decreased lung functions, premature mortality and cardiovascular diseases Perez *et al*. (2012). There have also been reports to suggest that high amounts of exposure to these particles towards pregnant woman may also lead to low birth weight, pre-term deliveries and even foetal death, Rappazzo *et al*. (2014), Trasande *et al*. (2016).

For humans that are exposed continuously to ultrafine particles, the result can be much more damaging. There are significant differences between coarse particles and ultrafine particles with regards to the behaviour during deposition and clearance in the respiratory system. Deposition mechanisms such as internal impaction, gravitational settling and interception which normally influence coarse particles, do not apply to ultrafine particles Oberdörster *et al*. (2005). The main deposition mechanism for ultrafine particles is through diffusion due to displacement when they collide with air molecules Oberdörster *et al*. (2005). The International Commission of Radiological Protection developed a mathematical model to predict the deposition of inhaled ultrafine particles in the nasopharyngeal, tracheobronchial, and alveolar regions of the human respiratory tract under normal breathing conditions. Although this only applies to singlets (not aggregates), it was found that significant amount of ultrafine particles were found deposited in the three regions mentioned.

It was also reported that 90% of inhaled 1 nm particles are deposited in the nasopharyngeal compartment while only approximately 10% in the tracheobronchial region, and essentially none in the alveolar region. For the case of 5 nm particles, the deposition was approximately 30% of the inhaled particles in all three regions. Finally, 20 nm particles have the highest deposition efficiency in the alveolar region of about 50%. Ultrafine particles generally behave like gas molecules and will penetrate down to the alveoli and can translocate further into the cell tissue and circulation system. These particles may be more toxic, based on their greater number, larger content of redox-active compounds, such as PAHs, and greater surface to mass ratio Araujo & Nel (2009). Despite these claims, there are however, inconclusive findings on the impact of ultrafine particles towards human health. There are several reasons for this; the difficulty in standardizing measurement methods, equipment limitations for ultrafine particles and the heterogeneous definitions of ultrafine particles (Heinzerling *et al*. 2016).

Nevertheless, the above findings should suffice as a reason for the legislative bodies to act on regulating P_M for the benefit of human health.

1.2.3. Latest P_M emissions regulations on GDI engines

To date, more and more GDI based vehicles are being sold in many countries due to the popularity of the technology which gives higher power output than PFI but at the same time being very fuel efficient. Some manufacturers are making full use of this opportunity to sell GDI vehicles in various countries before any stricter emissions legislation is being imposed, particularly emissions related to P_M, Archer (2013).

Table 1.2: Summary of EU legislation limiting particulate emissions for passenger cars featuring DISI engines. Taken from Bielaczyc *et al*. (2014), Johnson & Joshi (2017), Schoenhaber *et al*. (2017)

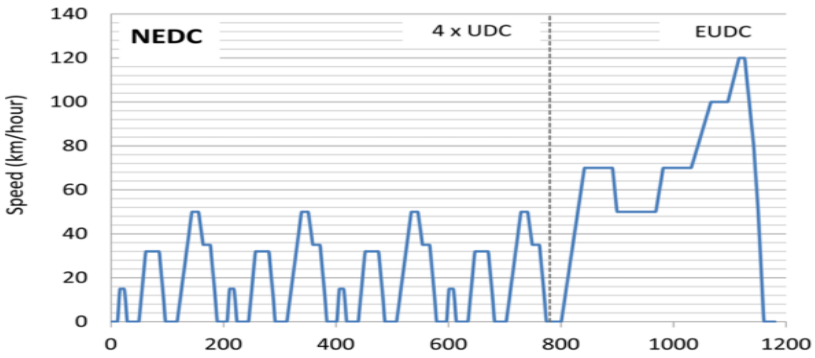
Legislative stage	PM (mg/km)	PN (#/km)	Test cycle	Phase-in period
EU/ Euro 5a	5.0	None	NEDC	2011-2012
EU/ Euro 5b	4.5	None	NEDC	2013-2014
EU/ Euro 6b	4.5	6.0×10^{12}	NEDC	2015-2016
EU/ Euro 6c	4.5	6.0×10^{11}	WLTC	2017-2020
EPA/ Tier III	1.86	None	FTP-75	2017-2025
CARB / Exhaust Mass Emission Standards	6.21	None	FTP-75	2015
CARB / Particulate Standards	1.86	None	FTP-75	2017
CARB / Particulate Standards	0.62	None	FTP-75	2027
Japan / Post New Long Term	5.0	None	JC08	2009
China 5	4.5	None	NEDC	2017
China 6a	4.5	6.0×10^{12}	WLTC	2020
China 6b	3.0	6.0×10^{11}	WLTC	2023

The European Union (EU) has acted on various scientific recommendations by setting limits for solid emissions from vehicles featuring DISI engines. In the US, the Environmental Protection Agency (EPA) and California Air Resource Board (CARB) have made similar moves, and Japan followed Bielaczyc *et al*. (2014). A summary of these legislative limits is shown in Table 1.2.

At the moment, the EU seems to be the leading regulatory body to have studied and decided on a specific target for regulating P_M mass and number called Euro 6, with its implementation in 2014. The target for Euro 6 standards is to narrow the gap of the

emissions standard between diesel and light duty gasoline vehicles Chambliss & Bandivadekar (2015). Euro 6 is being introduced in stages and is expected to be fully implemented within the 2015 - 2020 timeframe. The first step was the introduction of Euro 6a, where no particle number limits or On-Board Diagnostic (OBD) requirements are imposed on gasoline vehicles.

In the Euro 6b stage, all new vehicle registrations after September 2015 had to meet Euro 6 standards, including full Euro 6 OBD requirement but with a relaxed PN limit for GDI engines. After three years of implementation, or approximately in 2018, Euro 6 will enter its third phase called Euro 6c where the stricter PN emission limit (equal to the diesel limit introduced with Euro 5b) becomes mandatory for all gasoline vehicles, final OBD threshold limits will be enforced, and Real world Driving Emissions (RDE) requirements will be introduced. Together with this, a new driving cycle called the Worldwide Harmonized Light Vehicles Test Cycles (WLTC) will also be introduced to replace the New European Drive Cycle (NEDC).



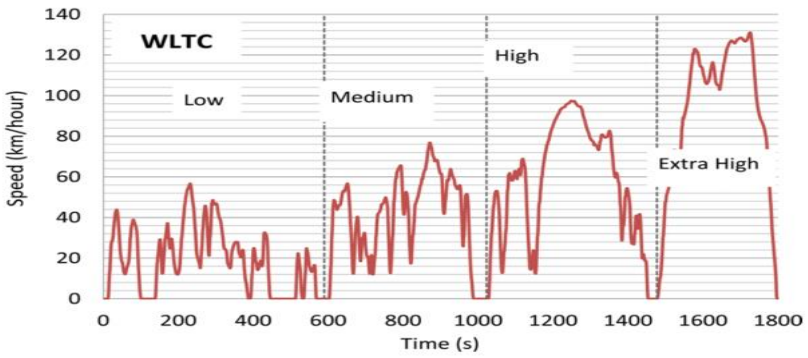


Figure 1.9: NEDC vs typical WLTC driving cycle. Adapted from Marotta *et al*. (2015)

In the US, despite being more strict and ambitious on reducing the PM magnitude, there are no efforts yet on regulating PN like many other countries. The California Air Resources Board (CARB) are targeting a reduction of 90% in PM in the span of more or less 12 years. For the case of the Environment Protection Agency (EPA), which regulates the remaining part of the US, sets a very challenging target of 1.86 mg/km. China on the other hand, runs a very similar regulatory program to the EU with both PM and PN being scrutinized. The implementation of these rules in China is slightly later than in Europe with the earliest only starting in the year 2020. China will also be adopting the WLTC beginning in 2023 after previously using the NEDC cycle. This information will be crucial to many vehicle manufacturers as China is known to be one of the biggest light duty vehicle markets in the world.

In Europe, as far as P_M measurements are concerned, there has been report of GDI type vehicles failing to even meet the Euro 5 limits when running the NEDC test. With the switch to the WLTC, vehicles are expected to undergo a more rigorous test that features more dynamic profiles and higher mileage than the NEDC, as shown in Figure 1.9. As a result, the P_M emissions are expected to be higher when tested using this cycle when comparing similar vehicles. The WLTC has a 45% reduction in overall idling time, 90% reduction on overall steady state cruise condition and a 57% increase in overall acceleration

and deceleration times. Idling and steady state cruise conditions normally have constant fuel/load map and can be easily optimized to meet emissions as well as fuel efficiency requirements. When it comes to acceleration or deceleration conditions, the fuel/load map is normally transient and can require very thorough and diligent effort to control various engine parameters to achieve optimized conditions. These parameters include injection timing, injection duration, spark timing, valve timing or even boost control. All of which contribute differently in the production of P_M.

1.2.4. Factors influencing P_M emissions in GDI engine

1.2.4.1. Fuel composition

In GDI engines, while many factors that contribute to the emission of P_M, the fundamental concept for reducing its production is by having a homogeneous air fuel mixture. A homogeneous mixture gives a stable global air-fuel ratio in which the fuel properties can play a part to achieve this. The characteristics of the distillation range of a certain fuel and its composition do have an impact on the evaporation process and consequently the global air-fuel ratio and homogeneity. In normal gasoline, the heavy components (which are normally dominated by aromatics) cause high T90 values in the distillation curve characteristics. Due to this, fuel evaporation takes time and homogeneous mixture can be difficult to achieve which eventually leads to the production of P_M. This is evident in the research work of Sobotowski *et al*. (2015) whereby a range of gasoline fuels with different aromatics content were tested for P_M using the same vehicle. It was found that aromatics tend to have significant impact towards PM, PN and also PAH emissions. A report by the U.S. Environmental Protection Agency 2013 showed that there were correlations between the T90 and T50 of gasoline with the P_M emissions when tested on PFI engines. Aikawa *et al*. (2010) in their work, developed a PM index as shown in equation

1.1, which indicates the potential P_M emissions, using the vapour pressure and Double Bond Equivalent (DBE) of each component in gasoline.

$$PM\ index = \sum_{i=1}^{n} \left[\frac{DBE_i + 1}{VP_{(443K)i}}\right] W_{ti} \qquad (1.1)$$

Due to the availability of many variations of gasolines, Aikawa *et al*. (2010) used the PM index to show the distribution of PM indices from various commercially available fuels around the world as shown in Figure 1.10. This index system achieved a good correlation when tested with commercial gasolines that had selected pure components added. However, these tests were conducted using a gasoline PFI engine equipped test vehicle which is known to already produce very low amount of P_M as previously described. Leach *et al*. (2013) used a similar indexing system called PN index and tested various types of splash blended gasoline with independent control of volatility and DBE in an SGDI engine. The results of these tests again showed a correlation with the PN index which establishes the high impact of fuel composition towards the production of P_M. The PN index is shown in Equation 1.2.

$$PN\ index = \frac{\sum_{i=1}^{n}[DBE_i + 1]V_i}{DVPE(kPa)} \qquad (1.2)$$

In contrast to aromatics, oxygenates (alcohol fuels) when blended into fuel, be it diesel or gasoline, have often been reported to suppress the development of particulates. Although, it is not as straightforward as one might think. The main principle of how alcohol gasoline mixtures can reduce P_M emissions is by having additional oxygen molecules in the fuel.

The presence of oxygen in the fuel molecule reduces the concentrations of key intermediate species required for the formation of aromatic soot precursors Price *et al*. (2007). However, there are many different claims as to how alcohol helps to reduce P_M emissions. Vuk & Vander Griend (2013) reported in their research that the use of ethanol gasoline blends of E10, E30 and E50 resulted in reduction of P_M compared to E0 by concluding that the ethanol content promotes evaporation of the mixture which helps the atomization process. This conclusion is very debatable and might be incorrect. Alcohol, as pure fuels are less volatile than gasoline (commercially available). Therefore, when higher alcohol fractions are mixed into gasoline, the mixture becomes less volatile which can be a problem in a cold-start condition.

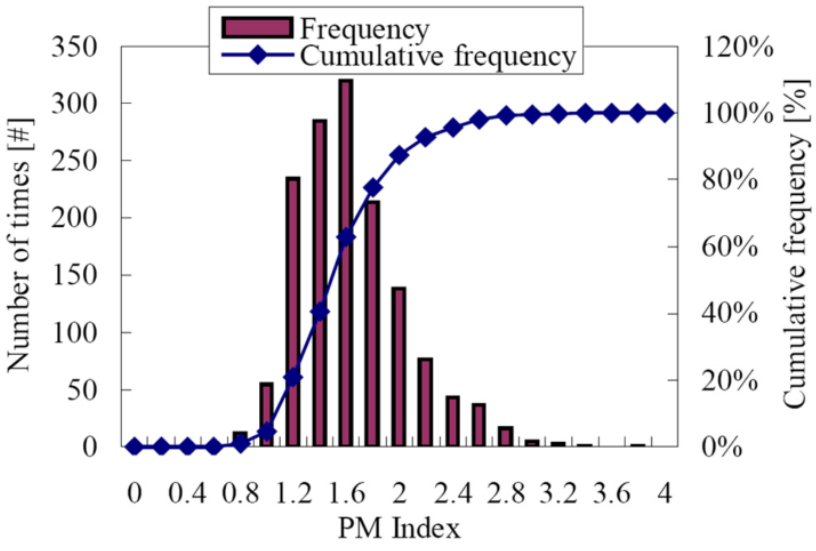


Figure 1.10: PM Index distribution of worldwide commercially available fuels (Aikawa *et al*. 2010)

The other problem is the energy content of a pure alcohol is much lower than the 45.8 MJ/kg of gasoline; e.g. methanol with 23 MJ/kg and ethanol with 29.7 MJ/kg. As a consequence of this, mixing alcohol into gasoline can lead to more fuel mass used for combustion in order to achieve stoichiometric condition which can cause more aromatics present per cycle despite being diluted. The effect will be more significant with pure

gasoline of high aromatics fraction blended with only small fraction of alcohol content. To make matters worse, pure alcohols, known to have very high latent heat of evaporation, can rapidly cool down surface temperatures if they make contact. This will be a problem for the engines using DI fuel system because gasoline alcohol mixtures might promote the creation of a liquid pool (on the piston surface).

The introduction of alcohol in gasoline changes many thermophysical properties of a mixture which in turn can produce many different findings in respect of the particulate emissions. In a report by Karavalakis *et al*. (2015), it was found that particulates in the accumulation mode were lowered by having a high oxygenate content and a low aromatics content in the fuel blend. The same trend was reported by Price *et al*. (2007) with various blends of oxygenated fuels such as E85, E30 and M30. In a report by Sobotowski *et al*. (2015) it was less evident however, for the case of lighter aromatics such as toluene whose boiling points fall well below the gasoline distillation end point. Chen *et al*. (2012) when testing gasoline ethanol mixtures in GDI engine reported an increase in PM as well as PN in the accumulation mode as the ethanol fraction is increased. Chen *et al*. (2012) claimed that the due to the high latent heat of evaporation, evaporation slows down and causes air fuel mixture in-homogeneities.

1.2.4.2. Spray characteristics and atomization

In order to achieve homogeneity in mixture preparation, fuel injected in the cylinder has to evaporate rapidly within the short period of time in an engine cycle. As there are many constraints and limitations from combustion chamber geometries to achieve this, the focus shifts to the injection system to manipulate the spray development. There are currently several popular methods of improving atomization in GDI engines being studied around the world; utilizing very high injection pressures, detailed (up to 350 bar)

manipulation of the injector nozzle flow holes (length to diameter ratio optimization) and non-deliberate/deliberate use of flash boiling in injection. All of which have a main purpose of reducing the fuel spray droplets size to promote evaporation Oh *et al*. (2011), Whitaker *et al*. (2011), Oudenijeweme *et al*. (2015), Farron *et al*. (2011), Xu *et al*. (2013) and Piock *et al*. (2011). Increasing the injection pressure produces a spray with a very high velocity that increases the potential for spray impingement which in turn counteract the effects of achieving better atomization. It is hypothesised in this research however, that flash boiling, even though managed to reduce droplets size, creates a different scenario that may not necessarily reduce P_M in GDI engines. Therefore, the flash boiling method as a means of P_M reduction is further studied in this research.

For the case of GDI engines using a homogeneous mode at part load operation, there are several pre-requisites for conditions that will lead to the occurrence of flash boiling during injection:

1. Fuel is heated to high temperature of close to 100°C through conductive heat transfer from the engine coolant in the cylinder head as well as combustion. Gasoline, which has a high saturation vapour pressure will already be close to a superheated state at this point. This happening is inevitable due to the close proximity of the DI injector to the combustion chamber.
2. Injection during the intake stroke; rapid movement of the piston causes the in-cylinder pressure to become sub-atmospheric (0.3 to 0.5 bar). Injection of gasoline at this stage increases the saturation vapour pressure ratio even more which causes the fuel to be definitely at a superheated state.

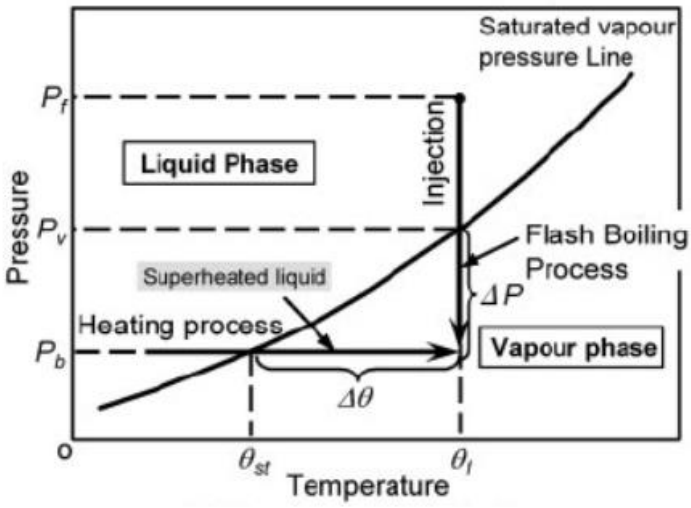


Figure 1.11: Typical saturated vapour pressure plot of a liquid fuel used as an explanation to how flash-boiling is achieved

This flash boiling phenomenon in GDI engine is better explained in Figure 1.11 which shows the fuel saturation vapour pressure against temperature. Flash boiling is a well-known phenomenon and is being utilized in many applications. The fundamentals of flash boiling development can be visualized as a hot fluid flowing through a nozzle as shown in Figure 1.12. The fluid is normally heated to a very high temperature and highly pressurized, causing it to be pushed through a small opening to a volume of significantly lower pressure; to a pressure significantly lower than the vapour pressure of the fluid. This depressurization event can be assumed to be almost instantaneous, so that the fluid attains a meta-stable state and any disturbance of the fluid can lead to the spawning of tiny vapour bubbles known as nuclei Neroorkar & Schmidt (2011). The nuclei will grow into larger bubbles because of the continuing vapour formation at the bubble surface. This entire process, starting from nucleation, is called flash boiling. The amount of vapour build-up in the nozzle governs the characteristics and physical shape of the spray.

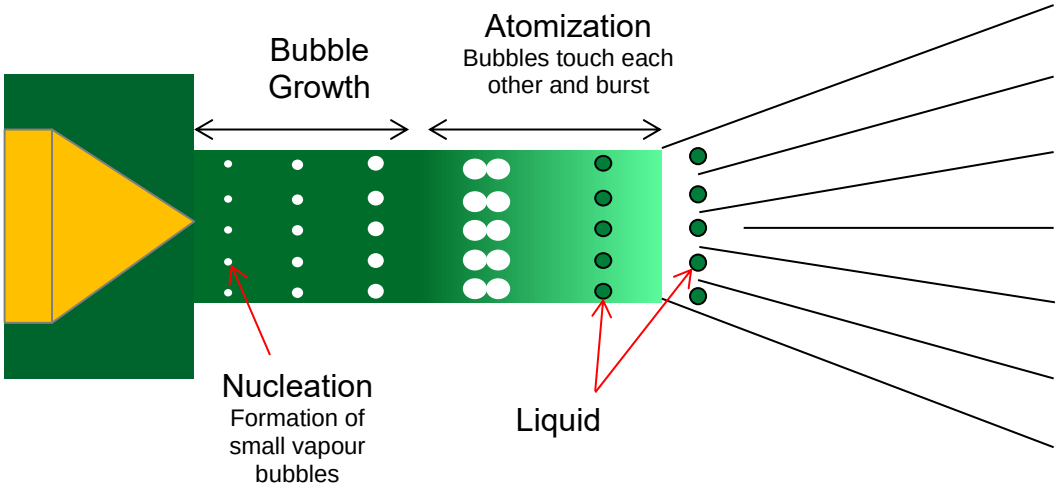


Figure 1.12: Development of flash boiling in a nozzle. Adapted from (Neroorkar & Schmidt 2011)

Since flash boiling normally occur in a very fast-moving fluid such as fuel injection, observation and any measurements of the event can be difficult without the help of high-speed camera. Even so, it will be difficult. To easily categorize the severity of a flash-boiling event, much of the literature in GDI engines has used the saturation pressure ratio, P_R:

$$P_R = \frac{P_{sat}}{P_{amb}} \qquad (1.3)$$

where P_{sat} is the injected fuel saturation vapour pressure and P_{amb} is the ambient pressure exposed to the injected fluid.

As a result of flash boiling, the spray structure and pattern are changed substantially. Many researchers have reported these changes in spray formation when flash boiling is observed Aleiferis & Van Romunde (2013), Parrish *et al*. (2010), Zeng *et al*. (2012), Chan *et al*. (2014), Price *et al*. (2015), Araneo & Donde' (2017); note that these findings are only from spray-guided injectors. Other types of injectors produce different results during flash-

boiling conditions and may not be relevant to this research. With flash evaporation sprays, the:

1. Individual spray jet cone angle increases as the saturation pressure ratio increases,
2. Spray penetration of individual jets decreases as pressure ratio increases,
3. Spray plumes coalesce between each other (as the pressure ratio increases) to combine into a single jet to produce a collapsed spray structure.

Despite a considerable amount of work looking into the flash-boiling condition in GDI injectors and the benefit claimed due to this phenomenon, there has been very little data that correlates directly of the effects of flash-boiling towards the production of P_M. Most of the research normally only observed a reduction in Sauter Mean Diameter (SMD) of the flash-boiling sprays and vaguely claimed that this will improve P_M emissions.

Flash-boiling has been observed before in a research relating to ICEs including Diesel engines. Kawano *et al*. (2001) in their research deliberately introduced flash boiling to the injection process, by mixing higher volatility fuel to a lower volatility fuel. And it was reported that the presence of flash boiling in the diesel injection led to significantly reduced particulate matter emissions. However, there was a trade-off, as NOx levels increased when flash boiling was present. In other research by Serras-Pereira *et al*. (2010), a custom designed nozzle channel was used to investigate flash boiling through imaging at a microscopic level. It was reported that spray angles were larger in locations where cavitation developed and an increased level of flash boiling showed a significant reduction in liquid penetration. Serras-Pereira *et al* also state that the characteristics of spray break-up for gasoline, n-pentane and iso-octane were the same at a 20^{o}C fuel temperature but all the fuels have different spray geometry changes and spray break-up times when heated to 120^{o}C.

The research by Zeng *et al.* (2012) showed a very detailed investigation on the spray characteristics and structures by using three single component fuels. Zeng *et al* categorized the results into three regions of spray structure which are: flare flashing, transition flash and non-flash boiling regions.

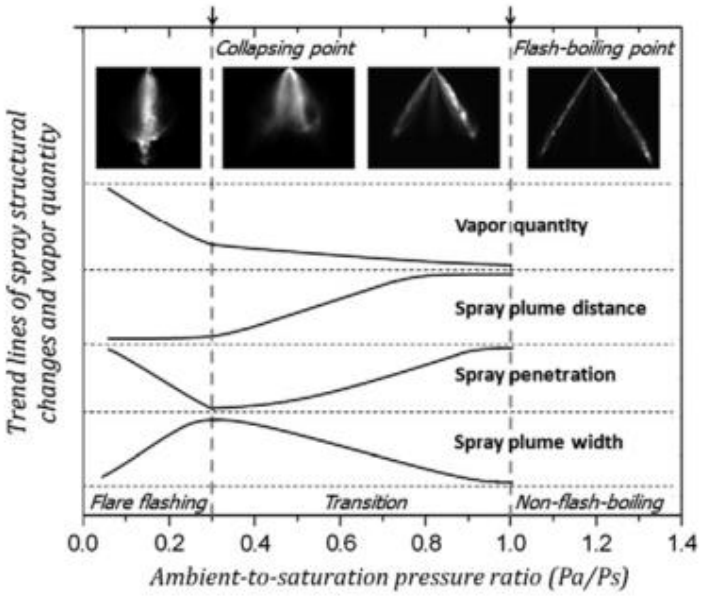


Figure 1.13: Categorization of flashing stages using saturation pressure ratio. Adapted from (Zeng et al. 2012)

It was also shown that changing the pressure ratio could lead to significant changes in the spray structure. In particular, the vapour quantity reduction as the pressure ratio drops is expected as the liquid evaporates faster with a higher temperature especially in the superheated region. Zeng *et al* also report that spray penetration is reduced in the transitional regimes as the pressure ratio is reduced, but after the tipping point at about a pressure ratio of 0.3, the flare flashing regime shows that penetration increases as the pressure ratio is reduced below 0.3. This contradicts some of the reports discussed in the next section that say spray penetration will decrease if the fuel is superheated and flashes.

While many expect flash-boiling spray to produce homogeneous mixtures in the combustion chamber, this may not be the case when the spray is subject to piston/wall impingement.

1.2.4.3. Wall/piston impingement of fuel sprays

Fuel impingement on cylinder wall/piston is one of the biggest contributors towards the production of P_M in a GDI engine. Though most of the findings are from a wall-guided GDI engine, the new SGDI systems are thought to have a similar problem. For an SGDI engine using a homogeneous mode, fuel injected during the intake stroke will be very likely to impinge on the piston and create a liquid pool. This is followed by a sooty diffusion flame from a pool fire during combustion Stevens & Steeper (2001). This is evident from the works of Velji *et al*. (2010) whereby formation and oxidation of soot for homogeneous and stratified operations were imaged and compared using laser techniques. For the case of oxygenated gasoline mixtures, the chances of having a liquid pool on the piston is much higher as alcohol is known to have a high latent heat of evaporation. Oxygenated mixtures, when impinged onto a piston surface will significantly cool the surface temperature more than gasoline Serras-Pereira *et al*. (2013). Despite its advantageous properties of providing more oxygen molecules, alcohol mixtures can present an even more troublesome trait.

Strategies to avoid fuel impingement in an SGDI engine usually end up contradicting the main objective of achieving a faster rate of fuel evaporation. e.g. by decreasing injection pressure, the spray velocity is reduced, and the impact of spray impingement is then also reduced, but at the expense of producing bigger fuel droplets which will diminish the evaporation rate. Another example is by injecting fuel late into the intake stroke, so that the injector tip distance to piston surface can be maximized, but this is countered by the reduced amount of time left for fuel evaporation. Multiple injections are another strategy to

minimize wall/piston wetting. Berndorfer *et al*. (2013) reported increased PN particularly when multiple injections strategy was used at cold engine conditions but surprisingly also in the warm conditions. It was also reported that multiple injections strategy causes an overall increase in the presence of larger droplet sizes that are normally found at the beginning and ending of an injection event.

Flash boiling has the potential to prevent the formation of a liquid pool on the piston surface. Chen *et al*. (2013) found in their research work that by introducing flash boiling, the penetration of the spray plume was reduced as compared to non-flashing sprays. As a result, a detailed quantification from the imaged spray showed that surface impingement is reduced by up to 40%. There is however very limited data on the dynamics of impingement from a flash-boiling spray in GDI engines. Most of the data comes from work on spray cooling for surface heat removal purposes.

One of the closest spray cooling comparison to the conditions similar in a GDI engine can be found in the work of Cheng *et al*. (2015) where Vacuum Flash Evaporation Cooling (VFEC) was studied. In VFEC, the flashing spray impinges on the heating surface in vacuum environment, removes heat from the surface by both flash evaporation and convection, resulting in intense, short duration cooling. This is very similar to the injection event and in-cylinder conditions found in a GDI engine running with a homogeneous mode. It is claimed that the heated surface experienced a higher reduction of temperature due to impingement of flash boiling sprays. In another work by (Cheng *et al*. 2012), the flash boiling spray is claimed to have produced a more uniform surface temperature reduction when impingement occurs. The flash boiling impingement phenomena is one of the aspects that will be explored further in this work to improve P_M emissions.

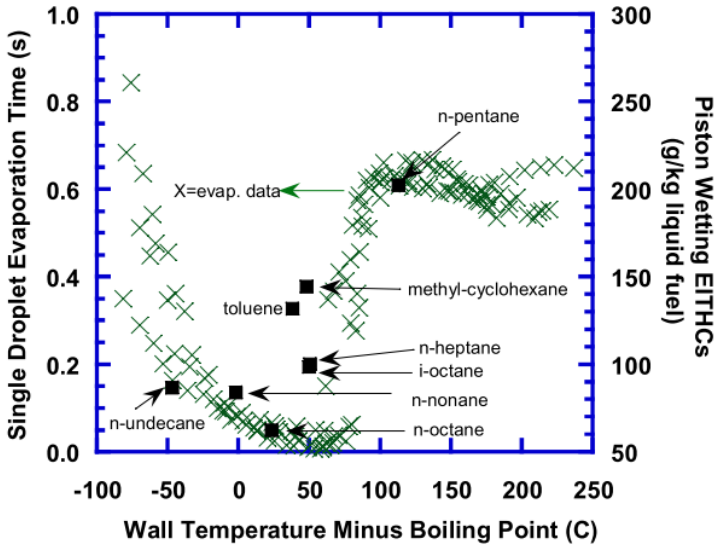


Figure 1.14: The Leidenfrost curve, Huang *et al*. (2001)

To prevent pool fires from occurring, spray cooling of piston surface needs to be reduced. However, understanding spray impingement on solid surface in depth can be very complex as there are so many parameters that can influence the fluid dynamics of fuel droplets, namely: surface tension, viscosity, density and temperature of liquid, diameter, velocity, and impact angles, Samenfink *et al*. (1999). There has not been much research done on spray impingement, be it on a research engine or on a benchtop rig. While it is difficult to segregate the effects of many different parameters that effects spray impingement in an engine, similar experiments conducted on a separate rig lack the transient parameters such as piston movement and a repetitive environment. Many have attempted to relate the spray-wall interactions based upon a knowledge of single droplet impacts. The studies of single drop impingement have been essential to understanding the relational character of spray impaction. However, these studies fail to quantitatively describe accurately many of the important phenomena occurring in dense sprays. It is mostly due to their inability to take into account the complex drop to drop interactions. It is important to close the gap between studies of impacting sprays and that of individual droplets, Moreira *et al*. (2010).

Trying to use single droplet data to backup dense spray results can lead to discrepancies. This is the case with the Leidenfrost phenomenon, which is one of the most debated issues when it comes to spray impingement in an engine. In the work of Warey *et al*. (2002), the authors analysed the size and mass of P_M emissions from a GDI engine using the Leidenfrost curve evaporation data (single droplet evaporation rate) to explain the Leidenfrost phenomena as shown in Figure 1.13. It was found that n-pentane, a very volatile fuel, when used in GDI engine produced bigger PM and PN magnitude than that of a less volatile fuel such as n-undecane. It was suggested that the Leidenfrost phenomenon occurs when liquid impinging on a surface with a temperature of significantly higher than of the liquid saturation temperature, forms a vapour layer underneath the fuel film resulting in a much slower overall evaporation due to lack of heat transfer. Huang *et al*. (2001) concluded in their literature that the Leidenfrost phenomenon did occur when fuel film is vaporizing from a piston top. This is proved by presenting the hydrocarbon (HC) emissions due to wall wetting as a function of the difference between piston temperature and the boiling point. The HC emissions data seems to correlate very well with the single droplet evaporation time.

While the impact of heat transfer from Leidenfrost phenomena is very much discussed among much single droplet experiment literature, it is not the case with experiments using dense spray. When devising an empirical correlation for heat transfer, most of the works focused on the liquid to solid contact parameters. However, there are discrepancies on claims for which parameter majorly governs the heat transfer at spray impact. These are a number of claims by many researchers which have been comprehensively summarized by Moreira *et al*. (2010): Velocity of the impacting droplets normal to the surface, time of contact, volume flux or mass flux, ratio between inertial and surface tension forces at impact, and wall superheating degree (T_{surf} - T_{sat}).

It is undeniable that piston/wall impingement will somehow occur in an SGDI engine across a wide range of operating conditions despite multiple ways of optimizing the spray behaviour. The way forward is to improve on film evaporation which can be done in many ways such as the manipulation of fuel composition or optimizing piston thermal properties.

1.3. Chapter summary

In this chapter, the GDI engine has been established as the current best technology that will be utilized for many years. Although many versions of the GDI engine are being explored such as wall-guided and air-guided DI systems, the homogenous mode SGDI engine is currently the preferred choice to be optimized in achieving the latest fuel efficiency and emissions legislation limit of Euro 6, particularly on PM and PN. Various legislation limits and methods from different areas of the world has been reviewed in this chapter. Based on many findings, a GDI engine is producing even more P_M than a diesel engine fitted with a DPF. Continuous exposure of P_M can lead to many health issues such as respiratory diseases, premature mortality, and cardiovascular diseases. As discussed in this chapter, there are new evidences that the impact would be much worse for human exposure towards ultrafine particles (size < 100 μm). These particles are known to be found in the emissions from GDI engines. The effects of fuel composition, spray dynamics for atomization and spray impingement on particulate emissions have also been reviewed in detail. These factors will be explored further in this research for better understanding.

2. Experimental Facilities and Analysis Tools

2.1. Introduction

As discussed in chapter 1, the problems with the SGDI engines were in achieving mixture homogeneity after the fuel injection event and several factors were listed that are known to influence this: fuel composition, spray development and efficient atomization, spray wall/piston impingement and in-cylinder conditions.

Several different compositions of model fuels were used throughout all the experiments, Fuels A, B, C, D contained 15% by volume methanol and fuels, Fuel E and Euro 5 contained no methanol. These will be described in detail in Chapter 3, with the fuel compositions given in Table 3.1. In order to understand better the sources of PM from GDI engines from these fuels, a series of studies was undertaken ranging using fuel spray imaging to particulate measurements from a single cylinder optical engine:

1. Spray rig tests to isolate the effects of fuel volatility/fuel temperature on vaporization rate, flash boiling characterization, homogeneity characterization and penetration (by eliminating air motion).
2. Spray impingement tests using the spray rig with a surrogate piston to investigate the effects of spray cooling using high sampling rate Thin Film Gauge (TFG) surface thermometers and potential fuel liquid pool formation on piston surface.
3. Fuel vapour pressure validation using a two-chamber measurement device in a temperature controlled bath to assess the accuracy of the UNIFAC correlation method predictions of the vapour pressure.
4. Motoring tests in an optical engine with a full optical liner in order to investigate interaction of the spray with the intake air motion and to assess the amount of impingement on the piston at different injection timings.

5. Combustion imaging through a quartz optical annulus at around 20°ATDC and onwards using a firing optical engine, with accompanying combustion burn rate analysis, in order to assess: the potential presence of diffusion flames resulting from piston impingement, the intensity of soot luminosity, and the effect of the spray character on the burn rate and combustion variability.
6. Particulate measurements for both the metal engine build and the engine build with the quartz optical annulus. This gives PM information at various fuel temperatures for comparison with combustion and spray images and metrics, allowing analysis of the contribution to PM from some of the different available sources, i.e. piston/liner impingement, poor vaporization rate/available time for vaporization, poor homogeneity, surface temperatures (annulus/piston material), in-cylinder rich combustion.

To achieve all the described experiments, various types of equipment were used throughout this research. This chapter will go into the details of all the equipment and analysis tools used and what was also developed.

2.2. Single cylinder optical engine

A single cylinder optical engine has been the choice for many researchers when investigating combustion characteristics due to the versatility of its build. The optical engine used for this research has a fixed cylinder head structure which imitates the Jaguar AJ133 combustion system, and it has a modular cylinder barrel build where many types of optically accessed components can be assembled. One of the prominent features of this optical engine is the Bowditch piston assembly which houses a static 45-degree mirror for optical access from underneath the piston as shown in Figure 2.1 (a) and 2.1 (b).

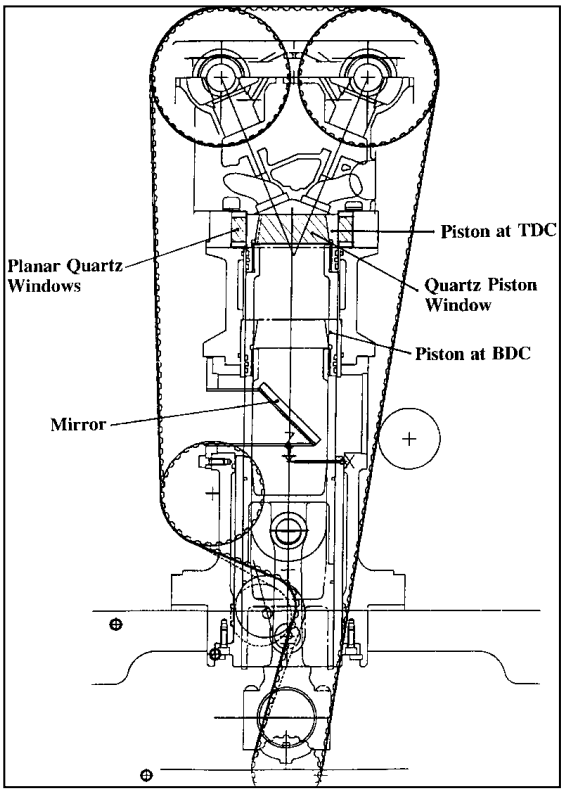


Figure 2.15 (a): Typical schematic of an optical engine with Bowditch piston and mirror installed.

Usually, images are taken through the mirror but for this research, a high-power LED is used with the mirror to illuminate the spray in the combustion chamber (refer to Figure

2.6). With this arrangement, the combustion chamber can be illuminated more uniformly and any unnecessary reflection from the cylinder liner can be avoided.

Having only one cylinder in this engine helps to reduce the cylinder operating variations that can be very difficult to control. Single cylinder engines also minimize the fuel usage which can be very costly, as in this work they are blended from pure components. As the engine is designed for optical access metal piston rings with lubrication could not be used, therefore Torlon rings were used. This setup is beneficial for this research as running without any lubrication will eliminate any influences of engine oil in producing P_M. To extend the piston rings lifespan with fired operation the cylinder barrel is built with a coolant jacket to reduce the wall temperature during operation. Other than that, the engine has to operate below 2000 RPM due to the high mass of the Bowditch assembly and bearing loads. The full specification of the optical engine is shown in Table 2.1.

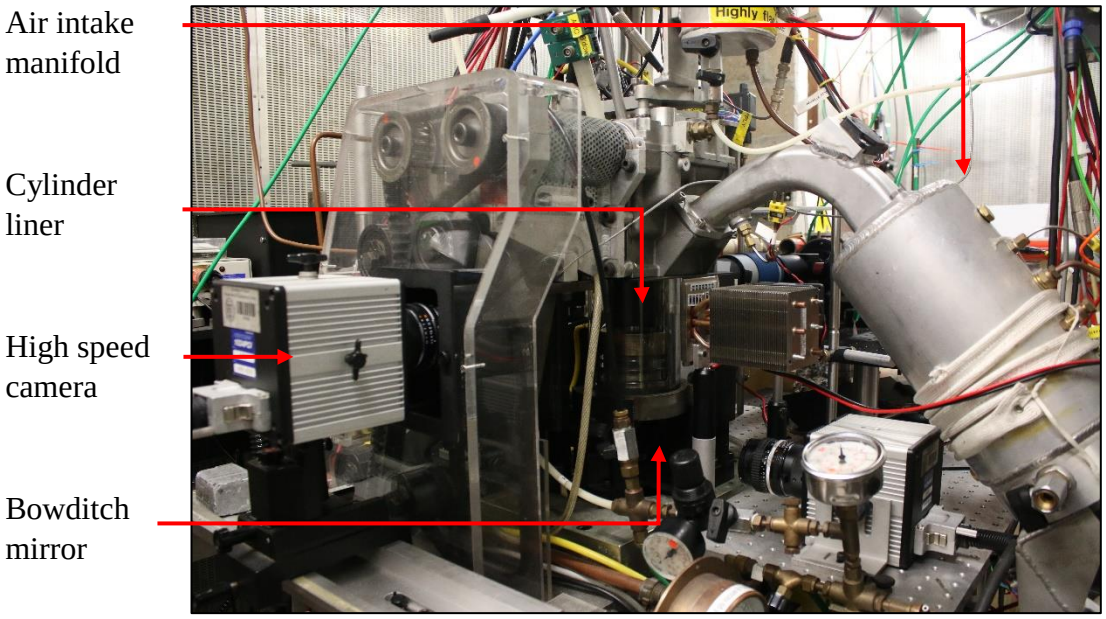


Figure 2.1 (b): AJ133 Single cylinder optical engine with Bowditch piston assembly.

Table -2.3: Single cylinder optical engine specification

Bore (mm)	89
Stroke (mm)	90.3
Cylinder capacity (cc)	562
Compression ratio	11.1
Direct injection fuel pressure (bar)	150
Port fuel injection pressure (bar)	3
IVO (CAD aTDC)	33.5
IVC (CAD aTDC)	241.5
EVO (CAD bTDC)	245
EVC (CAD bTDC)	5

The engine is connected to a DC dynamometer with a Control Techniques Four-Quadrant Controller. As for fuel delivery, the engine is equipped with port fuel injection and also the centrally mounted in-cylinder direct injection system. The PFI system is capable of supplying fuel at a pressure of up to 4 bar while the direct injection system uses a Heypac high pressure fuel pump that is normally operated at 150 bar. The fuel pressure of the DI system is closely monitored by having a pressure transducer mounted in the high-pressure fuel line with a calibration of 50 bar/V. Having two injection systems gives an added advantage; in the case of particulates measurements experiment, the PFI system is used with just iso-octane to warm the engine up until the exhaust temperature reaches about 300^{o}C (at least 10 minutes of engine operation) before then switching to the DI system with the blended test fuel.

The injector for the direct injection is a multi-holes six nozzles spray guided injector provided by Jaguar Land Rover. The injector holes are designed for the AJ133 engine to

meet a specific targeted spray foot print. Figure 2.2 shows the position and assembly of the injector in the cylinder head, which also shows the intended spray pattern of the SGDI system in the combustion chamber.

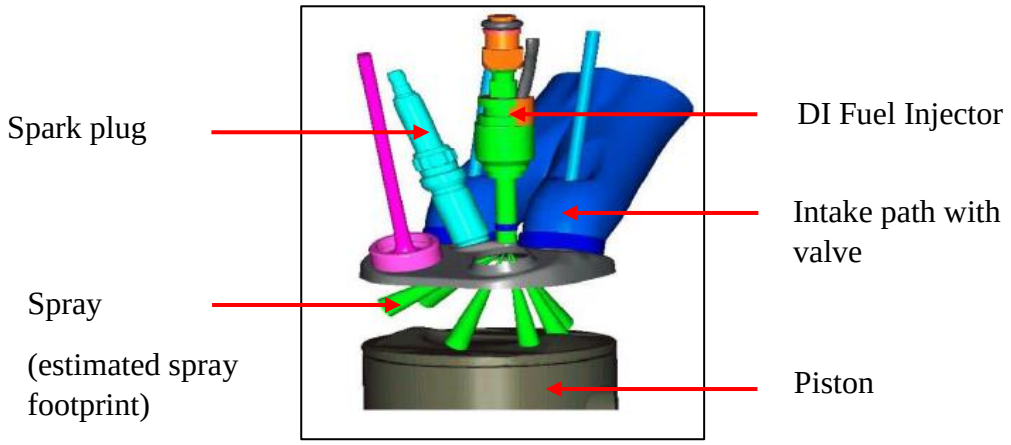


Figure 2.2: AJ133 Combustion system layout. Taken from (Sandford *et al*. 2009)

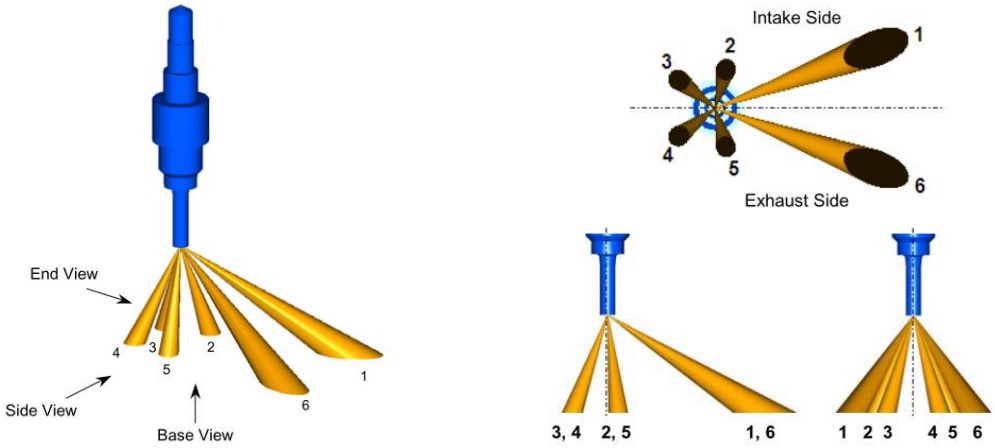


Figure 2.3: AJ133 6-multi-hole spray guided injector estimated spray footprint used in this research. (Serras-Pereira et al. 2007) used the same injector for their study

The AJ133 multi-hole spray guided injector is a vertical, centrally mounted, and positioned in a close spacing arrangement with the spark plug. Two distinctly symmetrical group of plumes are available on the intake and exhaust side of the optical engine as shown in Figure 2.3. Plumes numbered 1, 2 and 3 have different plume angles to each other, with

plumes 1 and 6 having the largest angle to the central axis of the injector. Plumes 1 and 6 are specifically designed to straddle the spark plug for when the engine is running in a stratified mode.

Thermocouples are installed in the intake, exhaust, fuel and cooling system to measure and record temperature readings. The volume flow rate of the air is measured using a Roots type positive displacement flow meter. In-cylinder pressure is measured using a water-cooled Kistler 6041A piezoelectric pressure transducer mounted in the cylinder head. The inlet air pressure is measured by a DRUCK PDCR A20-0800 transducer while exhaust pressure was measured by a water-cooled Kistler 4074A10 piezoresistive pressure transducer. The intake air can be heated and is controlled by a West self-tuning PID controller.

2.2.1. Optical engine build combinations

The optical engine has an almost similar specification to the AJ133 except that the cylinder block components are interchangeable and made of different materials. The nominal compression ratio is slightly reduced to make the optical components more durable. The single cylinder optical engine is designed to accommodate optical access for various research purposes (shown in Figure 2.4), therefore the components may not possess the same heat transfer characteristics as in conventional engines. This is one of the essential points that must be highlighted in this research because fuel impingement studies and the formation of particulates are dependent on the heat transfer characteristics of the different materials on the combustion chamber surfaces.

Engine components with different materials are used for this research in this engine; ranging from high grade Torlon piston rings, steel cylinder liner, full fused silica ('quartz') liner, fused silica annulus, aluminium alloy annulus to titanium alloy piston shell with a fused silica window or mild steel blank (Figure 2.5 (d) and (e)). To further understand the capabilities of the modular engine assembly, Table 2.2 gives an overview of type of cylinder barrel configuration used and each individual purpose in this research.

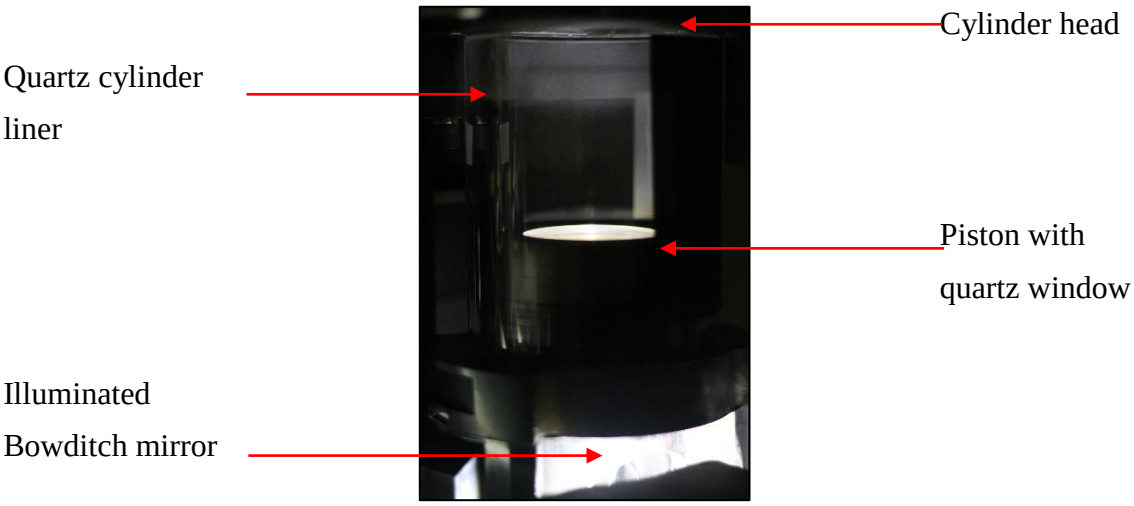


Figure 2.4: Example of combustion chamber illumination technique adapted for spray imaging during motoring

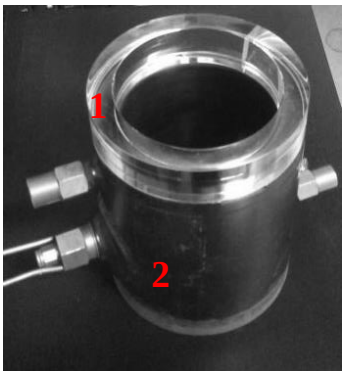
Assembly of various different optical engine setup

Cylinder Liner Combinations



Full quartz liner

(a)



(1) Quartz annulus
(2) Steel cylinder barrel

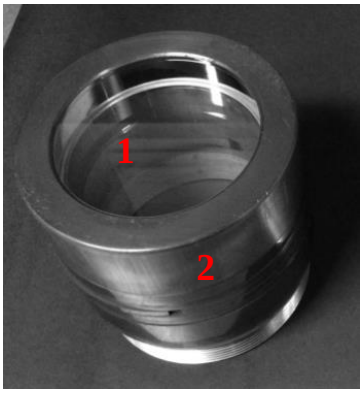
(b)



(1) Aluminium annulus
(2) Steel cylinder barrel

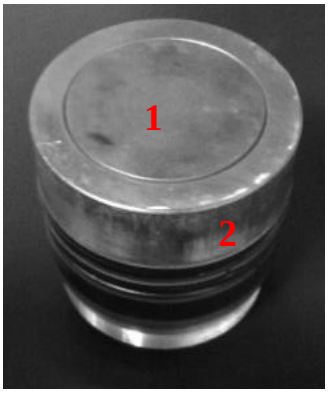
(c)

Piston Combinations



(1) Quartz Piston Window
(2) Piston Housing

(d)



(1) Steel Blank
(2) Piston Housing

(e)

Figure 2.5: Combination for all different optical engine setups; (a) – Full quartz liner with no liner water cooling, (b) – Quartz annulus coupled to a water-cooled steel liner with barrel pressure transducer, (c) - Aluminium annulus coupled to a water cooled steel liner with barrel pressure transducer, (d) Piston housing coupled to a quartz window (e) Piston housing coupled to a steel blank piece.

Table 1.4: List of engine built combination and the possible test procedures

Cylinder barrel assembly	Annulus	Piston Type	Experiments conducted
Full quartz barrel	None	Quartz piston window	1. High speed imaging of spray during motoring for spray characterization 2. High speed imaging of spray during motoring for Mie-scattering analysis 3. High speed imaging of spray during motoring for spray impingement study
Semi metal barrel	Quartz	Quartz piston window	1. Side view combustion imaging through annulus 2. Spray impingement and pool fire visual analysis 3. Particulates emissions investigation using Cambustion DMS500
		Full metal piston	1. Side view combustion imaging through annulus 2. Spray impingement and pool fire visual analysis 3. Particulates emissions investigation using Cambustion DMS500
Full metal barrel	Aluminium	Full metal piston	1. In-cylinder homogeneity analysis using Fast FID probe. 2. Particulates emissions investigation using DMS500 using various fuel compositions and injection strategies

2.2.2. Engine operating conditions and components durability

All of the experiments were conducted at low speed part load conditions; the engine was operated at 1000 RPM with a throttle opening of ~15% to give a manifold inlet pressure of 0.5 bar. This condition gives an opportunity for the superheated fuel to flash when sprayed into the chamber due to the significant drop in pressure. The cylinder head temperature was varied by controlling the heater in the engine coolant system and left to soak at a given temperature for at least 20 minutes before starting the experiment. This was to make sure that the fuel temperature in the injector was close to the same temperature as the cylinder head. The selected temperatures were 23°C, 60°C, 90°C and 105°C. The intake air was heated to 40°C to maintain consistency of the intake temperature as ambient air temperature changes from day to day. The air heater will only turn on when the engine is operating, so normally the engine was motored for few minutes to allow the heater to reach the required temperature before turning on the ignition.



Figure 2.6: Damaged standard gap piston rings and guide ring used in quartz liner that show evidence of overheating

Engine piston rings were normally inspected after a series of experiments and replaced if they had worn. The piston rings used for experiments with the metal cylinder barrel had the standard ring gap of 0.6 mm. For the case of the full quartz liner, the rings had to be gapped to 1.0 mm to account for the hotter operation of the rings when using the quartz liner. Compression pressure as well as intake pressure will be lowered if the piston

rings were damaged which could give inaccurate data. Figure 2.6 shows example of damaged standard piston rings that were used in the full quartz liner.

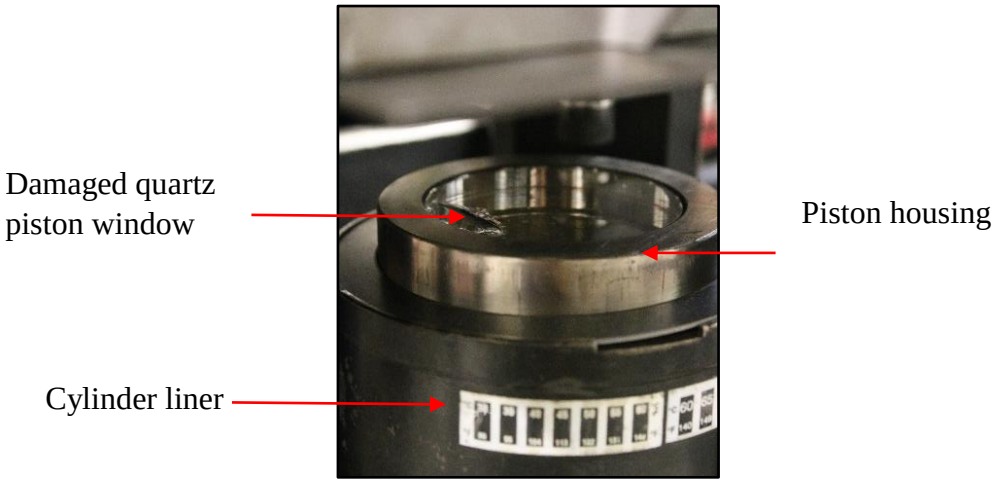


Figure 2.7: Example of damaged quartz piston window after several hours of intermittent use with combustion events.

All experiments using quartz components, which are known for being quite fragile and easily damaged as shown in Figure 2.7, were restricted to a maximum running time of 30 minutes regardless of whether the engine was in motoring or combustion mode. This was to let the quartz components cool down, which can improve durability and component integrity. Excessive temperature on the quartz liner or the annulus can lead to melting of the piston rings and guide rings due to excessive expansion, which in turn results in them ceasing to function and can damage the liner surface. The downtime period was normally used for cleaning the quartz component surfaces to maintain the imaging quality of the combustion or spray images. Soot as well as fuel deposits can build up on the quartz components and distort light to the high-speed camera.

One of the procedures that was considered essential when conducting these experiments was the changing of the existing test fuel to a different fuel blend. In order to maintain the composition of the new test fuel, the existing one had to be drained from the

fuel tank as well as the fuel line. Existing fuel in the tank was drained through the valves installed at the bottom of the tank. The only fuel left in the fuel system was low enough to be used during the engine warm-up phase.

2.2.3. Engine controls and data acquisition system

Engine basic operation, LED and camera triggering are controlled using the Engine Timing Control System (ETCS) panel as shown in Figure 2.8. Selection of fuel system, injection timing as well as duration can be changed according to desired operating conditions in this panel. The ETCS program was developed on the LABVIEW coding platform and connected to a National Instruments PCI–6602 high-speed counter/timer card. The DAQ systems consist of High Speed Data Acquisition (HDAQ) and also Low Speed Data Acquisition (LDAQ) system using PCI-6024E DAQ cards.

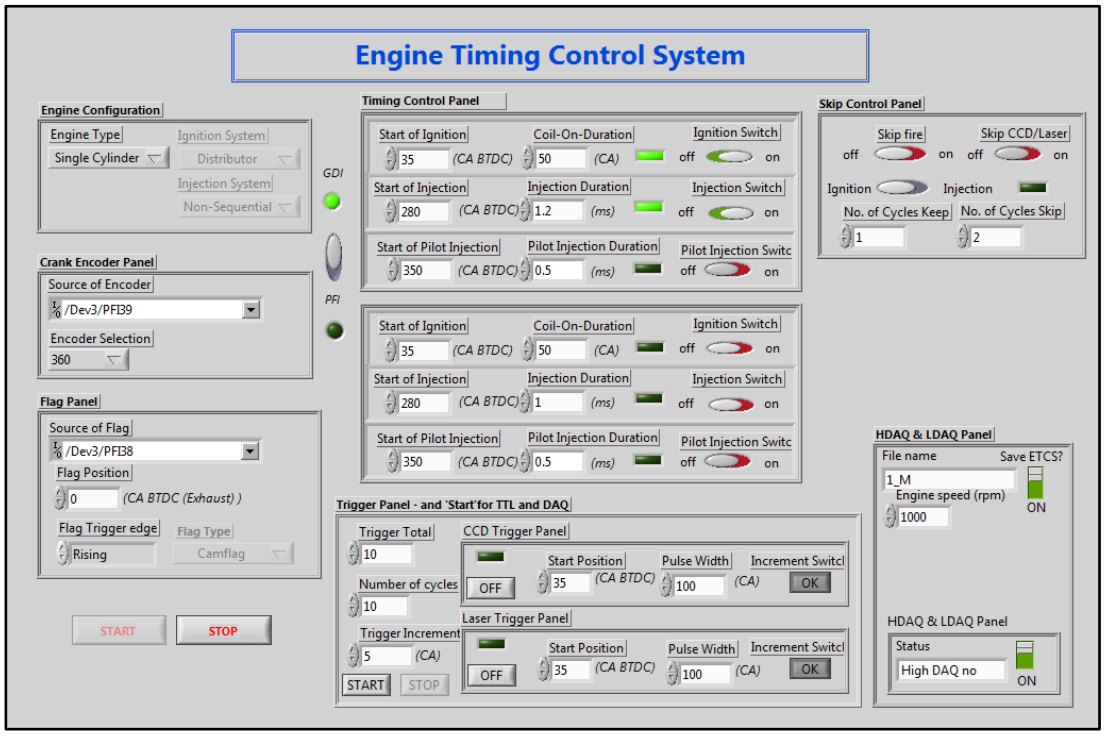


Figure 2.8: Graphic User Interface (GUI) of ETCS control system

Data that requires high frequency sampling such as in-cylinder pressure is recorded on the HDAQ system while lower frequency data such as intake air temperature is recorded on the LDAQ system. Full details of the software and hardware can be found in (Wang 2008). Previously, the DAQ system was operated in a different computer to the ETCS. The latest version of the software has now both ETCS and DAQ systems together in one computer to ease operation. When collecting data, the start button on the trigger panel is pressed first to send trigger signals to the LED and camera, then move over to the DAQ panel to press the green "log data" button (shown in Figure 2.9) to start logging engine data. For each experiment, a total of 300 cycles of engine data is normally logged. This is enough to give a good ensemble average of the data.

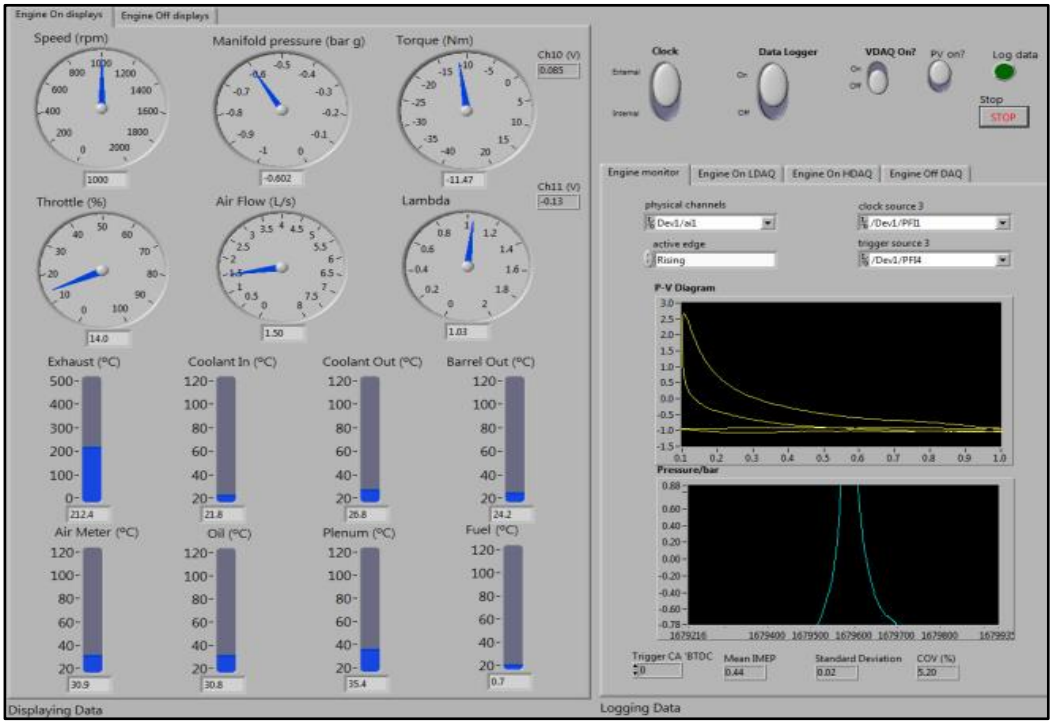


Figure 2.9: Graphic User Interface (GUI) of the DAQ system

The following are the example of important engine parameters that are logged from this software; Engine speed, engine torque, thermocouple temperatures, air flow rate, ignition timing, inlet manifold pressure, in-cylinder pressure, crank flag, injection timing

and air-fuel ratio. These data are used for post-processing in an in-house built engine analysis program called COBRA, to calculate important engine combustion behaviour such combustion burn rate, miss-fire estimations, in-cylinder pressure trace. Figure 2.10 shows the schematic of the typical optical engine hardware setup and how the communications are linked.

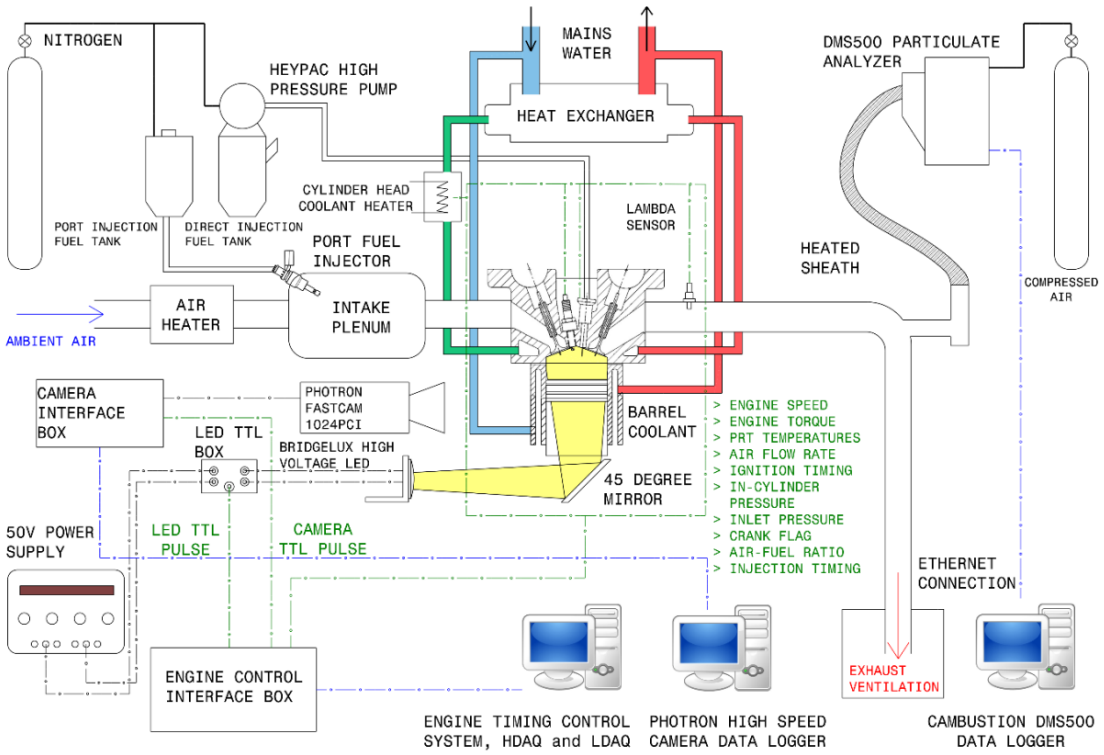


Figure 2.10: Schematic overview of a typical optical engine experiment setup utilizing the Bowditch mirror for illumination of combustion chamber

2.3. Optical Spray Rig

2.3.1. Spray rig setup and controls for spray characterization experiment

The optical spray rig was designed and built to allow for accurate imaging of the fuel spray behaviour, however there can be slight differences to the actual spray that is being injected into an ICE. Accurate imaging can be achieved due to the static nature of the operation as there are no moving pistons or valves that can create air entrainment and disturb the spray development during injection. With the spray rig, spray images can be obtained with better spatial access, less complication and fewer controls than are normally associated with optical engine operation. The spray rig uses the same quartz liner from the optical engine which has a cylinder bore of 89 mm and a visible axial length of 118 mm. The injector as well as the injector driver was carried over from the AJ133 Jaguar engine, and therefore should have similar characteristics.

The spray rig has been designed to meet the standards of air purging for spray characterization set by the SAE international (J2715 standard). The recommended mean purge velocity standard for any GDI injector test range from 1.3 m/s to 2.6 m/s (20 Hz injection frequency). For the test on fuel spray characterization, repetitive injections are utilized. If purging airflow is not operating correctly, residual drops from the previous injection may be present during the current injection being measured. A uniform, low velocity, flow field is a necessity, with the primary parameter being the mean axial velocity of this purging stream. The goal is to remove the residual drops and fuel vapour out of the test volume during the dwell period between consecutive injection events, and to achieve this without adversely influencing the spray parameters. It has to be noted that this standard was introduced about a decade ago in which GDI injectors used were mostly swirl injectors.

However, the type of injector should have minimal influence upon the rig design as it is only the spray geometry that is different while the fuel mass flow remains similar.

All of the experiments conducted on the spray rig for this research only used an injector frequency of only 5 Hz or less, which corresponds to about 600 RPM on the engine. With the estimation of 0.3 g of fuel to be added after each injection event, the flow rate required of the chamber at this injection frequency (and estimated equivalence ratio of 3 to 5) results in about 5 L/s. The mean purge velocity would then be about 1.8 m/s, which was expected to not influence the spray development at any stage during an injection event. This magnitude is well below the guide range provided by SAE International. The spray rig was designed to have a continuous air purging for simplicity and has a dual air inlet around the injector. The design of the spray rig has been optimized through validation of air flow in the chamber so as to minimize the influence of air entrainment towards spray. The details of this design and analysis are in the work of (Camm, 2016).

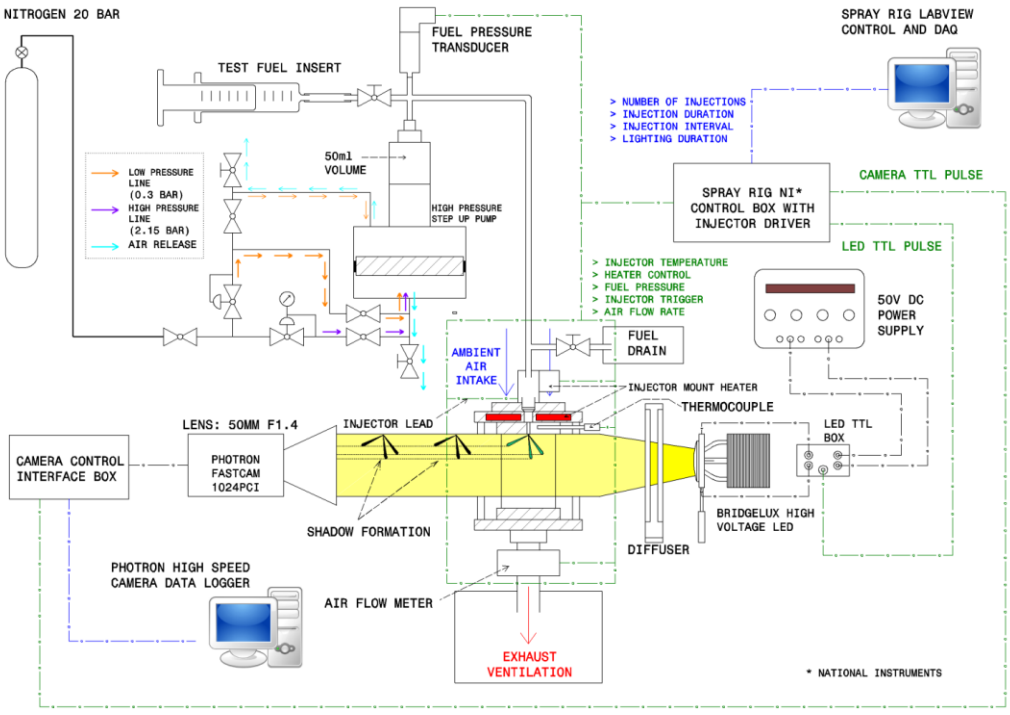


Figure 2.11: Schematic overview of the spray rig setup utilizing the back-lit illumination configuration.

The spray rig (Figure 2.11) has a pressure intensifier that is able to produce a high fuel pressure of up to about 300 bar. It was designed to accommodate the future potential of much higher injection pressure in GDI engines. First, 20 bar of nitrogen is supplied through the stainless steel pipe into a separate low and high pressure line. By controlling the valves on the low-pressure line, the fuel is drawn from a glass syringe to the fuel chamber when the large piston in the pressure intensifier is pushed downwards. The direction of the piston is then switched to prime the fuel to a pressure of about 20 bar using a valve on the low-pressure line while regulating the pressure at 0.3 bar. The pump has two different sized pistons connected together, with the piston that has a larger area giving a pressure ratio of 1:60. The low-pressure line was then switched to the high-pressure line that was regulated at 2.15 bar which generates 150 bar of fuel pressure.

A LabVIEW control panel has been developed to manage the injector as well as collecting pressure and temperature data. Injector parameters such as the number of injections, the injection duration and the injection interval were controlled on this panel. The control panel was used also to turn the injector mounting block heater on and set to a specific temperature with PID control. The fuel temperatures tested for experiments on the spray rigs were also the same as on the optical engine: 23°C, 60°C, 90°C and 105°C. The same method was adopted from the optical experiment which was to leave the fuel to soak at a targeted temperature for at least 20 minutes before doing any imaging.

The spray rig was used for two different setups; a backlit spray imaging experiment that outputs shadowgraph images or a direct illumination experiment that outputs Mie-scattering images. Backlit spray imaging is normally conducted with the high voltage LED placed at the opposite end of the high-speed camera as shown in Figure 2.9. Backlit imaging was selected for characterization studies because of the clear contrast between the background and subject, and also it produces a more uniform illumination of the spray image

that enables more accurate spray shape analysis. For the case of Mie-scattering, an optical system produces a collimated sheet-illumination in the chamber.

A 50 V power supply was used with a white LED array to give maximum illumination during injection which is then diffused using a double layer of tracing paper to make the image background intensity more uniform. The LED was only turned on when a trigger pulse from the control box was sent through during injection and it was set to last for 2 ms. This cycle was then repeated for 10 to 50 cycles to get a good ensemble average pattern. With short period of usage, the LED withstood the current which was about 6 times the limit for continuous operation.

2.3.1.1. Injector tip modification for temperature measurement and validation

In this research, fuel temperature has a major influence towards the development of the sprays. It is therefore important to understand the temperature changes during any or after multiple injection events. The injector mounting has 4 heating elements (≈25W each) (at an equal radial distance to the injector) in the injector mounting. The heaters are controlled by a built-in Labview digital PID controller. A reference platinum resistance thermometer is inserted close to one of the heater element to monitor and provide temperature feedback to the PID controller. The injector is bolted and held tightly onto a copper washer at the centre of this mounting block as shown in Figure 2.12. Due to the close proximity of the injector body to the mounting, there will be heat transfer from the heater element to the block and eventually to the fuel. However, there can potentially be fluctuations in the fuel temperature if the injector flowrate is increased due to a higher frequency or duration of injection or a higher injection pressure.

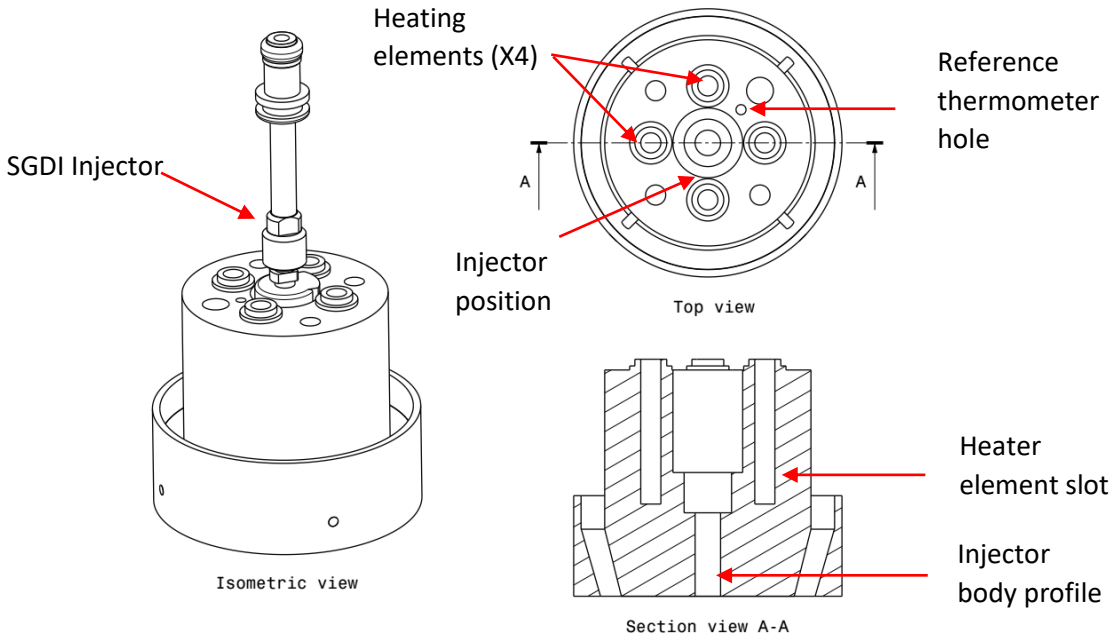


Figure 2.12: Detail drawing and typical assembly of the injector mounting block used on the spray rig.

The best possible position to measure the temperature change in the fuel is at the tip of the injector which is the end path of the fuel travel before being exposed through injection. To do this, the injector was modified by attaching a K-type thermocouple at the tip. It is important that his attachment however does not obstruct any of the injector nozzles or the spray plumes path. The probe was carefully spot welded onto the injector tip to obtain a rigid contact as shown in Figure 2.13. The end of the wire probe was fitted with a miniature type K connector that connected to a digital readout for temperature measurements. A very straightforward validation was intended for this experiment, therefore a simple K-type probe was adequate for validation purposes. Temperature data was collected at the end of many variations of multiple injection counts for comparison.

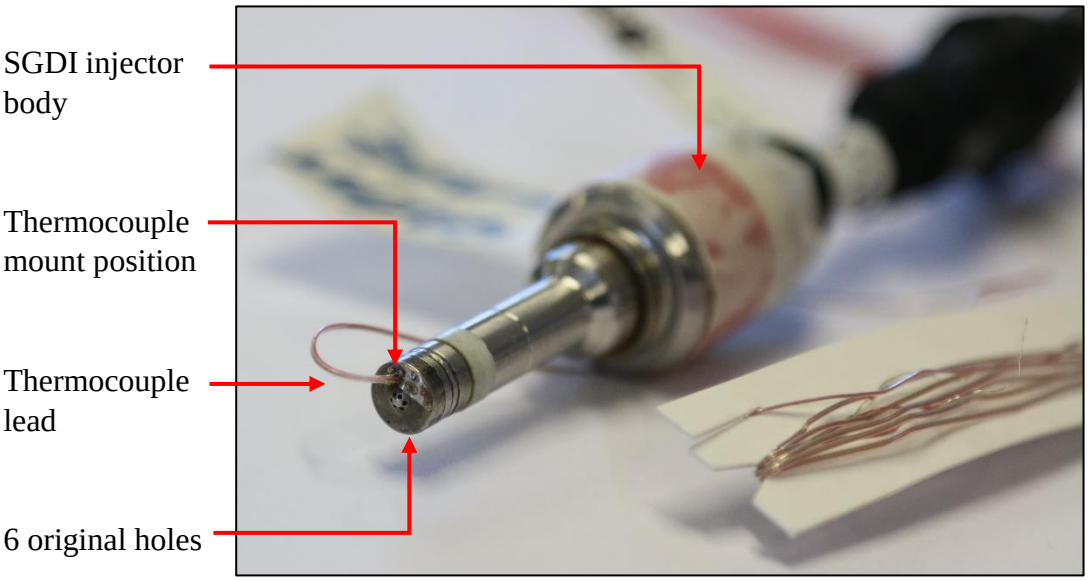


Figure 2.13: Modified GDI injector with thermocouple attached at the tip

2.3.2. Spray impingement experiment setup on the spray rig

For this experiment, the same spray rig is used again but with a different injector mounting setup and a surrogate piston installed to emulate the spray impingement phenomena. The fuel preparation method remained the same as previous experiment setup with changes only at the downstream where fuel is being injected. The injector was modified so that only one of the six holes was used, and the injector is mounted at a specific angle to so that the single fuel jet is vertical as shown in Figure 2.14.

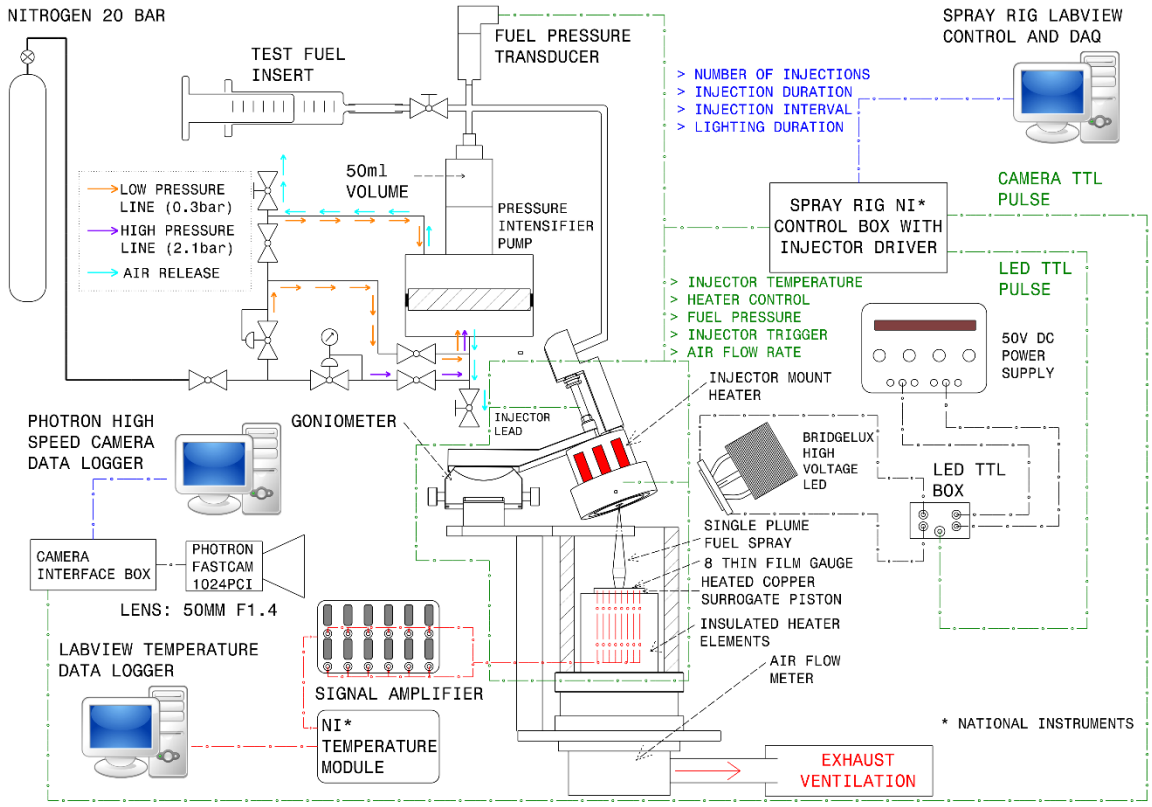


Figure 2.14: Schematic overview of spray impingement experiment setup

A bespoke multiple axis adjustable mount was fabricated to give the user the capability to better target the centre of the surrogate piston with an axial fuel jet. Preliminary studies of the spray angles of plumes from the AJ133 injector was researched from the literature as well as experiments using a high-speed camera and MATLAB post-processing software. The findings show very minimal discrepancies between the measured spray angles and from the literature. Despite this, it was decided that some angle adjustments should be allowed to account for any inaccuracy in the injector mounting assembly. Hence, the injector mounting body is attached to a goniometer as shown in Figure 2.15, to give flexibility in spray angle changes of up to 20 degrees in each direction. Three-dimensional positioning of the top of the injector is controlled by having slots and using shims.

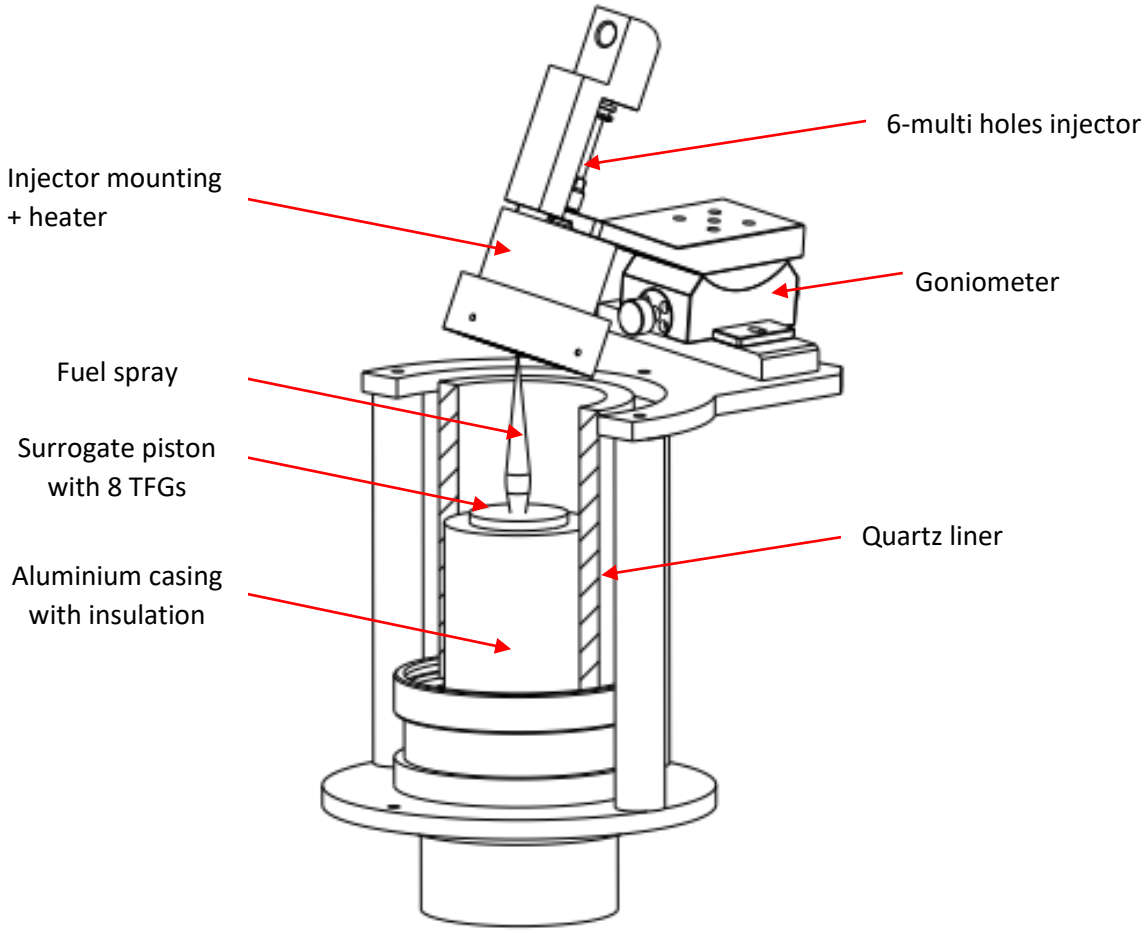


Figure 2.15: Schematic of Spray Rig Assembly for Spray Impingement Investigation

A Thin Film Gauge (TFG) (also called a direct-heat-flux gauge) is used to measure the surface temperature change when fuel impingement occurs. There is a total of 8 platinum resistance thermometer TFGs used on the surface of the surrogate piston. Originally, the TFGs come on a rectangular sheet as shown in Figure 2.16. The TFGs are then cut to the exact diameter (50mm) of the surrogate piston and attached to the piston surface. They are fabricated onto a strip of thin flexible 70 µm polyimide insulating layer (Upilex) tape with known positions as can be seen in Figure 2.16. The surrogate piston is made out of copper with holes for heater elements insertions. The copper piston is heated up to various selected temperatures and maintained whist fuel being sprayed onto the surface. Figure 2.17 shows the arrangement of the TFGs when attached onto the surrogate piston.

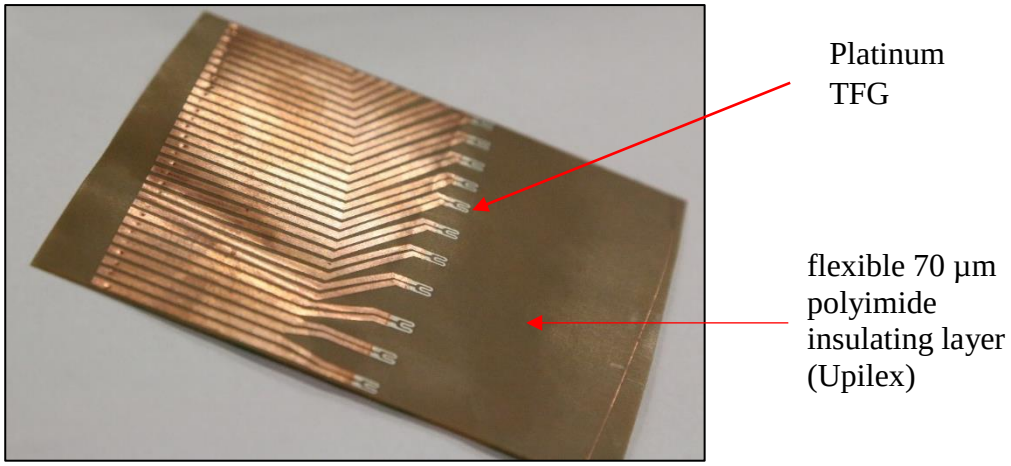


Figure 2.16: Example of new TFGs before installation

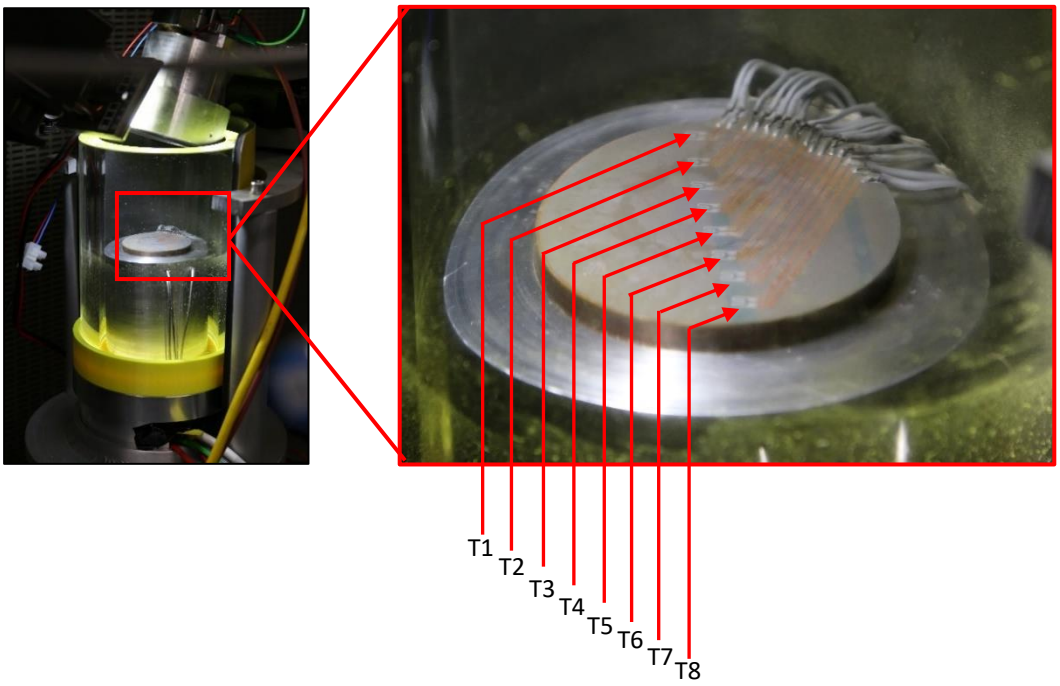


Figure 2.17: TFGs wired and installed on the surrogate piston

There is a total of 7 heating elements embedded in the surrogate copper piston, partially shown in Figure 2.18(a). To better maintain the piston temperature, it is wrapped with a thermal insulation foam and an aluminium casing. There is a 5 mm gap between the piston surface and the top of the aluminium casing to Melafoam insulation to reduce heat transfer from the surrogate piston to the casing; for the same reason there is also a small

annular gap at the top between the casing and piston. Two holes are drilled 5 and 15 mm from the piston surface for reference thermocouple insertion as shown in Figure 2.18(b). The piston has tripod legs that slide in the base of the spray rig for height adjustment. As can be seen in Figure 2.18(c), the single jet is targeted to hit the centre of the piston. In order to see a balanced distribution of temperatures on the piston, the TFGs, labelled T1 to T8, are arranged to be symmetrical from the centre with 4 on each side. The distance between each TFG is about 6 mm while the closest from the centre is at a distance of 3 mm.

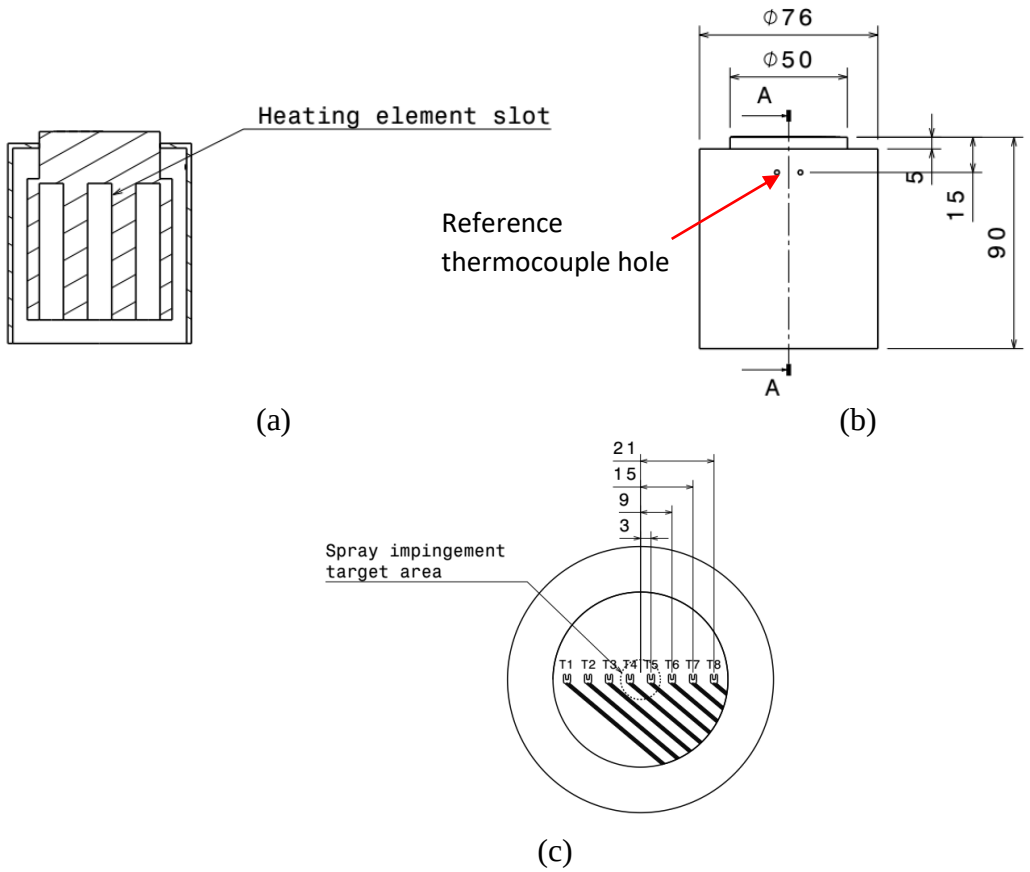


Figure 2.18: (a) Centre cross section drawing of the surrogate piston, (b) Detailed dimension of the surrogate piston assembly, (c) Detailed positioning of the TFGs and impingement target area

Each TFG on the Upilex strip varies in electrical resistance due to manufacturing variations. Preliminary electrical resistance test on each TFGs resulted in values ranging

from 42 Ω to 48 Ω. In order to obtain a uniform temperature measurement, each TFG is configured using a Wheatstone Bridge electrical circuit for voltage control as shown in Figure 2.19. A Wheatstone bridge is an electrical circuit used to measure an unknown electrical resistance by balancing two legs of a bridge circuit, one leg of which includes the unknown resistance of a component. In this configuration, R1 and R3 have fixed resistors of 470 Ω; R2 is the TFG with a fixed electrical resistance value; R4 consist of a mix of fixed value resistor and a variable resistor for balancing the bridge to give an initial zero voltage output. The Wheatstone bridge output is connected to a signal amplifier to raise the voltage for input to a National Instrument data acquisition card that reads out the temperature on the LabVIEW GUI.

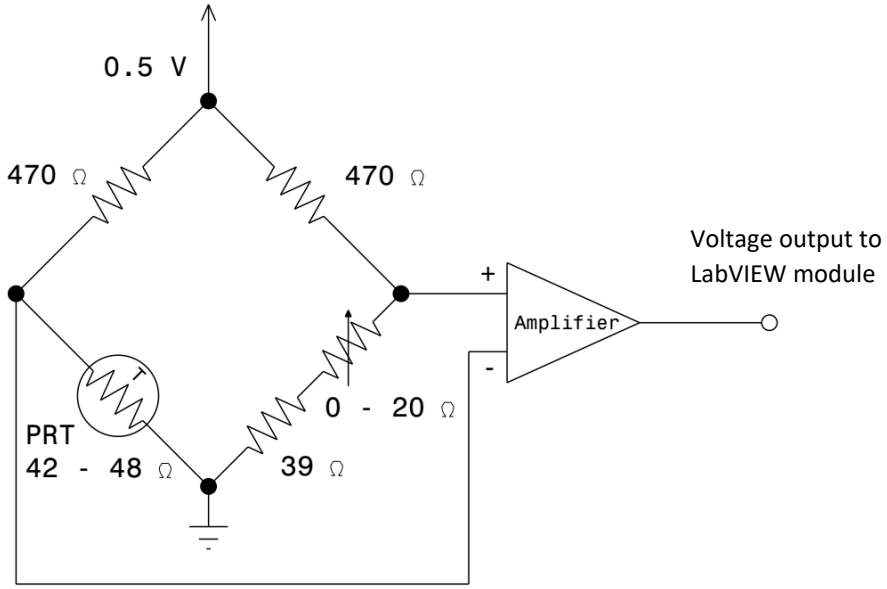


Figure 2.19: Detail schematic of a Wheatstone Bridge configuration used for obtaining voltage output from each of the TFGs

2.3.2.1. Heat flow and temperature distribution calculation using the finite difference method

Platinum gauge
sensor (0.04µm)

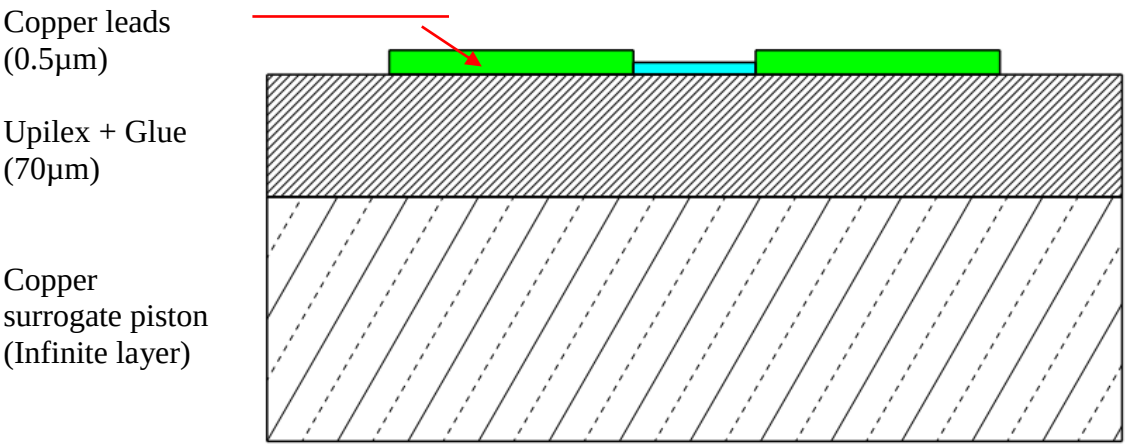


Figure 2.20: Detail illustration of the different material layers of the TFG and surrogate piston

For this research, heat flux analysis of the spray impingement period would give a deeper understanding of different fuel evaporation characteristics. To achieve this, a temperature distribution analysis of the thin film gauge is needed for the heat flux calculation. The temperature measurement TFG probe, when attached to the piston using an adhesive based Upilex will be the first layer to be impinged by the spray as shown in Figure 2.20. A preliminary thermal depth penetration calculation was used to identify if the calculation method should be for a single or multiple layer using the following equation

$$\delta \sim \sqrt{\alpha t} \qquad (2.1)$$

where δ is the total thermal penetration depth of the single layer, t is the time taken for heat to propagate through and α is the thermal diffusivity of the material layer defined in terms of thermal conductivity, k, material density, ρ, and specific heat, c, $\alpha = k/\rho c$. Previous publications have stated the importance of using a multiple layer calculation method when using this TFG (with Upilex and glue) on surfaces such as copper due to the huge difference in thermal properties. However, for this research the spray injection event only lasted a maximum of 2 ms for each test. A thermal penetration depth of 70 µm for the Upilex and glue layer requires a total of about 28 ms. Therefore, it was decided that the heat flux

calculation can be conducted with a single layer model to simplify the analysis whereby the Upilex layer was treated as a semi-infinite layer. The time dependent heat flux can be calculated using the two-dimensional heat conduction equation; two space coordinates and time. Consider the Fourier equation:

$$\frac{\delta T}{\delta t} = \alpha\left(\frac{\delta^2 T}{\delta x^2} + \frac{\delta^2 T}{\delta z^2}\right) \qquad (2.2)$$

An explicit finite difference representation of equation (2.2) is:

$$\frac{T_{i,j,k+1} - T_{i,j,k}}{\delta t} = \alpha\left[\left(\frac{T_{i-1,j,k} - 2T_{i,j,k} + T_{i+1,j,k}}{\delta x^2}\right) + \left(\frac{T_{i,j-1,k} - 2T_{i,j,k} + T_{i+1,j,k}}{\delta z^2}\right)\right]$$

(2.3)

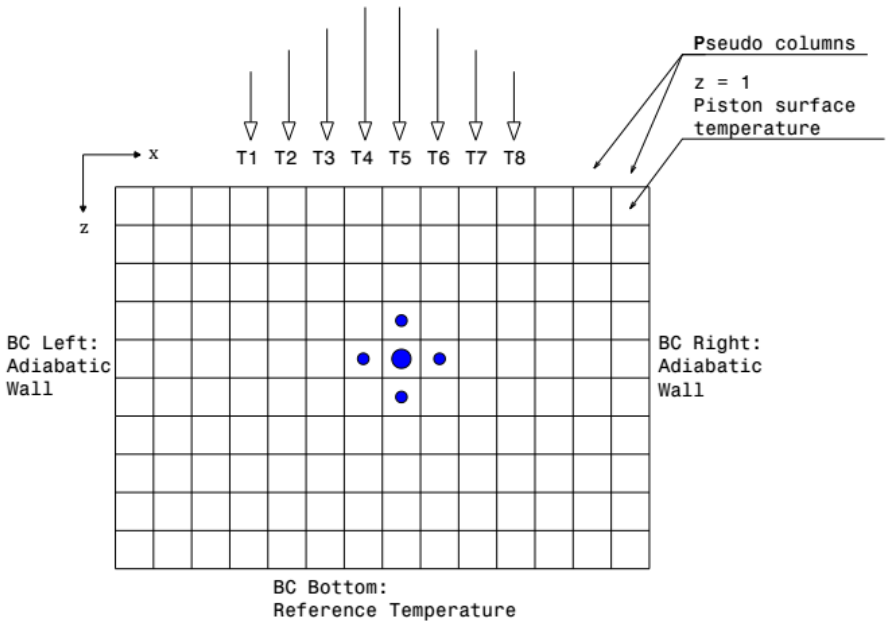


Figure 2.21: Illustration of the finite difference method mesh points and boundary conditions of the Upilex and glue layer

As shown in Figure 2.21, there are mesh points in the x-direction as well as z-direction. The coordinate of each mesh is defined by (x, z, t) by $x = i\,\delta x$, $z = j\,\delta z$, $t = k\,\delta t$. Each mesh point value is represented in terms of the known values on a previous time step. This method is however only stable for small forward time steps. For a problem which has

the boundary temperatures specified for $t \geq 0$ the limit of stability is given by Bayley et al. (1972):

$$\alpha\, \delta t \left[\frac{1}{\delta x^2} + \frac{1}{\delta z^2}\right] \leq \frac{1}{2} \qquad (2.4)$$

The boundary conditions for the finite difference calculation are:

$$-k\frac{\delta T}{\delta x} = q_s \qquad at\ z = 1 \qquad (2.5)$$

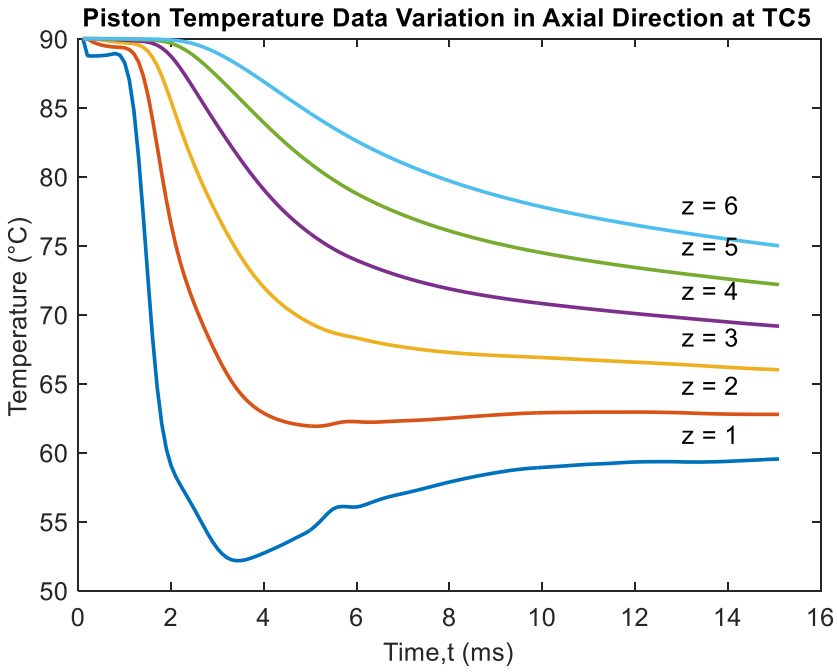
$$\frac{\delta T}{\delta x} = 0 \qquad at\ x = 1{,}14 \qquad (2.6)$$

$$\frac{\delta T}{\delta z} = 0 \qquad at\ z = \infty \qquad (2.7)$$

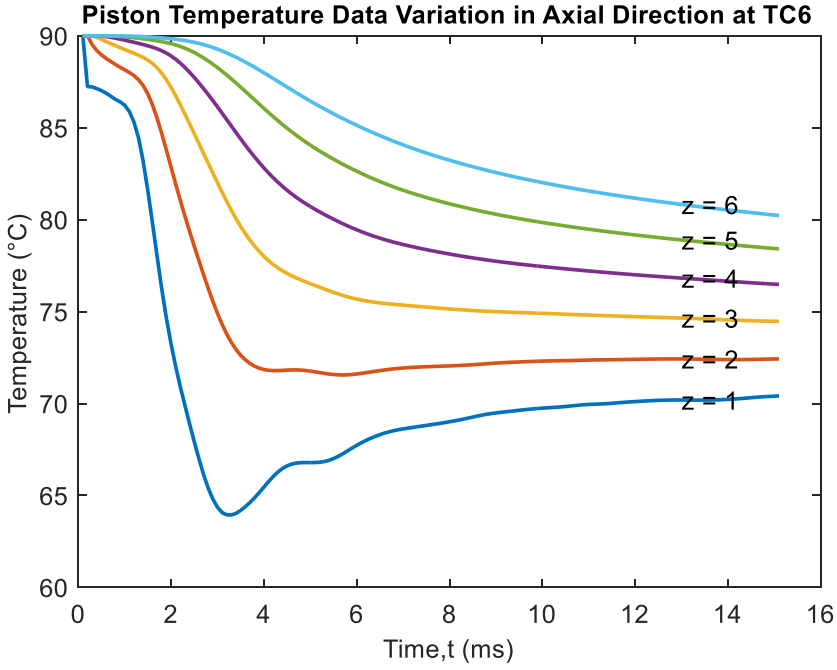
The initial condition is:

$$T(x, z, 0) = T_{initial} \qquad (2.8)$$

There are two additional pseudo columns on both the left and right wall that act as boundary conditions with no heat transfer in those directions. The lowest mesh points also act as an isothermal wall where the reference temperature was kept constant at all times. The heat flux is calculated at the surface where $z = 1$. The data acquisition runs at 10 kHz which records the data for 1 s, but only 15 ms of data is processed due to the very short injection timing event as shown in Figure 2.22. The depth scale in the *z*-direction is taken to be 10 μm (limited to maintain stability in the calculations; equation 2.4) per step while in the *x*-direction, each step is equivalent to 6 mm. Figure 2.23 shows the typical result of heat flux after post-processing the temperature data. Figure 2.24 shows an example of heat map of the single layer material



(a)



(b)

Figure 2.22: Typical temperature profile change (injection of 100 bar; 50°C M15 Fuel; 90°C piston temperature) at different depths of the single layer material for (a) TC5 and (b) TC6

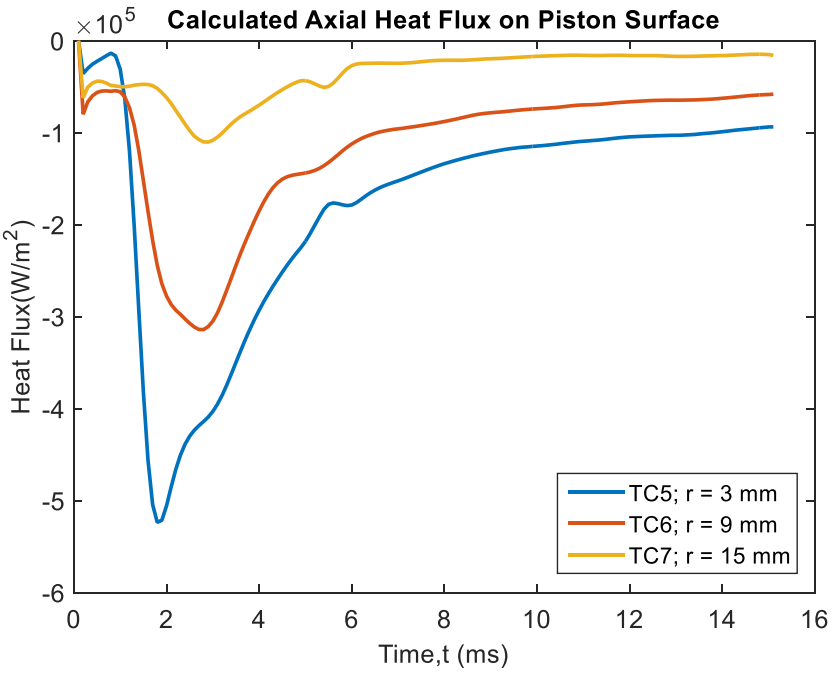


Figure 2.23: Typical axial heat flux profile change (injection of 100 bar; 50°C M15 fuel; 90°C piston temperature) at the surface of the single layer material for TC5, TC6 and TC7

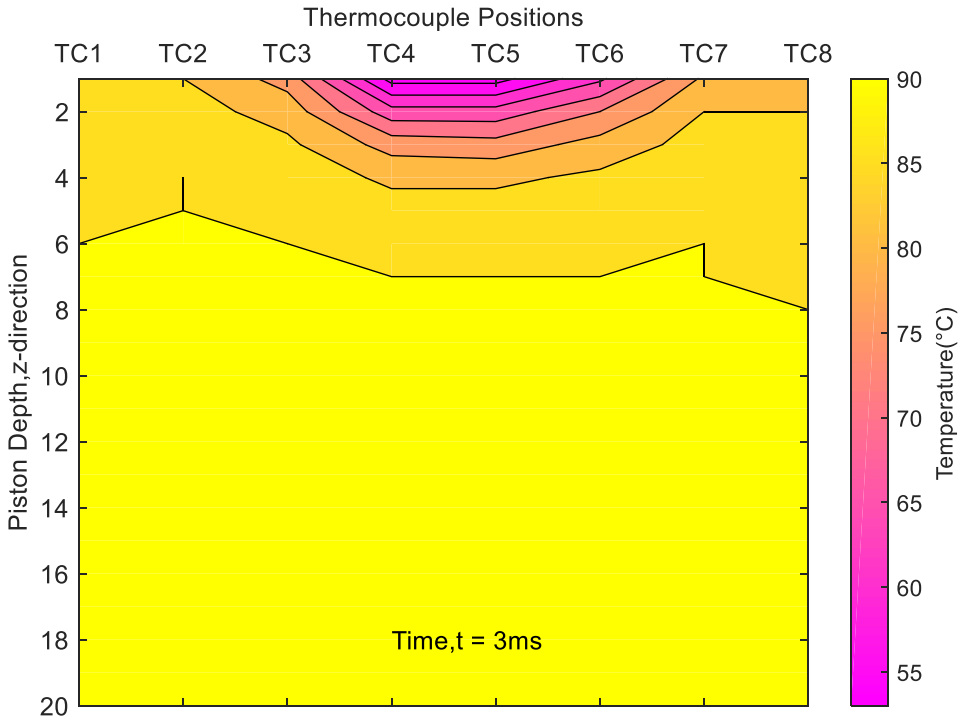


Figure 2.24: Typical temperature change (injection of 100 bar; 50°C M15 fuel; 90°C piston temperature) at the surface of the single layer material for all heat gauges at 3 ms after SOI

2.3.2.2. Injector tip modifications

For the spray impingement on piston experiments, only one plume out of six from a multi-holes SGDI injector was used, as shown in Figure 2.15. This is to make sure that all of the fuel mass that exits the injector is targeted to the surrogate piston and not the walls. The conditions for the tests vary in fuel temperatures from cold to elevated as well as using different volatility tests fuels. As a result of this, the spray geometry can change and might not exactly be directed to the surrogate piston. Figure 2.25 shows a comparison between an original AJ133 injector and a lightly modified one. As can be seen in Figure 2.25, five out of six nozzles of the tip injector have been sealed off by welding. It was the nozzle labelled number 6 in Figure 2.3 that was selected to be left open and used for this experiment. The fabrication work was outsourced to a precision fabricator to prevent any unnecessary damage to the original internal structure of the injector.

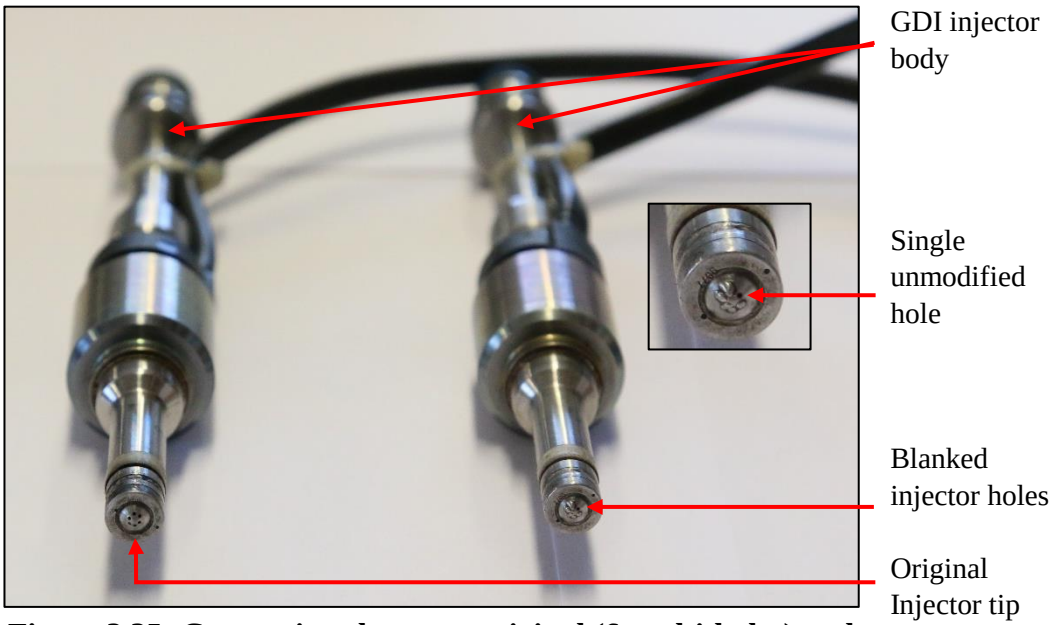


Figure 2.25: Comparison between original (6-multi-holes) and modified injector (single hole).

2.4. Vapour pressure measurement apparatus

The vapour pressure apparatus used is modelled and fabricated to the standards of ASTM D323 (Standard Test Method for Vapour Pressure of Petroleum Products (Reid Method)). The apparatus consists of two chambers, a liquid chamber and a vapour chamber as shown in Figure 2.26. Both the chambers are cylindrical vessel with a ID = 51 mm (requirement: 51 ± 3 mm). The vapour chamber was designed to have a length of 254 mm, with the inner surfaces of the ends slightly sloped to provide complete drainage from either end when held at vertical position. The liquid chamber has the same feature at the opening end of the cylinder. The requirement set by the standard is to have a vapour to liquid chamber volume ratio of 3.8 to 4.2. As a result, the liquid chamber cylinder length is chosen to acquire this ratio. A ball valve with an internal diameter of 12.7 mm is used at the opening of the liquid chamber to control the liquid movement into the vapour chamber. Measurements for some of the experiments start at sub atmospheric conditions therefore, another ball valve is installed in this apparatus to seal the 'vapour volume' when air is already at the lowest vacuum condition. A pressure transducer with measuring range of -1 bar to 2.5 bar gauge is used for this experiment as it is suitable for sub-atmospheric measurements.

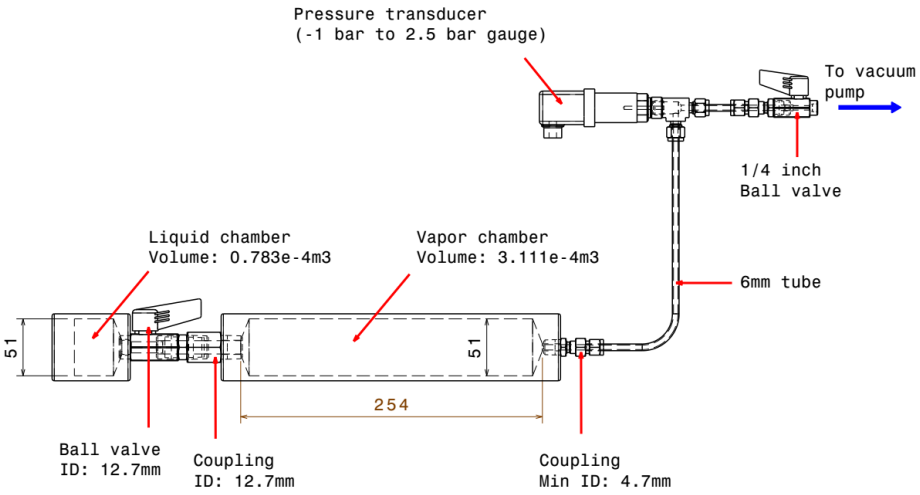


Figure 2.26: Detail drawing of the vapour pressure measurement apparatus assembly

2.4.1. Working principal

Although the standard mentioned is normally used for the measurement of Reid Vapour Pressure (absolute pressure at 37.8°C), it can still be used at various other temperatures. For this research work, this apparatus is used to validate the vapour pressure modelling of single and multi-component fuels created for tests. There is extensive use of the vapour pressure parameter in this research to be correlated with other parameters such as spray angle, penetration and even particulate emissions. It is therefore essential that the vapour pressure model of the fuels is validated and checked for accuracy. The method for the use of the vapour pressure measurement using this apparatus is described as follows:

1. The liquid chamber is positioned in a vertically with the valve opened. The test fuel is filled in the chamber until it overflows. The valve is closed and excess fuel is mopped away to prevent any unwanted vapour getting into the vapour chamber.
2. The liquid chamber is then connected to the vapour chamber using pipe fittings. Dowty seals are used for sealing between the connections.
3. The downstream end of the apparatus is connected to a vacuum pump with the ¼" ball valve opened. The vacuum pump is turned on and the pressure reading from the pressure transducer is recorded.
4. Evacuating the chamber can take few minutes; The valve is closed once the pressure transducer reading is stable and shows a reading close to 0.00 ± 0.001 bar. The pressure reading is checked again to confirm that there is no leakage (an increase in the pressure reading). The vacuum pressure reading is recorded.
5. Both the liquid chamber and the vapour chamber are then immersed in a water bath at a starting temperature of 25°C. Only the part of the 6 mm tubing is immersed together in the water bath while the rest has to remained above. About 15 minutes

of soaking time is allowed in order to achieve a uniform temperature in both chambers.

6. The liquid chamber valve is opened to allow the liquid to flow into the vapour chamber.
7. The apparatus is agitated vigorously and left to settle for at least 5 minutes before the pressure reading is recorded.
8. The water bath temperature is increased by 10°C every step and step 7 is repeated each time until a maximum temperature of 75°C/80°C is reached.

Once the test is finished, the apparatus is let to cool down to room temperature before the vacuum valve is opened. This is to prevent fuel vapour escaping to the atmosphere which can be dangerous. The apparatus is positioned vertically to allow the liquid fuel to flow back into the liquid chamber before the valve is closed. The liquid chamber is then disconnected for the fuel to be discarded. Both the empty chambers are normally left to open air for at least few hours to allow any of the discarded fuel vapour to escape.

2.5. High speed camera

A high-speed camera was used in both the spray rig and single cylinder optical engine experiments to capture spray as well as combustion images. A Photron FASTCAM-1024 PCI colour camera was used for combustion imaging while a similar but greyscale camera model was used for spray imaging. All of the images from the optical engine experiments used a lower resolution in order to increase the frame rate to 6000 fps. This was to allow a simple conversion of 1 frame every 1° crank angle to be used. The greyscale camera produced brighter images than the colour camera which had a colour filter array in

front of the detector; this meant that the shutter speed could be reduced to better capture fast moving sprays. Table 2.5 summarizes the camera configurations for various experiments.

Table 2.5: Summary of camera equipment and configuration used

Experimental Method	Equipment	Camera	Lens	Image Size	Frames per second	Shutter Speed	Frames per Cycle	No of Cycles
Motoring	Optical Engine	Photron Greyscale	28mm f/2.8	384 x 368	6000	1/ 15000	100	10
Combustion	Optical Engine	Photron Colour	50mm f/1.2	768 x 208	6000	1/ 6000	100	10
Static	Spray Rig	Photron Greyscale	50mm f/1.4	384 x 480	4500	1/ 35000	50	10

Combustion imaging through the annulus was captured without any external illumination in order to obtain raw data for 2D pyrometry analysis. With this method, combustion images were only captured beginning from 10°ATDC onwards as the piston moves down the cylinder. At this point, most of the combustion may already be close to its end, which resulted in a dark image. To overcome this, a 50 mm lens with a big aperture of f/1.2 and lowest shutter speed of 1/6000s were used to give brighter images. As for spray imaging on the optical engine, illumination was used, therefore a 28 mm wide angle lens with aperture of f/2.8 was adequate to capture sprays with a slightly elevated shutter speed. In the spray rig, a 50 mm f/1.4 lens was selected instead to reduce the angle of view and minimise image distortion.

2.6. DMS 500 Mk II Fast Particulate Spectrometer

2.6.1. Working principle

The DMS500 uses electrical mobility measurements to produce particle size or number spectra between 5 nm and 2.5 µm. This equipment uses a unipolar corona charger to charge each particle proportional to its surface area; there are equal numbers of positively and negatively charged particles. Figure 2.27 shows how the charged particles are introduced into a classification region which has a centrally mounted positive high voltage electrode. The central electrode is positively charged and attracts the negatively charged particles, but repels the positively charged particles towards the 22 available electrometer detectors on the side walls while drifting with the sheath flow air. Small particles are more mobile, therefore they are deflected earlier to the electrometers while larger particles travel further along the classification area as they are deflected less abruptly. When a particle hits a detector, its charge is conducted to ground through an electrometer amplifier which translates the current to a flux output of particles. Signals from the 22 electrometers are processed in real-time at 10 Hz to provide particle number or size spectral data.

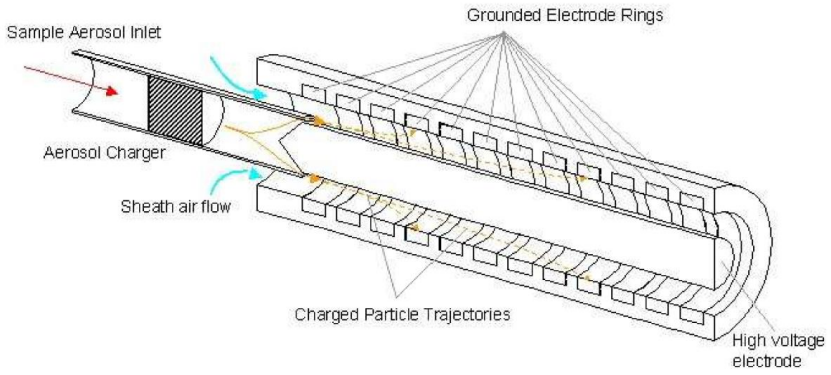


Figure 2.27: Cutaway view of DMS500 particle classification area. Adapted from (Cambustion)

The DMS500 operates at fixed pressure to eliminate any concern about online pressure correction algorithms. It samples through a choked orifice to discourage particle agglomeration. This facilitates the wide size range of the instrument, improves the time response and isolates the instrument from fluctuating sample pressure effects.

2.6.2. Digital filtering

In the previous chapter, it was said that this research will look into all sizes of particulates. However, it is also interesting to compare particulate results that goes through the PMP measurement protocol. Braisher et al. (2010) reported in his research on the method for the optical engine particulates emission raw results to be digitally filtered to replicate the PMP measurement protocol. This essentially removes the nucleation mode, which is subject to large variations since the number concentration is very sensitive to temperature and dilution effects. It was found that the optical engine particulates results can produce Coefficient of Variance (COV) of more than 50% and as a consequence, COV of 30% is deemed acceptable. Leach used a Wiebe function filter (Figure 2.28 and equation 2.9) so as not to rely on the poor lognormal fitting from the DMS500. The Wiebe function was modelled on the regulatory requirement of particle counters (Andersson et al. 2007) that are required to have 50% count efficiency at particle size of 23 nm and more than 90% efficiency for particle size of 41 nm.

$$1 - exp\left[-3.54\left(\frac{d_p - 14}{40}\right)^{1.09}\right]\left(d_p \geq 14\right) \quad f = 0\,(\mathrm{dp} < 14) \qquad (2.9)$$

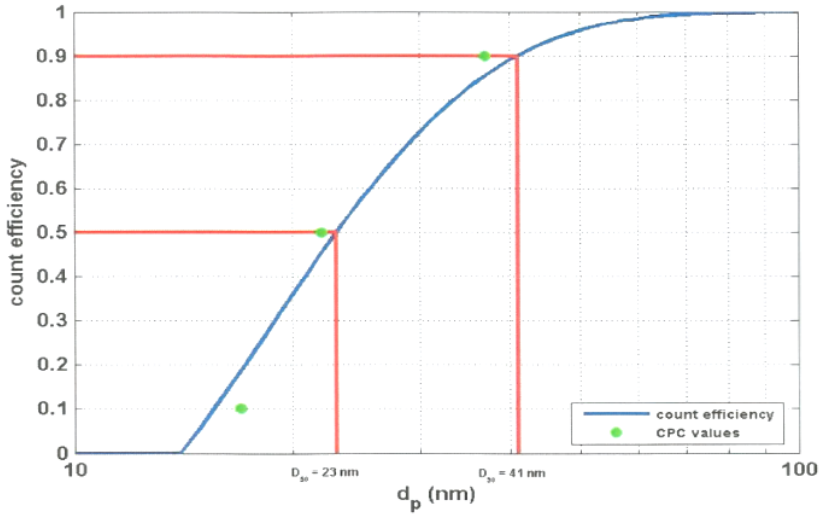


Figure 2.28: Count efficiency curve applied to DMS500 accumulation mode PN data

The correlation between lognormal fitting and Wiebe filter methods was good while standard deviation comparisons between both methods showed that the Wiebe filter produces lower results. Another reason for using this filter is that it suppresses the highly variable particles in the nucleation region (of 23 nm and below) which mimics the effect of a catalyst that is not present in the optical engine. MATLAB was used to apply the Wiebe function filter.

2.6.3. Total particulate mass calculation

With the DMS500, particle number size distributions are obtained and therefore it is possible to calculate the PM with the appropriate assumptions for the shape and density of the particles. The easiest method is to assume the particles to be spherical having a density of water at 1000 kg/m^3. However there has been reports of over-estimation of mass when using these simple assumptions. This is because particulates cannot only exist as single spheres but also as an agglomerate.

As the particle size distribution is a lognormal fit, the Hatch-Choate conversion equation can be used. This allow any type of average diameter to be calculated from the lognormal values of count mean diameter (CMD) using the following equation:

$$d_p = CMDexp\left[1.5\ ln\ \sigma_g\right] \qquad (2.10)$$

where σ_g is the geometric standard deviation. d_p is the diameter of a particle mass, multiplied by the total PN concentration, gives total particle mass concentration for that particular log-normal distribution. d_p can now be applied to the following equation to calculate the mass spectrum from a particle size spectrum:

$$mass\ (kg) = 1.72 \text{ x } 10^{-24} {d_p}^{2.65}\ (nm) \qquad (2.11)$$

This equation has been validated using a DISI engine by Symonds et al. (2008).

2.7. Spray image analysis tool (IMSPRAY)

2.7.1. Program description

Experiments with high speed imaging are known to produce large amounts of digital images captured sequentially. Therefore, a MATLAB GUI package called IMSPRAY has been written to assist in analyzing the spray characteristics in a much faster yet consistent and accurate way. With the capability of batch image processing, the user can select a method and define the necessary analysis parameters and then apply the same parameters to the whole set of images. The GUI package integrates and extends some of the previous work by the Engines Group related to image analysis. IMSPRAY was coded to follow the automotive SAE J2715 (Hung et al. 2008) standard for injection spray analysis measurement. The intention was to maintain the same standard for image analysis across all of the automotive industry. The main panel for IMSPRAY is shown in Figure 2.29.

The method of using IMSPRAY is for the user to analyze one image as a base example and then for the batch processing code to follow. There are two main type of image analysis option available on the program: Static Analysis and Dynamic Analysis. The program begins by forcing the user to enter key experimental parameters about the set of images to be imported (see Figure 2.29). Some of these parameters are used later in the calculation and analysis. This is also important for data management and identification when the results have been analyzed and exported. In order to ease the user when keying in the experimental parameters, the text file generated by the Photron high speed camera can be imported directly into the program so that all the camera settings will be extracted automatically. Figure 2.29 shows an example of the experimental parameters key-in panel. It is crucial for the user to select the correct option for “machine type” and “image angle”. Both of these settings have codes written specifically for each of the options.

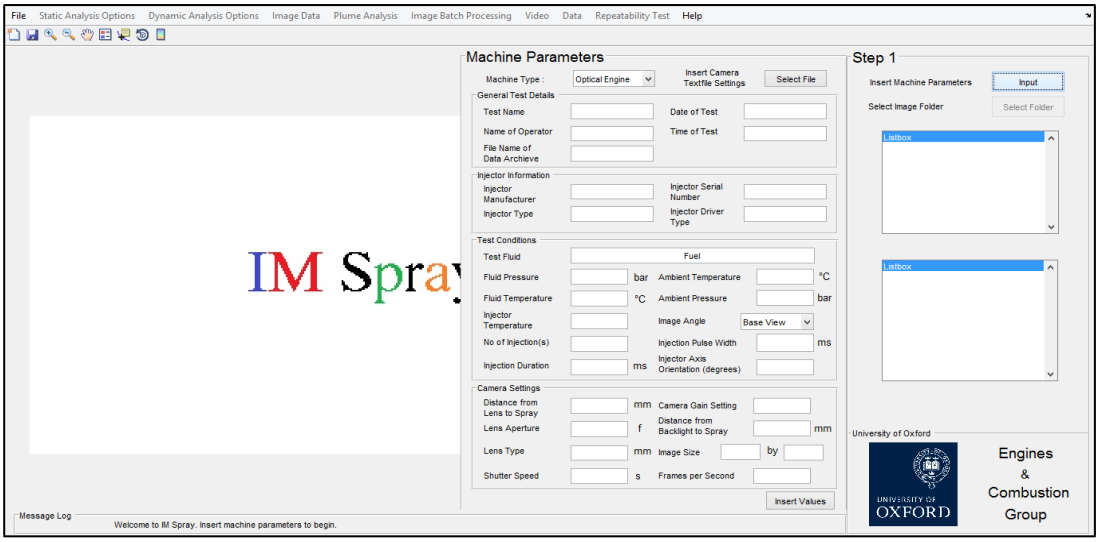


Figure 2.29: IMSPRAY GUI main panel

Background subtraction is common in image analysis techniques to eliminate unnecessary digital data and further segregate the subject. In IMSPRAY, the program can process either shadowgraph or Mie-Scattering images. The background image is normally taken from the first or second image of the set before the Start of Injection (SOI). Once the background has been subtracted, a built in function to remove noise is then used, whereby the program searches for average pixel values at the side walls of the subtracted image and turns all pixels with a below average value to either 0 (or 255 for shadowgraph images). The user can then select a thresholding method that is suitable for the current image. Thresholding methods are explained further in the next section.

False colour analysis enables the user to visualize the intensity of the spray in different areas of the plume. This method was used before but is further refined in this program to suit spray analysis. For this application, a function called ‘bwconncomp’ is added to allow the program to select only 500 or more pixels that are connected together. Figure 2.30 shows a summary of the IMSPRAY program work flow.

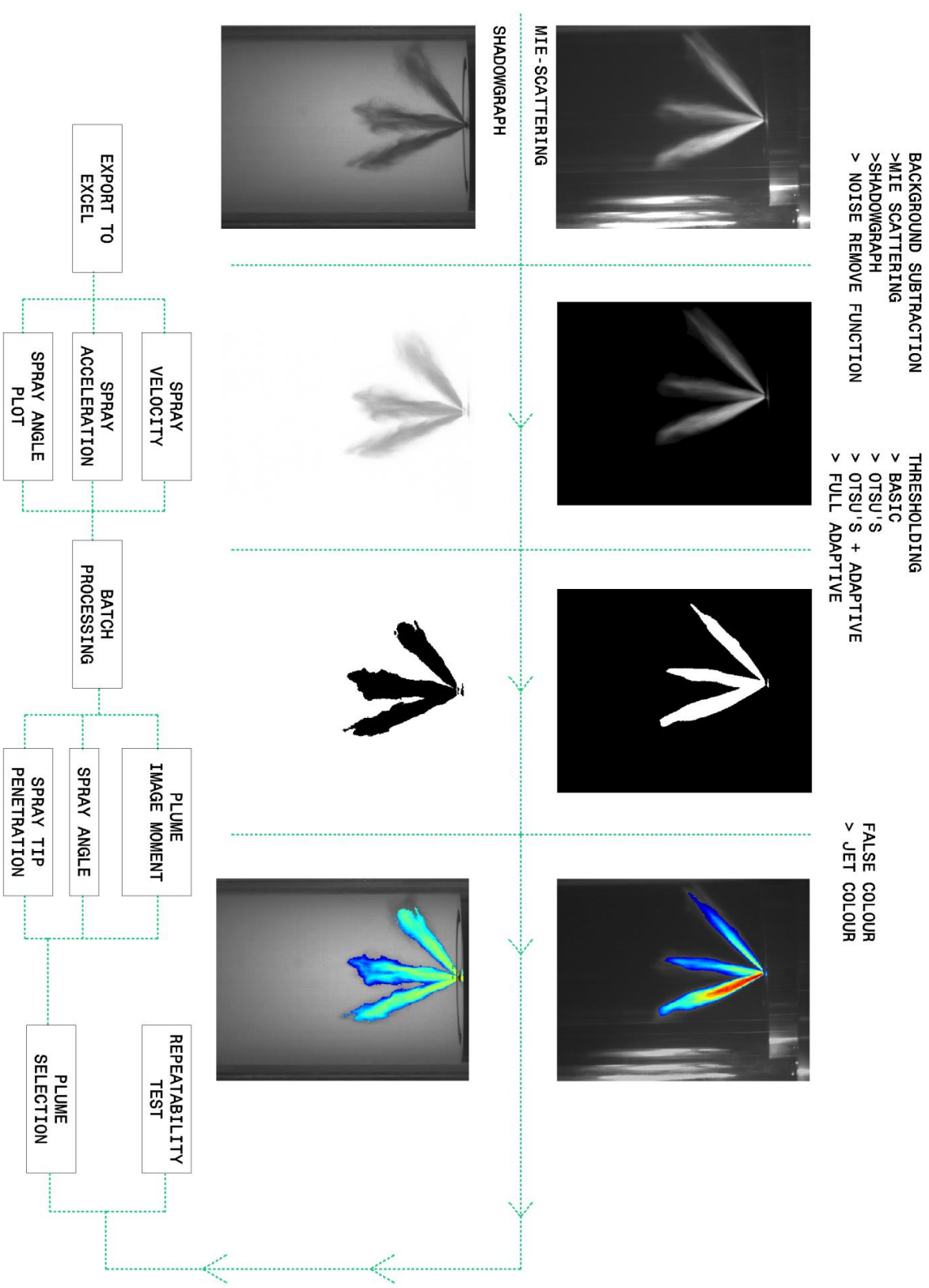


Figure 2.30: Overview of IMSPRAY program work flow

2.7.2. Image thresholding

Image thresholding or binarization is a method of turning a greyscale image with various pixel values into an image containing only “black” or “white” value pixels. This is one of the simplest methods of image segmentation. This method is very popular due to its ease of implementation whilst giving significant results. There are currently four available methods of thresholding developed in IMPSPRAY: “Basic”, “Otsu’s”, “Otsu’s & Adaptive” and “Full Adaptive”.

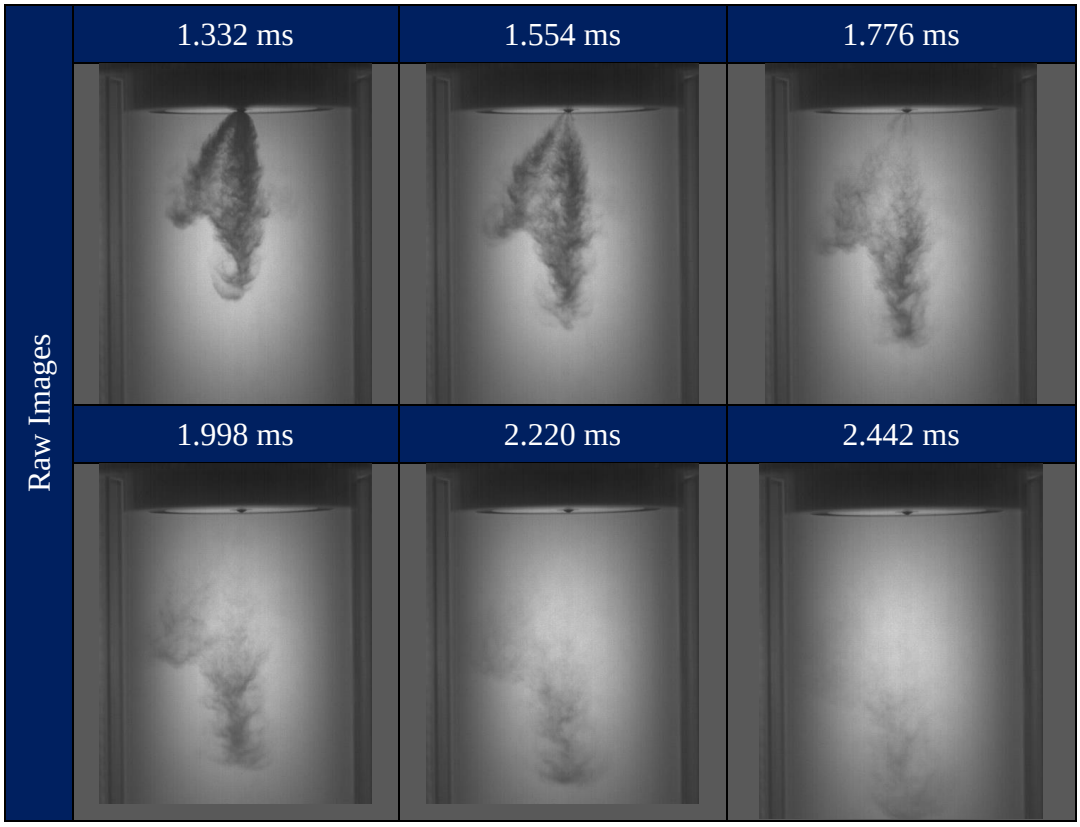
“Basic” thresholding method This method uses the global thresholding method where a thresholding value is inserted in the text box or scrolled at the swipe bar manually by the user. This is a trial and error method for preliminary investigation on the thresholding quality before further measurements are taken. Spray images can sometimes contain noise from Mie-Scattering or non-uniform illumination when in the shadowgraph setup. In such an event, the result of thresholding does not give a clean segmentation of the spray and the background.

“Otsu’s” thresholding method This method will compute the image binarization value through a Gray-Level histogram. The “Otsu’s” method basically chooses the threshold value to minimize the intraclass variance of the black and white pixels. This method normally fits well with shadowgraph experiments and during the injection event but performed poorly when segmenting images with a majority of liquid to vapour phase transition. Details on this method can be found from Otsu (1979).

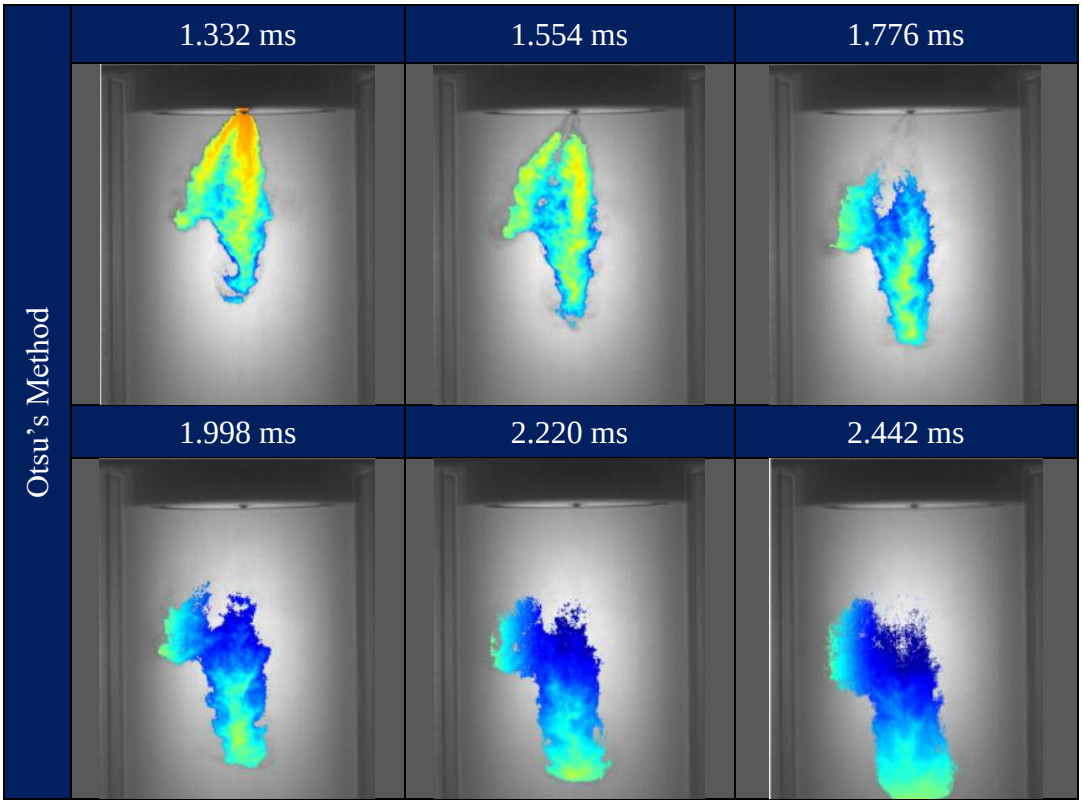
“Otsu’s & Adaptive” method This method is coded specifically for spray investigation purposes where, the program has the capability to detect if the injector is still injecting or has stopped. If the injection is still on-going, the program uses “Otsu’s” method and switches to the “Adaptive” method when injection has stopped. The “Adaptive Method” is

a method where binarization of the image is determined locally at every pixel. A predefined size mask is created at every pixel and the thresholding value is determined by comparing the local intensity versus the intensities of other pixels in the mask. A further description of this method is explained in Marques (2010). This method is developed to counter the weakness of "Otsu's" method when segmenting vapour from the image background, as the presence of liquid can sometimes overpower the vapour when intensity values are taken globally. This method, manages to capture the liquid to vapour phase transition that is important for spray penetration studies. Figure 2.31 shows a visual comparison of thresholding result between "Otsu's" and the "Otsu's & Adaptive" method.

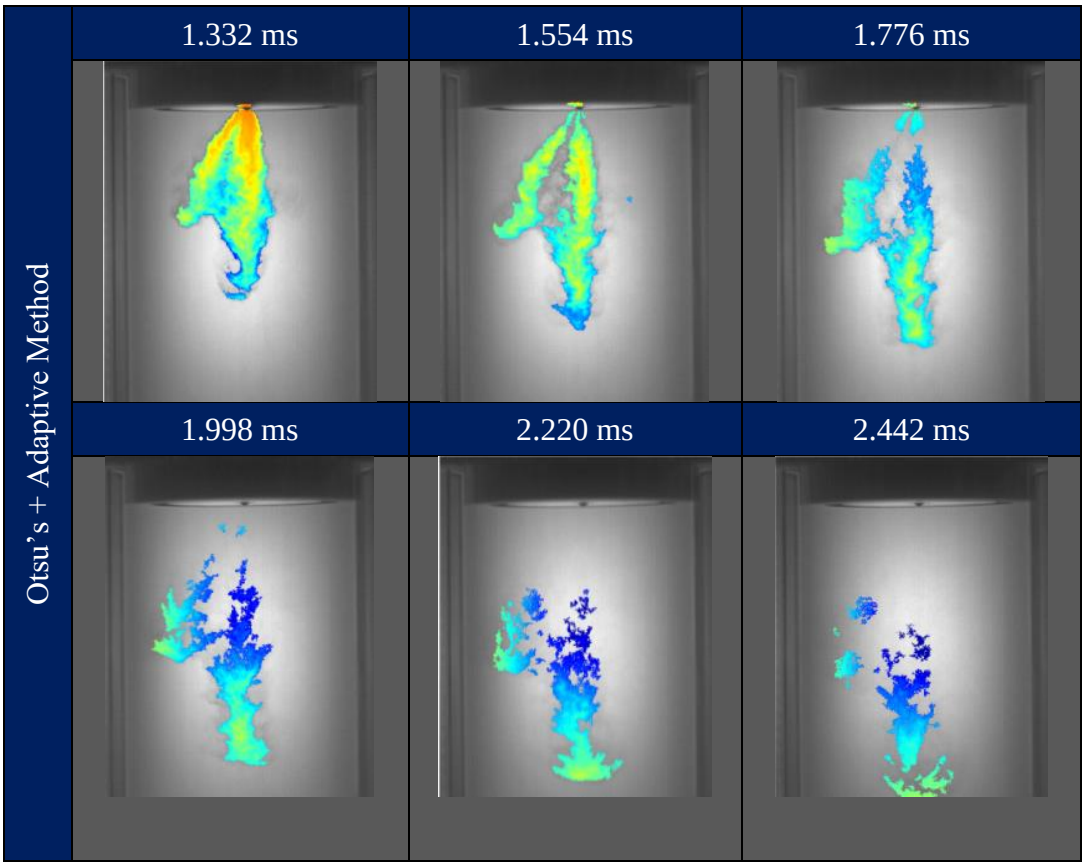
"Full Adaptive" method This uses the same application (as explained in previous section) of "Otsu's & Adaptive" method. Initially this method was only applied to investigate the liquid to vapour transition but it was found to give good spray segmentation with some Mie-Scattering spray images where illumination is highly non-uniform.



(a)



(b)



(c)

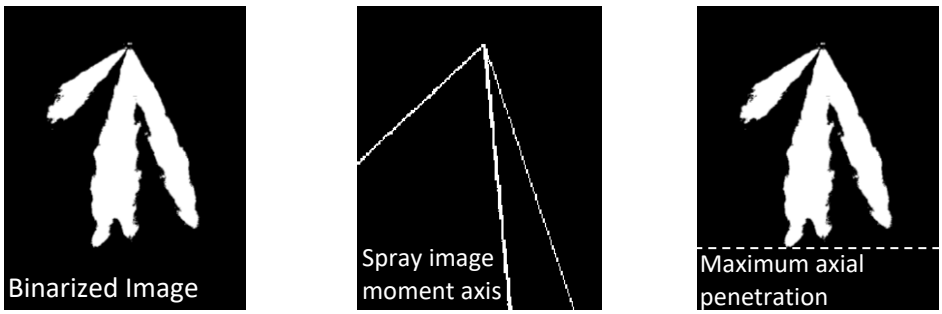
Figure 2.31: Comparison between (a) Raw Image, (b) Otsu's method (c) Otsu's and Adaptive method on spray segmentation at post injection

2.7.3. Spray image measurement standard (SAE J2715)

2.7.3.1. Spray penetration measurement

The spray penetration analysis code was scripted to find the farthest travel of the spray tip from the SOI. In this program, spray penetration is categorized into two parts: Axial penetration and penetration in terms of the 'image moment'. The MATLAB code works as follows:

1. The binarized image is used from first stage of image processing (Figure 2.32 (a))
2. An image with all zero value pixels of the same size is created; the injector tip point and plume centroids are connected using the 'STREL' function.
3. The lines are then extended to the end of the image as shown in Figure 2.32 (b).
4. Both Figure 2.32 (a) and (b) are then combined using a logical 'AND' to produce a new image Figure (c) that only has pixel values where the lines and sprays coincide.
5. Distances from injector tip to all pixels are calculated by using the 'bwdist' function.
6. The largest distance value is taken as a coordinate for plot of penetration against time.
7. Next, to find the axial penetration, the 'find' function is used on the binarized image to find all row and columns of the non-zero pixels.
8. The 'max' function is then used to find the maximum row of the non-zero pixel as shown in Figure 2.33 (c). The distance from the injector tip can then be calculated.



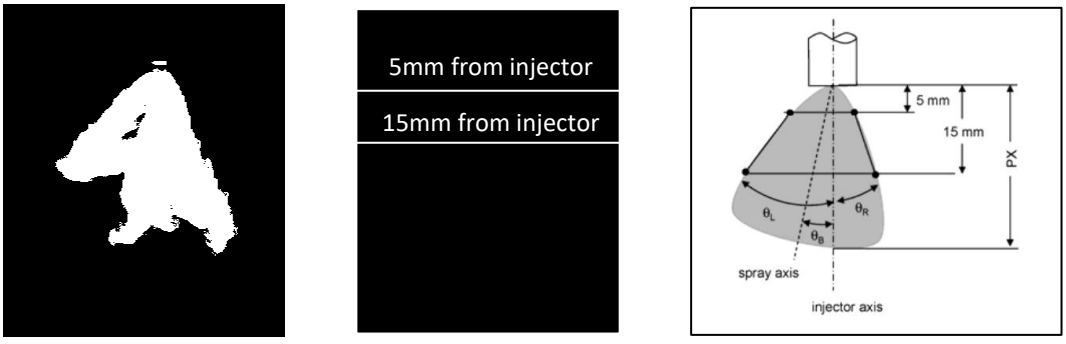
(a) (b) (c)

Figure 2.32: Images used for spray penetration analysis

2.7.3.2. Spray angle measurement

Spray angle analysis is important for this research as it influences the spray structure, especially when there is flash boiling as the spray geometry changes significantly. The codes written for this analysis follow the spray angle measurement standard set in SAEJ2715 (Hung et al. 2008) shown in Figure 2.33 (c). The program takes into account collapse and non-collapse characteristics of the spray; where if the spray does not collapse, all of the angles of each plume parameters are measured instead of only the ones on the far left and right walls. The MATLAB code works as follows:

1. A binarized image is used from the first stage of image processing (Figure 2.33 (a)).
2. An image with all zero value pixels of the same size is created; two lines measuring 5 and 15 mm from injector tip are created using 'STREL' function (Figure 2.33 (b)).
3. Both images Figure 2.33 (a) and (b) are then combined using a logical 'AND' to produce a new image that only has pixels values where the lines and sprays coincide.
4. The 'find' function is then used to locate all the non-zero pixels.
5. The miminum and maximum column with non-zero pixels are taken at both the 5 mm and 15 mm rows as coordinates. An 'IF' condition is placed that checks the number of non-zero columns on both rows and if the value differ, the spray is known as collapsed.
6. A line can now be plotted from the injector tip position and the spray angle is measured.



(a) (b) (c)

Figure 2.33: (a) & (b) Images used for spray angle analysis. (c) SAE J2715 spray angle measurement standard (Hung et al. 2008)

2.7.4. Spray repeatability measurement technique

The spray repeatability measurement technique is a useful tool to have for processing images from the spray rig. As mentioned before, a spray can change its shape when subjected to different temperatures. Doing multiple injections at high frequency can cause the fuel flowrate in the injector to become high. This can be a problem when doing experiments with controlled temperature environment to simulate flash boiling as there might not be enough time for the heating elements to properly heat up the fuel to a specific temperature. To investigate further, the high-speed camera was used to image multiple injections events and these images were post-processed using the MATLAB IMSPRAY program. The program worked as follows:

1. Raw image (Figure 2.34 (a)) from a specific frame (e.g ASOI = 0.7 ms) of the first set (e.g set #1 is for injection #1) of all total images is selected.
2. A total number of image set and camera fps is specified for the selection for the binarization process in the program.
3. All of the images are then binarized (Figure 2.34 (b) using any of the suitable methods mentioned before in section 2.7.2
4. The liquid spray region, which is displayed as white pixel has a grayscale value of 1 while a non-liquid region has a grayscale value of 0. The program will then count the number of times that each pixel coordinate that appears as 1 out of the total image set used.
5. All of the counts for each pixel coordinate is then converted into percentage values.
6. These percentage values are then plotted using a ‘jet’ colour profile to visualize the spray behaviour for all image sets; Figure 2.34 (c) (d)

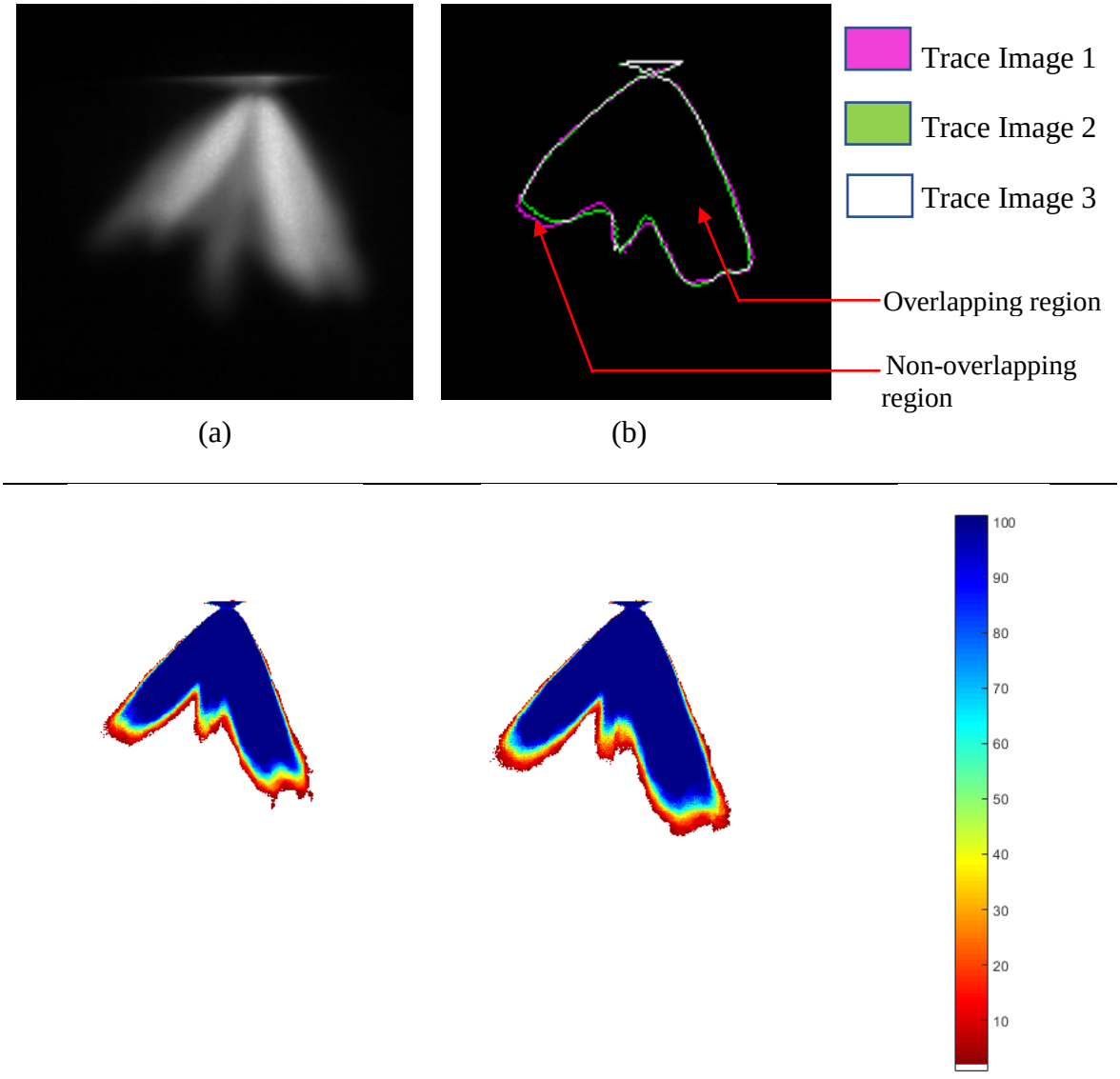


Figure 2.34: Compilation of high-speed images from ranging from (a) raw image, (b) binarized and parameterized spray image (c) final processed image for spray at 1.0 ms ASOI (d) 1.2 ms ASOI showing the likelihood of the presence of liquid

2.8. Chapter summary

In this chapter, the engines and rig-based experimental equipment used for the experimental work have been detailed. The engine used is the single cylinder engine with modular capabilities which can give optical access as well as a conventional full metal configuration. The rig-based equipment used are the spray rig (for spray characterization experiment, and spray impingement experiment) and the fuel vapour pressure measurement apparatus. The particulate measuring instrumentation, the DMS500, has been detailed, alongside the data analysis techniques for its output. The high-speed camera, for optical analysis of the spray (on the engine and rig) and combustion has been explained, alongside data analysis techniques coded into the IMSPRAY MATLAB program for the images taken.

3. Fuels, Fuels Modelling and Data Validation

3.1. Introduction

In this chapter, the development of model fuels and their performance are discussed in detail. Model M15 (15% methanol by volume) gasoline fuels have been created from pure fuel components, to give independent control of volatility, the heavy end content and the aromatic content, in order to understand the effect of the fuel properties on GDI fuel spray behaviour and the subsequent P_M number emissions.

The fuels are created based on the modelled distillation curves according to the ASTM D86 method. Reid Vapour Pressure (RVP), Temperature at 50% evaporated (T50) and Temperature at 90% evaporated (T90) are among the important controlled parameters when modelling a fuel's distillation curve. The vapour pressure of fuel mixtures is calculated using the UNIFAC correlation method. A non-oxygenated fuel and a commercial standard Euro 5 fuel were also tested for P_M as a performance benchmark.

In order to better understand and recognize the effects of volatility on P_M, a flash boiling criterion using the saturation pressure ratio is established for all fuels and used for making comparisons. Saturation pressure ratio is the fuel vapour pressure divided by the ambient pressure or the engine in-cylinder pressure. A vapour pressure measurement apparatus has been constructed (as already seen in Fig. 2.26) to validate the calculated vapour pressure using the UNIFAC method.

3.2. Oxygenated gasoline fuels

The past decade has seen various changes to gasoline fuels and their engine systems. Increased thermal efficiency targets, new environmental directives and tighter regulations on exhaust and evaporative emissions resulted in changes towards fuel delivery systems; engine hardware as well as the gasoline fuel characteristics itself. The oxygenated gasoline blends are increasingly being used to increase the renewable energy content of road transport fuels. The Renewable Energy Directive (RED, 2009/28/EC) mandates that 10% of sustainably-produced renewable energy must be incorporated into transport fuels by 2020.

In Europe, ethanol, ethers such as Ethyl-Tertiary-Butyl Ether (ETBE) and other oxygenates can be used in gasoline blending. Currently, the EN228 gasoline specification allows a maximum of 2.7 wt% of oxygen content while a maximum of 5% v/v ethanol or 15% v/v of ether. There is however a call by the European Technical Committee to increase the maximum limit to 3.7 wt% of oxygen which corresponds to a maximum of 10% v/v ethanol.

The drive for higher oxygenates content may lead to a significant change to the spray characteristics of the gasoline blend which can impact emissions and vehicle drivability and performance in hot and cold temperature conditions. This can be clearly seen by the shift of the distillation curve when higher concentration of oxygenate is blended into gasoline.

Hot Weather Driveability (HWD) of vehicles was found to be affected most strongly by the “front end” volatility of gasoline, especially the DVPE (refer to section 3.6 for the definition) and E70 values. According to published literature, modern vehicles using PFI technology are much less susceptible to HWD problems compared to older carburetted engines. Stradling et al. (2012) tested several GDI engine vehicles and found that they were not affected so much with volatility ethanol/gasoline blends.

Cold Weather Driveability (CWD) is affected most strongly by mid-range volatility, defined in Europe by the E100 volatility parameter. CWD performance is an issue for modern vehicles because it is linked to exhaust emissions under cold starting conditions. For splash blends of ethanol in gasoline, McArragher et al. (2004) stated that CWD performance was found to improve somewhat due to the higher volatility of the ethanol/gasoline blend. CWD performance degraded, however, when the ethanol/gasoline blend was at the same volatility level as a hydrocarbon-only fuel. This was because of ethanol's higher latent heat of vaporisation and a leaning effect on the air-fuel ratio (AFR) due to ethanol under open-loop engine conditions. Open-loop conditions typically apply in the first few hundred seconds after starting a cold engine before the exhaust after treatment system and lambda measurement system have reached a minimum operating temperature.

3.3. Methanol gasoline usage in China

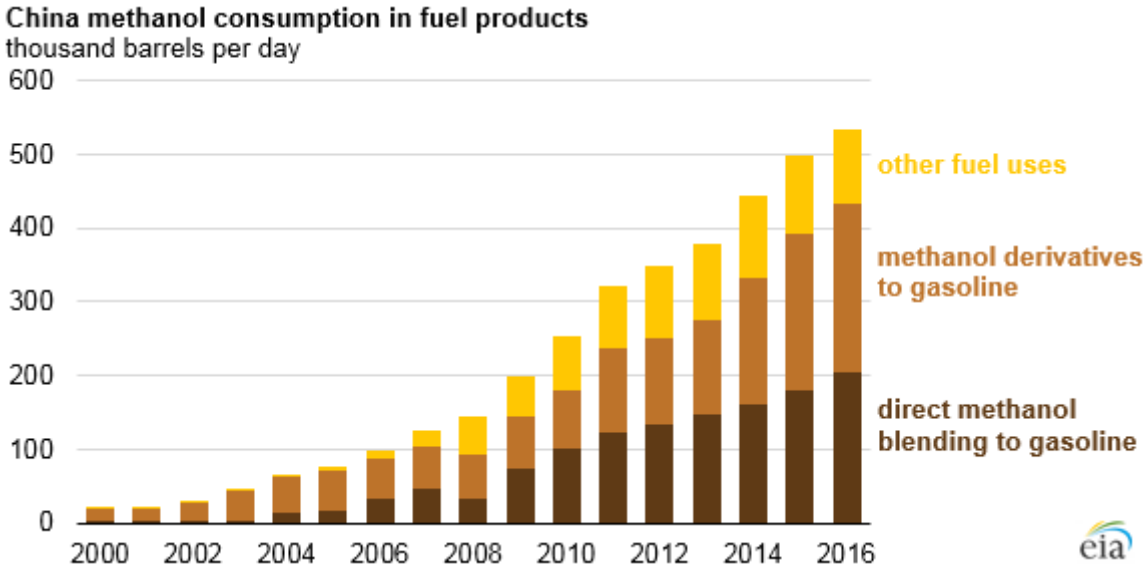


Figure 3.1: Methanol consumption in fuel products for domestic use in China. Source: U.S Energy Information Administration

China is currently the largest user of automotive methanol fuel. Since the year 2000, consumption of methanol has risen significantly and in 2016, the estimated consumption

was seen to reach 500,000 barrels per day, as shown in Figure 3.1. About two thirds of China's methanol feedstock is produced from coal with the remainder from coking gas and natural gas. The most common fuel available in many cities and provinces is M15 while M25, M30, M85 and M100 are also available in the domestic market. Typically, methanol is blended with a RON 93 gasoline fuel despite the availability of RON 90 and RON 97. As shown in table 3.1, there are currently 8 provinces in China that are already utilizing methanol gasoline fuel blends, with M15 and M85 being the popular choices.

Table 3.1: Chinese provinces and cities implementing methanol gasoline blends. Source: (a) National Bureau of Statistics of People's Republic of China. (b) Stratas Advisors, 2015

Provinces (a)	Cities	Pilot Program	Available Blends (b)
Shanxi Population: (36,500,000)	Taiyuan, Yangquan, Linfen, Pucheng, Datong, Shuozhuo, Xinzhou, Puzhong, Changzhi, Yuncheng, Luliang, Xi'an,	Implemented	M15, M30, M85, M100
Shaanxi Population: (37,327,000)	Xi'an, Baoji, Hanzhong, Quzhou,	Implemented	M15, M30, M85, M100
Zheijang Population: (55,600,000)	Quzhou, Hangzhou, Huzhou, Jiaxing, Taizhou, Jinhua	Implemented	M15, M30
Guizhou Population: (34,700,000)	Guiyang, Qiannan, Qianxi and Tongren	Implemented	M15, M85, M100
Gansu (25,575,000)	Pingliang, Lanzhou	Implemented	M85, M100
Hebei (73,326,000)	Tangshan	In progress	M15
Jiangsu (79,800,000)	Wuxi	In progress	M30
Ningxia (6,300,000)	Yinchuan	In progress	M15

3.3.1. Methanol gasoline blending characteristics

Methanol is a blending component made from a non-petroleum energy source such as coal, biomass and natural gas. Methanol as a blending component, burns very cleanly and has a very high-octane value. Over the years, methanol has been used in the automotive industry around the world as an additional resource to the already available commercial gasoline, either pure or as blend.

There are many papers that established the advantages of methanol fuel properties for gasoline engines. Besides the high-octane value, as well as having extra oxygen content, methanol can lower the boiling temperature of gasoline to improve fuel vaporization and it contains no sulphur – a contaminant that can poison catalytic converter operation.

Methanol has a nominal blending octane value (BOV) ranging from 129 to 134 Research Octane Number (RON). The high-octane rating of methanol provides a convenient and cost effective way to upgrade low octane gasoline components, such as low octane raffinate streams. The BOV of methanol is higher than other common blending octanes found in gasoline such as MTBE, toluene, xylenes and alkylates.

Despite the mentioned advantages of methanol (as well as other alcohols), it is also known for its susceptibility to pre-ignition and its corrosive attributes that can reduce the reliability and durability of the fuel systems in a vehicle. As a result, appropriate dosage levels of corrosion inhibitors are necessary for gasoline methanol mixtures, and fuel systems have to be made with materials that are compatible with methanol.

3.3.1.1. Physical properties

Like many other alcohols, methanol gasoline blending will always create a non-ideal mixture, which means that the extra OH molecules creates non-uniform intermolecular forces in the mixture. This means that whenever methanol is added to gasoline there is a change in the enthalpy of the solution. An ideal mixture will not face a gain or loss of heat during mixing. In an extreme case of non-ideal methanol gasoline blend, a phase separation can be seen.

One preliminary blending of M15 gasoline fuel saw a phase separation formed as shown in Figure 3.2. The methanol gasoline blend will separate into two phases if exposed to water in excess of the water tolerance for the ambient temperature conditions. The top phase (the larger part) normally contains the hydrocarbon portion of the gasoline with some methanol while the lower phase contains the water as well as the remaining alcohol portion of the gasoline mixture.

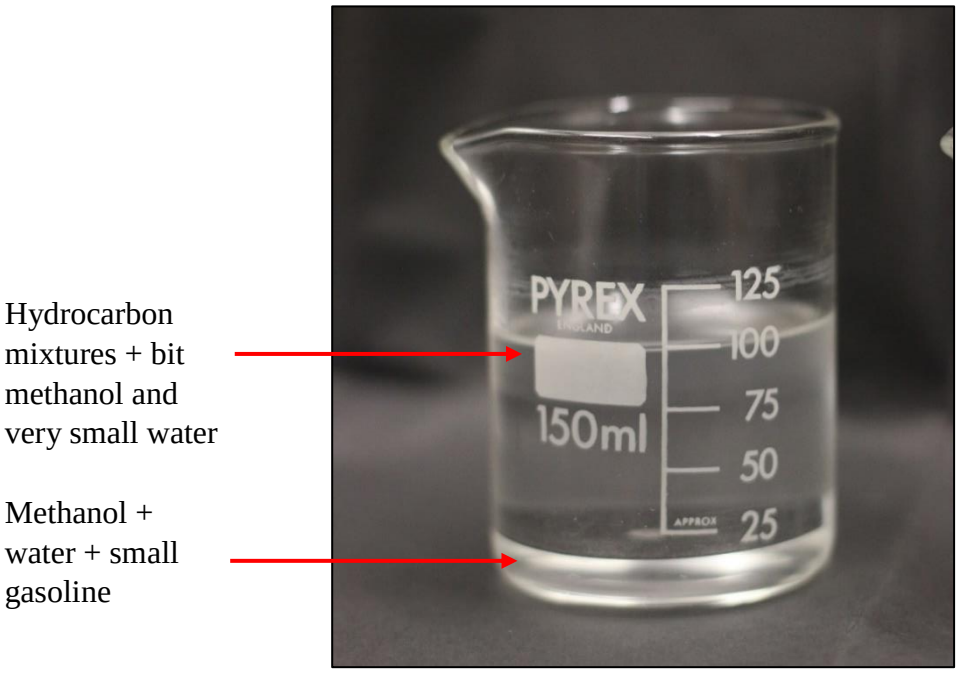


Figure 3.2: Example of phase separation of a gasoline methanol mixture without co-solvent

This blended M15 fuel consists of 15% methanol, 45% iso-octane and 40% n-pentane. Without the presence of aromatic compounds or a co-solvent alcohols (such as butanol) the methanol has poor solubility and phase stability in gasoline, especially in colder temperature conditions. This can be seen in the works of Owen & Coley (1995) in Figure 3.3, whereby various oxygenated gasoline blends (methanol and ethanol) were tested for water solubility. As shown in Figure 3.3, methanol has a lower water solubility saturation tolerance than ethanol and for both cases, increasing the percentage of the aromatic content in the mixture helps to increase the saturation level. As this research also looks into the development of P_M from oxygenated fuels, the aromatic portion that is added is sufficient to increase the mixture's water solubility.

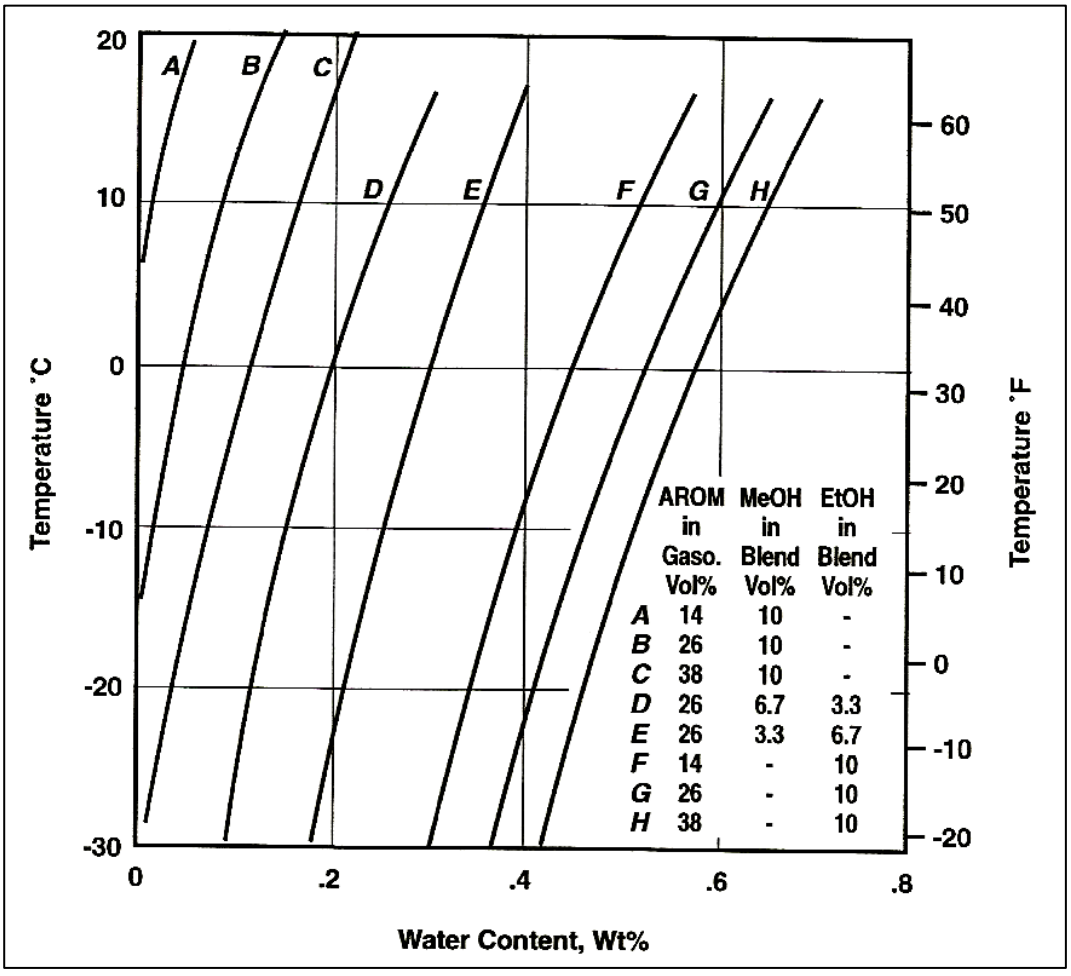


Figure 3.3: Water solubility saturation of various oxygenated gasoline mixtures at different temperatures (Owen & Coley 1995)

Methanol creates azeotropic mixtures with gasoline due to its non-ideal characteristics. This in turn changes the nature of evaporation of this mixture. Azeotropes can be defined as a solution of which the vapour has the same composition to its liquid. For example, an ethanol-water mixture on fractional distillation yields a solution containing approximately 95% by volume of ethanol. Once the composition has been achieved, the liquid and vapour have the same composition, and no further separation occurs.

When the methanol concentration in gasoline is increased, it is only the lower concentration levels that significantly impact the RVP change. Further increments of methanol concentration in gasoline, say > 10%, does not increase the vapour pressure as demonstrated in Figure 3.4. Figure 3.4 shows the result of modelled gasoline blends at different methanol concentration.

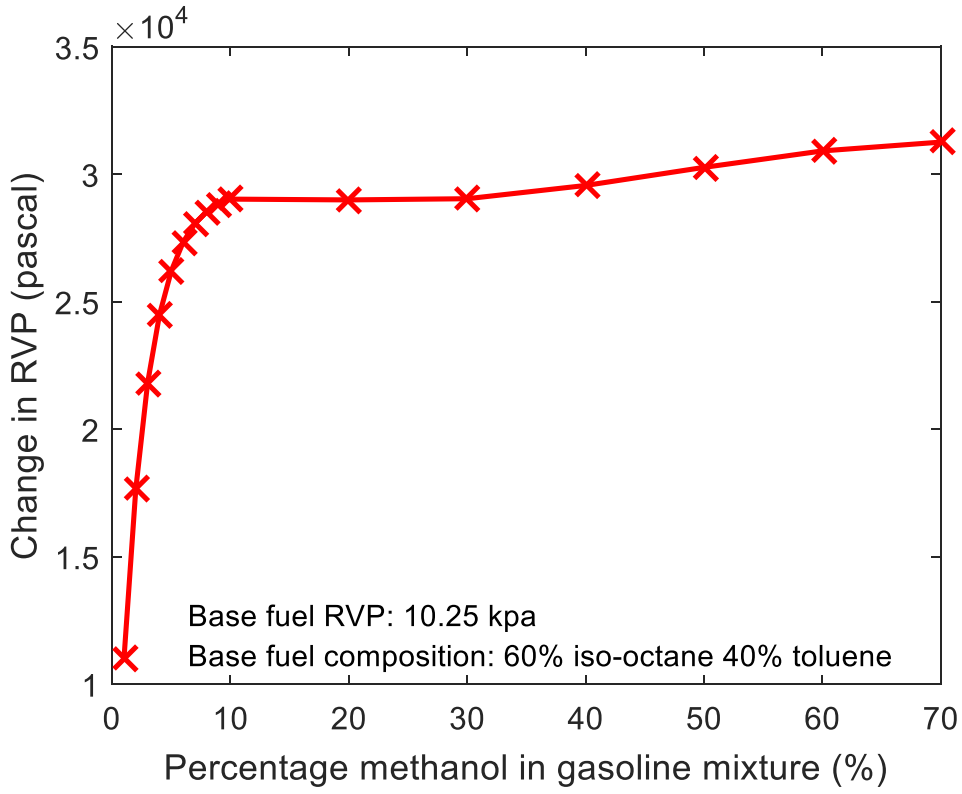


Figure 3.4: Modelled gasoline blend RVP change with different methanol concentration to show the effects of non-ideal mixtures

Adding methanol to gasoline is also known to distort the typical gasoline distillation curve. Due to its considerably lower boiling point of 64°C, methanol when added to gasoline, will produce a flattened curve in the early to mid-range of the distillation curve. Flattening the distillation curve means a larger portion of the fuel is evaporated at lower temperatures. This results in better fuel evaporation at cold engine operation and thereby a better cold-start performance. This is evident with some of the modelled distillation curve of fuels used in this research as discussed later in this chapter.

3.4. Evaporation modelling

The importance of fuel mixture preparation in GDI engine has been emphasized before. To achieve this, it is essential that the evaporation behaviour of a fuel is known which can help in optimizing engine operations. Commercial gasolines contain hundreds of different types of hydrocarbons which cannot be easily replicated. For this research, several fuels were designed to be able to precisely vary fuel parameters independently with the expectations that they have similar evaporation characteristics to the commercially available fuels. To do this, an evaporation model based on the Raoult's law was used.

3.4.1. Raoult's Law & UNIFAC

Raoult's law states that the vapour pressure of a solvent above a solution is equal to the vapour pressure of the pure solvent at the same temperature scaled by the mole fraction of the solvent present:

$$P_{solution} = \sum \quad x_{solvent}\, P_{solvent} \qquad (3.1)$$

Raoult's law only works for ideal solutions in which intermolecular forces are equal to those of their pure components. In an ideal solution, it takes exactly the same amount of energy for a solvent molecule to break away from the surface of the solution as if it was a pure solvent. An example of this is the mixture of n-butane and iso-butane.

As mentioned in section 3.3.1.1, the methanol mixture will never be ideal. Therefore, in order to make Raoult's Law work in the model, The Universal Functional Activity Coefficient method (UNIFAC) was introduced. The UNIFAC method was proposed by Fredenslund et al. (1978), so as to extend Raoult's Law to account for non-ideal mixing. The UNIFAC method is a group-contribution method, where the assumption is that a physical property of a fluid is the sum of the contributions made by the molecule's functional groups. This then contributes to a possible technique for correlating the properties of a very large number of fluids in terms of a much smaller number of parameters that characterize the contributions of individual groups. In the UNIFAC method, the activity coefficients in mixtures are related to the interactions between structural groups. The activity coefficient (γ_i) is separated in to two categories; the first provides a contribution due to differences in molecular size and shape, while the second provides a contribution due to molecular interactions. The following equations, Poling et al. (2001), for the UNIFAC method were used in MATLAB to model vapour pressures of the non-ideal mixtures:

$$\ln \gamma_i = \underset{combinatorial}{ln\, \gamma_i^C} + \underset{residual}{ln\, \gamma_i^R} \qquad (3.2)$$

$$\ln \gamma_i^C = \ln \frac{\phi_i}{x_i} + \frac{z}{2} q_i \ln \frac{\theta_i}{\phi_i} + l_i - \frac{\phi_i}{x_i} \sum_j x_j l_j \qquad (3.3)$$

$$\ln \gamma_i^R = \sum_k v_k^{(i)} \left(\ln \Gamma_k - \ln \Gamma_k^{(i)} \right) \qquad (3.4)$$

$$\ln \Gamma_k = Q_k \left[1 - \ln \left(\sum_m \theta_m \Psi_{mk} \right) - \sum_m \frac{\theta_m \Psi_{km}}{\sum_n \theta_n \Psi_{nm}} \right] \qquad (3.5)$$

$$l_i = \frac{z}{2} (r_i - q_i) - (r_i - 1) \qquad z = 10 \qquad (3.6)$$

$$\theta_m = \frac{Q_m X_m}{\sum_n Q_n X_n} \qquad (3.7)$$

$$\phi_i = \frac{r_i x_i}{\sum_j r_j x_j} \qquad (3.8)$$

$$r_i = \sum_k v_k^{(i)} R_k \qquad (3.9)$$

$$q_i = \sum_k v_k^{(i)} Q_k \qquad (3.10)$$

$$\Psi_{mn} = \exp\left(-\frac{a_{mn}}{T}\right) \qquad (3.11)$$

where x_i is the molar fraction of component i, θ_i is the area fraction, ϕ_i is the segment fraction, r_i is the normalised molecular Van der Waals volume, q_i is the normalised molecular surface area, Γ_k is the group residual activity coefficient and $\Gamma_k^{(i)}$ is the same in a solution of molecules of type i, $v_k^{(i)}$ is the number of groups of type k in the molecule i. Ideal mixtures will give a γ_i value of 1. If $\gamma_i > 1$, it is a positive deviation from Raoult's Law which causes the tendency of molecules to escape through evaporation to be much higher as the intermolecular strength is much lower. For the case of $\gamma_i < 1$ it is a negative deviation from Raoult's Law and evaporation is less likely to happen due to the strong intermolecular forces between the components. From the initial modelling of the vapour pressure using UNIFAC method, it is then further extended to predict the distillation curve of the mixture fuels. The modelling method of this program is explained in detail by Leach (2014) .

3.5. Gasoline model fuels

For this research, the focus was on the multi-component M15 fuel because of the suspected emissions problems and global interest mentioned in Chapter 1. There were several variations of the M15 fuels as well as non-M15 fuels modelled, blended and tested; Fuel A, Fuel A-, Fuel A+, Fuel B, Fuel C and Fuel D. The detail specifications of these fuels are shown in Table 3.2. A MATLAB program described in section 3.2 in this chapter was used for modelling the fuel evaporation characteristics.

Fuel A, Fuel A- and Fuel A+ were modelled with different volume fractions of n-pentane in order to vary the fuel volatility, with Fuel A+ expected to have the highest estimated Reid Vapour Pressure (RVP) value. Fuels B, C and D blends were deliberately modelled to contain high volume percentage of aromatics and long chain alkanes to have a high tail end boiling point on the distillation curve. The T90 values were over 46 K higher while the Final Boiling Point (FBP) value was 97 K higher compared to Fuel A.

To ease fuel identification, Fuel A, Fuel A- and Fuel A+ are categorized as ‘light-end fuels’ while Fuel B, Fuel C and Fuel D are the ‘heavy-end fuels’. The main purpose for having two different groups of fuel is to test the hypothesis that only the early regime (< T50) of the distillation curve that will cause a spray to flash regardless of having different T90 temperatures.

Table 3.2: Detailed specification of the modelled methanol gasoline blend fuels used

	Fuel A+	Fuel A-	Fuel A	Fuel B	Fuel C	Fuel D
Methanol Volume (%)	15	15	15	15	15	0
n-pentane Volume (%)	80	0	40	45	0	5
Iso-octane Volume (%)	5	82	42	0	45	55
Iso-butanol Volume (%)	0	3	3	0	0	0
n-decane Volume (%)	0	0	0	7	7	7
Undecane Volume (%)	0	0	0	5	5	5
Toluene Volume (%)	0	0	0	28	28	28
T50 (K)	305	368	324	327	380	380
T90 (K)	320	371	372	418	419	419
Final Boiling Point (K)	320	372	371	468	468	468
Calculated RVP (kPa)	121	40	85	87	37	15
Calculated RON	70	101	86	73	90	87

3.5.1. Oxygenated gasoline mixtures without aromatics (Light-end fuels)

The light-end fuels were modelled to specifically have different T50 (and lower) values in the distillation curve as shown in Figure 3.5. All of the light-end fuels have 15% methanol by volume but vary in volatility, which is controlled using different n-pentane percentages. These fuels were designed to be tested in the spray rig to establish the influence of T50 on the flash boiling of a spray. Therefore, aromatics were not inserted into the fuels. Fuel A and Fuel A- which contain a high percentage of iso-octane, required iso-butanol (3%) as co-solvent to prevent the mixture from having phase separation. The EN228 E100 is the European standard for gasoline distillation curve where evaporation must lie within the range of 46% to 71% of total evaporated volume at a temperature of 100°C. As for the EN228 E150 value, at a temperature of 150°C the minimum total evaporated volume has to be 75%. These light-end fuels do not comply to the European Standard but this is not a concern because they were not used in any of the engine experiments for particulate emissions tests. As explained in section 3.3.1.1, methanol tends to flatten the distillation curve due to its low boiling point.

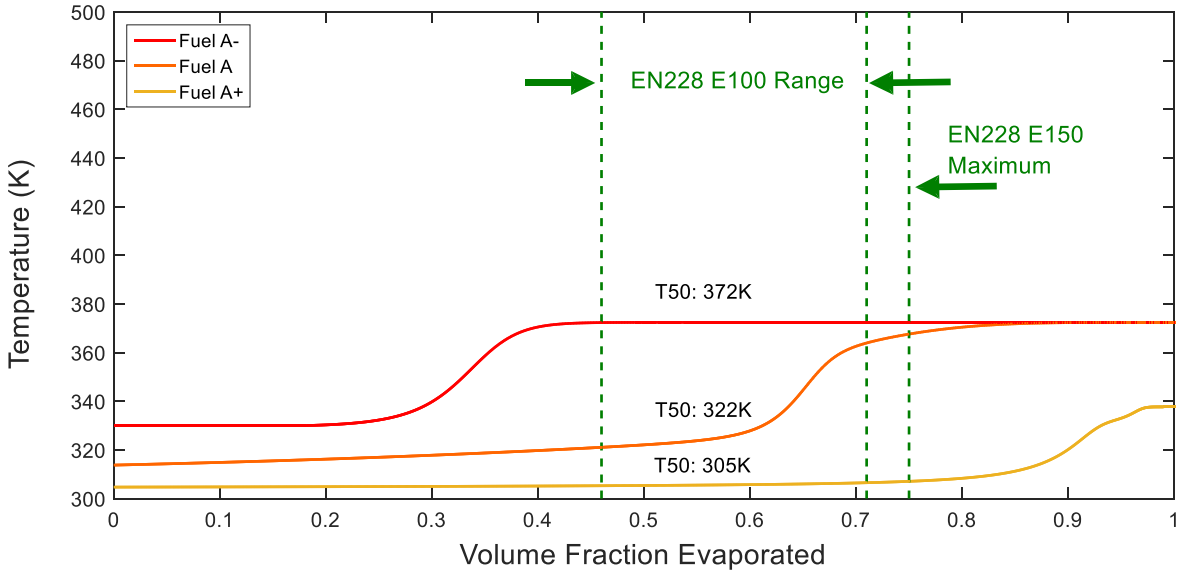


Figure 3.5: Modelled distillation curves of the light-end fuels

3.5.2. Oxygenated gasoline mixtures with aromatics (heavy-end fuels)

The heavy-end fuels were modelled to have similar T90 distillation values but to vary in their T50 (and below) values. The heavy component used in all fuels comprised of 28% toluene, 5% n-undecane and 7% n-decane. This is to mimic a conventional gasoline distillation end characteristic (T70 and above) as shown in Figure 3.6. An EN228 Euro 5 gasoline was also used for comparison purposes. Fuel B and C were modelled with 15% methanol but with different T50 values while Fuel D share the same T50 value with Fuel C but without any methanol content. Fuel D was deliberately modelled to have no methanol to show the impact on particulate emissions of non-oxygenated versus an oxygenated gasoline (Fuel C with similar T50 and T90 values). Fuel D on the other hand, is extremely volatile with 45% n-pentane, which is expected to cause the spray to flash boil very early at moderate fuel temperatures or slightly lower sub-atmospheric conditions. Fuel D is meant to test the hypothesis that an extremely volatile fuel, when flash boiling, will cause co-evaporation to be ineffective which will leave the heavy components unevaporated.

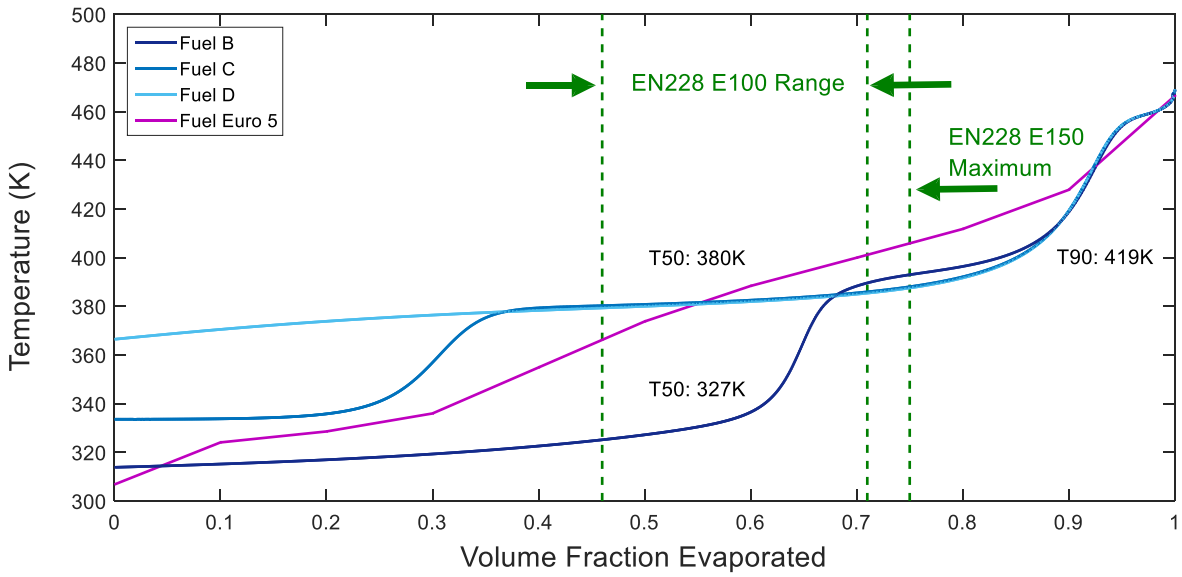


Figure 3.6: Modelled distillation curve of the heavy-end fuels

3.5.3. Establishing the saturation pressure ratio (Engine & Spray rig)

For this research, the modelled fuels undergo several different temperature and pressure conditions to test the susceptibility of each fuel to flash boiling and its impact on particulate emissions. To simplify the combination of these conditions, a simple pressure ratio, P_R equation is used:

$$P_R = \frac{P_{sat}}{P_{cyl}} \qquad (3.12)$$

where P_{sat} is the fuel saturation pressure and P_{cyl} is the ambient/cylinder pressure. As mentioned in chapter 2, the spray rig was built for test at ambient conditions (1.013 bar) while in the engine, in-cylinder pressure can vary from 0.3 bar to 0.6 bar depending on the injection timing selected. To better match these conditions to each other, P_r of each fuel and condition is used. The modelled P_r of each fuel in both spray rig and engine condition (0.5 bar) are shown in Figure 3.7 and the temperatures of which both apparatus can operate were selected. The fuel temperature in the spray rig had to be at slightly higher than in the engine due to the difference in ambient pressure.

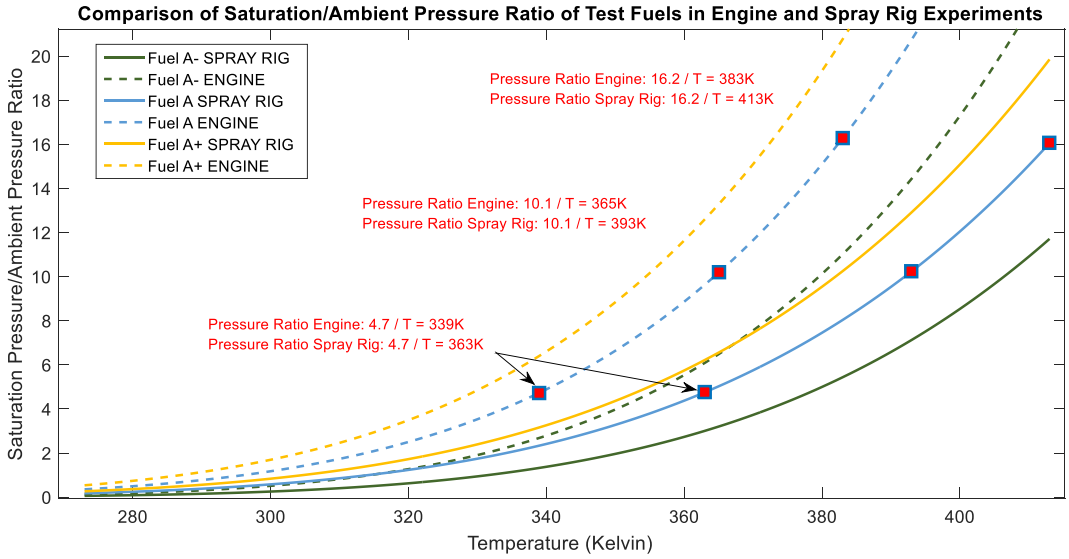


Figure 3.7: Pressure Ratio, P_r plot against fuel temperature used to match conditions in the spray rig and the optical engine

From table 3.3, it can be seen that matching the pressure ratios of the spray rig and the engine leads to different operating fuel temperatures; 23°C to 135°C for the spray rig and 23°C to 105°C in the engine. The two fuels (A and B) that have been used here, have a similar vapour pressure (calculated at 311 K) and similar early distillation curves up to the T50 point. However, Fuel B contains around 28% aromatic components (in the form of toluene) and a characteristic heavy end to the distillation curve with a T90 of 420 K. This represents a fuel whose hydrocarbons replicate the volatility and fraction evaporated specifications for a typical gasoline with a very high vapour pressure due to the addition of 15% by volume methanol. Previous experience with similar fuels has shown a high level of particulate emissions results with M15 fuel. In addition, two variants of Fuel A have been used – Fuel A+ is more volatile as it contains 80% n-pentane, and Fuel A$^-$ that is less volatile as it contains no n-pentane.

Table 3.3: Fuel saturation pressure ratios for Fuels A, A+, A- and B only. The matched highlighted entries show similar ratios that may be used for comparison between the spray rig and engine studies

	Fuel A / Fuel B				Fuel A-				Fuel A+			
	Rig (1.0 bar)		Engine (0.5 bar)		Rig (1.0 bar)		Engine (0.5 bar)		Rig (1.0 bar)		Engine (0.5 bar)	
Fuel temperature (°C)	Fuel vapour pressure (bar)	Pressure ratio	Fuel vapour pressure (bar)	Pressure ratio	Fuel vapour pressure (bar)	Pressure ratio	Fuel vapour pressure (bar)	Pressure ratio	Fuel vapour pressure (bar)	Pressure ratio	Fuel vapour pressure (bar)	Pressure ratio
23	0.44	0.43	0.50	1.00	0.21	0.20	0.21	0.42	0.72	0.70	0.72	1.44
60	1.95	1.93	1.95	3.90	1.07	1.04	1.07	2.14	2.66	2.59	2.66	5.32
90	4.82	4.76	4.82	9.64	3.05	2.97	3.05	6.10	6.30	6.15	6.30	12.6
105	7.18	7.09	7.18	14.4	4.78	4.66	4.78	9.56	9.21	8.99	9.21	18.4
120	10.4	10.2	10.4	20.8	7.22	7.05	7.22	14.4	13.1	12.8	13.1	26.2
135	14.6	14.4	14.6	29.2	10.5	10.25	10.5	21.0	18.1	17.6	18.1	36.2

3.6. Vapour pressure validation results

Vapour pressure validation exercise was conducted to validate the accuracy of the vapour pressure calculation model, especially for the non-ideal mixtures. This exercise is essential for this research as the vapour pressure of each fuel is translated into a saturation pressure ratio and correlated with spray characteristics and particulate emissions. Pure fuels (methanol, n-pentane and toluene) as well as mixtures were tested using the vapour pressure measurement apparatus from 25°C up to 75°C.

The vapour pressure of gasoline is normally measured in accordance with EN 13016-1 and is expressed as Dry Vapour Pressure Equivalent (DVPE). This standard uses a temperature of 37.8 °C (310.95 K). DVPE is intended to be equivalent to RVP and is calculated from a statistical correlation equation to give a dry Reid Vapour Pressure. The differences between Reid Vapour Pressure, DVPE and Air Saturated Vapour Pressure (ASVP), are all small (and comparable to uncertainties when they are measured or modelled); they are all essentially absolute vapour pressures.

3.6.1. Pure fuels

Pure fuels were used for initially to validate the accuracy of the apparatus used. The vapour pressure data for pure fuels can also be found in many publications but for this exercise the modelled data were used for comparison. The other reason for using pure fuels is to check if the fuels available for the experiment are not contaminated. As can be seen in Figure 3.8, all of the pure fuels are very closely matched to the available data with mean absolute error lower than 10 kPa. Methanol experienced the highest mean absolute error; probably due its susceptibility to water contamination which can easily change the properties of the fuel.

This error however is reasonably low and is not a big concern for the remaining experiments as these values are close to the repeatability and reproducibility magnitude of a similar method (ASTM D323) for gasoline vapour pressure measurement as shown in Table 3.4. The close agreement of the measured to the modelled data establishes that the apparatus used for this validation is good and suitable for vapour pressure measurements of the mixtures.

Table 3.4: Precision of vapour pressure test methods (George E. & Shah 2003)

ASTM Designation	Method Name	Procedure / Model	Range	Repeatability	Reproducibility
D 323	Reid Method	A (Gasoline)	35-100 kPa (5-15 psi)	3.2 kPa (0.46 psi)	5.2 kPa (0.75 psi)
		B (Gasoline)	35-100 kPa (5-15 psi)	1.2 kPa (0.17 psi)	4.5 kPa (0.66 psi)
		A	0-35 kPa (0-5 psi)	0.7 kPa (0.1 psi)	2.4 kPa (0.35 psi)
		A	110 – 180 kPa (16-26 psi)	2.1 kPa (0.3 psi)	2.8 kPa (0.4 psi)
		C	180 kPa (>26 psi)	2.8 kPa (0.4 psi)	4.9 kPa (0.7 psi)
D 4953	Dry Reid Method	A		3.65 kPa (0.53 psi)	5.52 kPa (0.8 psi)
		B (Gage)		4.00 kPa (0.58 psi)	5.38 kPa (0.78 psi)
		B (Precision)		3.58 kPa (0.52 psi)	4.27 kPa (0.62 psi)

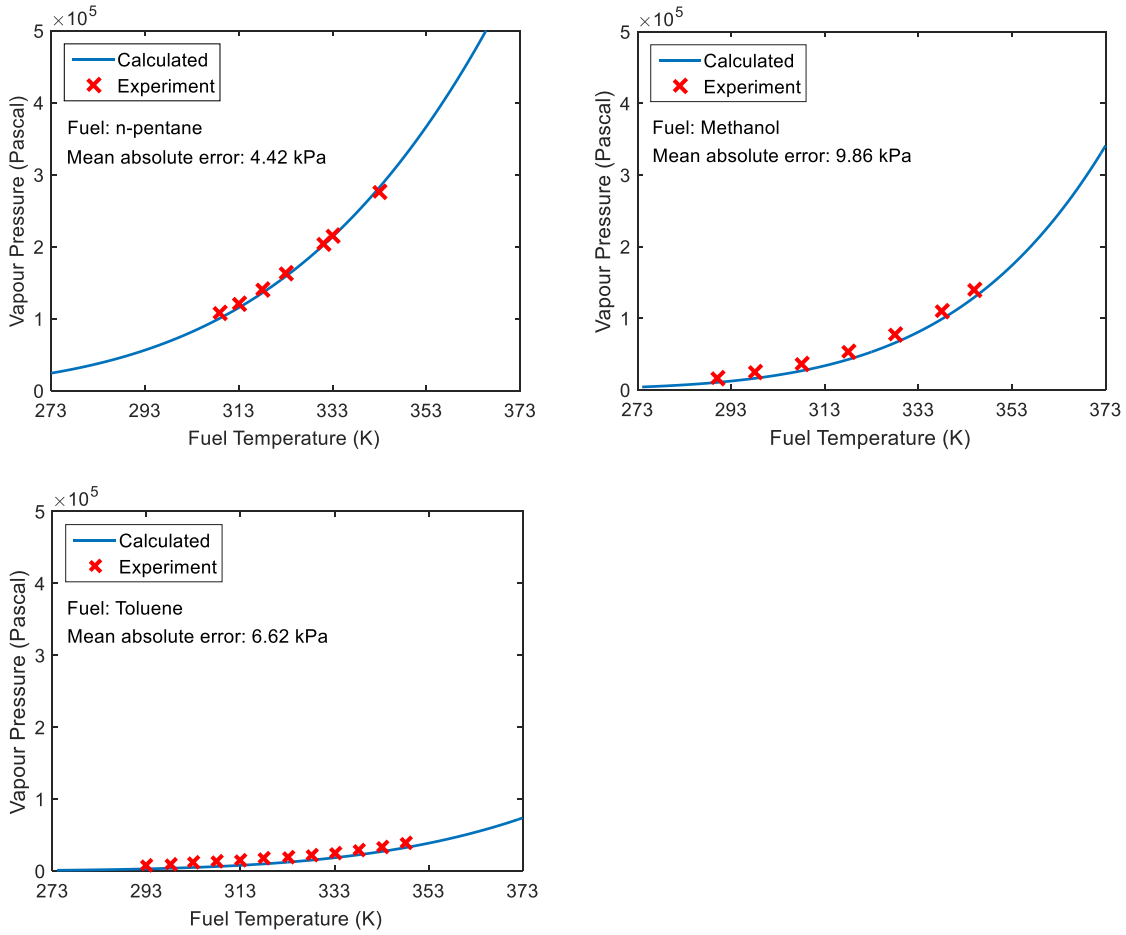


Figure 3.8: Modelled vs experimental vapour pressure data of pure fuels

3.6.2. Mixtures

For the mixture validation experiments, Fuel B, Fuel D and a random fuel mixture (40% iso-octane, 40% toluene, 20% methanol by volume) were used. These fuels were selected to show different levels of volatility and a comparison between ideal and non-ideal mixtures. Firstly, two out of the three results show that the modelled vapour pressure shows good agreement with the experimental results as shown in Figure 3.9. However, the Fuel B experiment result showed a slightly skewed trend at higher temperatures. A possible reason for this to happen is that part of the light fuel component (n-pentane) may have escaped during blending process as Fuel B has a very high RVP value at 87 kPa. The results from

the random fuel and Fuel D show that the UNIFAC method model has managed to closely predict the correct vapour pressure of the mixtures despite having non-ideal properties.

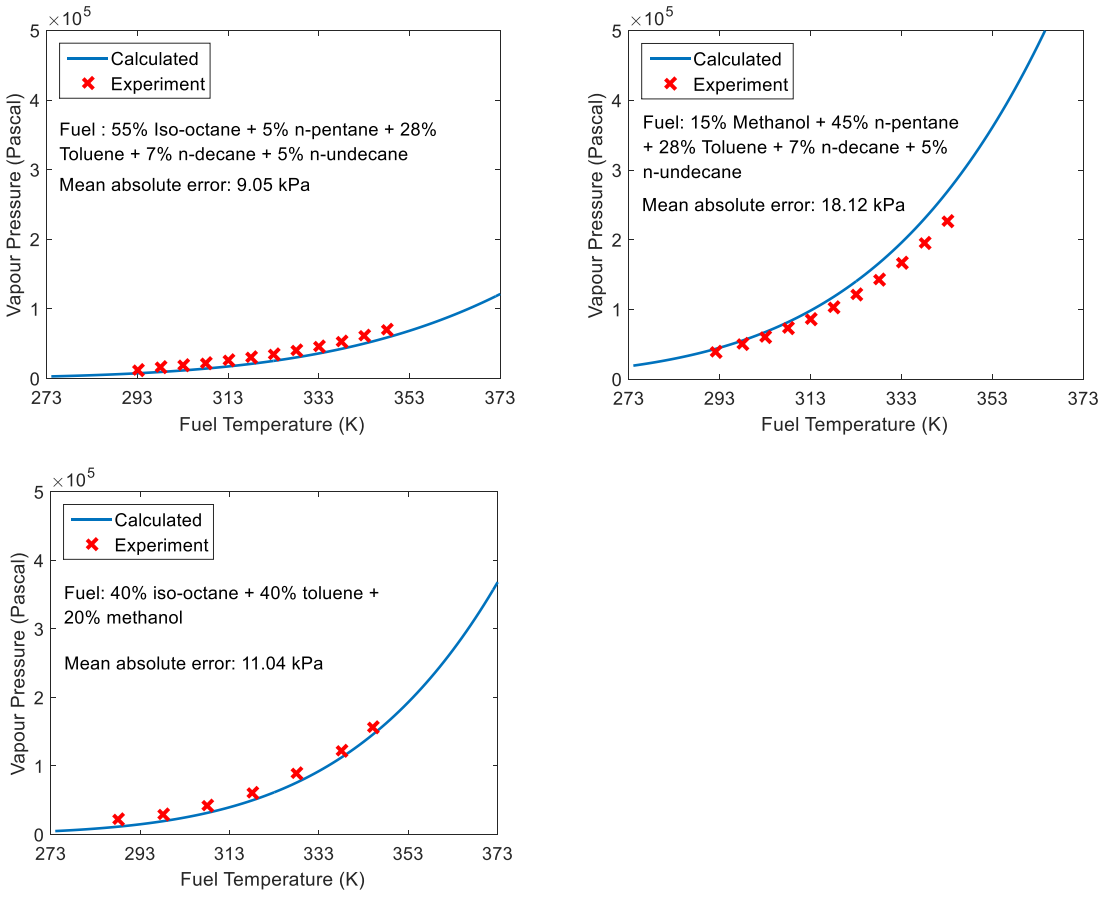


Figure 3.9: Calculated vs experimental vapour pressure data of various fuel mixtures

3.7. Chapter summary

In this Chapter, the issues and advantages regarding the use of methanol in gasoline blend in vehicles have been explored. As the shown in this Chapter, the popularity of methanol gasoline blends (M15 being most popular) is increasing every year especially in China where there is an abundance of methanol available. The physical as well as thermodynamic properties of gasoline-methanol blends which can impact the experiments in this research have also been highlighted. In order for the fuels to be designed for the

investigation of flash boiling and its impact, an evaporation model using Raoult's Law and the UNIFAC method written in MATLAB has been used to predict the behaviour of the fuels.

As a result, two different categories of fuel have been designed; M15 Fuels without aromatics but varying in volatility, M15 and non-oxygenated fuels that vary in volatility but have similar heavy component (aromatics and high carbon atom number alkanes) contents. The distillation curve of these fuels has been compared to show how they differ to each other.

Once the fuels were defined, a pressure ratio parameter was introduced to simplify fuel characterisation at different temperatures and pressures. With the pressure ratio known for all fuels, operational temperatures in the spray rig and the optical engine were able to be selected by matching them together despite having different ambient pressure conditions.

The MATLAB evaporation model has been validated against vapour pressure measurement experimental data using pure fuels and mixtures. The validation result of the pure fuels shows good agreement which proved that the apparatus and measuring method was working well. For the mixtures, only the most volatile mixture shows slight deviation (5~15 kPa) from the model but the others are in good agreement.

4. Spray Characterization Experiments and Results

4.1. Introduction

Spray characteristics are an important factor when studying the production of particulate matter in IC Engines. Parameters such as fuel temperature, injection pressure, injection duration, injection timing and fuel composition will affect the outcome of how the spray develops. This in turn influences the spray structure, spray tip penetration as well as the spray droplet sizes of every injection. Previous studies have shown that having control of these parameters has helped in reducing PM production in GDI engines.

This chapter begins with an investigation of spray characteristics from the AJ133 injector using fuel mixtures of different volatilities, namely the oxygenated Fuel A and its variants. Spray tip penetration as well as spray angle were measured at various fuel saturation pressure ratios. These conditions will be replicated on the optical engine in Chapter 5 for a better comparison and to check for correlations in PM production. The study here continues with a spray geometry comparison between Fuel A and Fuel B. As described in chapter 3, Fuel A and Fuel B have the same vapour pressure and T50 values but differ at their T90 values due to the presence of heavy components in Fuel B. The objective was to better understand the effects of heavy components present in mixtures on the spray geometry.

Further experiments on the spray rig continue with an investigation of the repeatability of the spray geometry at various fuel temperatures. The experiments were conducted using Fuel B sprayed and imaged for 50 cycles. As fuel spray geometry is known to change at different temperatures, it was essential to establish the repeatability of sprays even after multiple injection cycles. The concern was the ability of the surrounding heat source to heat the fuel or injector body in the time between injections at a particular fuel

mass flowrate. The final part of this chapter is the follow-up from previous section which investigates the change of injector tip temperature after various numbers of multiple injections. Simple modifications were made to the injector by attaching a thermocouple close to the side of the injector tip. This is more comparable to the operating conditions of the engine during motoring rather than with combustion. This can be more beneficial as the presence of combustion helps by having an additional source of heat into the injector tip.

4.2. Test conditions

Table 4.1: Experimental conditions for spray characterization

Experiments	Spray penetration measurements	Spray angle measurements	Spray geometry repeatability test	Spray geometry comparison between light-end and heavy-end mixtures
Injection pressure	50, 150 bar	50, 150 bar	150 bar	150 bar
Injection duration	2 ms	2 ms	2 ms	2 ms
Imaging setup	Backlit Imaging	Backlit Imaging	Mie-scattering	Mie-scattering
Illumination type	Pulsed 50V white LED	Pulsed 50V white LED	Pulsed 50V white LED	Pulsed 50V white LED
Fuel	Fuel A, Fuel A-, Fuel A+	Fuel A, Fuel A-, Fuel A+	Fuel B	Fuel A, Fuel B
Fuel temperature	23, 60, 90, 105°C	23, 60, 90, 105°C	20, 60, 90, 120, 135°C	20, 60, 90, 120, 135°C
Injector position	0° (Camera facing lead; Figure 2.3)	0° (Camera facing lead; Figure 2.3)	30°	30° clockwise
Injector type	GDI multi-holes 6 nozzle	GDI multi-holes 6 nozzle	GDI multi-holes 6 nozzle	GDI multi-holes 6 nozzle
Ambient temperature	15 – 18°C	15-18°C	15-18°C	15-18°C
Chamber pressure	atmospheric	atmospheric	atmospheric	atmospheric
Total number of image set	10	10	50	50

The experimental conditions for the four different experiments conducted are given in Table 4.1. All of which were conducted using high speed imaging and subsequently post-processed for extraction of numerical data.

Backlit imaging was used in the experiments for spray penetration and spray angle measurements, to maximise the contrast between the sprays and their background which can make boundary recognition easier during post-processing. As for the repeatability test and comparison between light-end and heavy-end mixtures, Mie scattering was chosen because data from both experiments were dependent on light luminosity at the post-processing stage. Two injection pressures were used for the spray penetration and angle measurements; 50 bar and 150 bar. The injection pressure of 50 bar, while not commonly used, has been tested by some manufacturers for the use of multiple injections per cycle in GDI engines and also to reduce the fuel pump work so as to improve fuel economy. Low injection pressures (such as 50 bar) give greater potential for the spray to collapse at very low pressure ratios due to the lack of momentum from the spray droplets which contributes to the geometry outcome. The 150 bar injection pressure is a nominal maximum pressure widely used by GDI engines.

As previously mentioned in chapter 2, the spray rig was operated at ambient pressure conditions. Therefore, to match the saturation pressure ratio of the fuel used in the engine (chamber pressure of < 0.5 bar), the spray repeatability test and geometry comparison had to be done at elevated temperatures of up to 135°C.

Only the Fuel A variants were used for spray penetration and angle measurements. These variants (with different volatilities) coupled with various tested temperatures were enough to cover wide range of saturation pressure ratios. The maximum pressure ratio achieved was close to 10. The full range of pressure ratios of Fuel A at all temperatures can

be seen in Table 3.3. Fuel B was one of the fuels used in the optical engine experiments, therefore using this fuel for the spray rig experiments will be a useful comparison.

The injector position was maintained at 0° for spray penetration and angle measurements to follow the SAE J2715 standard guidelines. However, for the remaining experiments, the injector was rotated 30° to increase visibility of all the spray plumes. This is also the angle where sprays were imaged on the optical engine. Having both spray rig and optical engine sprays imaged at the same angle gives a better understanding for comparison purposes.

4.3. Spray axial penetration measurements of the light end mixtures

Spray tip penetration measurement is a common method of study currently being used by many GDI engine researchers. This is because the behaviour of sprays can be unique to a particular injector design. Furthermore, in GDI systems, spray dynamics can be the driving factor towards piston or wall impingement which can lead to poor emissions. It must be noted that the spray characteristic studies in this research were not to establish or directly compare any differences with the findings in the previous spray characteristics literature. The findings from this chapter were used mostly to facilitate and be correlated to the PM experiments on the optical engine in the next chapter.

While spray tip measurements can be used to predict the time and period for which impingement occurs, spray angle measurements on the other hand are normally used to quantify the spread of fuel mass in the chamber or the severity of impingement.

To ease categorization of sprays for three different variation of fuel volatilities, the term pressure ratio, P_R which was introduced in Chapter 3 is used again. An injector is normally designed to have nozzles with specific targets in the combustion chamber. For the

AJ133 injector, its typical spray structure can be seen in Figure 4.1. Figure 4.1 shows the fuel spray of Fuel A- imaged from 0.8 ms to 2.0 ms ASOI at a temperature of 23°C. These false colour images were post-processed from raw images using the IMSPRAY MATLAB program. The post-processing method was described in detail in chapter 2.

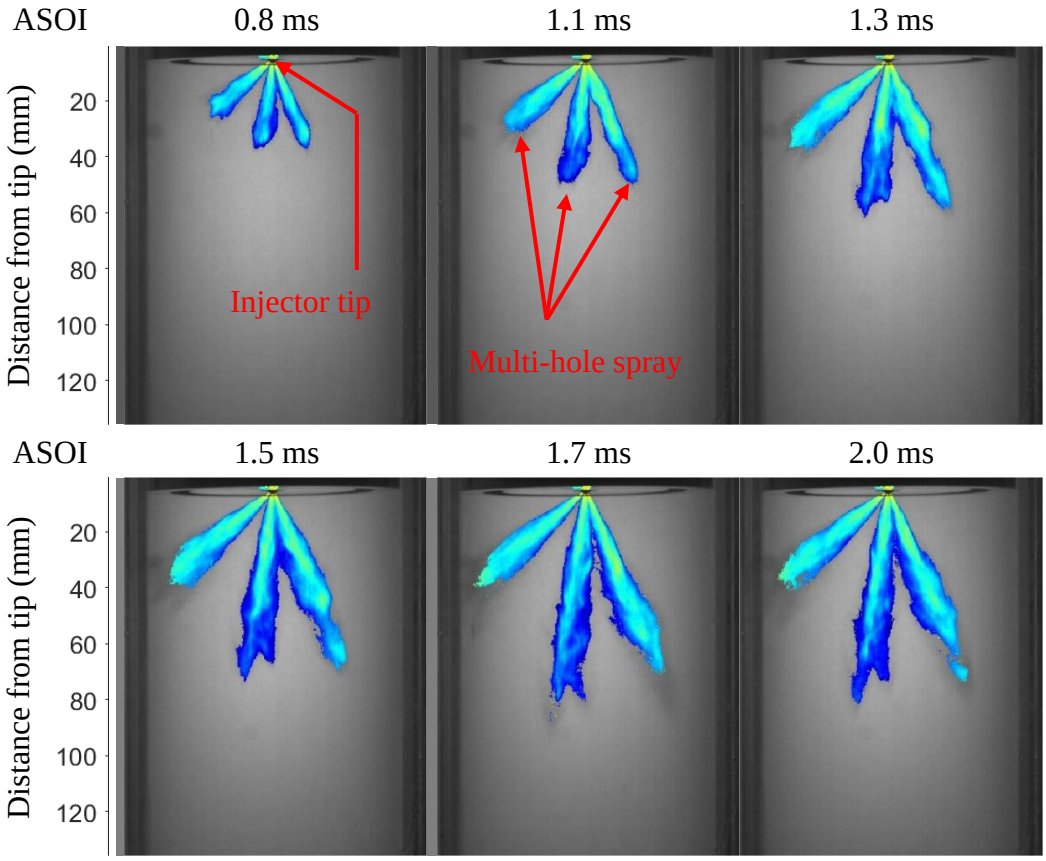


Figure 4.1: Typical processed false colour images of 50 bar fuel A- spray at 23°C fuel temperature from 0.8 ms to 2.0 ms

At low temperature of 23°C and $P_R < 1$, a subcooled condition for all of the A fuel variations, all of the plumes from the spray were very visible, with very minimal interactions seen between them. At $P_R < 1$, the evaporation rate was very low and could not influence any changes to the spray structure. However, as the fuels were heated up to certain temperatures or sprayed into a sub atmospheric conditions, P_R was then increased and the conditions got closer to a flash boiling stage. At $P_R > 1$, the flash boiling characteristics

started to appear in the sprays. This can be seen in Figure 4.2 where a series of captured images from Fuel A- sprayed at 50 bar and 150 bar are presented at various pressure ratios, P_R. Fuel A- was the least volatile among its variants.

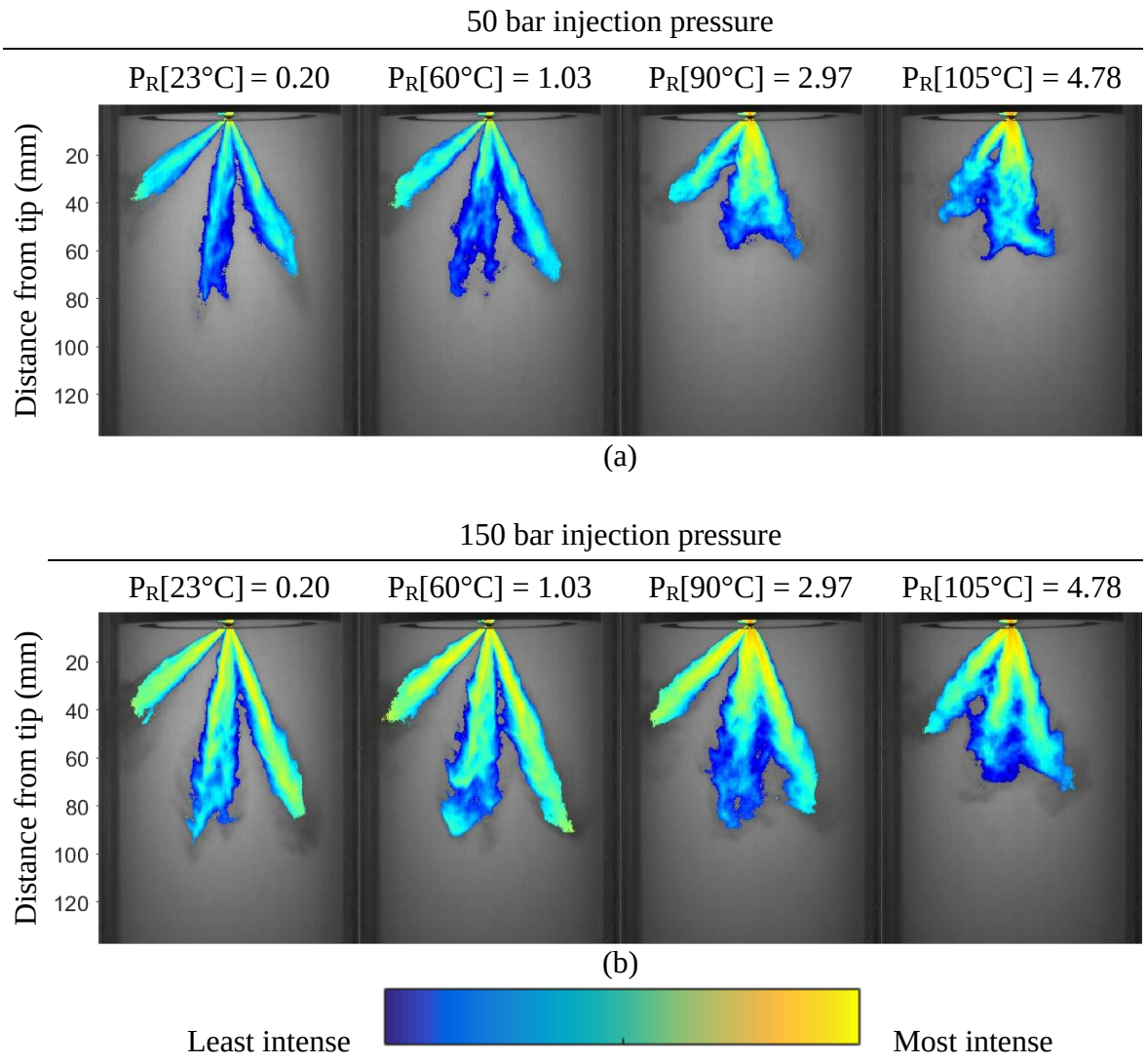


Figure 4.2: (a) 50 bar spray of Fuel A- captured at 2.0 ms ASOI for various pressure ratio ratings. (b) 150 bar spray of Fuel A- captured at 2.0 ms ASOI for various pressure ratio ratings.

As illustrated in Figure 4.2, at two of the lower temperatures, both sprays at 50 bar and 150 bar produced very similar spray structures. As P_R is further increased, the spray was seen to have entered the transitional flash boiling phase. At P_R = 2.97 and P_R = 4.78, as shown in the images, the sprays coalesced and caused a reduction in spray tip penetration.

This phenomenon of transition flash boiling begins with the 'swelling' of each spray plume or an increase in the cone angle. Similar behaviour was discovered by Zeng et al. (2012) where alcohol fuels were tested in a multi-hole injector and the spray cone angle was found to have increased at $P_R > 1$. Mojtabi et al. (2008) showed similar evidence by reducing the chamber pressure below atmospheric pressure when imaging gasoline sprays. However, no value of P_R was mentioned in this literature.

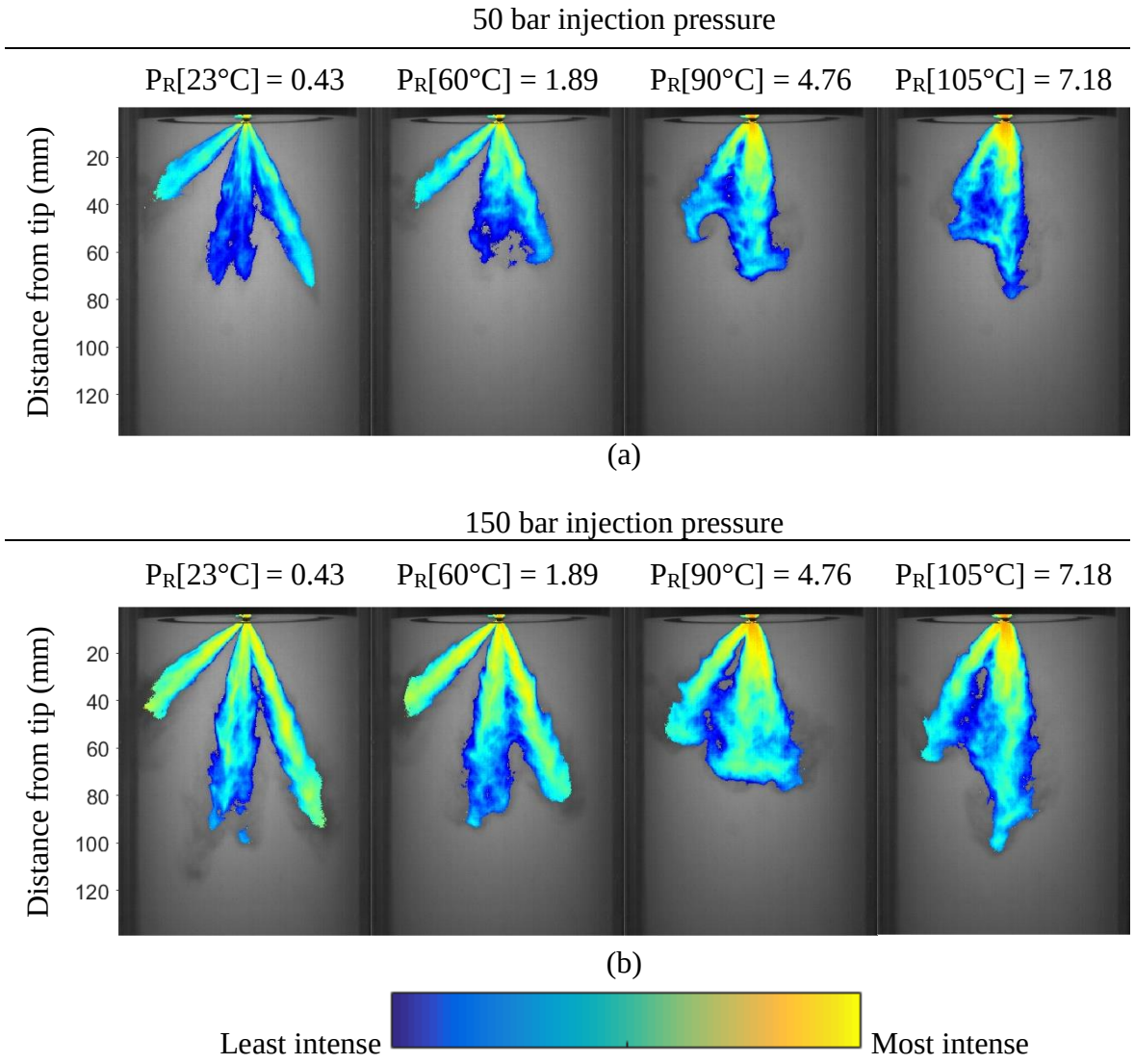


Figure 4.3: (a) 50 bar spray of Fuel A captured at 2.0 ms ASOI for various pressure ratio ratings. (b) 150 bar spray of Fuel A captured at 2.0 ms ASOI for various pressure ratio ratings.

At this stage, with minimal coalescing of plumes, low pressure toroidal structures were formed at the outer border of the spray structure that retard spray development by

swirling the droplets upwards. As the plume cone angle continues to increase, the overlapping of plumes become more severe, such that a low pressure condition was created close to the centre axis of the injector which starts the process of spray collapse. As for Fuel A, the maximum P_R achieved was $P_R = 7.18$. At $P_R = 4.76$ ($T_{Fuel} = 90°C$), the spray structure of Fuel A is similar to Fuel A- at $P_R = 4.78$ ($T_{Fuel} = 105°C$) where spray tip penetration can be seen to be quite poor.

Other than that, the spray for Fuel A at $P_R = 1.89$, the spray plumes were seen to have already coalesced when injecting at the lower injection pressure of 50 bar. However, at $P_R = 7.18$, the spray structure changed significantly when flash boiling happens at the flare flashing phase. The spray plume on the most right has seen to have combined with the middle plume resulting in a significant reduction in spray angle and concentrating the plumes to point in a more downwards direction. During the flash boiling conditions, micro explosions of bubbles happen close to the injector tip as liquid fuel exits the nozzle with rapid evaporation.

As explained in the literature of Zhang et al. (2013), by using PIV, the spray flow field showed that at the stage where plume interactions occur, the velocity towards the centreline increased drastically. By using a numerical study, Shen et al. (2017) demonstrated the gas pressure distribution during spray at flash and non-flash boiling conditions which explains this behaviour. Shen illustrated from simulations, that when the fuel is superheated, three obvious low pressure regions are observed in a vertical section: one is near the injector where the micro-explosion occurs and the two others are at the spray tip. Comparing with the velocity distribution, it was found that the low pressure regions make the gas move inwards. Micro-explosions occur as the fuel is discharged from the injector at the fuel temperature of 110°C and a large number of small droplets are produced. The droplets near the injector are pushed into the spray centre by the inward moving gas as the fuel is

discharged; this makes the spray collapse. At the spray tip, the inward moving gas also drags the droplets towards the spray centre, which prevents the spray from dispersing and strengthens the spray penetration.

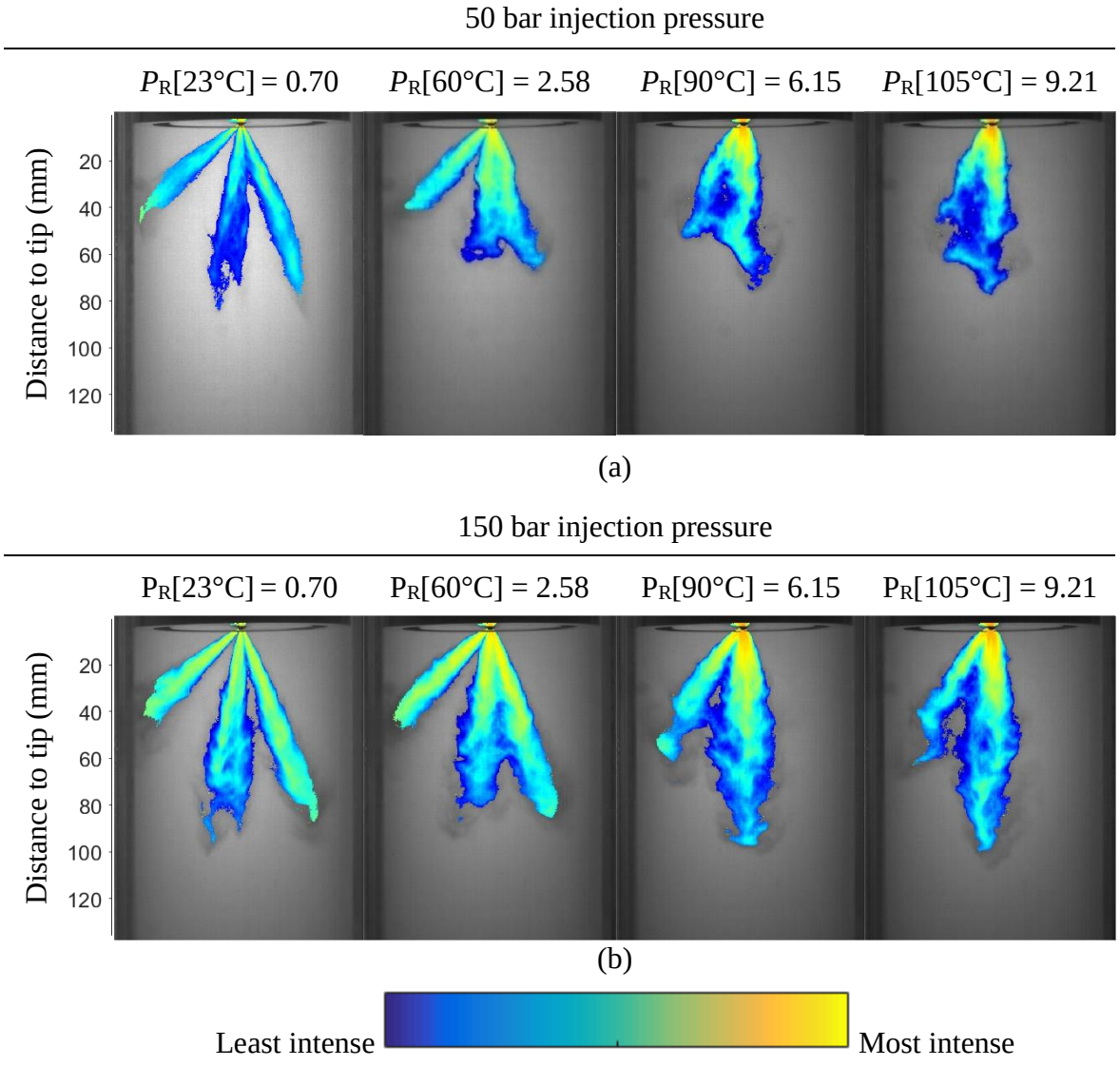


Figure 4.4: (a) 50 bar spray of Fuel A captured at 2.0 ms ASOI for various pressure ratio ratings. (b) 150 bar spray of Fuel A captured at 2.0 ms ASOI for various pressure ratio ratings.

A much higher pressure ratio for the fuel spray was achieved in this experiment by testing Fuel A+ (most volatile) at the temperature of 105°C. The fuel spray structures produced at all of the intended temperatures are illustrated in Figure 4.4.

Since Fuel A+ was tested at the same temperatures as the other variants, none of these temperatures were in the range of the transition flash boiling condition. This is evident from Figure 4.4, as the spray structures at temperature of 90°C and 105°C were already in the flare flashing phase, while sprays at 60°C only show an increase in cone angle at each plume. At P_R = 1.89 and an injection pressure of 50 bar, there was minor interactions between the plumes but not enough to cause it to collapse. As shown in Figure 4.4, the Fuel A+ sprays at P_R = 6.15 and P_R = 9.21 are very similar in terms of structure. This suggest that the flare flashing phase is at $6 < P_R < 9.2$. To get a better picture of the tip penetration trends of the sprays presented earlier, tip penetration has been measured in detail from the images and is plotted in Figures 4.5, 4.6 and 4.7.

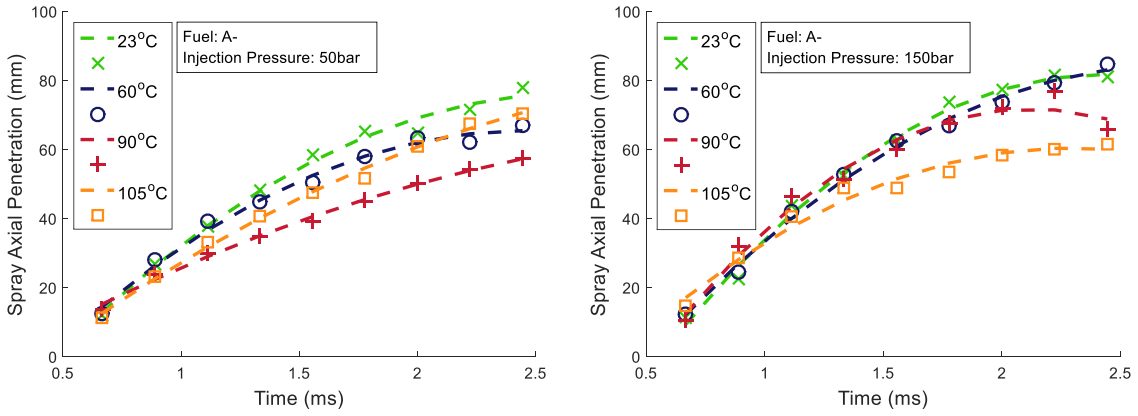


Figure 4.5: Spray axial penetration against time of Fuel A- injected at (a) 50 bar and (b) 150 bar at various temperatures

Figure 4.5 shows the spray tip penetration measurements for Fuel A- (the least volatile) experimented at 50 bar and 150 bar. The broken line coloured in green represents the coldest fuel temperature at 23°C while the one in orange is the highest fuel temperature at 105°C. As expected, the penetration trend begins with a linear trend before arriving at a plateau. Despite the 150 bar injection pressure, which produces higher momentum for the fuel droplets to travel, the maximum travel distances only differ by 5-15 mm. It has to be

noted that for the 50 bar injection pressure for fuel A-, the least distance travelled by the spray was at 90°C while for 150 bar it was at 105°C. The reason for this was illustrated earlier in Figure 4.2 showing that the 50 bar spray collapsed at a slightly lower temperature due to a lack of momentum to maintain the spray geometry.

Figure 4.6 shows the spray tip penetration measurements for Fuel A (mid volatility) experimented at 50 bar and 150 bar. At 50 bar injection pressure, Fuel A being slightly more volatile than Fuel A-, began collapsing (transition stage) at a much lower temperature of 60°C (refer to Figure 4.3), which causes penetration to be only close to 60 mm which is very much shortened, and also reached a plateau value first.

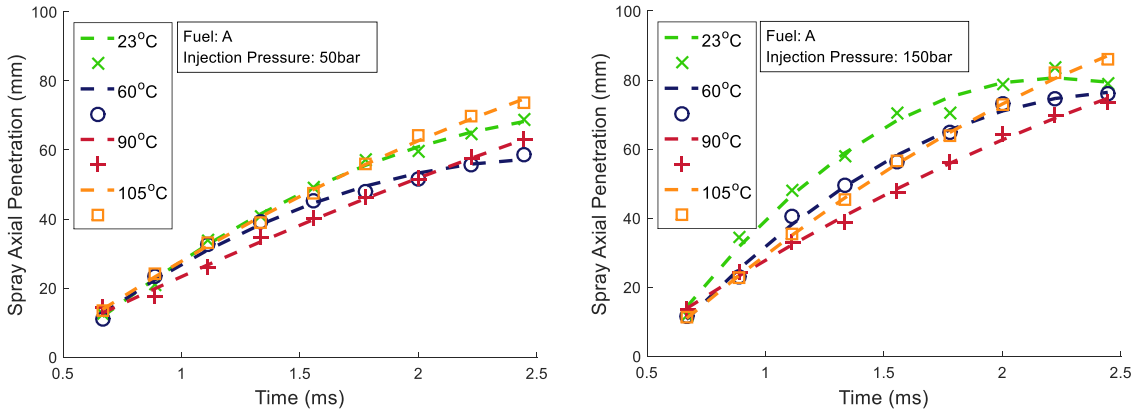
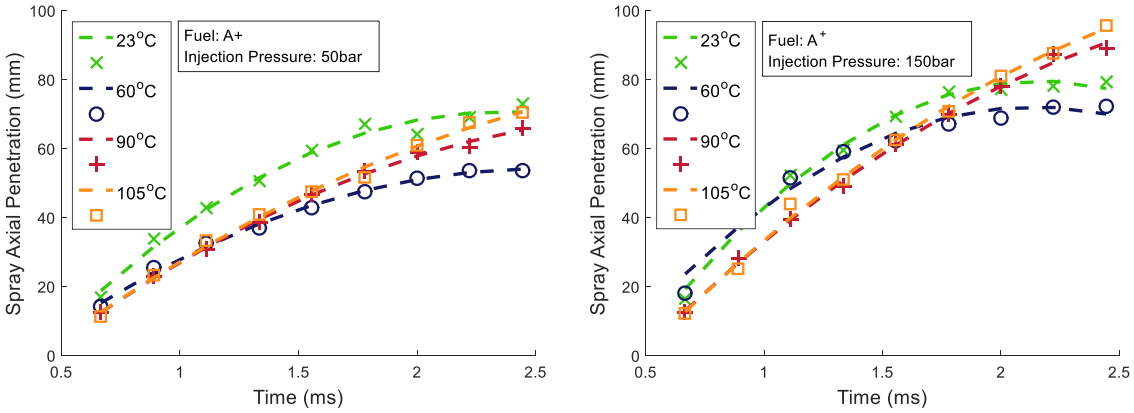


Figure 4.6: Spray axial penetration against time for Fuel A injected at (a) 50 bar and (b) 150 bar at various temperatures

However, at higher temperatures, as P_R gets much closer to the flare flashing condition, the collapsed spray travelled with very consistent momentum to penetrate much further, even up to 2.5 ms. For the case of 150 bar injection pressure, the spray collapsed at a slightly higher temperature of 90°C but travelling at a very consistent velocity up to the 2.5 ms period, which confirms that the spray is already in the flare flashing condition. For both injection pressures, the spray penetrated at the highest temperature.

Figure 4.6 shows the spray penetration at 50 bar and 150 bar for Fuel A+ (the most volatile). The penetration trend of the 50 bar injection for Fuel A+ is quite similar to Fuel A, except that at temperature of 90°C and 105°C they were very similar. As for the 150 bar injection pressure, the penetration trend is also very similar to Fuel A, however, at the post-collapsing condition (temperature of 90°C and 105°C), the spray travelled at a higher and consistent velocity up to the period of 2.5 ms. Fuel A+ travelled further at high temperatures and reached close to 100 mm from the injector tip.



(a) (b)

Figure 4.7: Spray axial penetration against time of Fuel A+ injected at (a) 50 bar and (b) 150 bar at various temperatures

As can be seen from Figures 4.5, 4.6 and 4.7, in general, at $P_R < 3$, the spray tip penetration trend is non-linear but with considerably greater penetration. As P_R reaches the transitional flash boiling region, the spray tip penetration becomes very poor with a non-linear trend due to the start of spray coalescence and then collapse. With a further increase in P_R, the fuel enters the flare flashing region which produced a properly collapsed spray which switches to a linear penetration rate (consistent velocity) that can penetrate better than under non-flashing conditions. This will cause a problem if it happens in the engine as deeper penetration might cause fuel to impinge on the piston surface.

It has to be noted that the sensitivity of the spray penetration measurement exercise has been tested by comparing two different thresholding method. This has been explained in detail in Hanis et al. (2016) where by a set of 50 spray images for Fuels A and B and at each temperature was subject to background subtraction then thresholding to identify the spray plumes. Two thresholding strategies were tested: a flat threshold of 8% and a varying threshold that started at 8% and reduced to 2% by the 50^{th} image. By inspection, the 8% threshold gave a good qualitative representation of the early spray but missed much of the spray after the end of injection, which was captured best with a 2% threshold. However, with the 2% threshold spurious light is captured earlier on.

After thresholding, the axial penetration was calculated (not accounting for perspective errors) and spray pixel values summed to give a spray integral indicative of the amount of spray present. In Figure 4.8, the spray axial penetration for Fuel B is presented for both thresholding methods. The error bars show one standard deviation from 50 images for the varying threshold and show there is a good comparison in spray penetration between the two methods. Error bars plotted on figure 4.8 show typical levels of variation from 1ms to 4ms. This information helps understand the uncertainty in Figures 4.5 - 4.7, where error bars were not plotted for reasons of clarity.

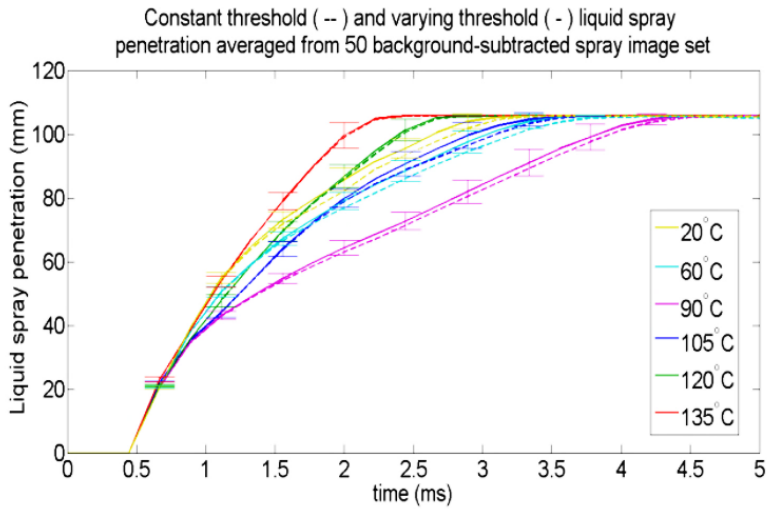


Figure 4.8: Spray penetration comparison from the two thresholding techniques. Each spray reaches a steady value once it leaves the field of view. The varying threshold reduced from 8% at SOI to 5% at EOI and 3% at 4 ms ASOI

4.4. Spray angle measurements of light end mixtures

Backlit images were used to identify the spray angles in accordance with SAE J2715 for the Fuel A variants at a range of fuel temperatures, to quantify the amount of spray collapse induced by flash boiling. Figure 4.9 shows a compilation of all the background subtracted 50 bar injection sprays imaged at different P_R values. Figure 4.10 shows a plot of the measured spray angle at various temperatures for injection pressure of 50 bar. Figure 4.11 shows a compilation of all the background subtracted 150 bar injection sprays imaged at different values of P_R. Figure 4.12 shows a plot of the measured spray angle at various temperatures for the injection pressure of 150 bar. All of the images shown were taken at 1.5 ms after the first appearance of the fuel.

As predicted, the most volatile fuel A^+ collapsed tremendously and developed the narrowest spray angle at the highest temperature. This is a reduction of approximately 33% of the spray angle for this fuel when the temperature changes from 23°C to 105°C, whilst the least volatile fuel only changed by 20%. This confirms the trend that, for a multi-hole injector, increasing levels of P_R would cause a greater collapse of the spray, grouping the plumes together, and causing the fuel to be concentrated into a narrower region.

The sprays injected at 50 bar however, are more susceptible to collapse due to the lower initial momentum from the injector tip, which makes it difficult for the spray to maintain its geometry. As a result, the spray collapsed at a slightly lower P_R. The spray angles in average were much smaller at 50 bar compared to the ones injected at 150 bar.

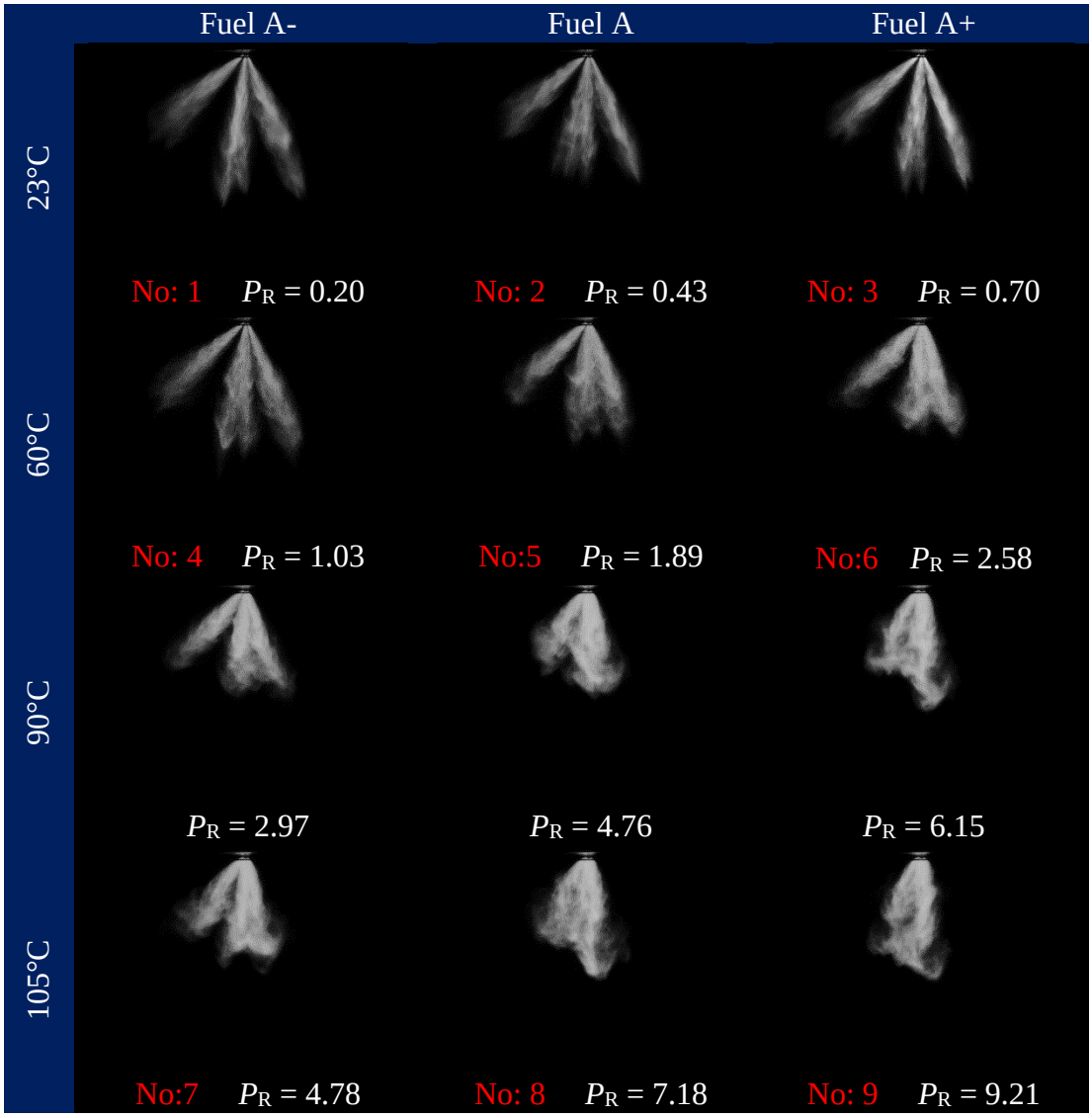


Figure 4.9: 50 bar fuel spray imaged (background subtracted) at 1.5 ms after SOI for Fuel A, Fuel A- and Fuel A+

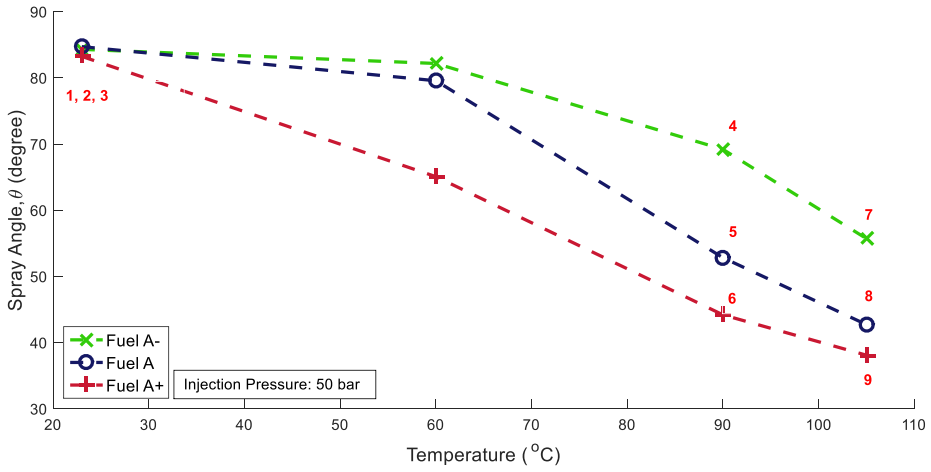


Figure 4.10: Measured spray angle plot for Fuel A, Fuel A- and Fuel A+ at 50 bar and various fuel temperatures; the numbers refer to the images in Figure 4.8

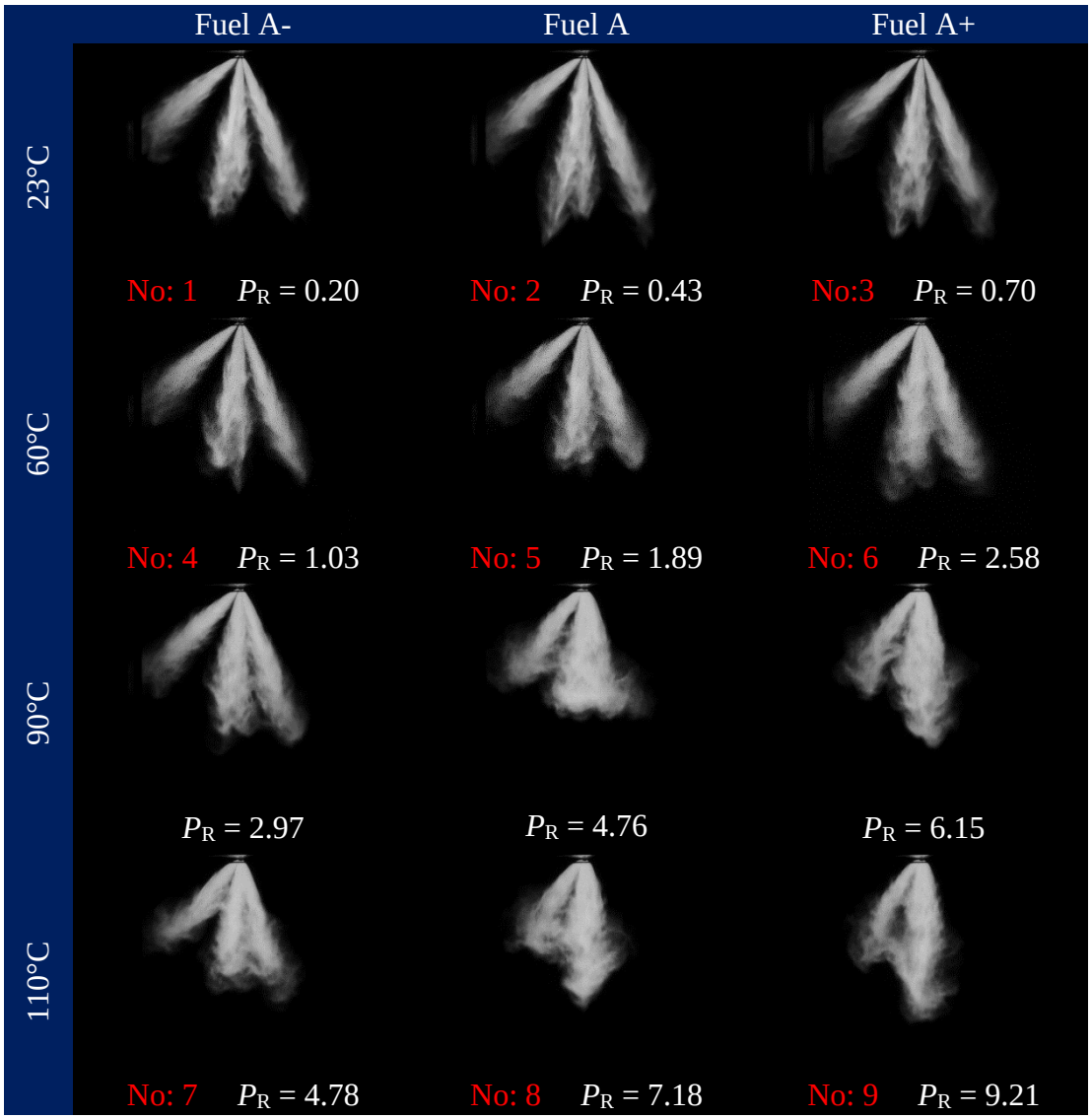


Figure 4.11: 150 bar fuel spray imaged (background subtracted) at 1.5ms after SOI for Fuel A, Fuel A- and Fuel A+

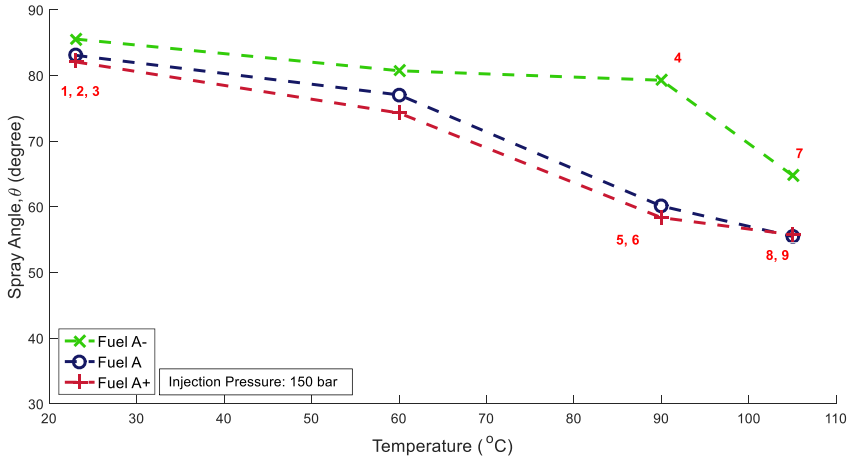


Figure 4.12: Measured spray angle plot for Fuel A, Fuel A- and Fuel A+ at 150 bar and various fuel temperatures; the numbers refer to the images in Figure 4.10

4.5. Spray geometry comparison between light and heavy mixtures

Figure 4.13 shows the spray images of Fuel A and Fuel B for three temperatures at different times after the start of injection. The selected temperatures for this experiment were meant to deliberately show the non-flash boiling phase, the transition phase and flare flashing phase of the fuels. These images have been post-processed with false colouring at the identified spray region. The details of these experiments can be found in Table 4.1.

As can be seen in Figure 4.13, for both fuels, the geometry of the spray were similar to each other from 667 µs ASOI up to 2444 µs ASOI (which is the end of injection). It is only at the temperature of 135°C that the difference between the fuels can be seen at the injector tip. The false colour scheme was used to approximately show the intensity from the Mie scattering technique whereby light scattering is proportional to the surface area of the liquid droplets in the image. The result of higher intensity at the region of the injector tip for Fuel B than Fuel A suggests that there was a high presence of the heavier components still in liquid form flowing through the spray. The other observation is that the similar spray geometry suggests that it is only the early section of the distillation curve of fuels that dictates the outcome of the spray. The differences in the final third of the distillation curve did not make much difference to the flashing event.

Both of these findings are actually a concern from an engine mixture preparation perspective. This is because, if a very volatile gasoline (with for example 40% aromatics) that go through flare flashing during injection will create a concentrated region of unevaporated aromatics and be ejected at a very high velocity with a high possibility of impingement on the piston surface. Mixture homogeneity will then be very poor.

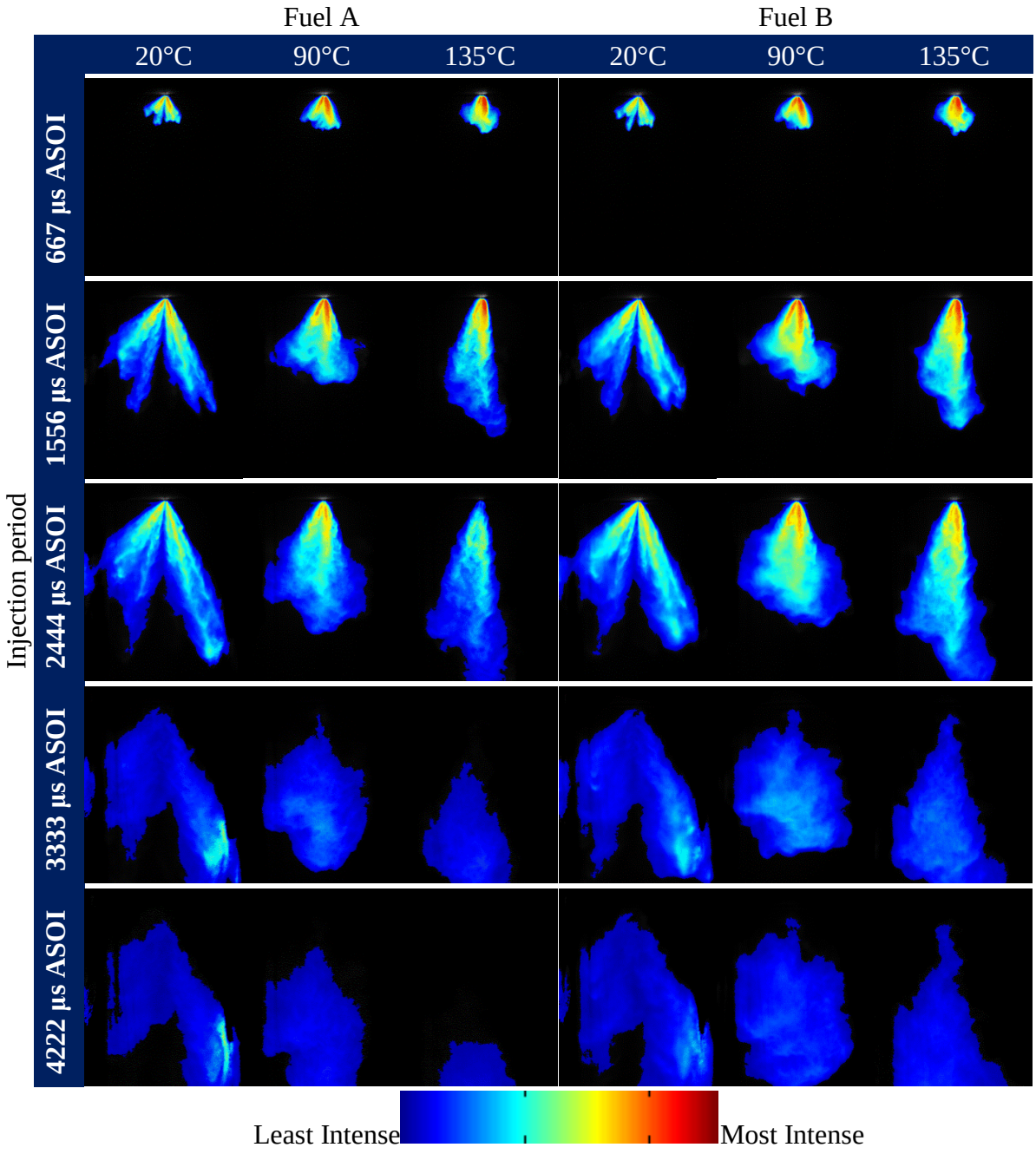


Figure 4.13: Spray event of Fuel A and Fuel B imaged for three temperatures at different times after the start of injection. The demanded injection duration was 2 ms.

4.6. Spray repeatability test of the heavy fuel mixture at various fuel temperatures

Figure 4.14 shows the pixel appearance probability of Fuel B (RVP = 87 kPa) analysed at different times After the Start of Injection (ASOI) and at various temperatures. These injections were run at a rate of 10 Hz which is equivalent to about 1200 RPM. From the images, it can be seen that at all conditions, the 100% pixel appearance (labelled PP_{100}) occurs over more than 50% of the total spray geometry.

The result shows that as the temperature is increased, the 100% pixel probability decreases from around 70% at 20°C to 50% at 135°C. This is expected because a flash boiling spray produces more geometric variations, especially around the spray edge which under flare flashing conditions, evaporates arbitrarily.

This proves that the repeatability of the spray geometry, (which is influenced significantly by the fuel temperature) is very good at this frequency, even after 50 injections. The worry was that the high injection rate could possibly cause the fuel to not have enough time to be heated up to the intended temperature.

It has to be noted that this exercise was to prove that the spray rig test was comparable to the conditions found in the optical engine. This is essential for the investigating the influence of flash boiling on the P_M emissions. For the engine case, heat from the engine coolant (after few minutes of running) as well as heat from the combustion event (that will heat the injector tip) should make it much easier to maintain the fuel temperature. Therefore, the spray rig results are suitable to be compared to the engine in terms of the expected spray geometry at any particular temperature.

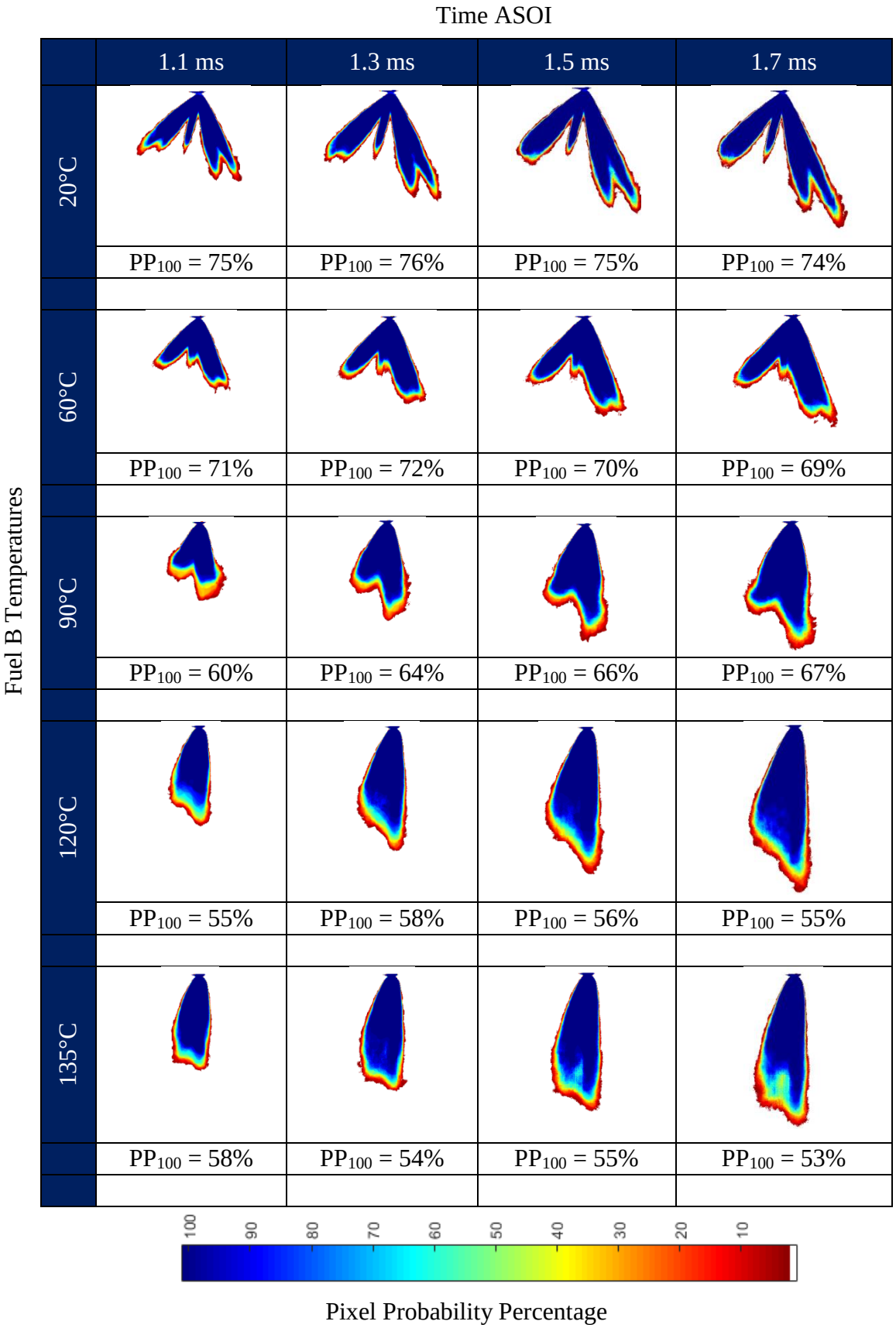


Figure 4.14: Pixel probability percentage test from cold to superheated condition for Fuel B

4.7. Injector tip temperature measurement for multiple injections

To further establish the effectiveness of the fuel heating in the spray rig, an AJ133 injector had a thermocouple spot welded to its tip for temperature measurements as described in section 2.3.1.1. The experiment was conducted using methanol as fuel and was heated up to temperatures of 90°C and later 120°C. A single injection, with 5, 20 and 40 injections were used and the temperature change was recorded. Injections were set at 10 Hz (equivalent to 1200 RPM in the engine). Injection duration was slightly longer than in the engine at 2 ms.

As can be seen in Table 4.3, there was only a change of about 5 K in temperature at the injector tip even after 40 injections for the first trial. This suggest that the flowrate of the fuel exiting the injector was within the capability of the heaters to heat up the incoming fuel. The same can be seen in trial 2, which had a reduction of about 6 K at the injector tip after 40 injection events. The thought is that on the engine, the difference from the coolant temperature to the injector tip will be smaller due to the heat available from the cylinder head and combustion gases, without any air cooling other than from the intake valve during induction. It is therefore concluded that the spray rig tests were reliable for comparisons with the engine experiments.

Table 4.2: Temperature measurements of the injector mount and injector tip before and after single/multiple injections

Number of injections	**1**	**5**	**20**	**40**
Injector tip temperature post injection trial 1 (°C)	88	87.7	85.6	85.4
Injector mount/body temperature trial 1 (°C)	91.5	91.5	91.5	91.5
Injector tip temperature pre-injection trial 1 (°C)	90	90	90	90
Injector tip temperature post injection trial 2 (°C)	115.6	115	114.4	114
Injector mount/body temperature trial 2 (°C)	121	121	121	121
Injector tip temperature pre-injection trial 2 (°C)	116	116	116	116

4.8. Chapter summary

In this chapter, spray characterization of the AJ133 under various states (non-flash boiling, transition and flare flashing) have been explored on the spray rig using a variety of fuels; Fuels A-, A, A+ and Fuel B.

The light-end fuels with independent control of volatility were used to properly observe the change in spray geometry with the change in P_R. It was found from observation that the P_R range for the transition flash boiling was around $5 > P_R > 2$. For the case of flare flashing, it was observed to start when $P_R > 5$.

The transition phase of flash boiling produced a high reduction of spray tip penetration whereby the spray was only beginning to collapse. When fuel was injected at the flare flashing condition, the spray geometry changed significantly as $P_R > 5$. Plume coalescence was seen during the flare flashing phase, which resulted in the spray becoming a high velocity single jet with a downward trajectory. As a result, the spray tip penetration was measured to be very large for the flare flash boiling condition. This contradicts with many findings that flash boiling reduces penetration. Further investigation of the fuels was done with the comparison of Fuel A and Fuel B spray geometry as a result of having different T90 values but similar RVP and T50 values. It was observed that the early section of the distillation curve dictates the outcome of the spray geometry regardless of the difference in final section (T90). Fuel A was observed to have a lesser spray intensity in the Mie scattering experiments than Fuel B close to the end of injection event, suggesting that the heavy component might be evaporating much more slowly towards the end.

To better understand and confirm that the results from the spray rig were reliable, two additional experiments were conducted; a spray repeatability test, and injector tip temperature measurements. It was observed that the repeatability of the sprays on the spray

rig was very good overall with pixel presence within the spray section ranging from 70% at cold condition to 55% at much higher temperature. More variability in the spray was seen at higher temperatures, due to the more random evaporation rate around the spray edge. This proves flash boiling to occurs even with successive rapid injection rate of fuel as heat transfer from the injector mount to the injector body and the fuel is very effective and rapid.

The final section of this chapter shows the result of injector tip temperature change measurements for single and multiple injections. It was observed that the injector temperature only changes up to a maximum of 6 K after 40 injections. This suggests again that despite the high injection rate, the fuel that comes into the injector body will have enough time to be heated up to the surrounding temperature of the injector mount. The temperature in the engine will be much higher than in the spray rig due to the occurrence of combustion. Therefore, this strongly suggest that flash boiling can occur consecutively in a conventional engine if the injector temperature is high enough to cause the fuel to have $P_R > 2$.

5. Single Cylinder Optical Engine Experiments and Results

5.1. Introduction

This chapter begins with the investigation of spray in the optical engine which has a combustion system similar to the AJ133 engine. This is partly a validation exercise as to how the spray behaves when comparing engine to spray rig conditions. First, the engine was only motored so as to obtain the in-cylinder pressure trace which is essential for understanding the injection behaviour at different timings. This was done for both a natural aspirated configuration as well as when boosted. The chapter continues with some in-cylinder spray imaging of the modelled fuel which was heated to various temperatures. Other than validating the spray behaviour similarity between the engine and spray rig, in-cylinder spray imaging is capable of highlighting the severity of spray impingement on the piston surface. As discussed previously in Chapter 1, spray impingement onto the wall/piston surface is known to be a major factor that leads to particulate production.

The second part of this chapter continues with the particulate matter experiments using the full metal configuration of the optical engine. These experiments used three heavy model fuels (B, C and D) and a Euro 5 fuel as a base fuel. The experiments include:

- Filtered vs unfiltered particulate data comparison of the model fuels,
- Correlation of flash boiling sprays to particulate number and mass using pressure ratio,
- Lambda sweep experiment for investigation of spray cooling effects on the piston surface.

5.2. Pressure ratio investigation using in-cylinder pressure measurements during motoring

5.2.1. Naturally aspirated

Spray imaging in optical engine can provide valuable characteristics of the spray when being injected into the cylinder. In contrast to the spray rig, the cylinder pressure in the engine is below atmospheric pressure and can vary during early injection. This in turn changes the condition of the fuel when injected into the cylinder. The motoring experiments were conducted with only Fuel B as this fuel was the most volatile of all. Figure 5.1 shows the measured trace of the optical engine cylinder pressure during the intake stroke for the engine with a coolant temperature of 23°C. There were 3 important parameters that may influence the effectiveness of the spray homogeneity which can be extracted from this plot:

- in-cylinder pressure at point of injection,
- piston surface distance to injector tip,
- total time (in CAD) before ignition.

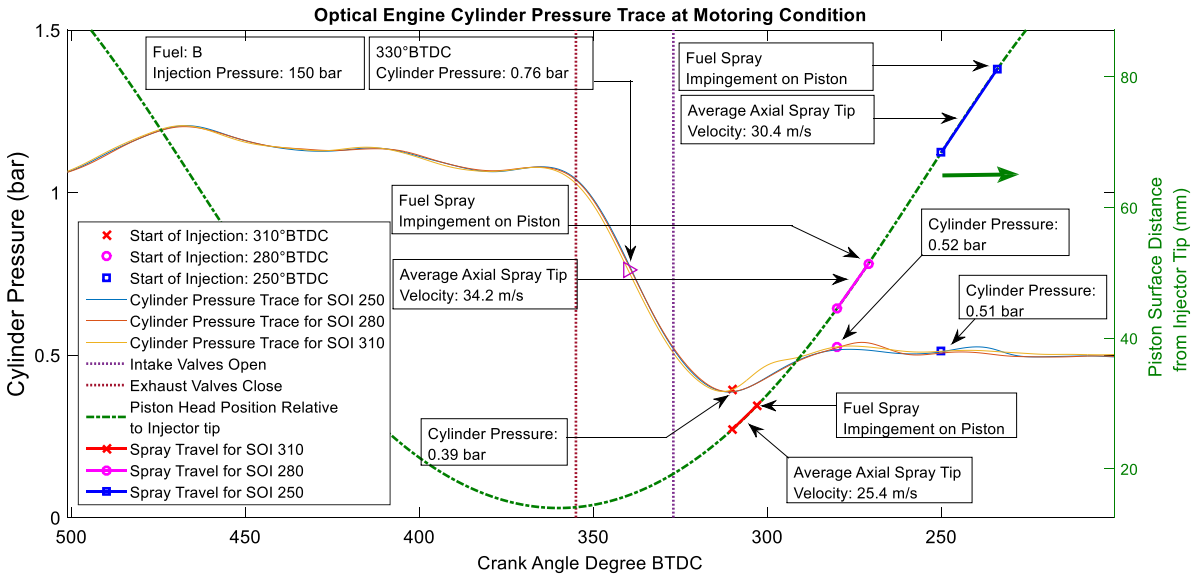


Figure 5.1: Optical engine motoring pressure trace and injection strategies during the intake stroke for the natural aspirated engine configuration.

As shown in the Figure 5.1, the intake pressure dropped from almost atmospheric as the exhaust valves are closed to as low as 0.39 bar at 310°BTDC, before returning to the nominal value of 0.5 bar from 280°BTDC onwards. Typically, flash boiling can be achieved quite readily by gasoline (with temperatures from above about 60°C) due to the sub-atmospheric conditions. The sprays at each of these conditions can be seen later in Figures 5.3, 5.4 and 5.5. It can be seen that cylinder pressure increases slightly as the fuel is injected. The spray tip velocity is difficult to trace in the optical engine without access to the pent-roof window, therefore a simpler average tip velocity is calculated from observation of the fuel impingement onto the piston surface using the high-speed camera and the calculated piston displacement distance from the injector tip. As a result, the average spray tip velocity values were not significant enough individually to reveal the difference at a range of conditions. The production engine has a cam phasing unit, and at part load there is negative valve overlap; this is a consequence of the fixed valve period, and the late inlet valve closure. Late inlet valve closure is used so as to reduce the effective swept volume of the engine, and thereby reduce throttling losses. There is also a reduction in the effective compression ratio, but it is the expansion ratio (which is unchanged) that has a greater impact on the engine efficiency. So, overall, late inlet valve closure leads to a reduction in the fuel consumption.

5.2.2. Forced induction

Figure 5.2 shows the motoring pressure trace of the optical engine with boosted operation. Figure 5.2 shows the cylinder pressure trace from a zero boost up to a maximum of 0.9 bar of boost. As expected, engine boosting causes the pressure trace to change from the naturally aspirated configuration. As can be seen in Figure 5.2, every increase in boost pressure will narrow the window that flash boiling might occur (assuming an optimal engine coolant temperature of around 90°C) by having a sub-atmospheric in-cylinder pressure. The

green square in Figure 5.2 highlights the available range in which flash boiling can happen with a span of only about 50°. It is only the case for 0.3 bar and below that the sub-atmospheric condition can be achieved and be maintained even after 200°BTDC.

The problem with this situation is that injection strategies are now very constrained. The green square span in Figure 5.2, is not an ideal range if one wants to prevent spray impingement. At 330°BTDC, the distance from the injector tip to the piston surface is only 14 mm, which will definitely lead to severe fuel film build-up when subjected to spray impingement. While injections at these CAD range is uncommon, they are normally utilized for high BMEP engine configuration engines, where injection durations have to last longer than usual in order to achieve a stoichiometric air fuel ratio.

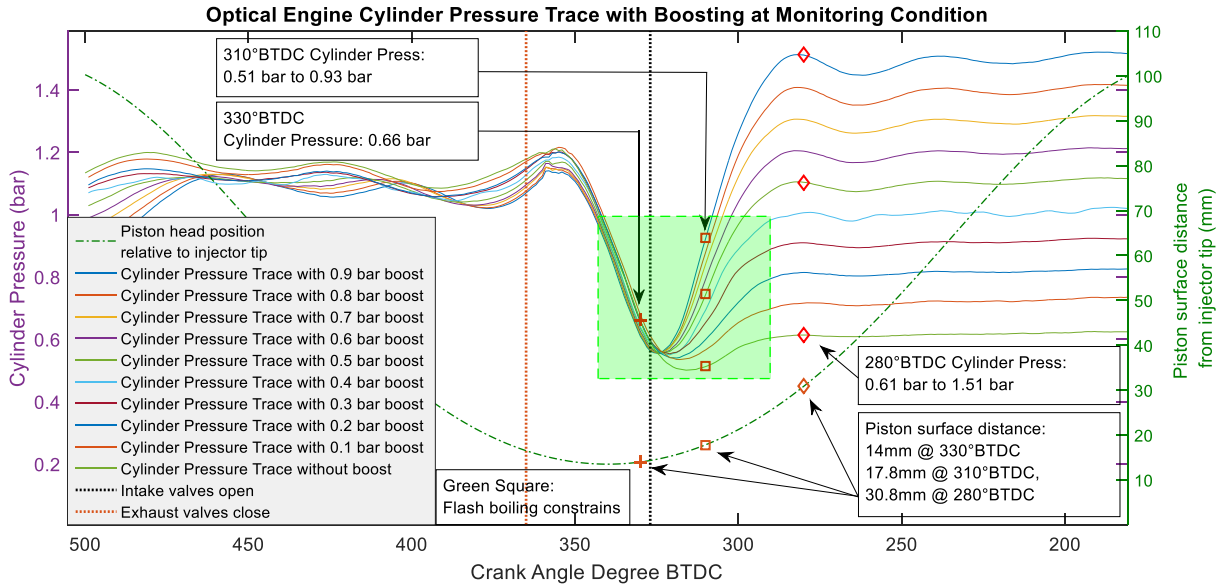


Figure 5.2: Optical engine motoring pressure trace and injection strategies during intake stroke for the forced induction engine configuration.

Injecting late would cause problems due to insufficient time for fuel evaporation. This is made worse when using oxygenated fuel mixtures that have a lower volumetric energy density than conventional gasoline. Long injection durations using oxygenated fuel mixtures (which have high enthalpy of vaporization) can cause the piston surface to cool

down significantly and subsequently have a fuel film. This will lead to very poor air fuel mixture homogeneity and severely rich combustion with diffusion flames on the piston surface. If the injector used is capable of injecting fuel at much higher flow rate, then injecting late (after 280°BTDC) is not a problem, but there is still a problem of having a high back pressure during the intake stroke (for the case of 0.3 bar boost and above) where flash boiling will definitely not occur and the evaporation rate is poor.

5.3. Engine motoring spray imaging results

As discussed in Chapter 1, spray tip penetration alone does not necessarily portray the severity of the fuel impingement on the piston. Figures 5.3, 5.4 and 5.5 show high speed images of spray development in the optical engine at fuel temperatures of 25°C, 60°C, 90°C and 105°C at injection timings of 250°BTDC, 280°BTDC and 310°BTDC respectively. It has to be noted that only the un-boosted in-cylinder configuration was used for these imaging exercises. This is due to the uncertainty in the strength of quartz material in handling high compression ratio cycles and also particularly if there is combustion. Other than that, only Fuel B was selected for this experiment because one fuel was sufficient for validation of the in-cylinder pressure ratio influence on spray development. Changes in fuel properties (volatility) will only change the pressure ratio and produce spray geometry accordingly as established in Chapter 4. Table 5.1 was constructed to better compare the pressure ratio of the heavy fuels when used at different injection timings and temperatures. At a slightly earlier injection timing of 310°BTDC, the in-cylinder pressure averaged at 0.3 bar while at later timings of 250°BTDC and 280°BTDC, the in-cylinder pressure was around 0.5 bar nominal.

As expected from these images, it can be seen that the spray geometries at each particular pressure ratio show similarity to the ones captured from the spray rig. This

strengthened the usefulness of the data (spray angle, spray penetration) gained from the spray rig. Apart from that, these images also show the development and severity of spray impingements on piston surface at various crank angle timings which was not available in the spray rig.

Generally, the injection timings of 250°BTDC and 280°BTDC were able to show the proper spray developments due to the slightly further distance from the injector tip to the piston surface. At the coldest fuel temperature of 23°C, the spray plumes were spread quite uniformly around the cylinder which in a way promoted evaporation better than at other fuel temperatures. At higher temperatures, when the spray has collapsed, a bulk of the spray can still be seen close to the piston surface, suggesting that the evaporation rate had deteriorated and causing severe spray impingements. Other than that, the spray intensity remained very intense, suggesting a higher droplet density (smaller droplet spacing to diameter ratio) and therefore a higher local droplet surface area with this spray, possibly due to the concentration of droplets as the plumes are drawn together. This can be seen when comparing the spray presence at 234°BTDC for all temperatures. It has to be noted that in this experiment, the quartz piston surface was used for illumination purposes. Therefore, any estimation of spray evaporation may be inaccurate due to the significantly different conductivity, density and thermal properties of metal and quartz. This problem will be discussed in detail at section 5.5.3 later in this chapter.

As discussed previously in Chapter 4, $3 < P_R < 5$ produced very poor spray penetration, which in an engine environment will help in preventing/reducing impingement as can be seen in Figures 5.3 and 5.4 for 60°C fuel temperature. Although spray impingement may have been prevented at this temperature, the collapsed spray remains as a cloud that has a poor evaporation rate. For the case of $P_R > 5$, the spray tip impinges much

earlier than others suggesting that the spray was travelling at a much higher velocity and also longer.

Spray conditions at 310°BTDC were slightly different from the rest, due to the close proximity of the piston surface to the injector tip and the slightly lower in-cylinder pressure that increases the P_R value for each fuel temperature used. From the observation in Figure 5.5, despite the higher P_R conditions, the spray characteristic differences were difficult to distinguish. Spray impingement occurred as quickly as the second frame at 307°BTDC. As a result, the spray characteristics may seem to not have any major impact on the evaporation rate. It was instead fuel mixture properties such as heat of vaporization, viscosity and liquid surface tension (this is discussed later in section 6#) that will influence the evaporation rate. This can be seen in Figure 5.5 at 301°BTDC and 299°BTDC where a similar quantity of spray plumes remained near the piston surface for all fuel temperature conditions.

Table 5.1: Pressure ratio values for Fuels B, C and D at different temperatures and injection timings (in-cylinder pressure)

	Fuel B				Fuel C				Fuel D			
	250°/280° BTDC (0.5 bar)		310° BTDC (0.3 bar)		250°/280° BTDC (0.5 bar)		310° BTDC (0.3 bar)		250°/280° BTDC (0.5 bar)		310° BTDC (0.3 bar)	
Fuel temp (°C)	Fuel vapour pressure (bar)	Pressure ratio	Fuel vapour pressure (bar)	Pressure ratio	Fuel vapour pressure (bar)	Pressure ratio	Fuel vapour pressure (bar)	Pressure ratio	Fuel vapour pressure (bar)	Pressure ratio	Fuel vapour pressure (bar)	Pressure ratio
23	0.49	0.97	0.49	1.63	0.18	0.36	0.18	0.60	0.08	0.16	0.08	0.27
60	1.89	3.80	1.89	6.32	0.95	1.90	0.95	3.17	0.35	0.69	0.35	1.16
90	4.66	9.32	4.66	15.5	2.75	5.50	2.75	9.17	0.89	1.78	0.89	2.98
105	6.93	13.8	6.93	23.1	4.35	8.70	4.35	14.5	1.35	2.70	1.35	4.50
120	10.0	20.0	10.0	33.4	6.60	13.2	6.60	22.0	1.97	3.94	1.97	6.56
135	14.4	28.1	14.4	46.9	9.67	19.4	9.67	32.3	2.79	5.58	2.79	9.33

		Fuel Temperature

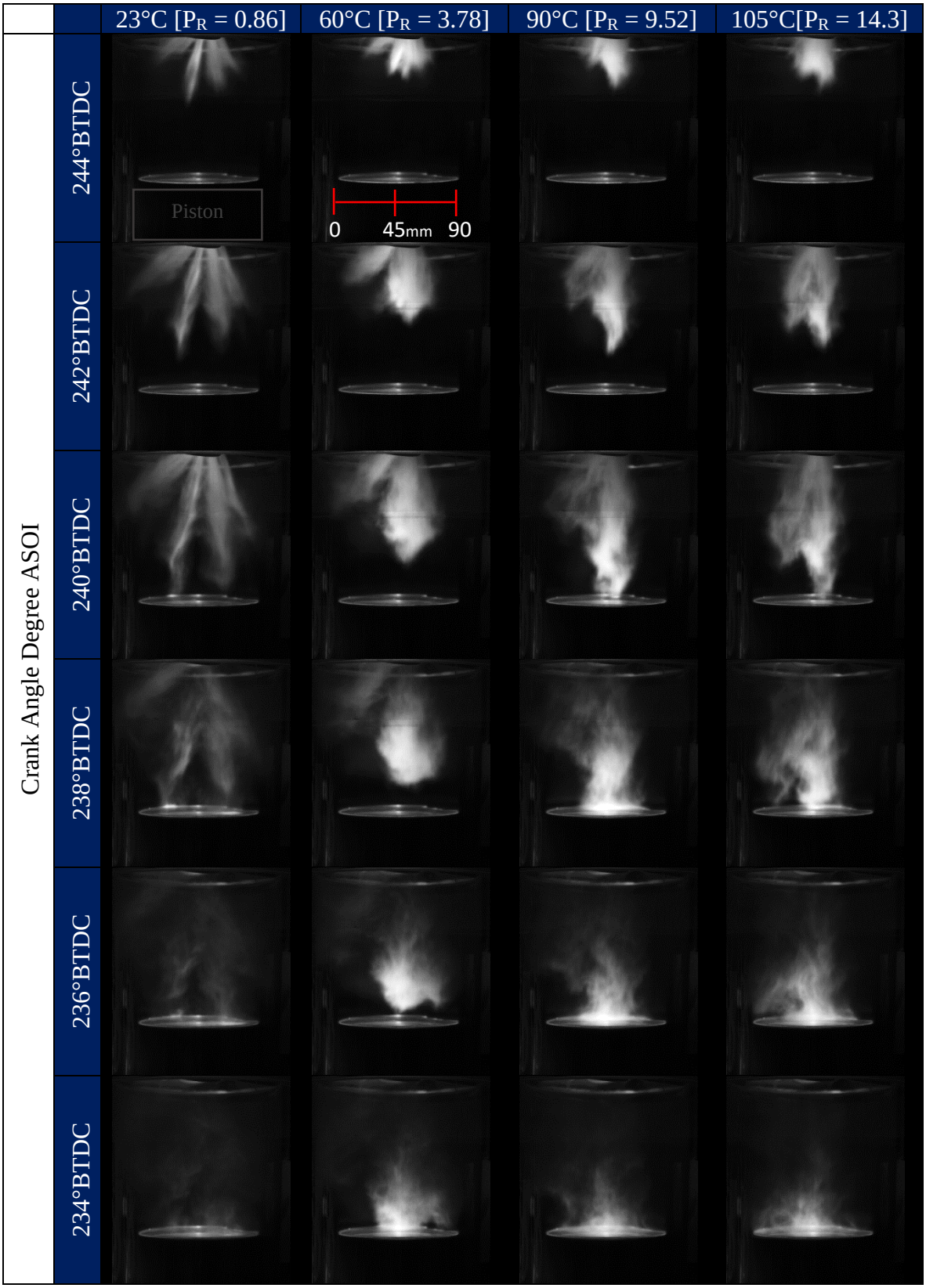


Figure 5.3: High speed images of sprays at various temperatures injected at 250°BTDC taken from the optical engine during motoring operation.

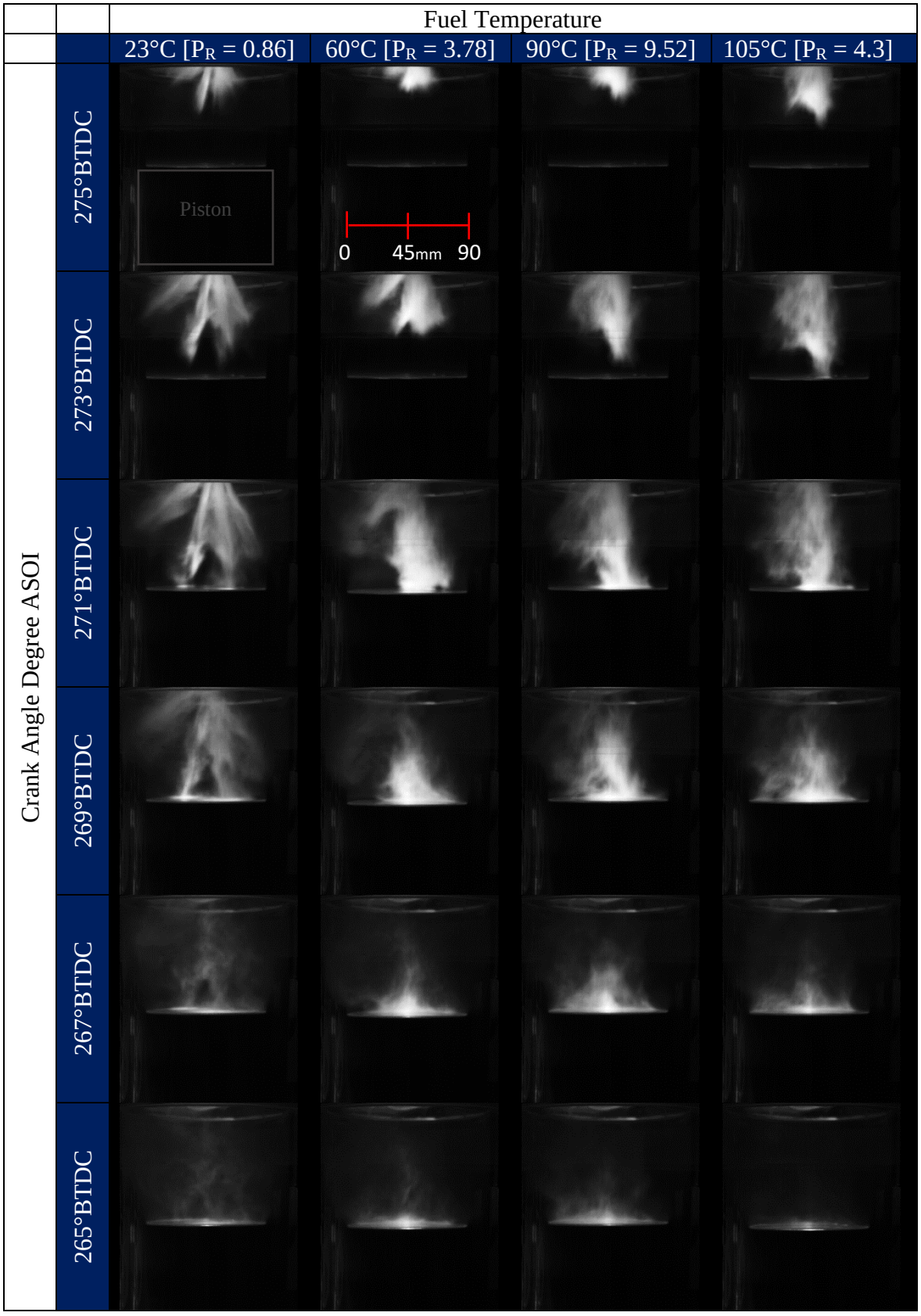


Figure 5.4: High speed images of sprays at various temperatures injected at 280°BTDC taken from the optical engine during motoring operation.

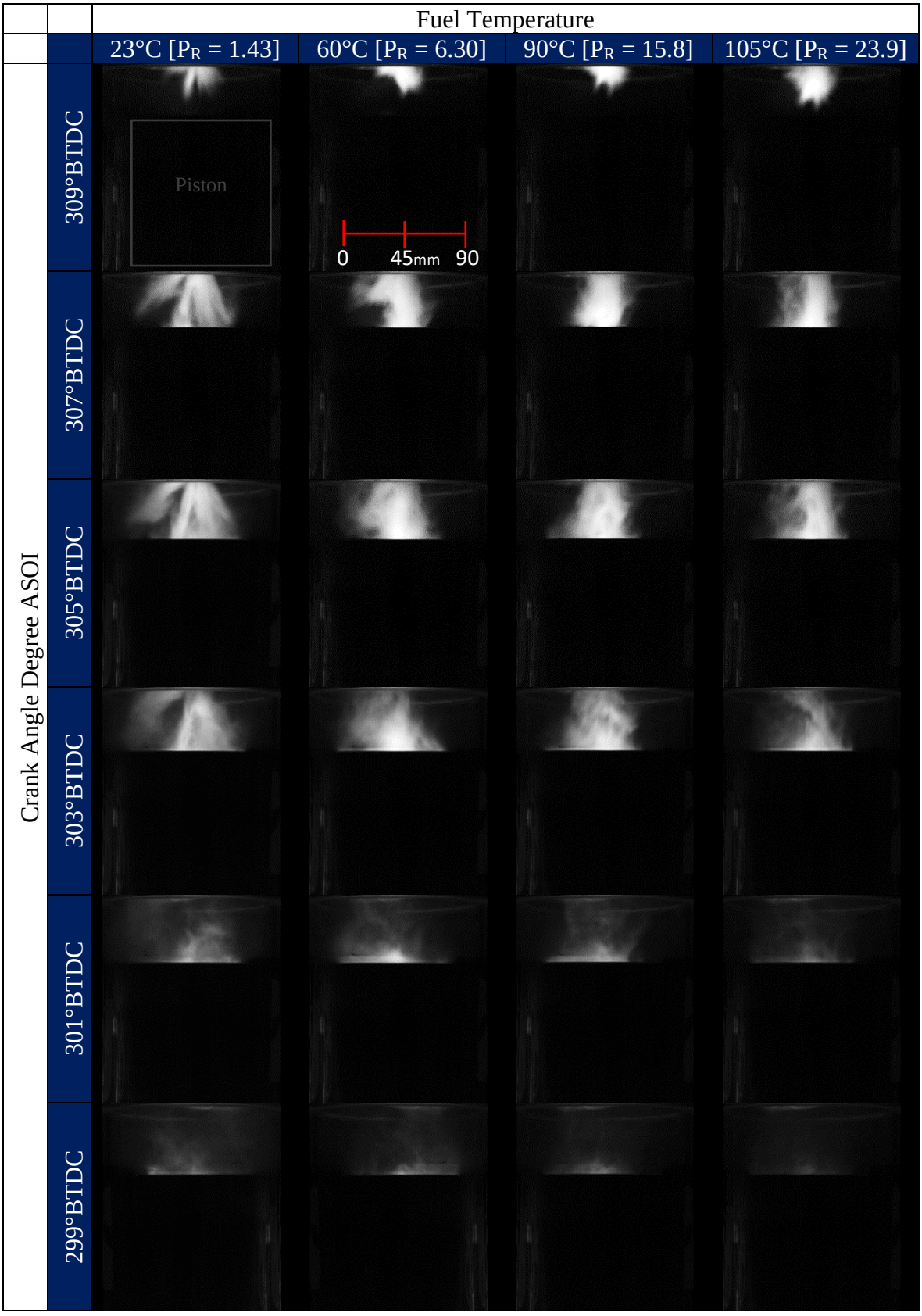


Figure 5.5: High speed images of sprays at various temperatures injected at 310°BTDC taken from the optical engine during motoring operation.

5.3.1. Integrated spray intensity comparison between light-end and heavy-end mixtures

Figures 5.6 and 5.7 show the semi-quantitative measurements of spray intensity for Fuels A, A-, A+ and the heavier Fuel B at different temperatures and injection timings. In a Mie-scattering setup, fuel droplets that remain in liquid form will continue to scatter light until they vaporise. Evaporation performance is measured by the amount of time the fuel spray remains in liquid form. The spray images taken using the high speed camera were processed using MATLAB by summing the pixel intensity of a background subtracted image at every CAD. A standard deviation value was then calculated from the 10 cycles of spray imaging and used for plotting error bars. All A fuels show the same trends for all injection timings, with Fuel A- evaporating slowest at both low and high temperatures while Fuel A+ evaporates fastest when injected at the highest temperature of 105°C. Fuel B was tested under similar conditions to the experiments with Fuel A. It has to be noted that the magnitude of the spray intensity between fuels cannot be compared. This is because the tests were conducted on a different day, of which the imaging equipment was removed and reinstalled. This may cause variations in the illumination setup or engine condition (cleanliness of the quartz barrel may let through more light to the camera).

These results were analysed to investigate the evaporative performance and pattern of Fuel B that has a high T90 temperature. It can be seen in Figure 5.7 that at all injection timings the fuel evaporation was very poor with a fuel temperature of 23°C but improved to achieve a similar evaporation rate to that of the Fuel A when at temperatures of 90°C and 105°C. At high temperatures, the fuel spray has a higher tip velocity and impinges on the piston leaving only some of the total fuel to disperse in the cylinder before evaporating. The persistence of the fuel suggests that it remains present in liquid form but probably in smaller droplet sizes.

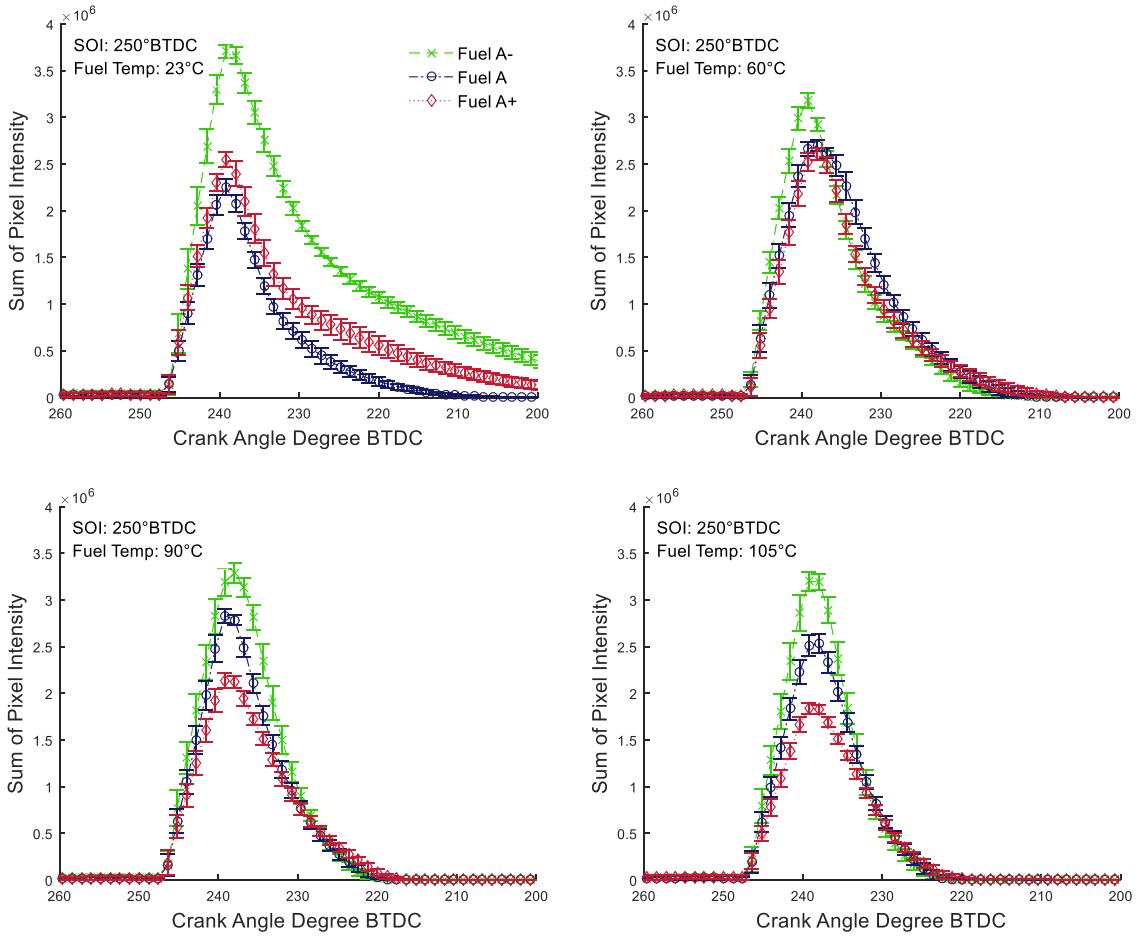


Figure 5.6: Integrated pixel intensity for fuels A-, A and A+ sprays during engine motoring at injection timings of 250°BTDC at temperatures of 23°C, 60°C, 90°C and 105°C to give a semi-quantitative measurement of the fuel quantity present. The error bars show the standard deviation from 10 measurements.

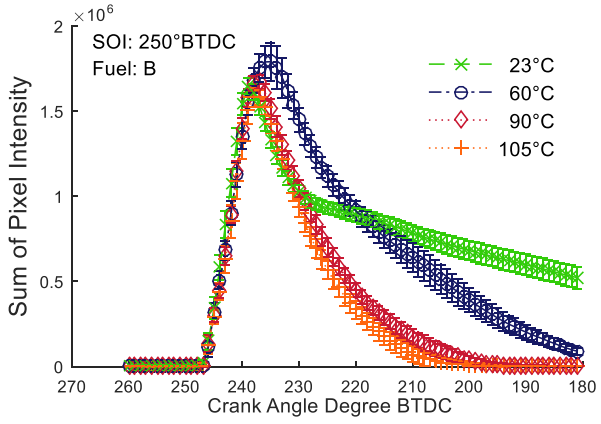


Figure 5.7: Integrated pixel intensity for Fuel B sprays during engine motoring at injection timings of 250°BTDC at temperatures of 23°C, 60°C, 90°C and 105°C to give a semi-quantitative measurement of the fuel quantity present. The error bars show the standard deviation from 10 measurements.

5.4. Combustion imaging of non-flashing and flashing fuel condition

Combustion imaging is normally conducted to identify or possibly quantify the soot production of a cycle through flame intensity measurements. Diffusion flames, as commonly known, tend to produce high levels of red component pixel intensity than do pre-mixed flames when imaged. Some researchers have used this technique to compare and quantify (to a certain extent) the soot presence in flames using image processing techniques.

Figure 5.8 shows a series of high-speed images of combustion flames ranging from CAD of 20°BTDC to 35°BTDC for Fuel B tested at 4 different temperatures (from non-flashing to flashing). It has to be noted that the fuel was injected at 280°BTDC for all temperature variations. These images were taken using the optical engine with the quartz annulus and metal configuration cylinder liner. At 20°BTDC, the combustion is considered to be in a late stage where flame propagation has already covered the full diameter of the liner. However, this is the best stage to visualise diffusion flames that can linger on the piston surface. As expected, it can be seen in Figure 5.8 that as the fuel temperature is increased, the flame intensity for all three colour components is reduced. This is possibly due to the effects of combustion phasing (i.e. combustion occurs much earlier when cylinder head temperature is increased). In an engine environment, fuel temperature is directly matched through cylinder head temperature which as a result may influence compression pressure as well as flame propagation behaviour.

From Figure 5.8, it can be seen that the green and blue components are the ones to experience more reduction in intensity than the red component. This can be seen in the subplots of each image where the Red, Green and Blue components' intensity is extracted horizontally from a single row of the flame.

From a general point of view, one might conclude that flash boiling may have improved the fuel mixture homogeneity which would then reduce the occurrence of diffusion flames in the cylinder. However, Figure 5.19 shows that particulate number in the exhaust actually increases (the opposite trend) as the fuel temperature is increased (from transitional to flash boiling conditions). This result shows that semi-quantitative measurements of soot through imaging may lead to false conclusions and must therefore be treated with caution when flash boiling is introduced.

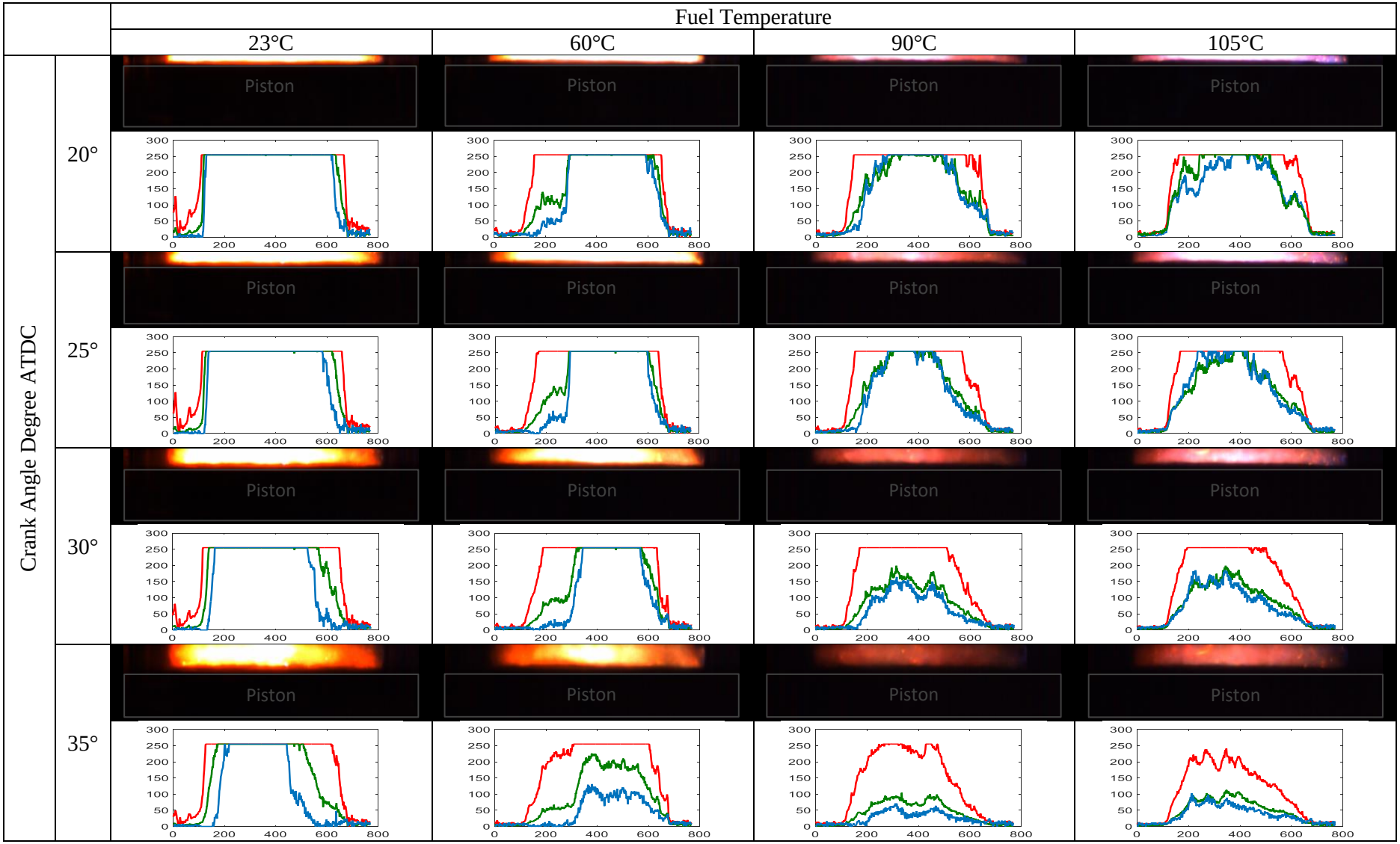


Figure 5.8: High speed imaging of combustion from the side using the optical engine. Result of injecting Fuel B at 280°BTDC at various fuel temperatures. Plots shows the combustion intensity through the RGB colour distribution across the cylinder

5.5. Particulate matter results

5.5.1. Unfiltered vs Filtered (Wiebe Function) particulate matter data comparisons

As explained before in Chapter 1, particulate emissions produced from the GDI engines can actually consist of a much smaller size than the 23 nm limit set by the legally compliant CPC analysers. The reason this is being highlighted is because the flash boiling phenomenon, which is known to reduce droplet size, might actually lead to high production of nucleation mode particles. In order to be sure, the results obtained from the heavy fuel engine experiments have been analysed as filtered (using a Wiebe function) as well as unfiltered data. It has to be noted that the optical engine was not equipped with a three-way catalyst that does remove smaller particles. This can be seen from the work of Chen et al. (2012) in Figure 5.9, when compared with the pre-catalyst PN samples, the post-catalyst samples exhibited a significant reduction in the PN concentrations, especially for the nucleation mode which generally has a particle size of less than 30 nm . To improve repeatability, data was only logged once the exhaust temperature has reached 300°C.

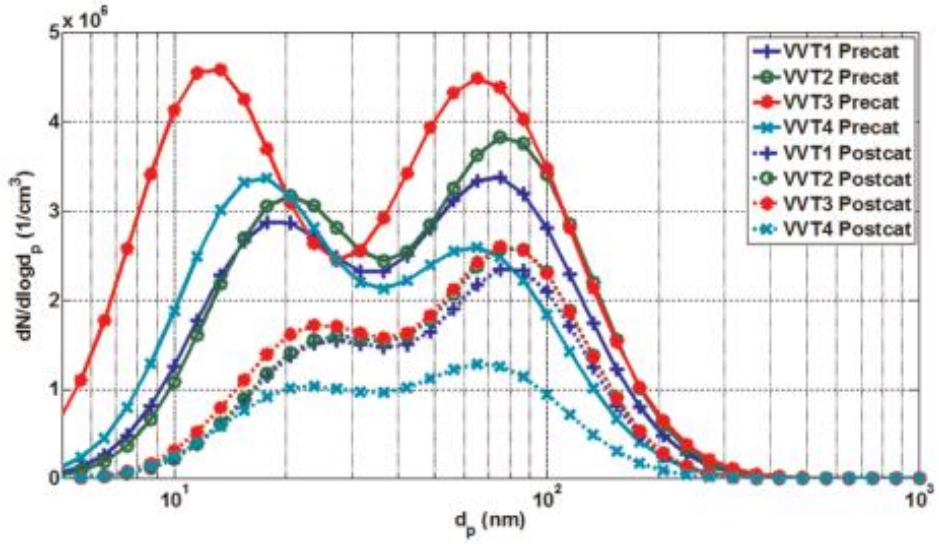


Figure 5.9: size-resolved mass concentrations of PM emissions before and after the catalyst at different valve timings. Adapted from (Chen et al. 2012b)

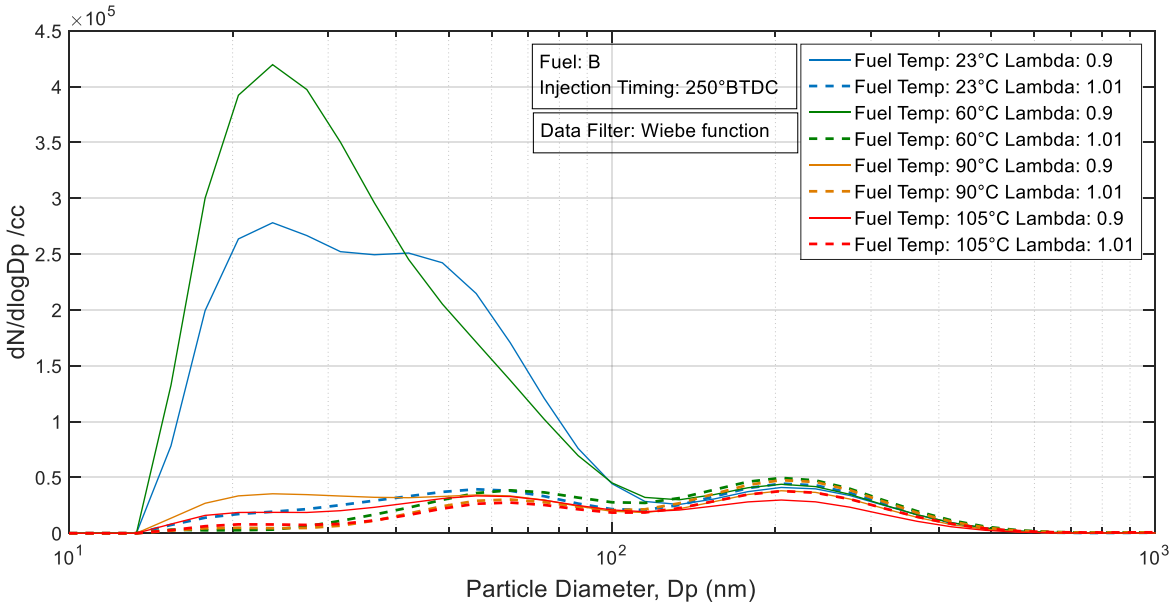


Figure 5.10: Wiebe filtered particulate size distribution for Fuel B at various cylinder head temperatures injected at 250°BTDC with λ of 0.9 (solid lines) and 1. (broken lines)

In this section, only Fuels B and C were used for comparison as they are oxygenated fuels. Only injection timings of 250°BTDC and 280°BTDC were tested because as seen in the high-speed images previously, these injection timings provide more space for the spray to develop, which for the case of the flash boiling investigation would help to avoid effects attributable to spray impingement effects. Given the importance of even slight rich mixture excursions on PN emissions, a lambda of 1.01 was chosen as the stoichiometric condition to avoid any slight rich mixture excursions due either to cycle-by-cycle variations or as lambda was under open loop control. It has to be noted that in this section, the plot comparison is to highlight the difference in the production of particulate matter rather than the outright numbers or mass. The mass will be analysed in depth in the next section.

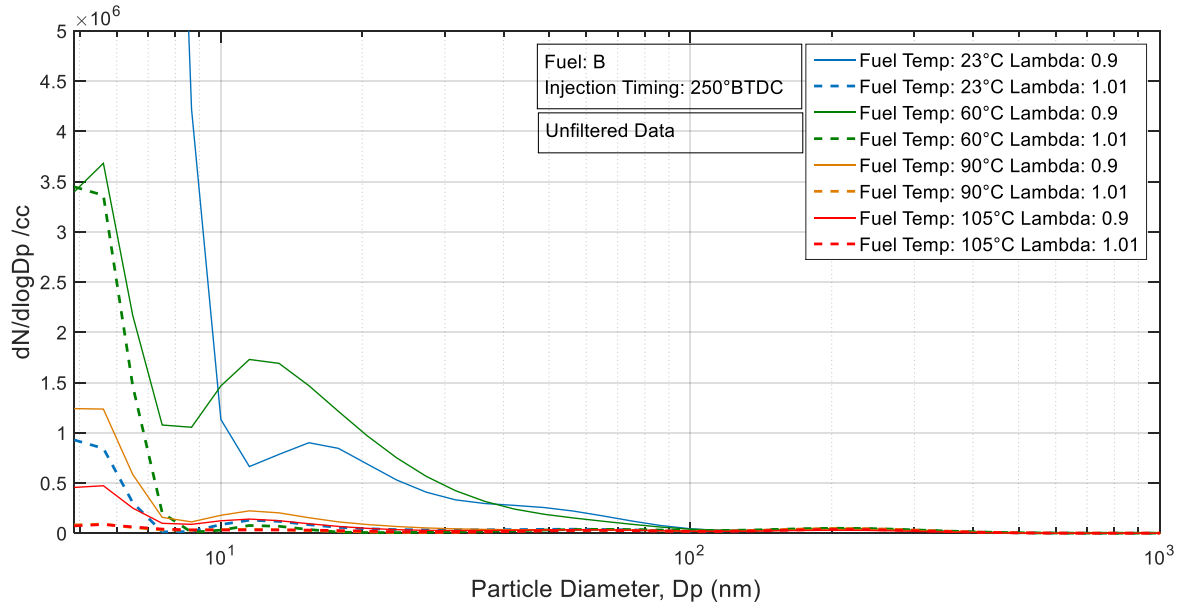


Figure 5.11: Unfiltered particulate size distribution for Fuel B at various cylinder head temperatures injected at 250°BTDC with λ of 0.9 (solid lines) and 1.01 (broken lines)

Figures 5.10 and 5.11 show the filtered vs unfiltered particulate data from the engine test using Fuel B (RVP = 87 kPa) at an injection timing of 250°BTDC. The filtered data, shows that the maximum PN achieved was sized close to 30 nm at a temperature of 60°C followed by 23°C. For the case of the unfiltered data, a fuel temperature of 23°C gave the greatest PN emissions with sizes below 10 nm; the number reduced as the fuel temperature was increased. Figure 5.12 and 5.13 show the filtered vs unfiltered particulate data from engine test using Fuel C (RVP = 37 kPa) at a similar injection timing of 250°BTDC. Generally, for this slightly less volatile fuel, the peak PN for both the filtered and non-filtered data were shifted to a much bigger particulate size. For the filtered data, the average was at the range from 40 nm to 50 nm while for the filtered data, it was from 4 nm to 8 nm.

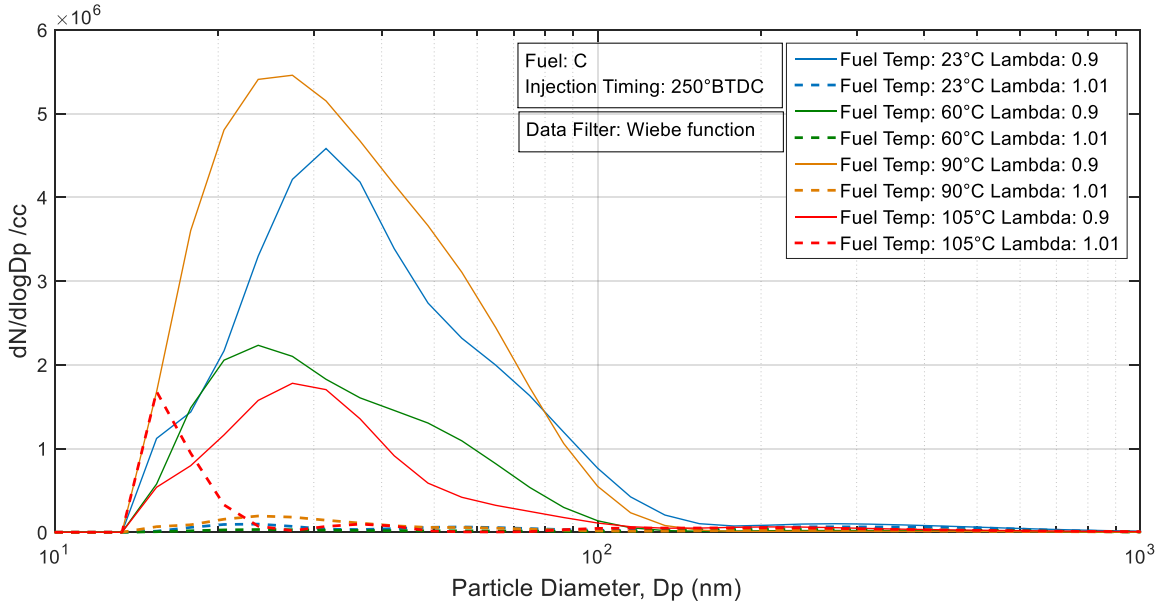


Figure 5.12: Wiebe filtered particulate size distribution for Fuel C at various cylinder head temperatures, injected at 250°BTDC with λ of 0.9 (solid lines) and 1.01 (broken lines)

At injection timing of 250°BTDC, Fuel B undergoes transitional flash boiling stage at a temperature of 60°C (P_R = 3.80) while Fuel C needs to be at 90°C (P_R = 5.50). It has to be noted that at this stage, spray penetration is at its lowest. As a result, it can be seen in Figures 5.10 and 5.12 that these temperatures produced the highest accumulation mode particle numbers. This is suspected to be because of the grouping of the plumes into the bulk liquid which reduces the surface area to volume ratio of the liquid droplets, which in turn slows evaporation. Although this also happens at a higher P_R for both fuels (flare flashing stage), these sprays travel further to cause piston impingement that results in fuel splash, which breaks up the liquid bulk and evaporates easily due to being at superheated conditions. For the case of injection timing at 280°BTDC, shown in Figure 5.14 and 5.16, with the piston surface much closer, it was clear for both Fuels B and C that PN was highest at the superheated temperatures of 90°C and 105°C. As the piston surface is closer, the high velocity of the spray tip (as a result of spray collapse) impinges severely and causes

significant cooling. This in turn, creates a fuel film on the piston surface which subsequently produces diffusion flames.

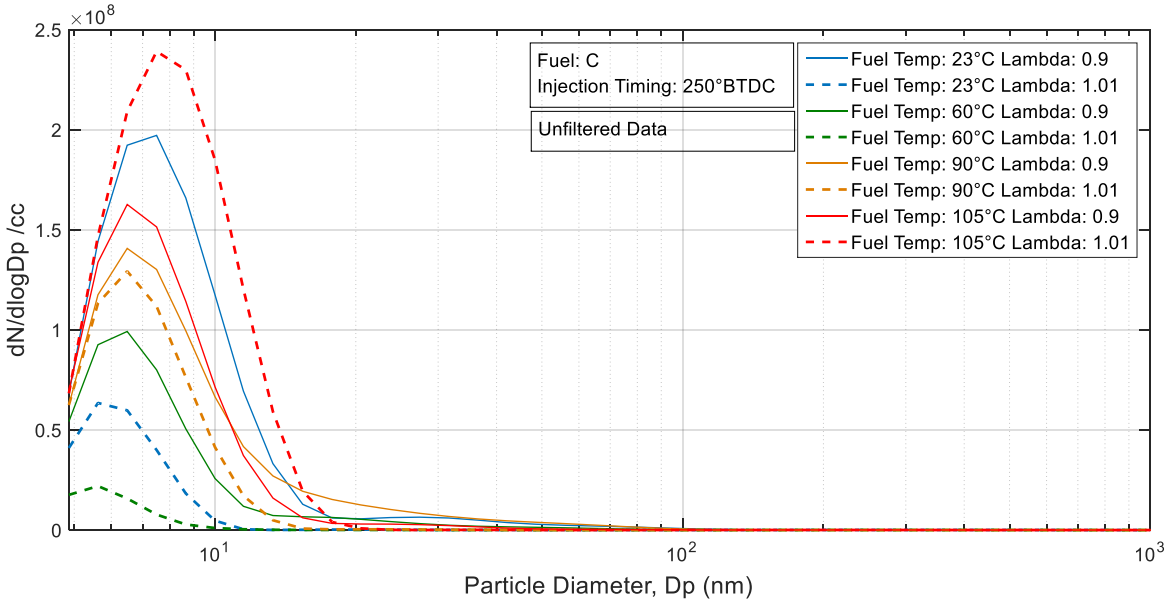


Figure 5.13: Unfiltered particulate size distributions for Fuel C at various cylinder head temperatures, injected at 250°BTDC with λ of 0.9 (solid lines) and 1.01 (broken lines)

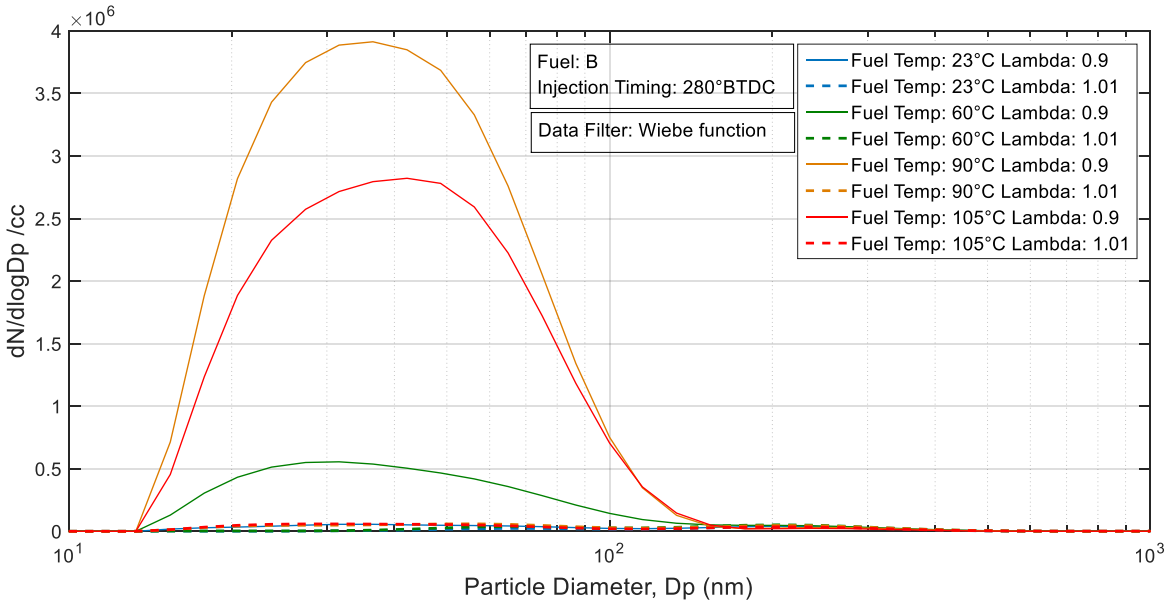


Figure 5.14: Wiebe filtered particulate size distribution for Fuel B at various cylinder head temperatures, injected at 280°BTDC with λ of 0.9 (solid lines) and 1.01 (broken lines)

The unfiltered data from Figures 5.11 and 5.13 show contradicting trends of the PN peak location for the nucleation mode compared to the accumulation mode. For Fuel B, there was a clear monotonic decrement of PN from lowest fuel temperature to the highest. This would suggest that the spray geometry for Fuel B, as well as spray impingement, was not a major influence on production of the nucleation mode. However, for Fuel C, the results for the nucleation mode does not show any obvious trends. As with Fuel B, the nucleation mode for Fuel C was recorded at the lowest temperature. However, at a temperature of 105°C (P_R = 8.70), Fuel C recorded the second highest magnitude in the nucleation mode which could possibly be due to flash boiling. A similar trend was also seen in Figure 5.17 for Fuel C at an injection timing of 280°BTDC. At this injection timing, for Fuel B, as shown in Figure 5.15, the flash boiling phenomena seems to have a significant impact on the size distribution of particulates. However, the nucleation mode particles trend was similar to the 250°BTDC test point with a monotonic increment of PN with a reduction of fuel temperature.

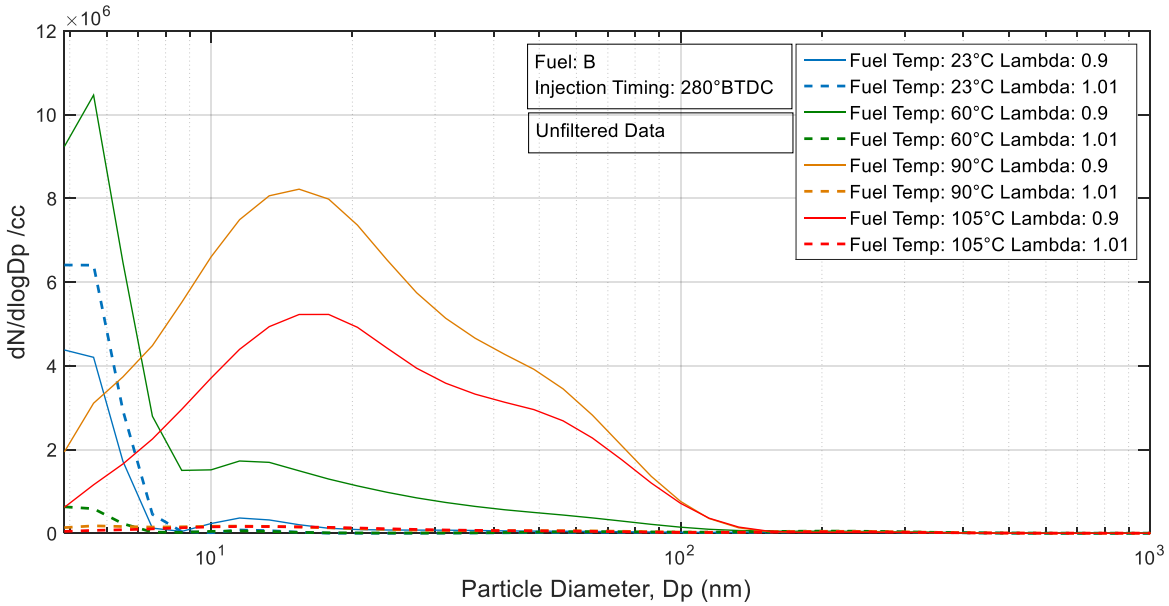


Figure 5.15: Unfiltered particulate size distribution for Fuel B at various cylinder head temperatures. Injection at 280°BTDC with λ of 0.9 (solid lines) and 1.01 (broken lines)

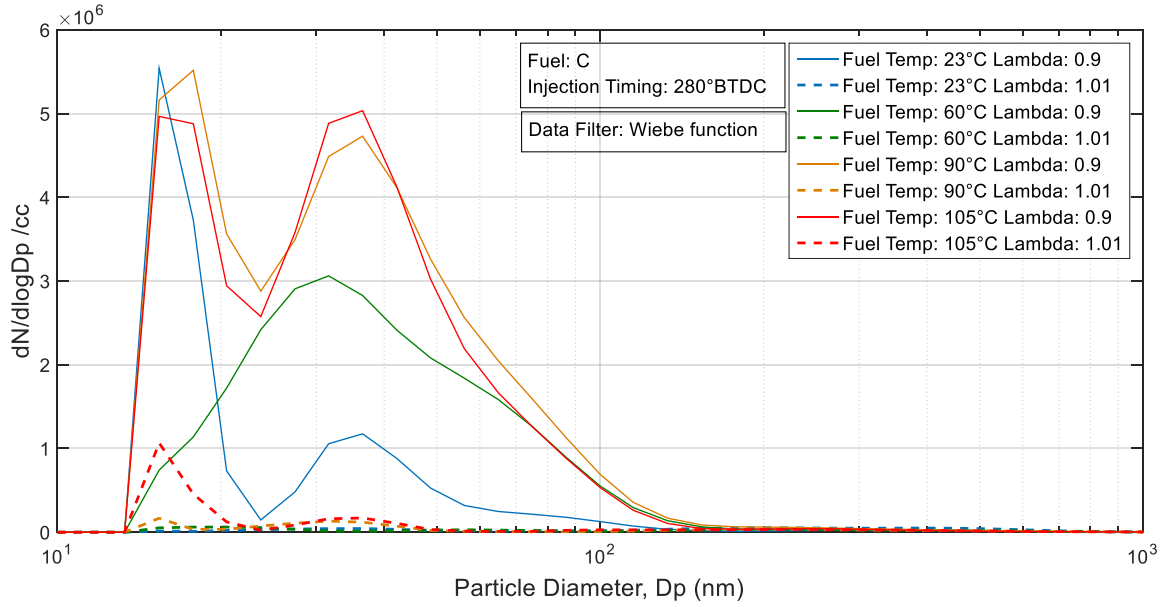


Figure 5.16: Wiebe filtered particulate size distribution for Fuel C at various cylinder head temperatures. Injection at 280°BTDC with λ of 0.9 (solid lines) and 1.01 (broken lines)

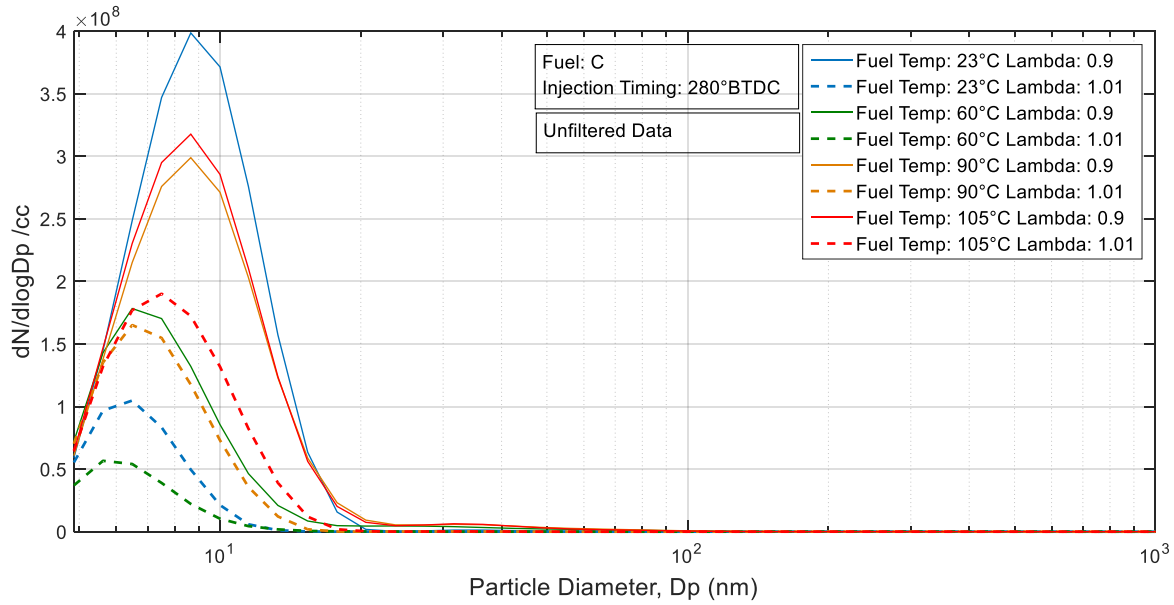


Figure 5.17: Wiebe filtered particulate size distribution for Fuel C at various cylinder head temperatures. Injection at 280°BTDC with λ of 0.9 (solid lines) and 1.01 (broken lines)

5.5.2. Particulate number and mass of heavy mixtures at various injection timings

Figures 5.18, 5.19 and 5.20 show the total particulate number distribution as well as total particulate mass for different pressure ratios, P_R, for Fuels B, C, D and a Euro 5 fuel at different injection timings. It has to be noted that all of these data were taken from experiments with engine operation at Lambda of 0.9. These plots summarise the multiple factors that influence the spray behaviour during engine operation which are: fuel volatility, fuel temperature and in-cylinder pressure (injection timing) to correlate it with the total particulate number and mass. The injection timing of 250°BTDC represents data with fuel spray impingement on the piston surface at a very minimal level, followed by increased impingement with 280°BTDC and finally the most severe impingement with the 310°BTDC injection timing. In the plots, the flash boiling regime has been defined to start from P_R = 3, which is the transitional flash boiling stage. It was not possible, however, to incorporate any spray impingement indication in these plots except by correlating the high-speed images to the P_R established before.

As expected, for all plots, the total particulate number magnitude varies significantly with volatility for each of the heavy fuels, with the least volatile Fuel D being the highest while Fuel B had the lowest. Other than that, from the plots, it was clear that Fuel D produced on average, the highest total particulate mass, followed by Fuels C and B. Fuel D (without methanol), produced high variations of total mass at different conditions. This can be seen in the plots where the total mass for Fuel D increased significantly whenever the P_R is much closer to entering the flash boiling regime (the transitional stage) and a sudden reduction in size as P_R moves further into the flash evaporation regime. This could suggest that without oxygenates in fuel mixtures, flash boiling could be significant in helping evaporation, but it is not so effective for oxygenated fuel mixtures.

For the B and C M15 fuels, flash boiling does not seem to impact the total mass as much. However, there are changes in the magnitude of the total particulate number. For example, with Fuel B, the particulate number seems to have increased with temperature with minimal changes in total mass in the flash boiling regime at the injection timing of 280°BTDC, suggesting that flash boiling was reducing the particulate size but at the same time producing more particulates instead. This however is not always the case, Fuel B produced less particulates when in a flash boiling regime at 250°BTDC injection timing, which was thought to have helped by the reduction in spray impingement severity, while the case of 310°BTDC had a much higher value of P_R due to a much lower in-cylinder pressure and more time available for evaporation.

Although these plots are capable of showing the impact of flash boiling towards P_M, other factors such as spray impingement may diminish the effects or even worsen the homogeneity of the air/fuel mixture, especially for injection at 310°BTDC. Unless a low in-cylinder pressure can be achieved (say below 0.5 bar) with the piston at mid-stroke or lower, so as to avoid spray impingement, then flash boiling would offer no benefit.

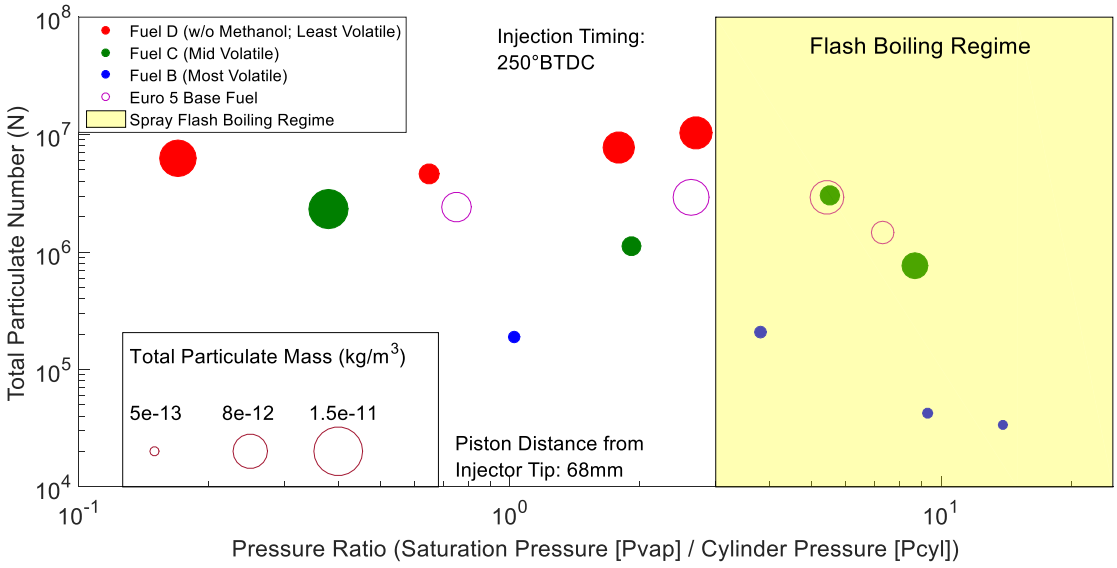


Figure 5.18: Total particulate number distribution of Fuels B, C, D and Euro 5 injected at 250°BTDC across different pressure ratios, P_R. The size of the circle represents the total mass calculated empirically.

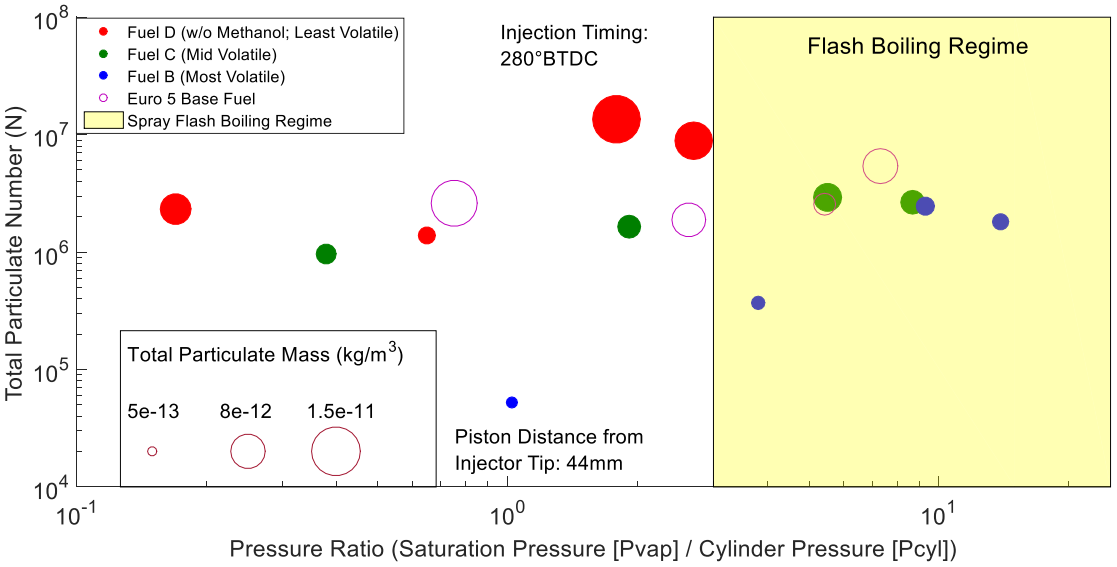


Figure 5.19: Total particulate number distribution of Fuels B, C, D and Euro 5 injected at 280°BTDC across different pressure ratios, P_R. The size of the circle represents the total mass calculated empirically.

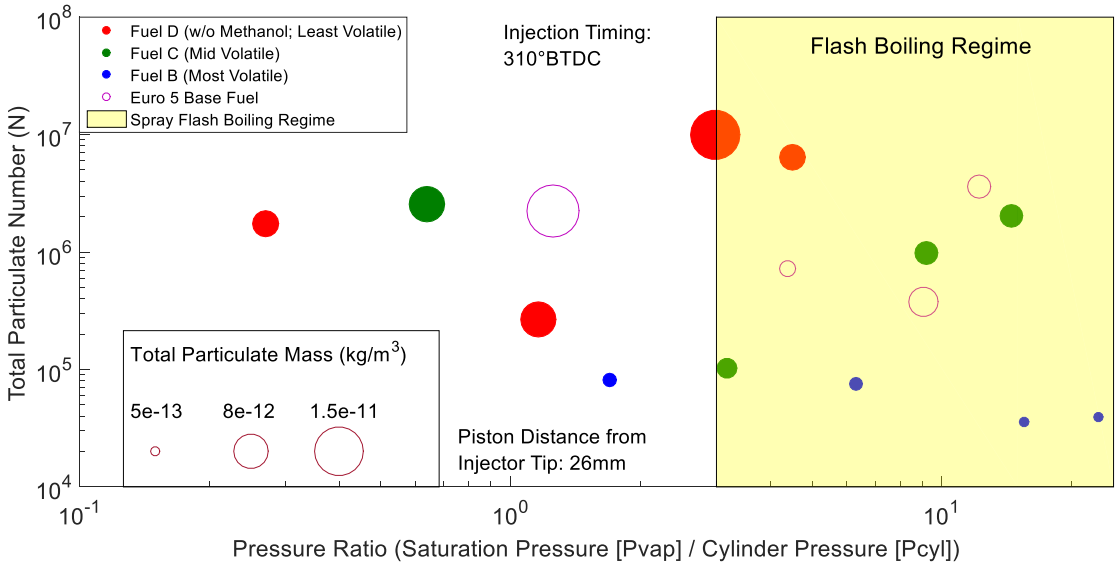


Figure 5.20: Total particulate number distribution of Fuels B, C, D and Euro 5 injected at 310°BTDC across different pressure ratios, P_R. The size of the circle represents the total mass calculated empirically.

5.5.3. Performance comparison of quartz against metal engine components

In this research work, the optical engine has been used with various liner configurations which are made of either metal or quartz. Quartz components were used for both illumination and imaging purposes. Though effectiveness of heat transfer is measured by these three parameters: (i) Thermal conductivity, (ii) material density and (iii) specific heat capacity. Quartz as a material, has a high specific heat capacity of about 703 J/(kg K) while only about 480 J/(kg K) for carbon steel. This close to 50% difference in value may be significant for the investigation of particulate production in an engine. The hypothesis is that when fuel spray impinges on a quartz surface, heat transfer to the fuel would be much higher than steel and thereby improve its evaporation rate. As a result, there can be discrepancies in the particulate data number as well as the size distribution.

The differences in P_M emissions might be explained by reference to the thermal contact parameters of the different material combinations. An important parameter for determining

the heat flow when two materials at different temperatures came into contact is the thermal contact parameter $\sqrt{\rho ck}$. The depth of thermal penetration (δ) is derived by $\sqrt{\alpha t}$. $\delta = \sqrt{\frac{k}{\rho c} t}$ (see section 2.3.2.1)

The amount of heat removed per unit area will depend on the product of the density and heat capacity, and the depth of thermal penetration

$$q = \delta \text{ x } (\rho c) = \sqrt{\rho ck\, t}$$

In the absence of evaporation and convection, the ratio of the thermal contact parameter will determine the temperature at the interface.

Table 5.2: Thermal properties comparison

	Material density, ρ ($kg.m^{-3}$)	Specific heat, c ($J.kg^{-1}.K^{-1}$)	Thermal conductivity, k ($W.m^{-1}.K^{-1}$)	$\sqrt{\rho ck}$ ($J.m^{-2}.K^{-1}$)
Iso-octane	692	2440	0.1	168848
Quartz (fused silica)	2200	703	1.48	2702480
Steel	7850	480	50.2	189153600

Figure 5.21 and 5.22 confirms the hypothesis mentioned earlier in this section. An experimental particulate measurement from the optical engine using the metal piston *vs* quartz have been conducted using Fuel B at different temperatures. It can be seen in Figure 5.21, that the total particulate numbers are much higher for all temperatures tested for the metal piston compared with the quartz piston. The highest discrepancies can be seen at 90°C, where particulates produced with the metal components are three times higher than with quartz. However, at a temperature of 105°C, the total particulate number magnitude difference between the materials was negligible. Also, the CoV for particulate data with quartz is many times higher, suggesting that the effects of piston surface cooling due to spray

impingement have high cycle-to-cycle variations. This is possibly due to a much higher temperature difference which causes the Leidenfrost effect to occur. Despite this, the total mass data for test at 23°C fuel temperature shown in Figure 5.22 was very low which means that particulates produced were small particles.

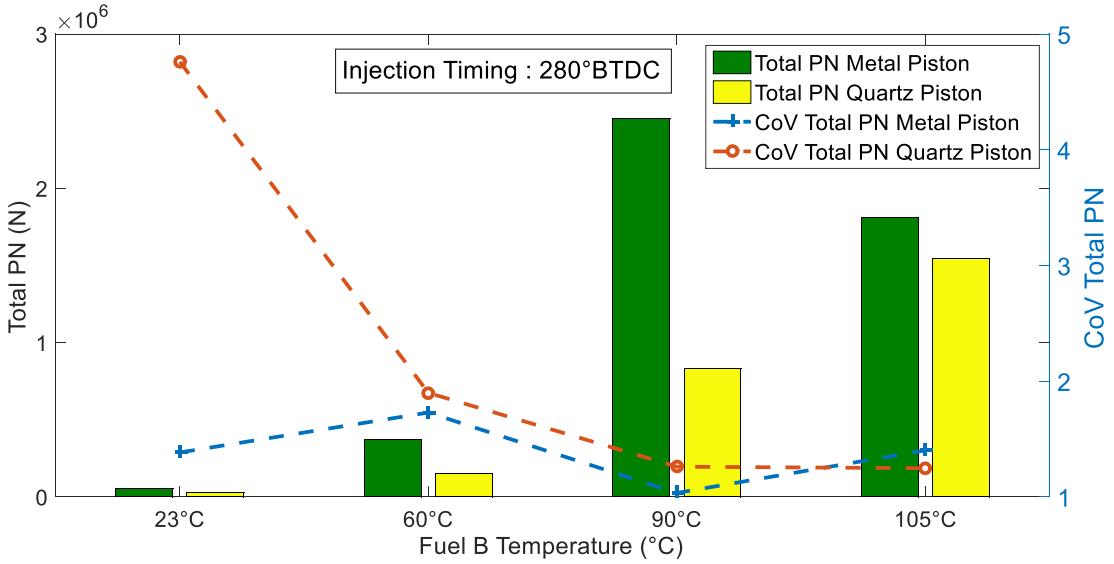


Figure 5.21: Compilation of total PN data extracted from optical engine tests using quartz and metal pistons. Fuel B was used at temperatures of 23°C, 60°C, 90°C and 105°C. Broken lines show the COV of the Total PN data for both metal and quartz pistons.

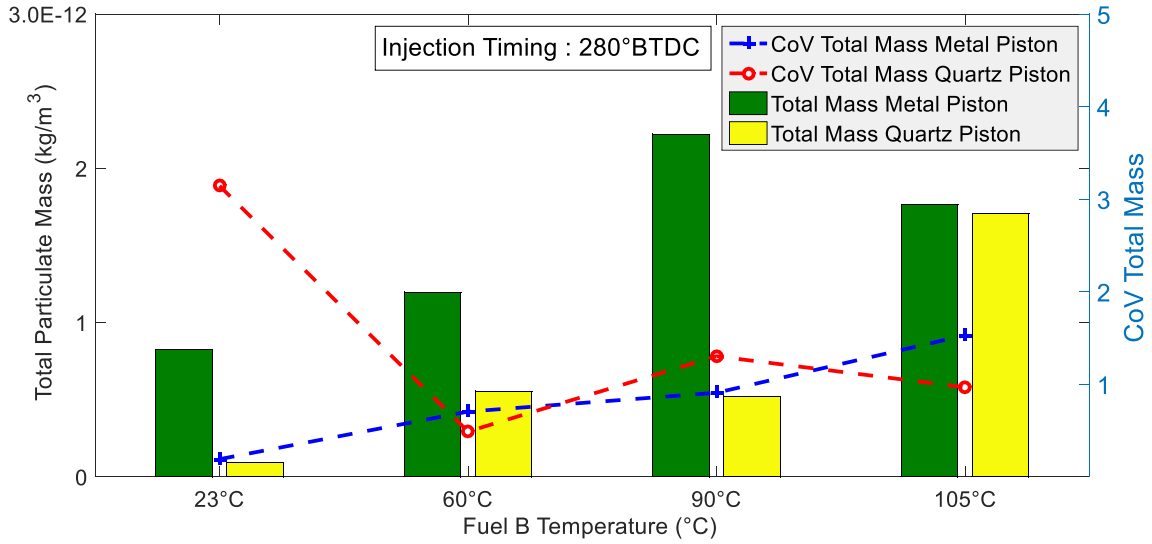


Figure 5.22: Compilation of total PN data extracted from optical engine tests using quartz and metal pistons. Fuel B was used at temperatures of 23°C, 60°C, 90°C and

105°C. Broken lines show the COV of the Total PN data for both metal and quartz pistons.

5.5.4. Lambda sweep of two distinctly different in-cylinder pressure ratio (R_P) fuels, injection timings of 310° and 340°BTDC.

As shown in previous discussions, injection timing, which determines the in-cylinder pressure can be a significant influence if flash boiling was to be used as a method to counter particulate production. To investigate this further, a simple lambda sweep experiment using the same optical engine and heavy fuels was devised. In this experiment, two injection timings were used; 310°BTDC and 340°BTDC. The two injection timings are only 30° apart, but actually differ significantly in in-cylinder pressure. At 310°BTDC, the in-cylinder pressure was about 0.3 bar while at 340°BTDC it was 0.97 bar, which is more than triple the earlier the value. The engine coolant was set to 90°C, and this is capable of causing flash boiling for both fuels at 310°BTDC but not at 340°BTDC. The distance from the piston surface to the injector tip for injection at 340°BTDC was 14.4 mm while at 310°BTDC it was 26.6 mm. The difference of about 12.2 mm was less than 20% of the total travel capability of the spray plume, therefore the spray velocity upon impact on the piston surface was similar.

For this experiment, Fuel B and C were used to compare the possibility of over cooling the piston surface which could significantly increase the particulate matter output during combustion due to diffusion flames. This is possibly happening in boosted engines when the injection duration is much longer to accommodate the increased fuel flow. This in turn, causes the piston surface to be exposed to lengthier spray cooling effects. Combustion imaging was not attempted for this experiment, but only particulate measurements were taken. Similar procedures for particulate measurements were used in order to eliminate volatiles from the data. The Wiebe filter was applied to all results to replicate the legally compliant particle counting instruments, this also reduces the CoV in the data and is then

dominated by the accumulation mode. The lambda steps used for this experiment were 1.01, 0.9, 0.85 and 0.8.

Figures 5.23 and 5.24 show the particulate size distribution results for the lambda sweep experiment at injection timings of 310°BTDC and 340°BTDCfor Fuel B. Figures 5.25 and 5.26 show the particulate size distribution results for the lambda sweep experiment at injection timings of 310°BTDC and 340°BTDC for Fuel C.

For both injection timings, the result at 310°BTDC produced much higher values of particulate number than at 340°BTDC at any lambda values tested for both Fuel B and C. This might suggest that the time available for fuel mixture evaporation before combustion with injection at 340°BTDC has a much higher impact than that of flash boiling for fuels or the increased injector to piston distance at 310°BTDC. For Fuel B, there seems to be a very irregular trend on particulate number when looking at the lambda sweep. One would expect to have a monotonic increase of the particulate emissions with the reduction in lambda due to the increase in combustion richness that promotes incomplete oxidation.

Fuel D results show slightly different magnitudes in particulate size distribution output. For both injection timings, the plots show small differences in the average values of the particulate distribution magnitude for lambda values of 1.01, 0.9 and 0.85, but to drastically increase in magnitude when the lambda value was at 0.8. This could suggest that at this lambda value, significant piston surface cooling has occurred which has probably reduced the evaporation rate of the fuel. Piston surface cooling could result in the build-up of a fuel film on the piston surface which creates an in-homogeneity in the air fuel mixture and also to have pool fires. Using oxygenated fuels could possibly be more devastating due to the fact that alcohols have higher heats of vaporization than gasoline. This however, can

be ameliorated by having a really volatile fuel such as Fuel B, which did not show any significant rise in particulates as lambda values were decreased to a very low value.

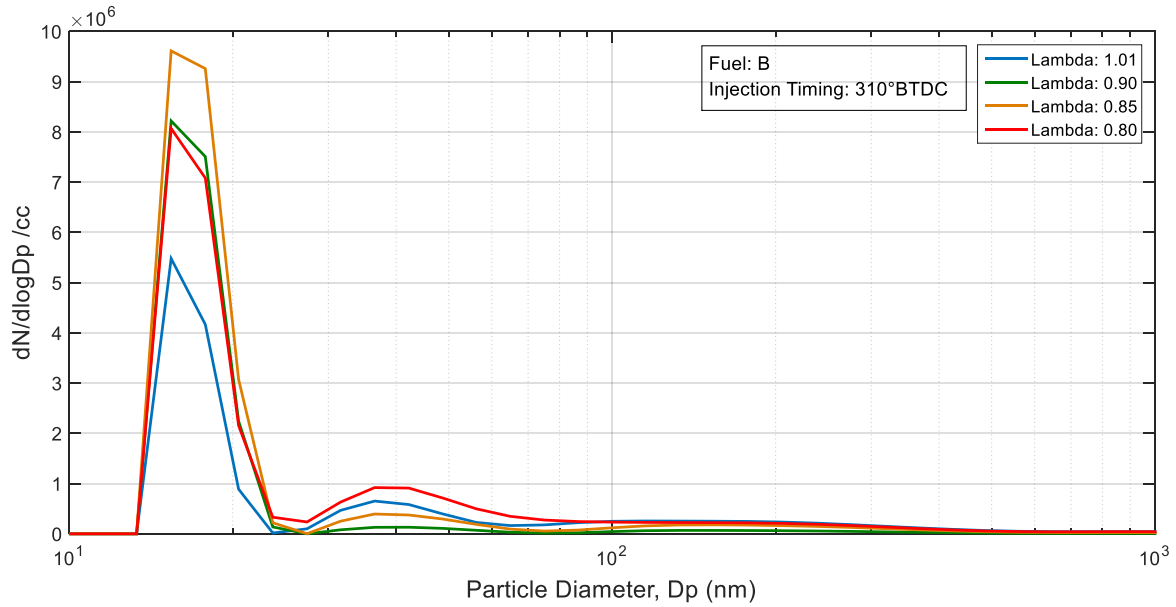


Figure 5.23: Particulate matter size distribution from the optical engine lambda sweep experiment using Fuel B at an injection timing of 310°BTDC. Fuel temperature was set to 90°C for all the test points.

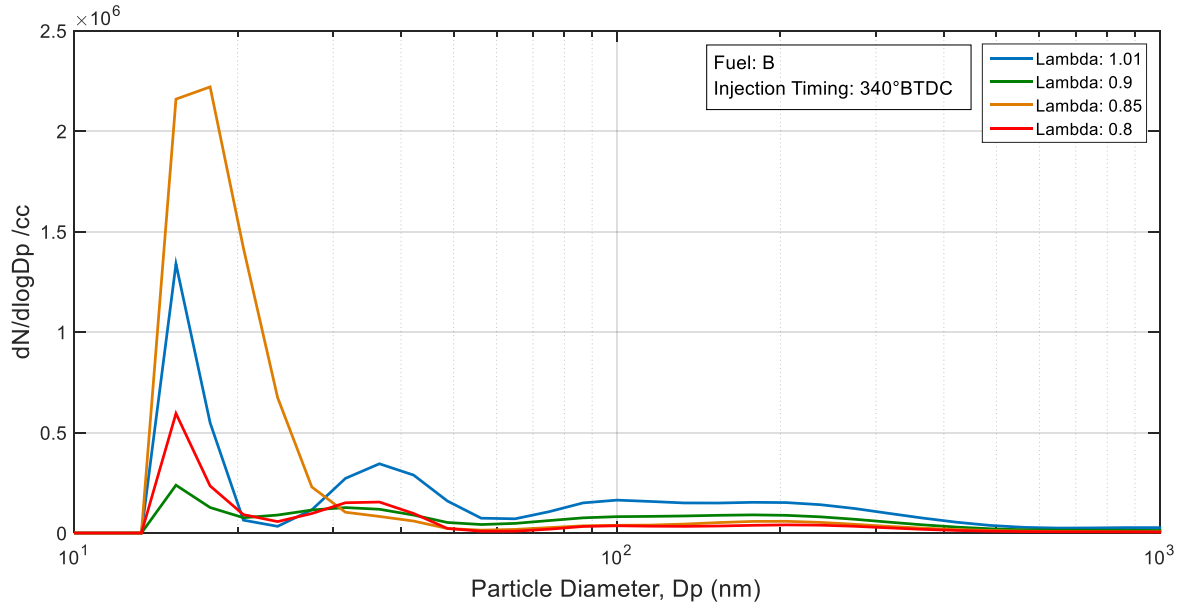


Figure 5.24: Particulate data size distribution from the optical engine lambda sweep experiment using Fuel B at an injection timing of 340°BTDC. Fuel temperature was set to 90°C for all the test points.

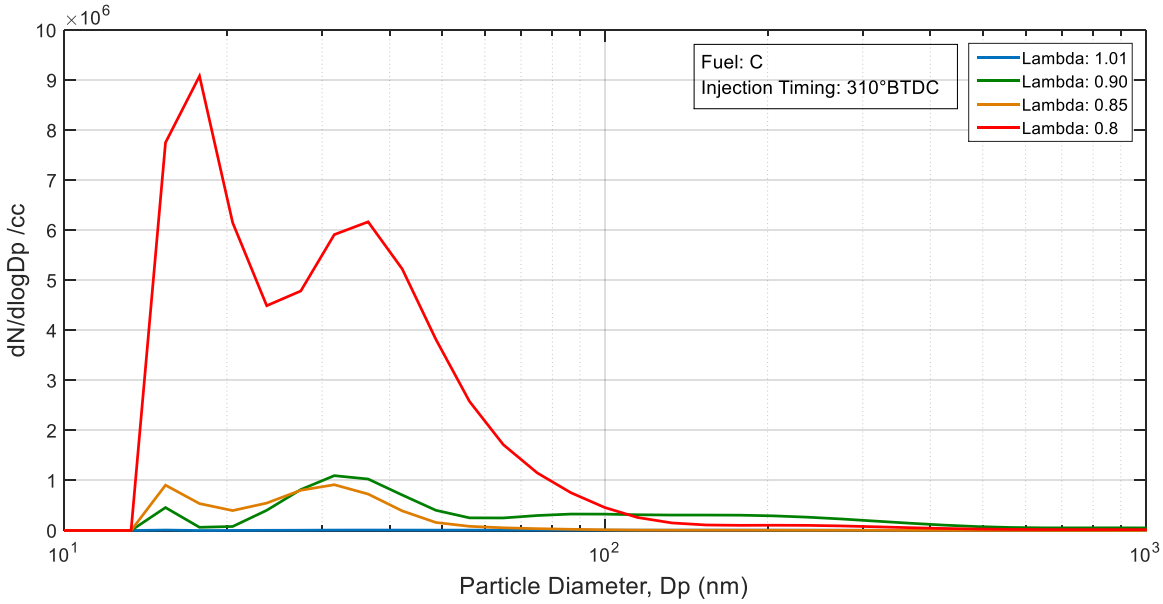


Figure 5.25: Particulate data size distribution from the optical engine lambda sweep experiment using Fuel C at an injection timing of 340°BTDC. Fuel temperature was set to 90°C for all the test points.

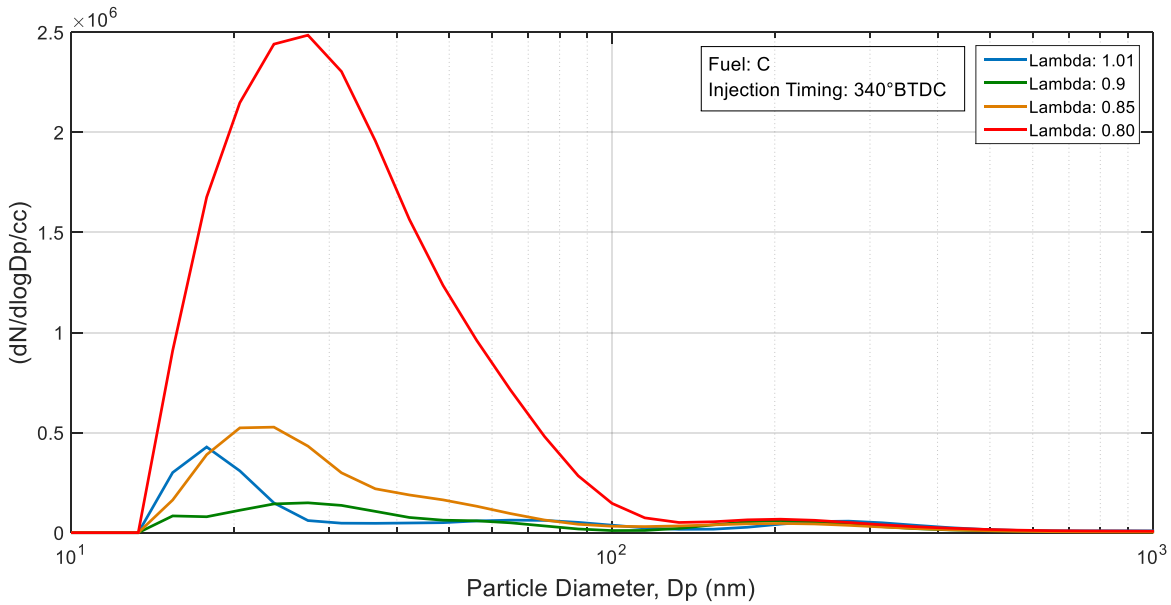


Figure 5.26: Particulate data size distribution from the optical engine lambda sweep experiment using Fuel C at an injection timing of 340°BTDC. Fuel temperature was set to 90°C for all the test points.

5.5.5. Chapter summary

In the beginning of this Chapter, a detailed analysis of the in-cylinder pressure trace of a non-boosted and a boosted engine was first explored. The boosted engine configuration proves to have a much narrower window of opportunity to introduce flash boiling. Spray characteristic validation experiments were done at injection timings of 250°BTDC, 280°BTDC and 310°BTDC. It was found that the spray development images in the engine were comparable to the spray images captured in the spray rig. This was followed up by some combustion imaging that shows some discrepancies in correlating flame intensity towards particulate emissions.

The Chapter continues with particulate measurement experiments with the full metal configuration of the optical engine using heavy fuels at different injection timings and different temperatures to explore the influence of flash boiling. First, several data sets for unfiltered and filtered data were compared. It was observed that fuel volatility has a beneficial impact, even if flash boiling does not occur.

Fuels B and C produced contradicting trends for nucleation and accumulation mode particulates. To better understand this situation, plots correlating PN and PM towards flash boiling were made. It was found that flash boiling did not necessarily reduce particulate number but instead reduced the mean particulate size which can lead to lower total mass (PM). Other than that, flash boiling had more impact on the non-oxygenated Fuel D than the other M15 fuels.

A simple but essential experiment comparing the quartz and metal pistons was devised. It was observed that the quartz engine component, when used in particulate measurements, may cause discrepancies due to having significantly different thermal properties that alter the mixture homogeneity. Finally, a lambda sweep experiment using

very early injection timings showed that spray cooling effects on the piston surface at very rich conditions could lead to higher particulate matter emissions.

6. Single Jet Spray Impingement Experiments, Results, and Validation

6.1. Introduction

Following the results in the previous chapter, a new type of experiment was constructed to further investigate the effects of fuel spray impingement on mixing performance. It is thought that fuel with a low volatility can create a liquid pool on the piston surface when spray impingement occurs. This will then cause poor homogeneity of the fuel mixture which then translates into incomplete combustion with diffusion flames or pool fires on the piston surface. The objective of the experiments in this chapter was to investigate how different fuel composition affects the spray cooling on the piston surface, especially with the oxygenated mixtures. Other than that, there has been very little information from the literature on the effect of gasoline flash sprays that impinge on a piston surface. By using a single jet spray, a deliberate spray impingement can be achieved while having minimal variations on the spray geometry that can possibly skew measurements.

The first section of this chapter reviews the different spray characteristics from different fuels injected at various temperatures. A series of high speed images of single jet sprays were compared and analysed for all the fuels used. These visualizations were meant to help understanding the single jet spray geometry at different increments of fuel temperature. From these images, the spray angle of a single jet spray was also extracted for correlation with the saturation pressure ratio and the total heat flux distribution. The heat flux distribution will be discussed later in section 6.4 of this chapter. Different spray angles give different spray impact characteristics and therefore different heat flux distributions on the piston surface.

The next part of this chapter (section 6.3.1) looks into the temperature map distribution of the piston surface for which a 2D finite difference method (described in

section 2.3.2.1) was used to analyse the data. A comparison of a 2D heat map would help in analysing the different thermal penetration depths of different sprays. To give better confidence in this calculation, a validation exercise of the 1D and the 2D calculation methods was made and analysed.

The final part of this chapter (section 6.4) discusses the results of heat flux measurements from the spray rig using both pure fuels and mixtures. The data outcome for this experiment was to look into the transient temperature change on the piston surface during fuel impingement for different fuel compositions. These data can then be used to calculate the heat flux at the surface. The temperature data can give a good insight into how different fuels evaporate with spray impingement. However, instead of just using heat flux values, a total energy gained or removed value was used to compare fuel compositions, different injection pressures, fuel temperatures, piston surface temperatures and also spray distances. To achieve this, a simple integration of total heat flux against time was calculated from the start time of spray impingement till the end. A comprehensive plot comprising a number of different parameters were produced to easily compare multiple parameters.

6.2. Experimental test conditions

The spray impingement investigation was devised based on the findings from the optical engine experiments. From those results, many important factors were identified that

were influencing the severity of spray impingement, which can lead to the production of particulate matter. The full list of experimental conditions is shown in Table 6.1.

The fuels used for this experiment consist of pure component and mixtures. The pure components used for this experiment are methanol and n-pentane. Methanol and n-pentane are normally used in mixtures to increase the volatility of gasoline fuel mixtures, however these components have significantly different enthalpy of evaporations and specific heats individually, and these can affect the heat transfer during impingement. As for gasoline mixtures, Fuels B, C, D and Euro 5 were used. These fuels share almost similar heavy-end (T90) distillation curve characteristics while respectively having different volatilities (see Table 3.2). The gasoline fuel mixtures were previously used for experiments in Chapter 5. A maximum temperature of 140°C was selected to make sure that flash boiling was achieved as these experiments were conducted at atmospheric conditions and not equivalent to in-cylinder engine conditions (0.5 bar).

Table 6.1: List of experimental conditions used for spray impingement experiment

Experimental Conditions	Value
Fuels	n-pentane, methanol, Fuel B, Fuel C, Fuel D, Euro 5
Fuel Temperatures (°C)	25, 50, 80, 110, 140
Surrogate Piston Temperatures (°C)	30, 60, 90, 110
Injection Pressures (bar)	50, 100, 200
Injector Tip Distance to Piston (mm)	30, 50, 75
Injection duration (ms)	2.0
Ambient Temperature (°C)	18-23
Number of Injections	1

The surrogate piston temperatures selected for these experiments were 23°C, 50°C, 80°C and 110°C. The maximum temperature used for this experiment was limited to 110°C due to the limitation of the adhesive on the TFG which can detach at higher temperatures. Although the surface temperature was not as high as the steady state operating condition of a piston in the engine, this was enough to cause rapid evaporation of some fuel during

impingement. Furthermore, only a single injection was used for all conditions, as the heater was not rapid enough to maintain the temperature at the original value after every injection.

Injection pressures of 50, 100 and 200 bar were tested for this experiment to emulate different spray impact and splash patterns on the piston surface. Injection duration was kept constant to take into consideration of having more fuel mass when having different injection pressures. All of the injection pressure values used are quite commonly used in many conventional GDI engines. Other than that, the injector tip distance to the surrogate piston was also varied to match the conditions when different injection timings were used in the engines. These distances were extracted from the experiments on the single cylinder optical engine where 30, 50 and 75 mm represents 310°BTDC, 280°BTDC and 250°BTDC respectively.

6.3.High speed imaging results

High speed imaging of the sprays was used to identify the characteristics of this single plume injection. The spray can vary in geometry, jet tip velocity and rate of luminosity. The raw images were analysed using the IMSPRAY MATLAB program for background subtraction as well as spray angle measurements. Figure 6.1 shows the description of a typical raw image extracted from the experiment. As described in section 2.3.1.1, the injector has been modified to produce only single jet of spray so as to reduce the influence of spray geometry (i.e collapsed spray phenomena during flash boiling) in impingement studies.

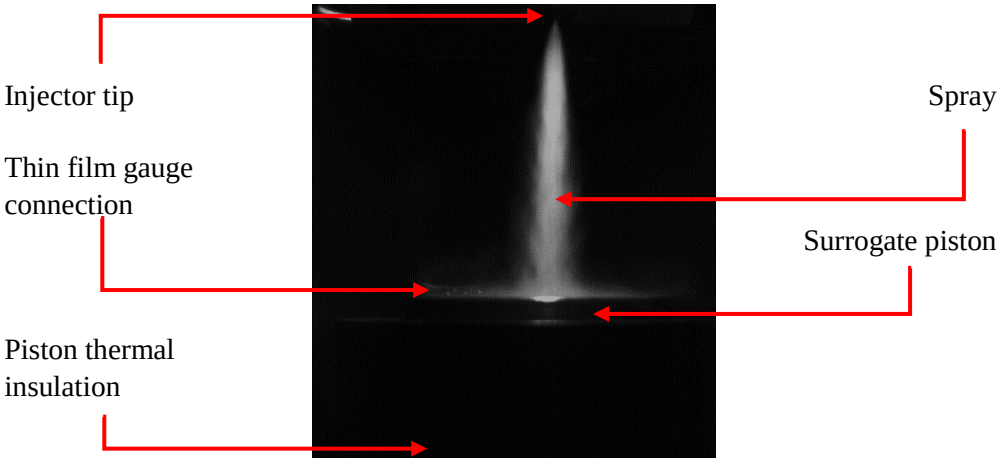


Figure 6.1:Typical image composition of spray from captured from the experiment

The camera was triggered together with the injection and was set to 5000 FPS, in which the interval between images was at 0.2 ms. Due to the massive amount of data obtained from this work, only several images were selected to be presented in this section. All of the fuels, except for the Euro 5, listed in Table 6.1 were used. The results presented here were taken at injector tip distance of 75 mm from the surrogate piston surface. The images selected for all case starts at 0.8 ms ASOI and ends at 1.8 ms ASOI. This was enough to demonstrate the start of various impingement phenomena on the piston surface. Only the hottest piston surface temperature (110°C) has been selected to be shown here. From preliminary observation of the images, it was found that there was no distinct difference (that can be seen from the current image resolution) to the spray upon impingement. Therefore, the effects of piston surface temperature towards spray impingement (i.e Leidensfrost phenomena) was not possible to be analysed in depth from these images. It has to be noted that the spray was very slightly angled due to the limitations of the apparatus. However, the impact of this misalignment was minimal, as the spray tip was still targeted to the centre of the piston.

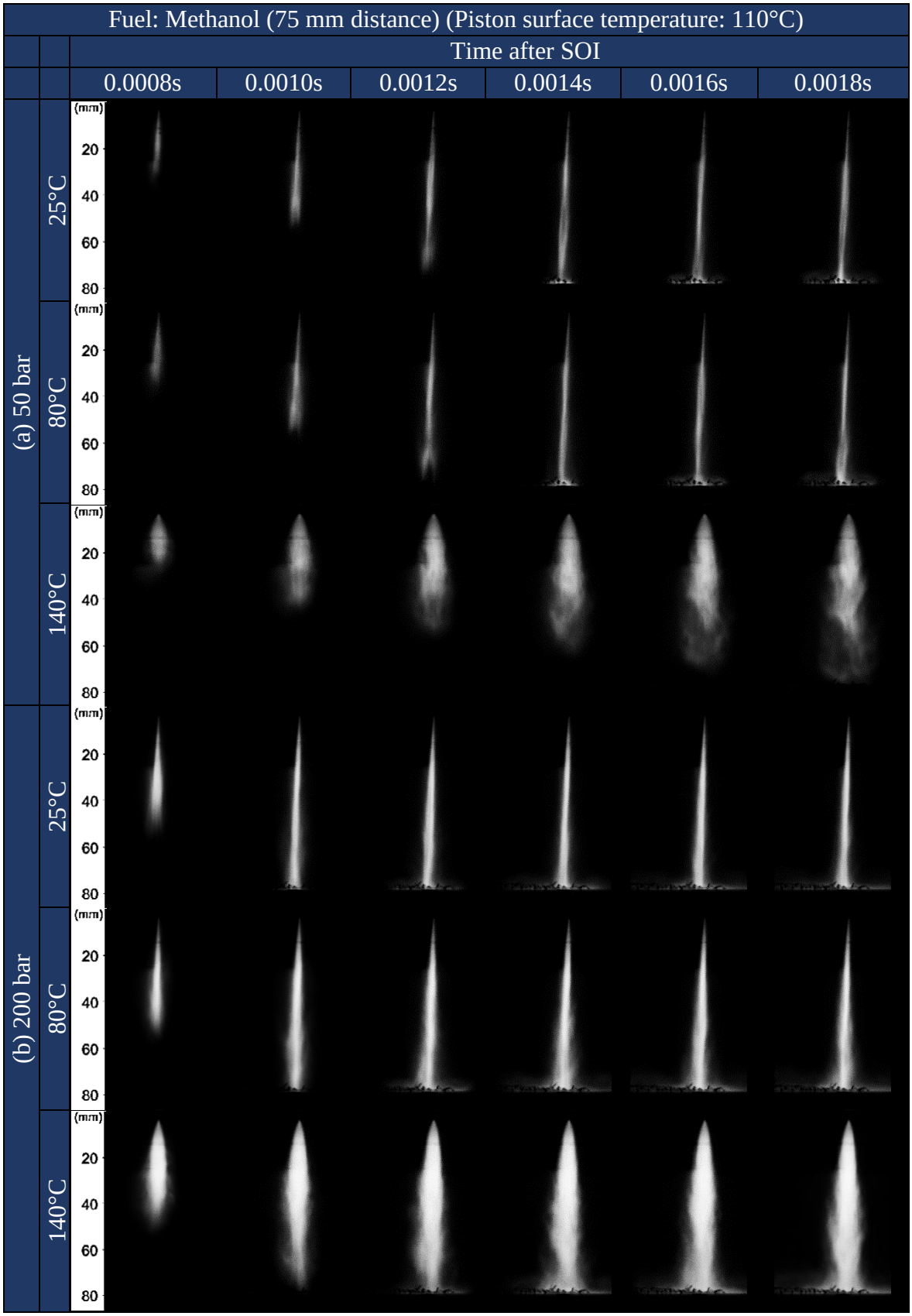


Figure 6.2: (a) 50 bar and (b) 200 bar single plume spray of methanol injected towards the TFG at temperatures of 25°C, 80°C and 140°C

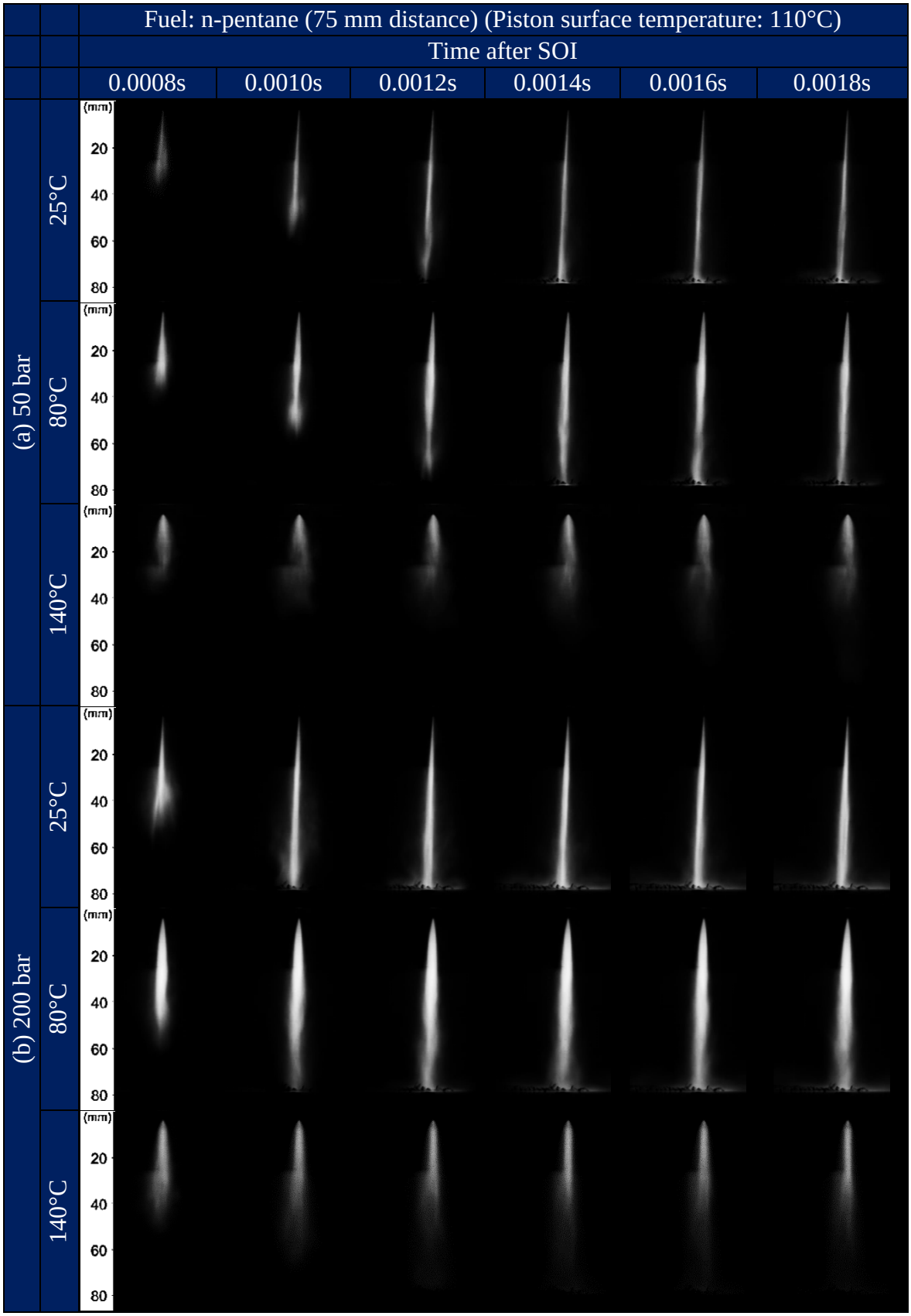


Figure 6.3: (a) 50 bar and (b) 200 bar single plume spray of n-pentane injected towards the TFG at temperatures of 25°C, 80°C and 140°C

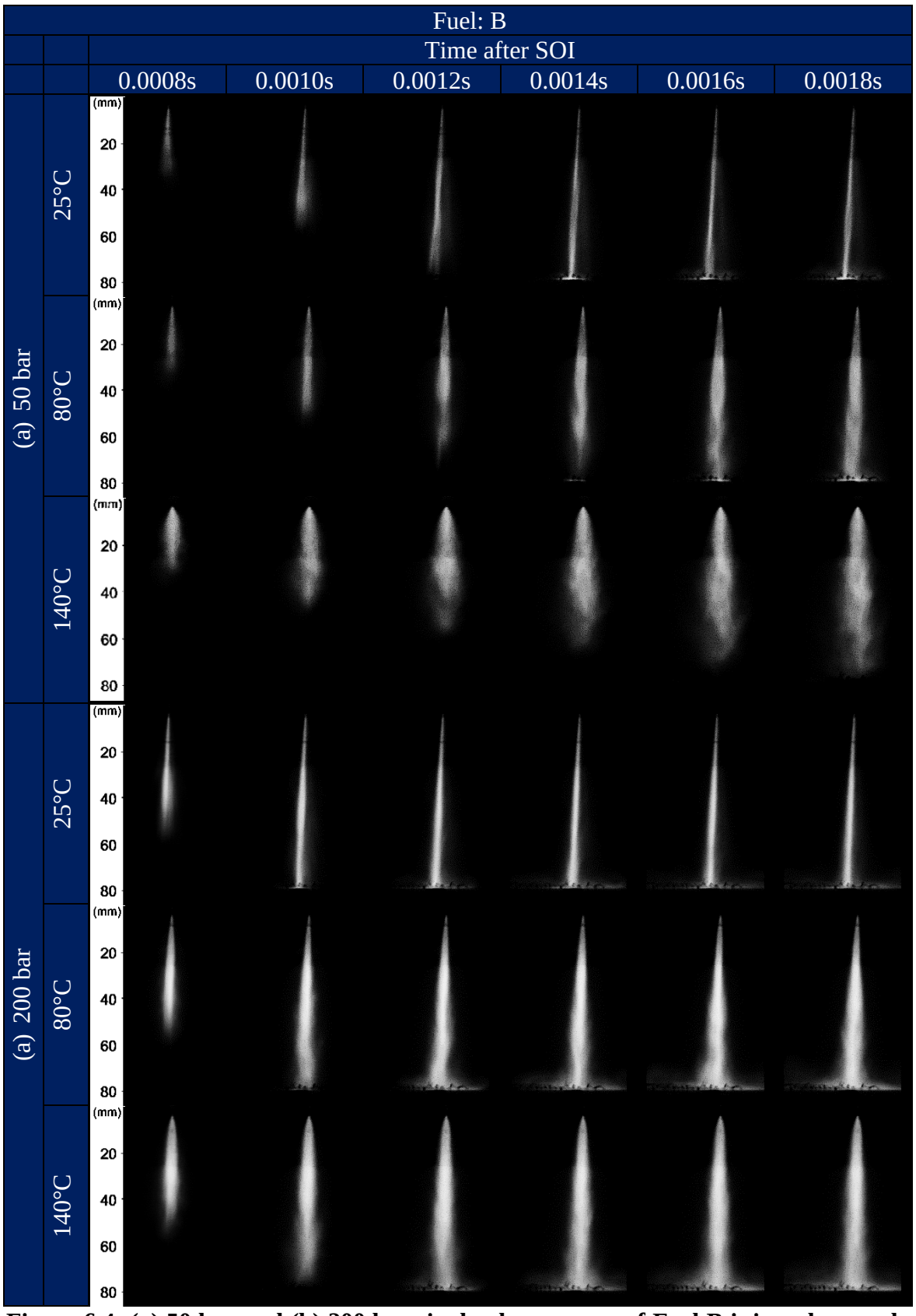


Figure 6.4: (a) 50 bar and (b) 200 bar single plume spray of Fuel B injected towards the TFG at temperatures of 25°C, 80°C and 140°C

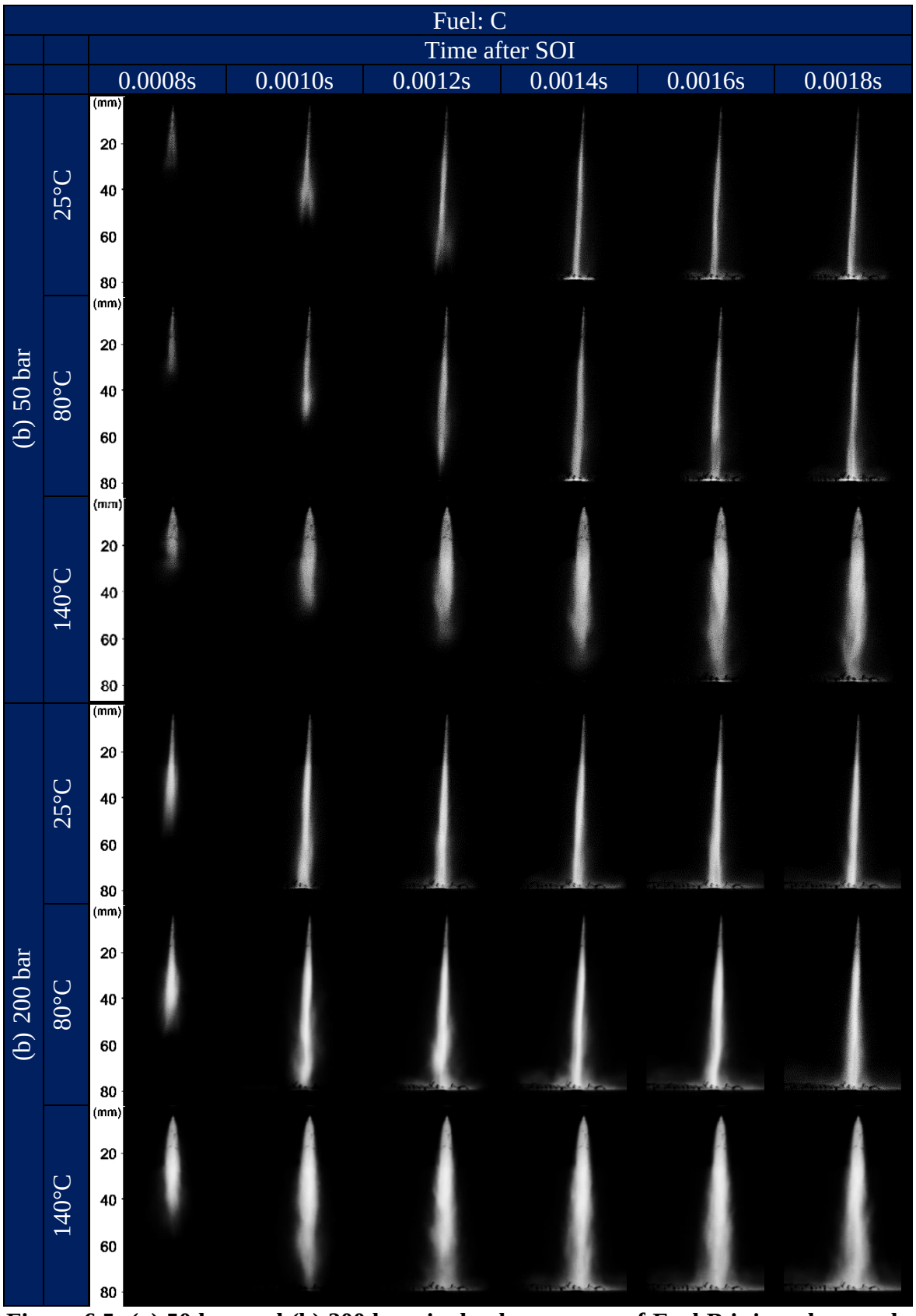


Figure 6.5: (a) 50 bar and (b) 200 bar single plume spray of Fuel B injected towards the TFG at fuel temperatures of 25°C, 80°C and 140°C

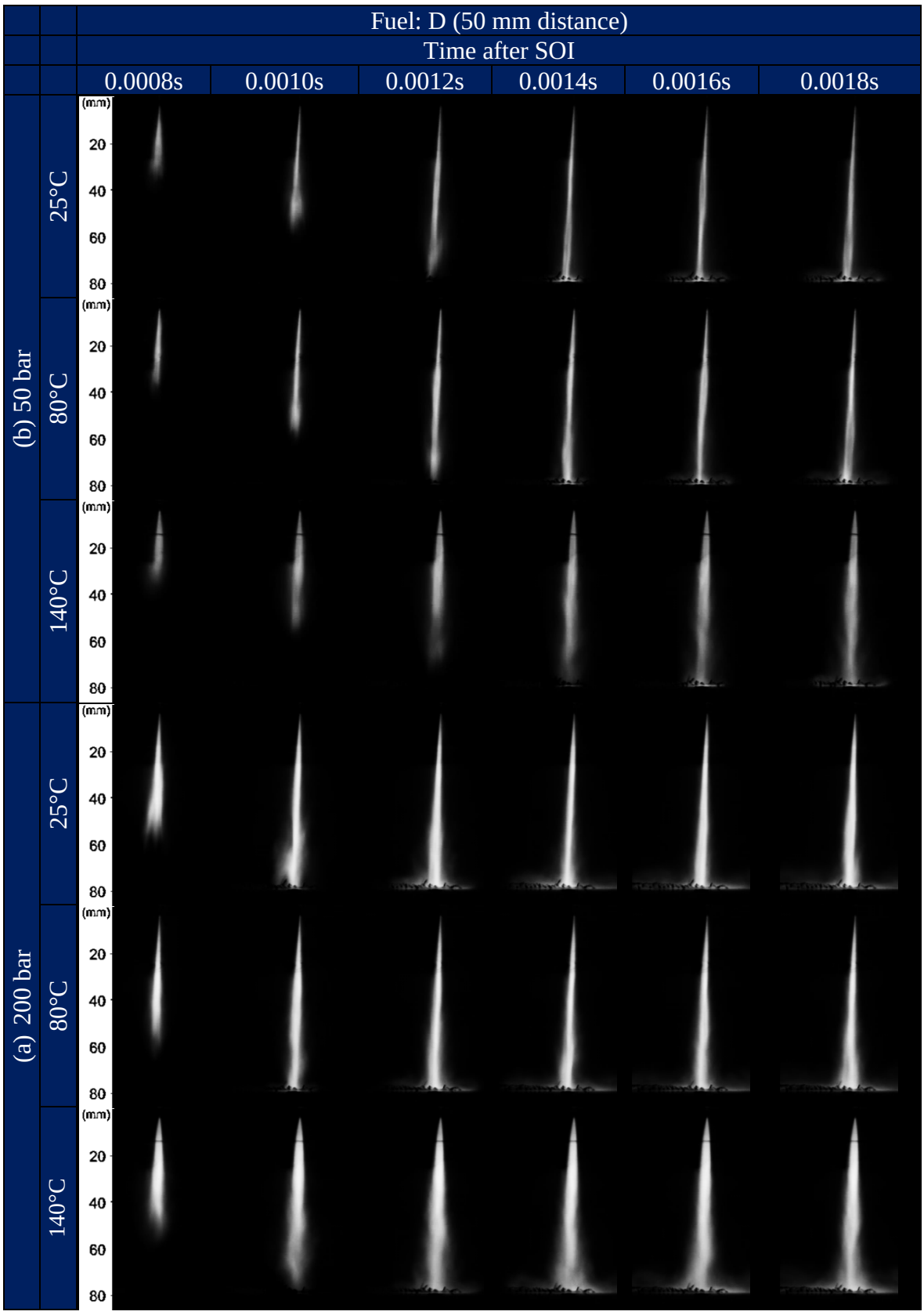


Figure 6.6: (a) 50 bar and (b) 200 bar single plume spray of Fuel D injected towards the TFG at temperatures of 25°C, 80°C and 140°C

Figure 6.2, 6.3, 6.4, 6.5, 6.6 show high speed images of the single jet fuel spray of pure n-pentane, pure methanol, Fuel B, Fuel C, and Fuel D targeted at the surrogate piston. The Figures also show the parameter variations in fuel temperatures as well as injection pressures. The discussion on the single jet characteristics is as follows:

Pure n-pentane vs pure methanol – At temperatures of 25°C and 80°C, at 50 bar injection pressure, both fuels show similar spray geometry, penetration rate but slightly different spray intensities. It was only at 200 bar injection pressure that the 80°C fuel spray of n-pentane showed signs of much earlier transition to flash boiling by having an increased spray angle. However, at a temperature of 140°C where both were at flare flashing conditions (even at atmospheric condition), the spray for each fuel were very distinct. Pure methanol produced a large angle spray that was very visible from 0.8 ms up to 1.8 ms where impingement was obviously seen. For the case of n-pentane, the visibility of the spray was poor when the travel distance for the 50 bar injection was only about 30 mm from the injector tip and barely touching the surrogate piston surface. Similarly at 200 bar injection pressure, the spray tip distance improved, but was only minimally in contact with the piston surface. As expected, at this temperature, n-pentane which has only about 30°C lower boiling point would have much higher P_R than methanol ($P_{R_npentane}$ = 13.2 ;$P_{R_methanol}$ = 10.8). Both of which were already in the flare flashing region based on these saturation pressure ratio (P_R) values.

For the cases of Fuel B, Fuel C and Fuel D mixtures, when comparing the spray geometry, it is much more interesting to focus when they are at high temperatures or are flash boiling. As can be seen in Figure 6.4, at a temperature of 140°C and 50 bar injection pressure, Fuel B (Light components: 15% methanol & 45% n-pentane) has a spray geometry as well as a plume tip velocity that mimics closer to pure methanol than n-pentane. However, at 200 bar injection pressure and 140°C fuel temperature, the spray was more intense and with a smaller spray angle (probably due to the characteristics of the heavy components).

Fuel C (light components: 15% methanol & 45% iso-octane), as shown in Figure 6.5, at 140°C and injection pressure of 50 bar, only showed a slight increase in spray angle which is assumed to be the effect of having methanol in the mixture. At 140°C and 200 bar injection pressure, the spray plume width was much smaller than for the 50 bar injection pressure, and showed only very minimal signs of flash boiling. However, the intensity of the spray can be seen to be much more obvious than Fuel B.

Fuel D (light components: 55% iso-octane & 5% n-pentane), as shown in Figure 6.6, at a fuel temperature of 140°C & 50 bar injection pressure never showed any increase in spray angle due to having a much higher boiling point. The same can be seen for the case at 200 bar injection pressure and 140°C fuel temperature. As a result of this, more heat transfer is expected from the thermometer nearest to the centre of the piston. The thermometers at the outer radius will have to depend on splash effects to be able to have any heat transfer from the piston surface.

6.3.1. 2D Piston surface heat map results

Apart from high-speed images, temperature changes on the piston surface were also measured during the impingement event. From these results, heat penetration depth as well as a surface heat map can be calculated. The details of the calculation method have been discussed in detail in section 2.3.2.1. The advantage for having this is to ease visualization of the various impingement pattern and liquid spray distribution on the piston surface when testing different fuels or different injection pressures. It should be noted that in this section, only observations are described. Discussion on the impact of the different fuel behaviours will be associated further with the total heat energy exchange data later in section 6.4.2.

Figure 6.7 and Figure 6.8 both show 2D heat maps of the piston surface for methanol vs n-pentane injected at 50 bar and 200 bar respectively, at temperatures of 25°C, 80°C and 140°C. For 50 bar injection pressure, methanol and n-pentane produced similar heat map pattern at 25°C, with n-pentane cooling slightly better than methanol. However, at 80°C n-pentane was already showing very minimal surface temperature change, suggesting very low fuel mass impingement on the surface, while methanol remained similar to when the temperature was 25°C. There were also changes from the initial temperature at the outermost thermometers such as TC7 and TC8. As expected, at 140°C, n-pentane was much worse while methanol, despite having a higher temperature than the piston surface, still managed to reduce the surface temperature. For the case of 200 bar injection pressure, the same can be seen to happen, except that n-pentane, this time, travelled further (even at temperature of 80°C) to cause a slight temperature change on the piston surface.

Figure 6.9 and Figure 6.10 show 2D heat map comparisons between Fuel B, Fuel C and Fuel D, injected at temperatures of 25°C and 110°C. Figure 6.9 shows the comparisons for an injection pressure of 50 bar while Figure 6.10 is for 200 bar. Generally, it can be seen that

the 50 bar injection produced two distinct 2D heat map patterns - for all fuel mixtures, the cold fuel causes temperature reduction more centrally where as the hot fuel effects almost all of the thermometers on the piston surface. This is again due to the flash boiling phenomena that widened the spray angle, which was also exaggerated even more with a low injection pressure. Other than that, Fuel B was the best at cooling the piston surface when injected cold, but the poorest when injected at high temperature as can be seen in Figure 6.9. For the case of 200 bar injection however, Fuel B had the best cooling effect at both cold and hot temperatures. In Figure 6.10, the 2D heat map for cold fuel show that the outer thermometers such as TC6 and TC7 had temperature change which did not happened at 50 bar injection. This is possibly due to the splash effect of the fuel spray that can impact the neighbouring thermometers. A more detailed comparison of the heat energy exchange data will be made later in Section 6.4.2.

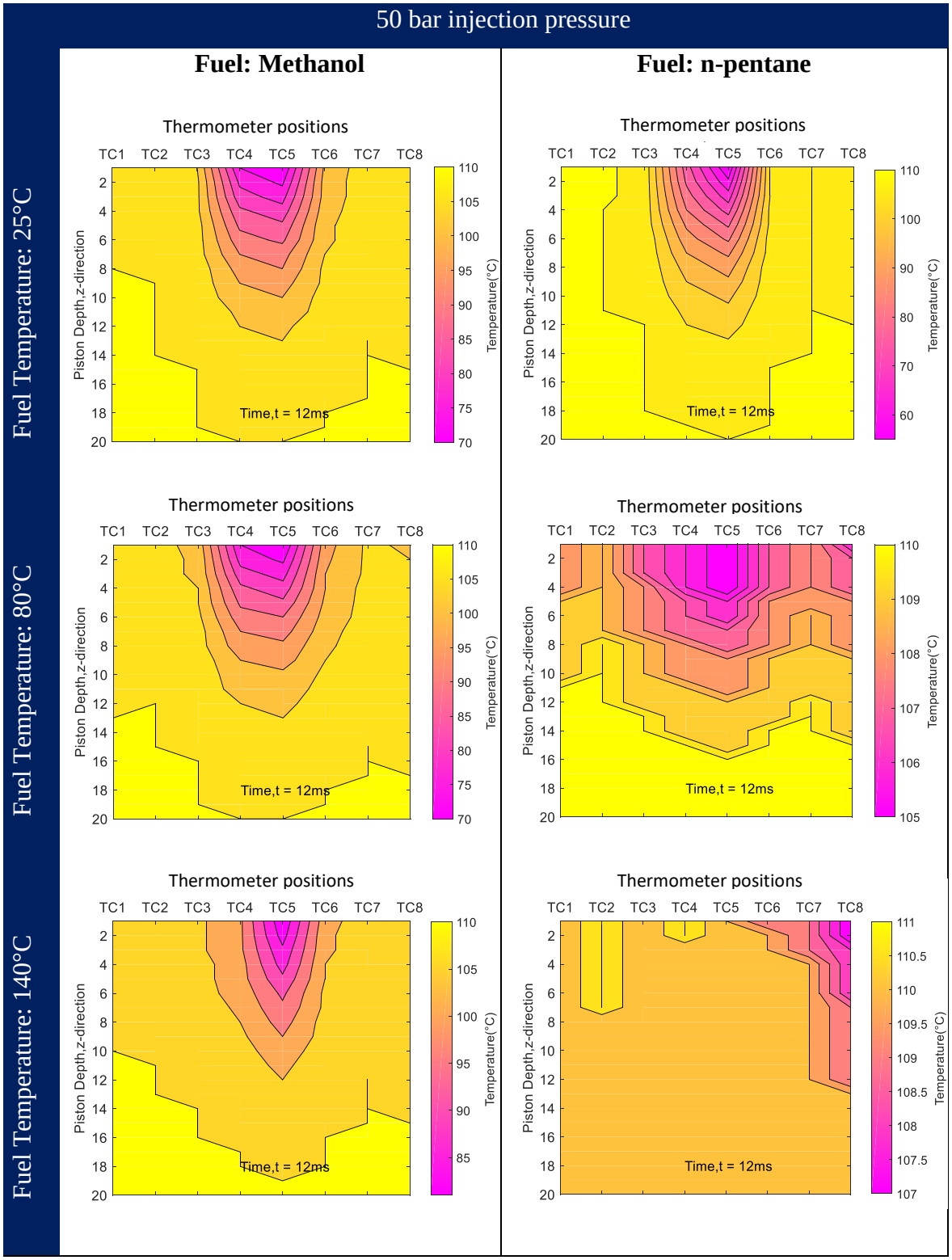


Figure 6.7: 2D heat map result comparisons between methanol and n-pentane pure fuels injected at 50 bar injection pressure and temperatures of 25°C, 80°C and 140°C. The piston surface temperature shown for all are at 110°C. Heat map iteration shown for all are at 12 ms ASOI. Note: 1) z-direction actual distance: 10µm/step 2) x-direction actual distance: 6mm/step

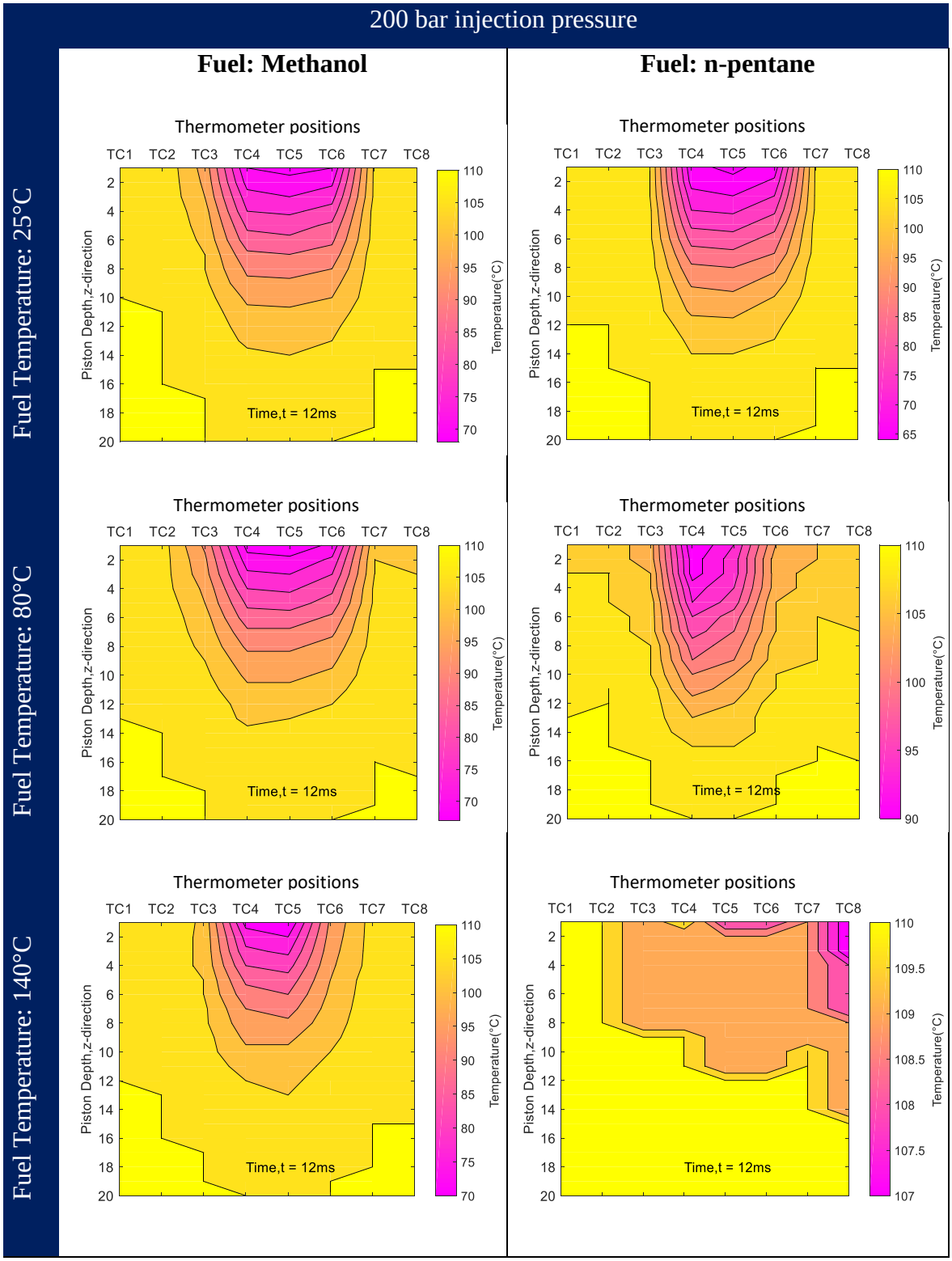


Figure 6.8: 2D heat map result comparisons between methanol and n-pentane pure fuels injected at 200 bar injection pressure and temperatures of 25°C, 80°C and 140°C. The piston surface temperature shown for all are at 110°C. Heat map iteration shown for all are at 12 ms ASOI. Note: 1) z-direction actual distance: 10µm/step 2) x-direction actual distance: 6mm/step

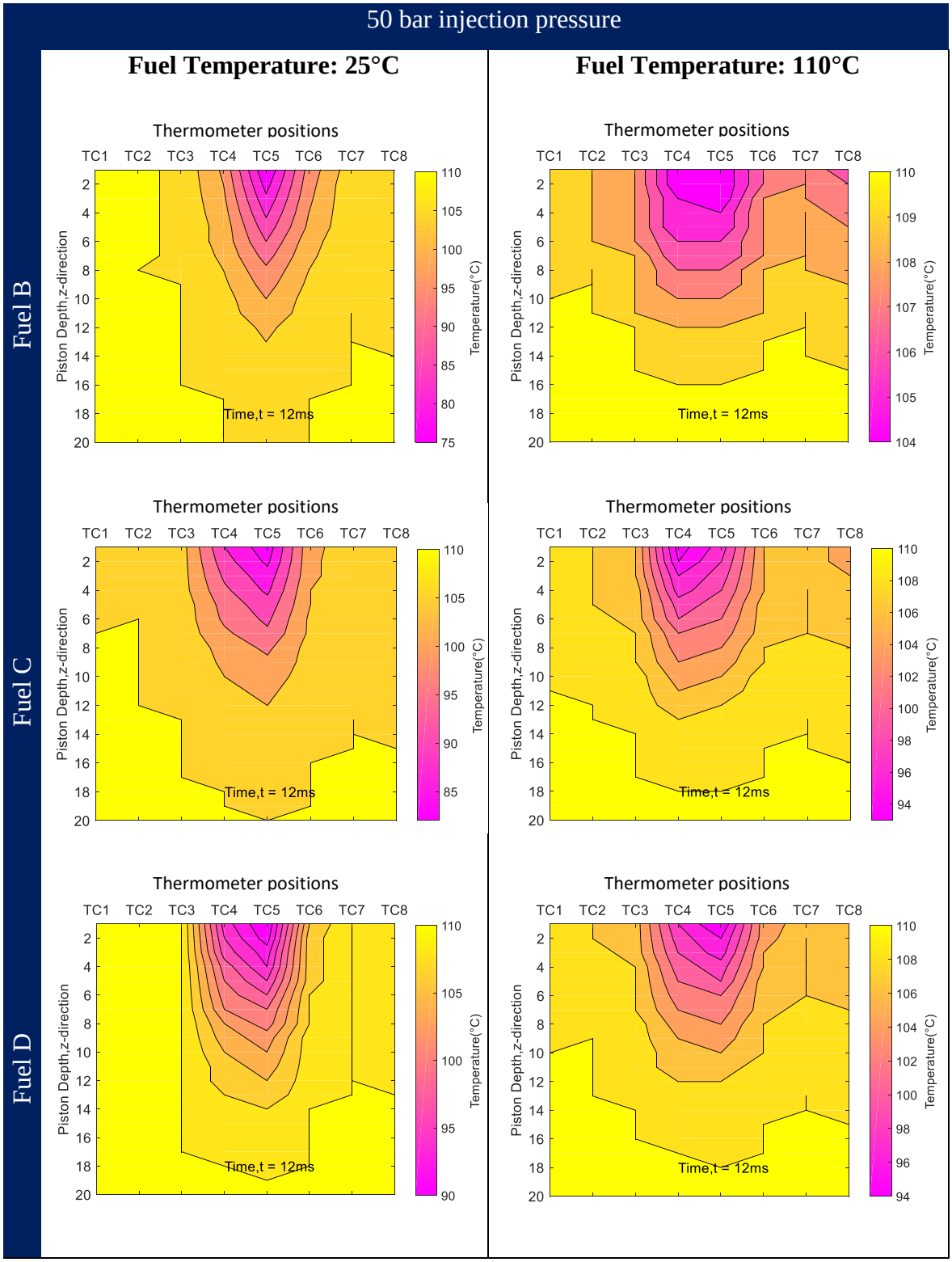


Figure 6.9: 2D heat map result comparisons between Fuel B, Fuel C and Fuel D injected at 50 bar injection pressure and temperatures of 25°C and 110°C. The piston surface temperature shown is at 110°C. Heat map iterations shown for all are at 12 ms ASOI. Note: 1) z-direction actual distance: 10µm/step 2) x-direction actual distance: 6mm/step

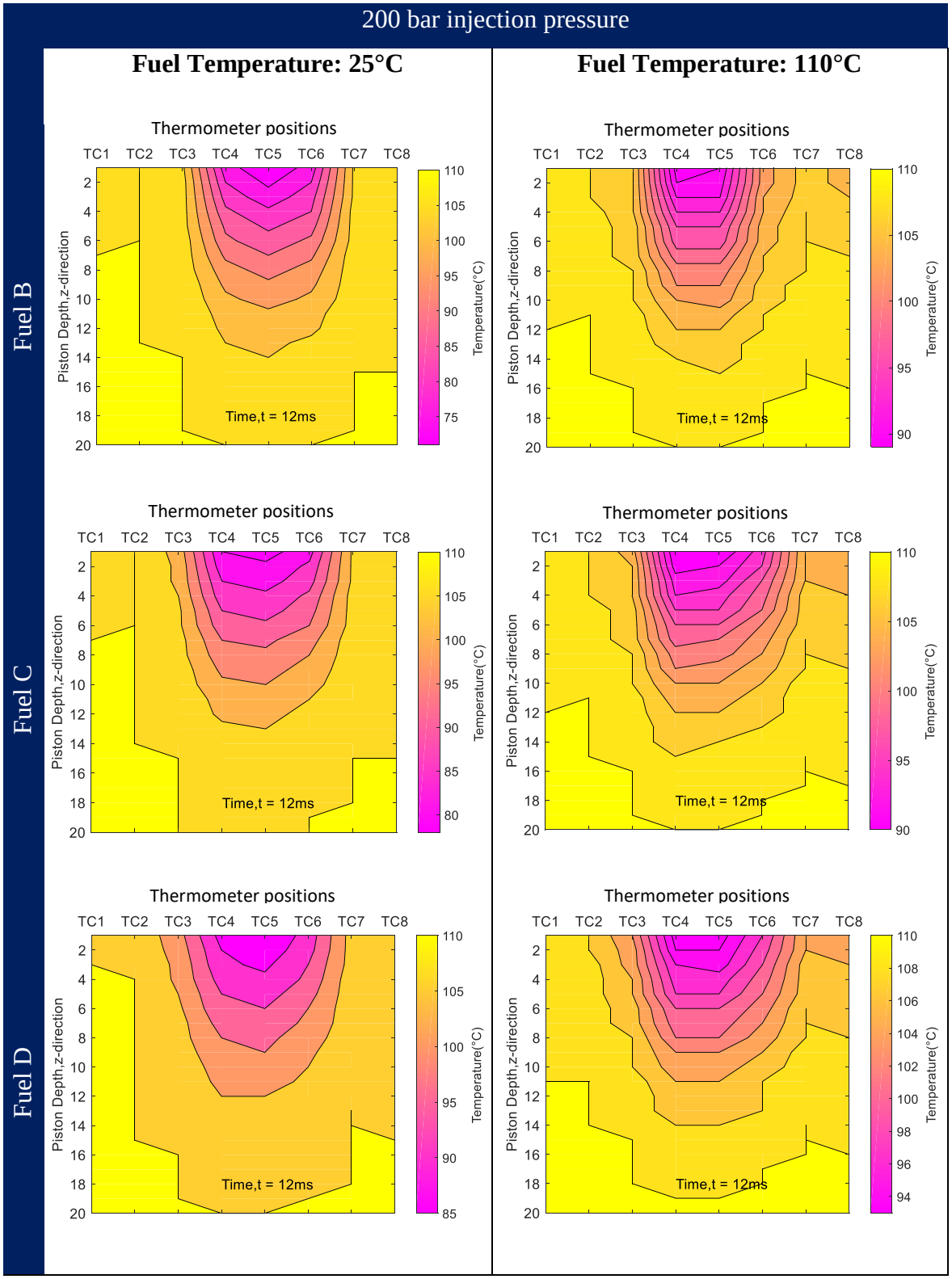


Figure 6.10: 2D heat map result comparisons between Fuel B, Fuel C and Fuel D injected at 200 bar injection pressure and temperatures of 25°C and 110°C. The piston surface temperature shown is at 110°C. Heat map iterations shown for all are at 12 ms ASOI. Note: 1) z-direction actual distance: 10µm/step 2) x-direction actual distance: 6mm/step

6.3.2. 1D and 2D finite difference method calculation validation

The results in Section 6.3.1 were calculated using the finite difference method as described in Section 2.3.2.1. The availability of multiple thermometers on the piston surface which were arranged with equal spacing to each other made it possible to easily apply the finite difference method in a 2D arrangement. Using the finite difference method in 2D can produce different temperature results if there is heat transfer laterally between the nodes.

The best way to validate the necessary analysis was to first do a 1D model to find the penetration depth of each thermal wave. Subsequent to this, use the temperature data to calculate the lateral heat flux value on any of the available nodes. For this case, the lateral heat flux of TC5 to TC6 on the second node in from the surface were calculated and compared when using the 1D and 2D finite difference model. The calculated heat flux against time for the 1D and 2D models is shown in Figure 6.11. From the figure, it can be seen that the difference between the two models was minimal and as a result, the 1D model could have been used for this setup.

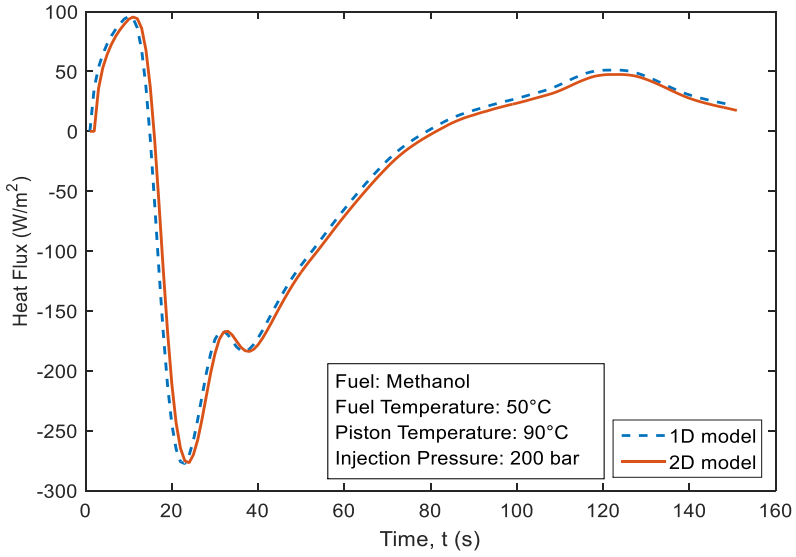


Figure 6.11: Calculated lateral heat flux of TC5 to TC6 comparison using 1D and 2D finite difference models. Plot shows heat flux values of the second node axially from the piston surface.

6.3.3. Comparison of latent heat of evaporation of the pure fuels and mixtures used for the spray impingement experiments.

Latent heat of evaporation of the liquid fuel is one very important factor when determining the effectiveness of surface cooling. Data on the latent heat of evaporation of pure fuels can be found readily in the literature. However, for liquid mixtures, it has to be measured experimentally or be modelled, as hydrocarbon/alcohol mixtures are non-ideal

In section 3.4.1, the usage of UNIFAC as well as the Antoine equation to model vapour pressure, V_P of mixtures against temperature, T has been discussed in depth. Calculating the latent heat of evaporation can be done by expressing the P_{vap} vs T linearly using the Clausius-Clapeyron relation as shown in equation (6.1)

$$\ln P = \frac{-\Delta H_v}{R}\left(\frac{1}{T}\right) + C \qquad (6.1)$$

where ln P is the natural logarithm of the vapour pressure, ΔH_v is the latent heat of evaporation, R is the universal gas constant (8.314 J/K mol), T is the absolute temperature and C is a constant. A plot of ln P vs $1/T$ produces a straight line in which the slope corresponds to $\Delta H_v / R$. Another method of calculating ΔH_v is by using the activity coefficients obtained through UNIFAC to multiply to the individual latent heat of evaporation of pure components , ΔH_{vi} as follows

$$\Delta Hv = \sum_i \gamma_i \Delta H_{vi} \qquad (6.2)$$

assuming that the latent heat ΔH_{vi} of the pure component i is known or may be obtained from the combination of the Clausius-Clapeyron equation and the Antoine equation for the saturation properties. It should be noted that both methods produce identical results as discussed in much detail by Tamir (1982).

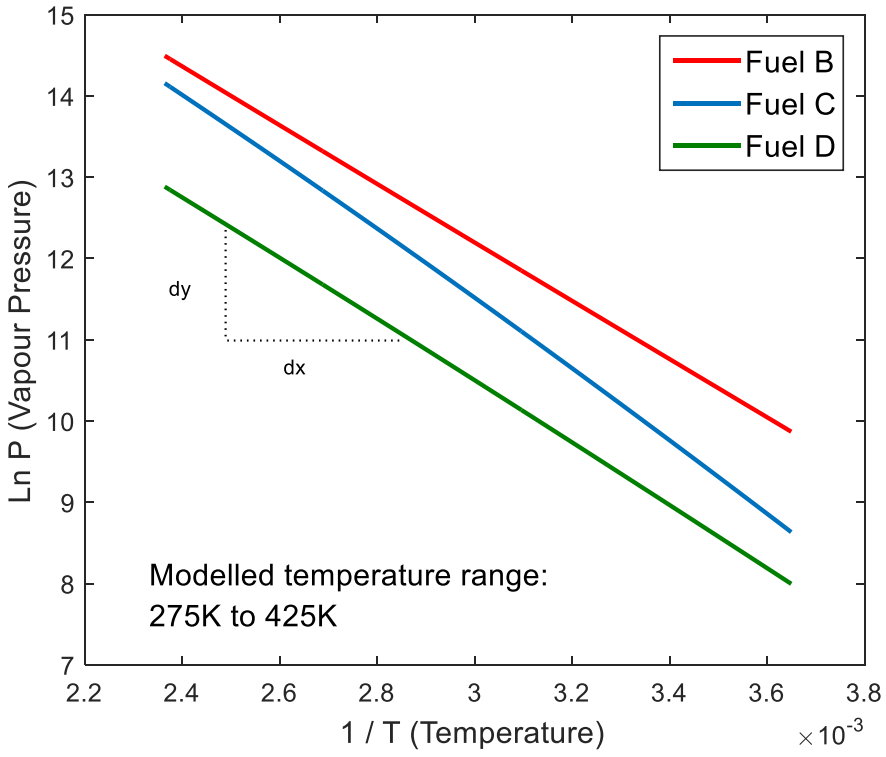


Figure 6.12: Linear plots for expression of P_{vap} vs T to become $ln\ P$ vs $1/T$ for Fuel B, Fuel C and Fuel D

Figure 6.12 shows Ln P vs $1/T$ plot for Fuel B, C and D. As expected and already known from chapter 3, Fuel B is the most volatile, followed by Fuel C and finally the least volatile being Fuel D. As can be seen in Figure 6.12, Fuel C was the least linear compared to Fuel B and D. From this plot, ΔH_v of all fuel mixtures were extracted at each of the particular temperatures used for the spray impingement experiments. The value for ΔH_v was calculated using $\pm\Delta T$ = 1 K of the desired points.

Table 6.2 shows the latent heat of evaporation of pure fuels used for the mixtures of Fuel B, C and D. Although only n-pentane and methanol were used in the spray impingement experiments, the other pure fuels data were calculated using the above method just for understanding each characteristic individually. For a single mol, methanol and n-pentane do not differ significantly in ΔH_v. However, n-pentane has twice the value of molar mass to

methanol which when used at stoichiometric conditions would give different outcome. This can be seen in Table 6.2 where methanol when calculated for 1 kg of fuel showed very high value in ΔH_v, at almost 3 times more than other pure fuels. All of the other pure fuels had very close ΔH_v magnitude which produces very low standard deviation value among them. It can be seen from Table 6.2, for all of the pure fuels, that with the increase in temperature, the ΔH_v magnitude decreases, with n-decane and n-undecane showing the most significant reduction in ΔH_v at the highest temperature, being close to 15% lower than the original value at the coldest condition.

Table 6.2: Modelled and measured latent heat of evaporation values for pure fuels at various temperatures. (*) values obtained from (Vladimír & Svoboda 1985)

Latent Heat of Evaporation ΔH_v (MJ/kg)							
		Pure Fuels					
		methanol	**n-pentane**	**Iso-octane**	**n-decane**	**toluene**	**n-undecane**
Fuel Temperature (°C)	**25°C**	1.16*/ 1.17	0.37*/ 0.38	0.31*/ 0.31	0.36	0.41*/ 0.42	0.36*/ 0.36
	50°C	1.17	0.37	0.30	0.34	0.40	0.34
	80°C	1.15	0.36	0.29	0.33	0.38	0.33
	110°C	1.13	0.36	0.28	0.31	0.37	0.31
	140°C	1.11	0.36	0.27	0.30	0.36	0.30

Table 6.3 shows the latent heat of evaporation of the mixtures of Fuel B, Fuel C and Fuel D calculated at various temperatures. Except for Fuel B, which only slightly changed, Fuel C and D again show a reduction in ΔH_v as temperature was increased. As can be seen from the data in Table 6.3, the Fuel C mixture resulted in having slightly higher ΔH_v than Fuel B and significantly more than Fuel D. Fuel D, without any methanol content, has the lowest

value of ΔH_v at about 30% less than Fuel B and C. Fuel B and Fuel C when compared, have different volatilities but almost similar ΔH_v and as a result will highlight the effectiveness of methanol when flash evaporation occurs. Fuel D having the lowest ΔH_v will act as a control fuel that will highlight the effectiveness of the heavy components (similar amount in Fuel B and C) in spray cooling which will not be affected by any geometry changes when the fuel temperature changes due to its low volatility.

Table 6.3: Modelled latent heat of evaporation for fuel mixtures; Fuel B, Fuel B and Fuel C.

Latent Heat of Evaporation ΔH_v (MJ/kg)				
		Fuel Mixtures		
		Fuel B	**Fuel C**	**Fuel D**
Fuel Temperature (°C)	**25°C**	0.44	0.47	0.30
	50°C	0.44	0.45	0.29
	80°C	0.44	0.44	0.29
	110°C	0.44	0.43	0.29
	140°C	0.44	0.42	0.28

6.4. Piston surface heat flux results

6.4.1. Heat flux calculation of piston surface temperature

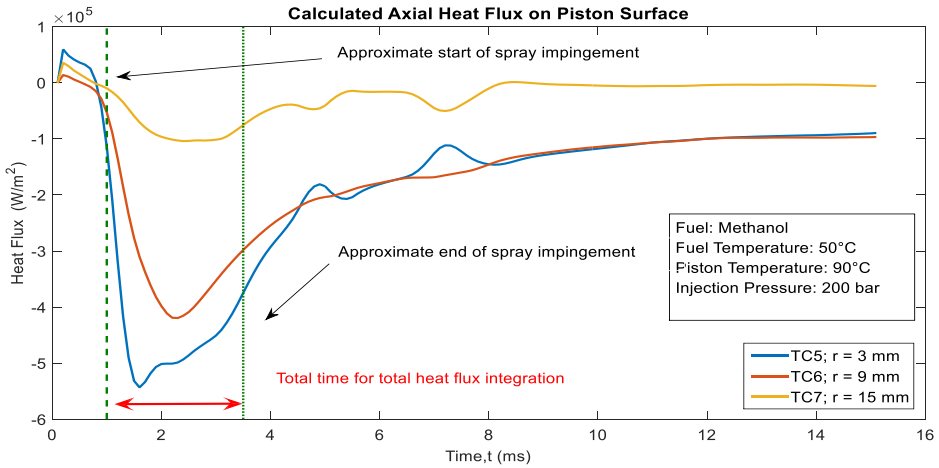


Figure 6.13: heat flux plotted against time that can be integrated to get total heat flow during impingement.

As elaborated earlier in Section 6.2, there were many parameters that were varied for this work and the will give a huge amount of heat flux data. To simplify things, this work will focus on the spray impingement event on the piston surface which signifies when spray cooling happens. To do this, the surface heat flux results (calculated using the finite difference method) will be integrated against time, specifically only during the spray impingement event, as shown in Figure 6.13. The start and end time of spray impingement has been carefully selected with the help of high speed images. Furthermore, a buffer of two frames before and after spray impingement were included to the total time for integration. This will result in the total heat energy exchange on the piston surface.

Figure 6.13 shows the calculated axial surface heat flux from one of the experiments using pure methanol. As shown in Figure 6.13, three thermometers have been selected; TC5, TC6 and TC7. This is to include the possible factor of spray angle widening due to spray flash boiling which will distribute the fuel mass more laterally. The total heat energy results are plotted, compared and discussed in section 6.4.2.

6.4.2. Total energy exchange calculation during impingement period

6.4.2.1. Pure fuels comparisons

In the previous section, the description of obtaining the total heat energy from the spray impingement experiments has been discussed. Heat flux data from all fuels were used to obtain the total energy exchange during spray impingement events. In this section, firstly the pure methanol and n-pentane results are discussed. Figures 6.14, 6.15, 6.16, 6.17, 6.18 and 6.19 are plots of n-pentane *versus* methanol. These figures differ in injection pressures as well as the surrogate piston distance from the injector tip.

All of these figures share the same plotting method. There are two y-axes in each plot: Total heat energy removed or added, and measured spray angle of the single plume. In the x-axis, each tick tells the temperature of the fuel (labelled 'F') as well as the piston surface (labelled 'P'). The x-axis ticks alternate between 30°C and 110°C piston surface temperature while fuel temperature increases as the results progress to the right. Only two surface temperatures were shown in the plots as only these different extreme temperatures should potentially show any significant change in the heat transfer. The total heat energy values are plot using stacked bars, in which there are three colour gradients for each fuel. The darkest colour signifies the closest thermometer to the centre of the surrogate piston while the lightest is the furthest.

These are the following observation from all of the plots in this section that compares the effectiveness of spray cooling when using pure n-pentane and methanol:

1. Methanol removes more heat from the surrogate piston when the piston surface has a high temperature of 110°C, while n-pentane consistently removes more heat from the surrogate piston when the piston surface has a low temperature of 30°C. This happens at all cases of injection pressure and injector distance. One of the reasons for this to

happen is due to the much lower latent heat of evaporation of n-pentane as compared to methanol (Table 6.2) which causes evaporation to be much faster on hot surfaces. On a cold surface, on the other hand, surface cooling is more dependent on a fuel with a much lower boiling point and gains from evaporative cooling.

2. A higher injection pressure causes more heat to be removed from the piston surface for both fuels. This is due to more fuel mass being injected at a higher pressure. However, above the saturation temperature (possibly with flash boiling), n-pentane was less effective in surface cooling due to its inability to travel far to cause impingement on the piston surface. At an injection pressure of 50 bar, n-pentane was ineffective at 80°C (seen in Figure 6.15) while for 100 bar and 200 bar this only at 110°C (seen in Figure 6.17 and 6.19).
3. Since the impact of the spray plume was targeted at the centre of the piston diameter, R = 3 mm, in general, experiences the most heat removal for all cases. However, heat removal from the piston surface was much higher at R = 9 mm, for the case when the piston distance to the injector tip was at 75 mm instead of 50 mm. An increase in piston distance produced a spray with a slightly wider impact surface area, especially when there's flash boiling (compare Figure 6.16 to Figure 6.17).
4. Observations from the high piston surface temperature results, show that the heat removal magnitude for methanol has only <10% reduction at every 30 K increase in fuel temperature. However, a monotonic reduction of heat energy magnitude can be seen for n-pentane from the coldest fuel temperature to the hottest as shown in Figure 6.17 and Figure 6.19. Methanol, even at conditions where fuel temperature was higher than the piston surface temperature still managed to remove heat from the piston surface. Other than as a result of having high latent heat of evaporation, methanol liquid droplets travelled further to cause impingement, unlike n-pentane. This can be seen when

comparing the high-speed images of Figure 6.2 and Figure 6.3 in previous section. N-pentane effectiveness was very dependable on its spray characteristics which change with fuel temperature.

5. For all cases, methanol consistently produces a much larger spray angle than n-pentane. The significant increase in spray angle for methanol can be seen to begin when the temperature increases from 80°C to 110°C, with an increase from about 5° to about 15°. This however did not seem to impact the effectiveness of cooling for R = 9 mm and R = 15 mm. The magnitude of total heat energy removed from R = 3 mm remains the highest for all fuel temperatures. The n-pentane results did show, for some conditions, a more equal distribution of heat removal across the three thermometers, especially at a fuel temperature of 80°C (transitional flash boiling). This can be seen in Figure 6.14, Figure 6.16 and Figure 6.18.

These pure fuel experimental results will be interesting to be compared to when they are used as mixtures in the next set of experiments. The individual characteristics of these fuels when at flash boiling conditions will definitely affect the spray differently in mixtures depending on their percentage in the composition.

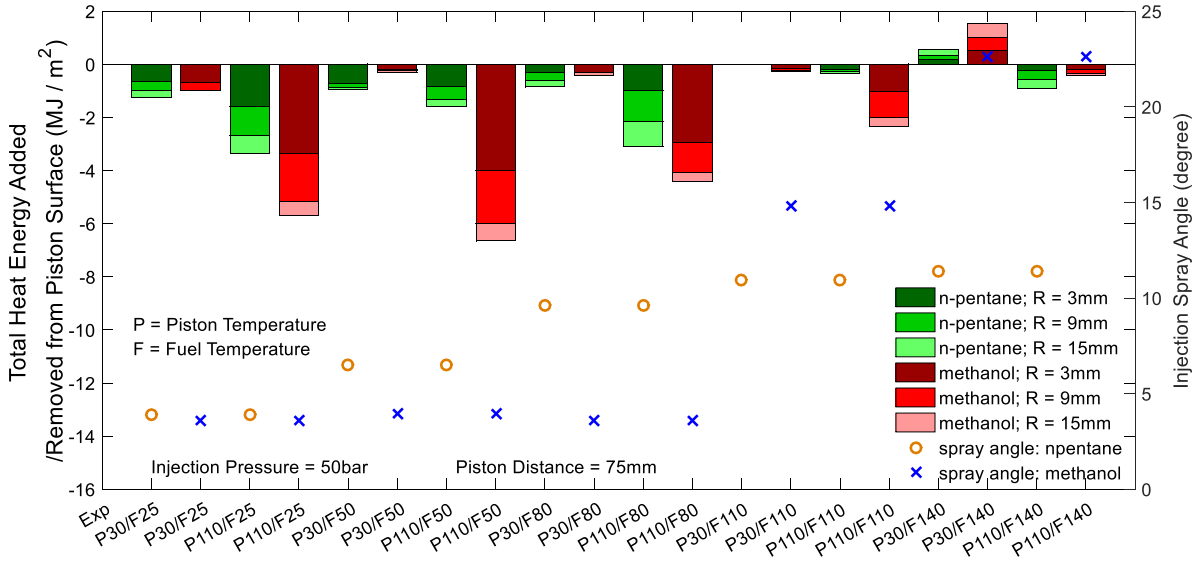


Figure 6.14: Comparisons of total heat energy added or removed from the piston surface at temperatures of 30°C and 110°C during a single jet impingement event. Fuels compared here are n-pentane and methanol injected at a pressure of 50 bar and at 75 mm from the piston surface. The darkest colour gradient represents the nearest thermocouple to the centre of the piston while the lightest is the furthest. The markers in the plot show various spray angles of the spray plume at different fuel temperatures.

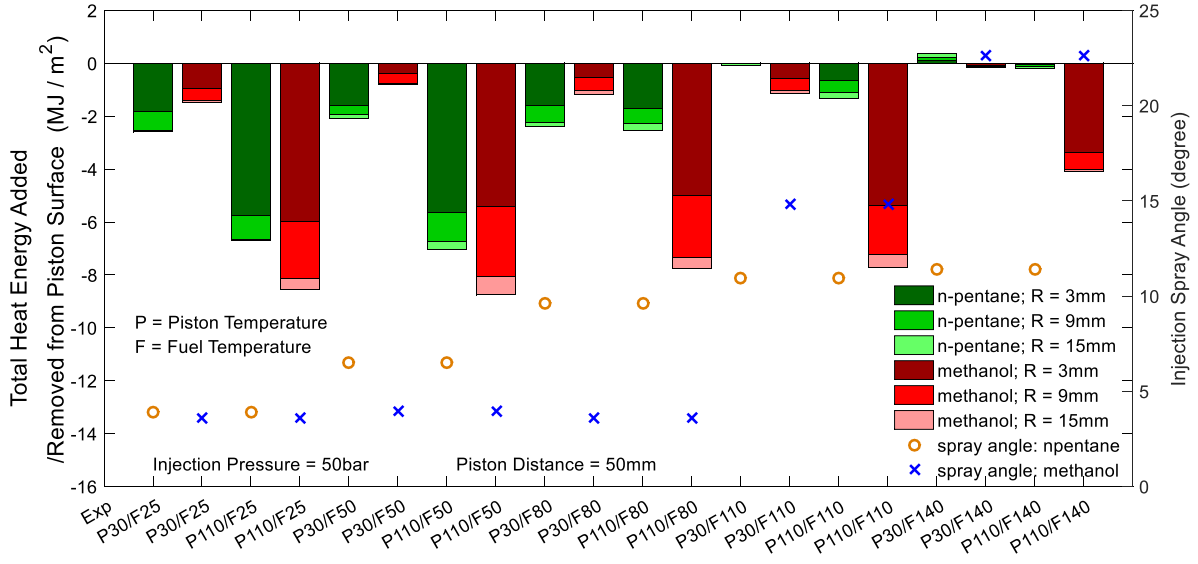


Figure 6.15: Comparisons of total heat energy added or removed from the piston surface at temperatures of 30°C and 110°C during a single jet impingement event. Fuels compared here are n-pentane and methanol injected at a pressure of 50 bar and at 50 mm from the piston surface. The darkest colour gradient represents the nearest thermocouple to the centre of the piston while the lightest is the furthest. The markers in the plot show various spray angles of the spray plume at different fuel temperatures.

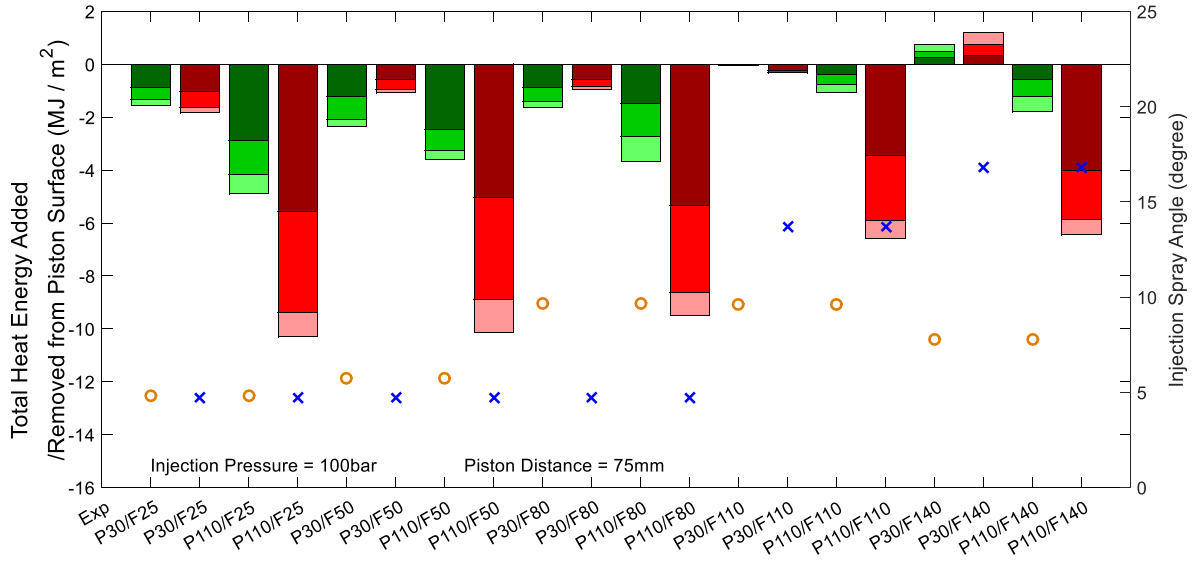


Figure 6.16: Comparisons of total heat energy added or removed from the piston surface at temperatures of 30°C and 110°C during a single jet impingement event. Fuels compared here are n-pentane and methanol injected at a pressure of 100 bar and at 75 mm from the piston surface. The darkest colour gradient represents the nearest thermocouple to the centre of the piston while the lightest is the furthest. The markers in the plot show various spray angles of the spray plume at different fuel temperatures.

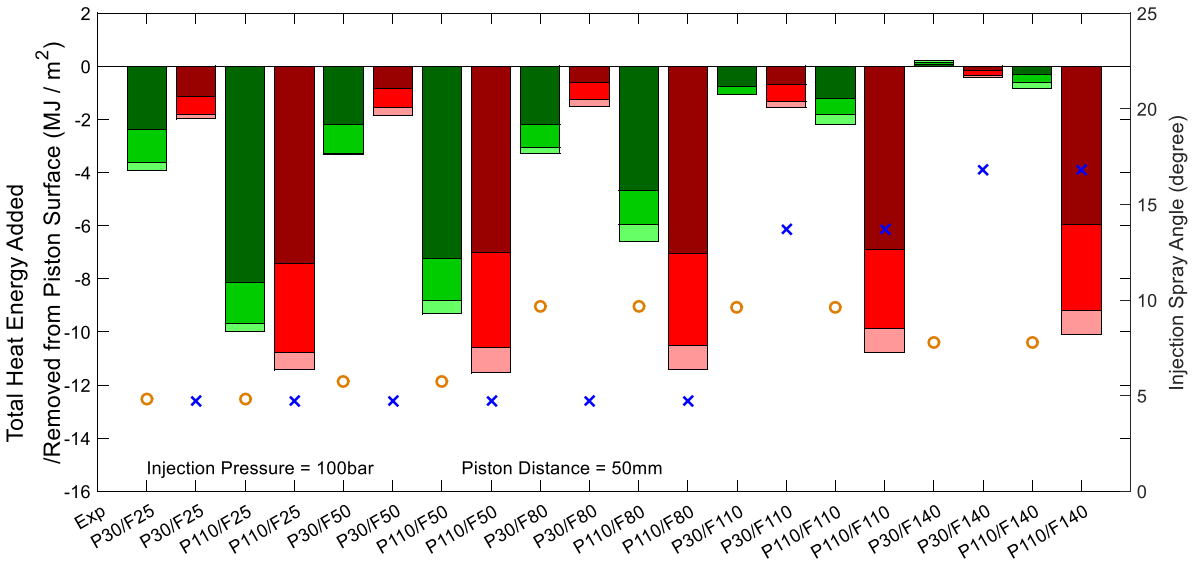


Figure 6.17: Comparisons of total heat energy added or removed from the piston surface at temperatures of 30°C and 110°C during a single jet impingement event. Fuels compared here are n-pentane and methanol injected at a pressure of 100 bar and at 50 mm from the piston surface. The darkest colour gradient represents the nearest thermocouple to the centre of the piston while the lightest is the furthest. The markers in the plot show various spray angles of the spray plume at different fuel temperatures.

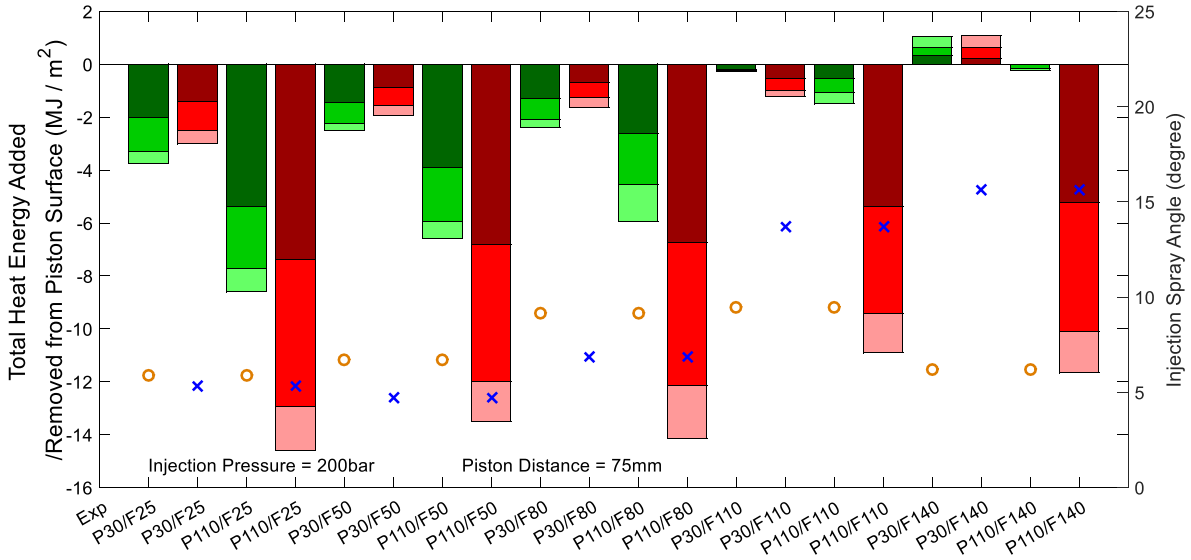


Figure 6.18: Comparisons of total heat energy added or removed from the piston surface at temperatures of 30°C and 110°C during single jet impingement event. Fuels compared here are n-pentane and methanol injected at a pressure of 200 bar and at 75 mm from the piston surface. The darkest colour gradient represents the nearest thermocouple to the centre of the piston while the lightest is the furthest. The markers in the plot show various spray angles of the spray plume at different fuel temperatures.

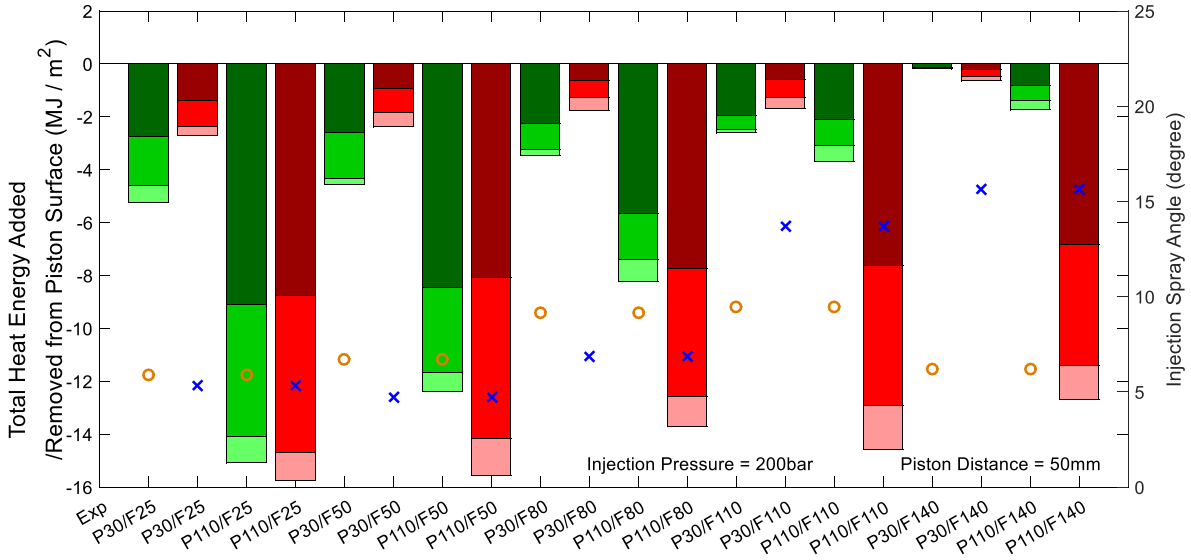


Figure 6.19: Comparisons of total heat energy added or removed from the piston surface at temperatures of 30°C and 110°C during a single jet impingement event. Fuels compared here are n-pentane and methanol injected at a pressure of 200 bar and at 50 mm from the piston surface. The darkest colour gradient represents the nearest thermocouple to the centre of the piston while the lightest is the furthest. The markers in the plot show various spray angles of the spray plume at different temperatures.

6.4.2.2. Mixture comparisons

In this section, the results for the total heat energy exchange during spray impingement for fuel mixtures are discussed. The method for results plotting is similar to that in section 6.4.2.1. The varied parameters also remained the same (i.e injection pressure, piston distance, fuel temperature, surface temperature) as in section 6.4.2.1 except for the fuel used. The fuels used for comparison in this investigation were Fuel B, Fuel C, Fuel D and the Euro 5 gasoline. The results for all parameter variations have been plotted in Figures 6.20, 6.21, 6.22, 6.23, 6.24 and 6.25. The overall observations and discussion for these plots are as follows:

a) As expected the 50 bar injection pressure produced the lowest magnitude of heat flow as compared to the 100 bar and 200 bar injection pressure, due to a much lower fuel mass that impinged on the piston surface. As can be seen in Figure 6.20, no specific trends can be seen from these results, possibly because of the difficulty of the spray to maintain its plume geometry when fuels droplets are travelling at a much lower velocity regardless of any fuel temperature. Again, similar to the previous results from single components, the heat removed was obviously more for the heated piston surface temperature than the non-heated one.

b) At all injection pressures, and for both the 30°C as well as the 110°C piston surface temperature, it can be seen that for a piston distance of 75 mm, the magnitude difference in the heat flow was less distinct when comparing each fuel. At 50 mm piston distance, the heat energy magnitude of Fuel B and Fuel C were significantly higher than Fuel D and the Euro 5 gasoline. However, this only happens for fuel temperatures below 80°C which is sub-saturation for Fuels B and C. One of the reasons why Fuel B and Fuel C were removing more heat was due to them being significantly more volatile than Fuel D, despite having small differences in latent heat of evaporation which improves the

evaporative cooling. The total mass of Fuels B and C that evaporated from the hot piston surface were much higher specifically during the injection event than with Fuel D. This can be seen in Figure 6.23, where the magnitude of heat removed at R = 3 mm for the same temperature conditions were higher for Fuels B and C, while being not much different at R = 9mm or R = 15 mm. As discussed in section 6.4.2.1, the effect of distance was significant, due to the ability of the fuel to travel further. In the case of the mixtures, this point is further strengthened when Fuel B, Fuel C and Fuel D were giving out similar results for all temperatures above 80°C, as seen in Figure 6.25.

c) It can also be seen in Figure 6.23 and 6.25 that Fuel C removes slightly more heat than Fuel B, despite being the more volatile one. One possible reason for this is as shown in Table 6.3; Fuel C has almost similar value of latent heat of evaporation to Fuel B but being less volatile allows more fuel mass to travel and escape evaporation to finally impinge on the piston surface. This also shows that below the saturation temperature, the different compositions lead to a greater difference in heat flow when there is a shorter distance from the injector tip to the piston surface. This is due to the behaviour of all the components, especially the ones with a low boiling point (i.e. n-pentane), to travel together through the spray plumes and finally impact on the surface. This would also suggest that for sprays above the saturation temperature, the fuel mass that manages to impinge on the piston surface will only comprise the heavy components, since the fuels tested in this experiment share the same 40% by volume of heavy components. As a result, the heat removed in tests above the saturation temperature were very similar for Fuel B and Fuel C to Fuel D and the Euro 5 gasoline. However, there is also a spray geometry factor that can cause slight variations when the lighter fuels such as Fuels B and C flash boil.

d) For the case of a cold surface temperature, at 30°C and for both piston distances, Fuels C and D show a very monotonic decrease in heat removal from the coldest fuel temperature to the hottest. However, Fuel B did not show a consistent trend. At temperatures of 110°C and 140°C, at all injection pressures and distances, Fuel B added thermal energy to the piston surface instead of its removal. Other than that, at these temperatures, due to the flash boiling phenomena, equal heat addition (i.e Figure 6.22 and 6.24) distribution can be seen on the TFGs for the three different locations. At superheated temperatures, the early evaporation of the lighter components (i.e Fuel B) during flash boiling leaves more heavy fuel components behind that have resulted in similar heat flow magnitude when comparing all three fuel mixtures.

These heat transfer results give a better understanding of how different fuel characteristics might potentially affect the production of particulate matter. The fundamental issue with piston surface cooling was an unevaporated fuel film as a result of spray impingement, that subsequently creates diffusion flames during the combustion event. In this section, the effects of injection pressure, distance and fuel composition have been explored to find correlation to the production of particulate matter in a GDI engine. However, one parameter remained untested which is the availability of time for fuel evaporation which could be a significant factor that may overrule some findings here.

As proven in Chapter 5, fuel with a high volatility alone does not guarantee good air fuel mixing to help reduce particulate matter emissions. One conclusion that can be drawn from the results in this section is that the heavy components will dominate the final outright heat exchange at the piston surface while the lighter components contribution is very dependable on various other factors (i.e. spray geometry, fuel temperature). These factors were shown to have a minimal influence at low fuel temperature operation but the opposite at superheated conditions.

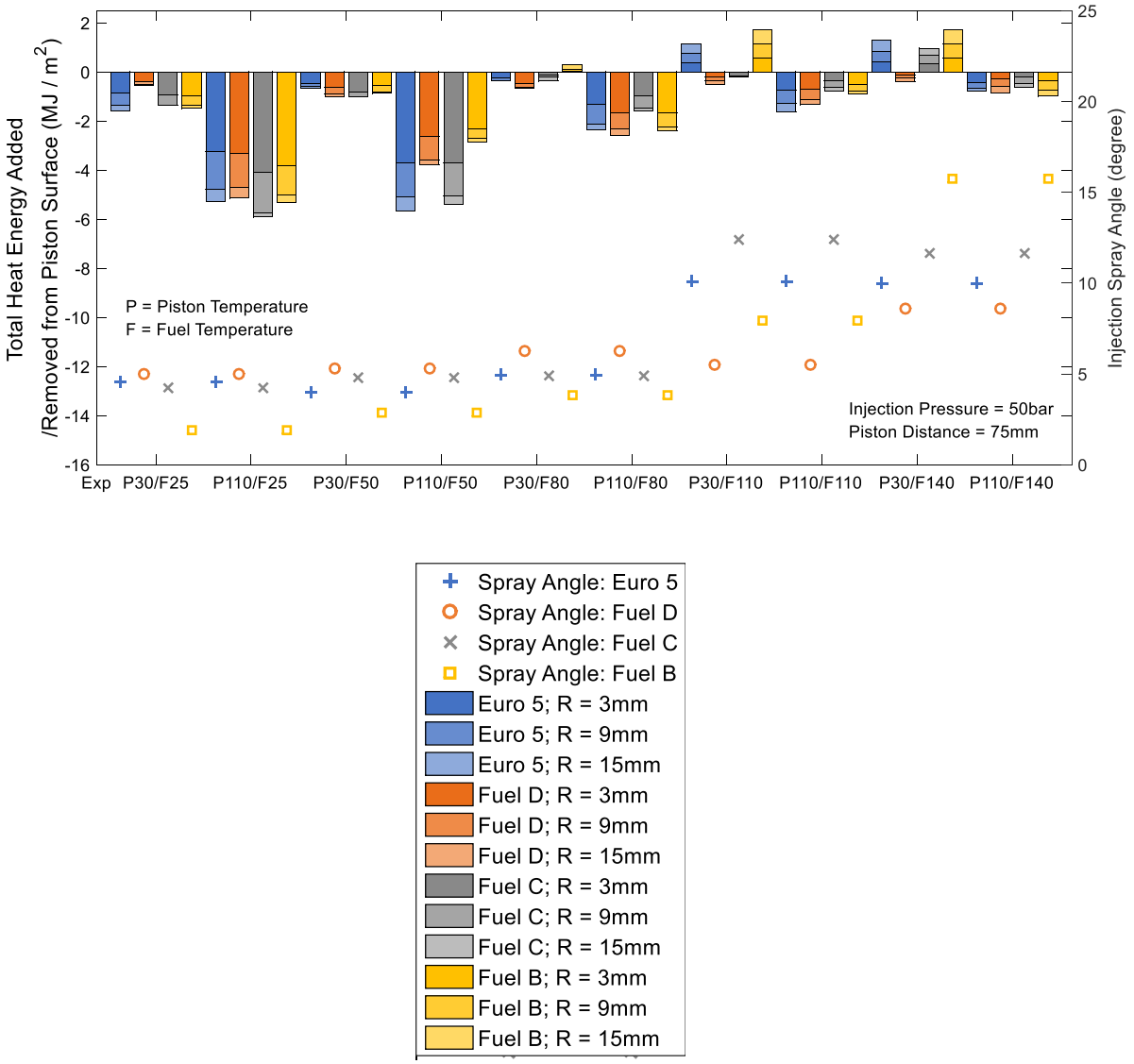


Figure 6.20: Comparisons of total heat energy added or removed from the piston surface when heated to temperatures of 30°C and 110°C during a single jet impingement event. Fuels compared here are Fuel B, Fuel C, Fuel D and Euro 5; injected at pressure of 50 bar and 75 mm from the piston surface. The darkest colour gradient represents the nearest thermometer to the centre of the piston while the lightest is the furthest. The markers in the plot show the spray angles of the spray plume at different tested fuel temperatures.

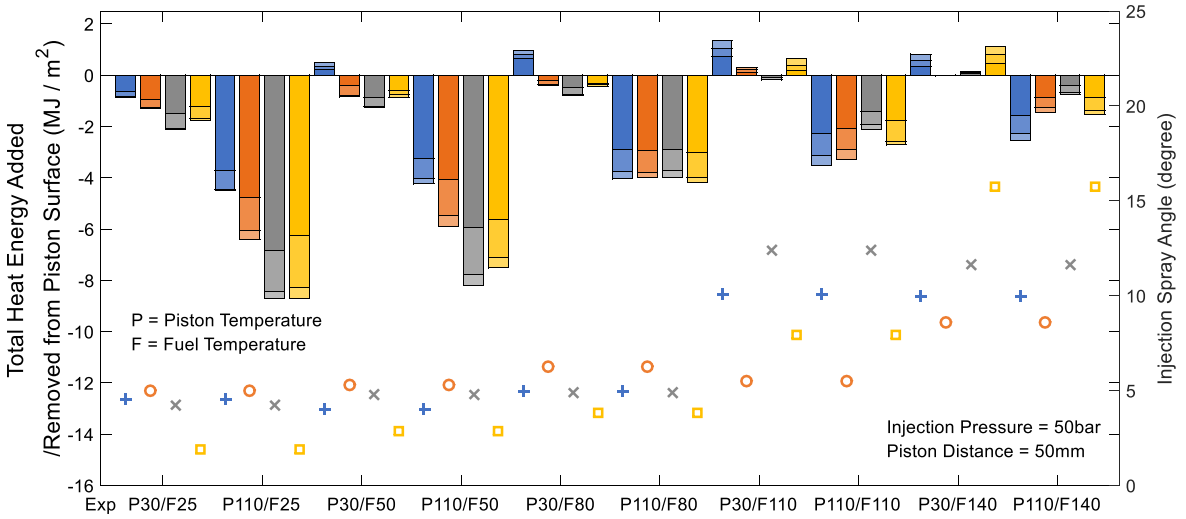


Figure 6.21: Comparisons of total heat energy added or removed from the piston surface when heated to temperatures of 30°C and 110°C during a single jet impingement event. Fuels compared here are Fuel B, Fuel C, Fuel D and Euro 5; injected at pressure of 50 bar and at a distance of 50 mm from the piston surface. The darkest colour gradient represents the nearest thermometer to the centre of the piston while the lightest is the furthest. The markers in the plot show the spray angles of the spray plume at different tested fuel temperatures.

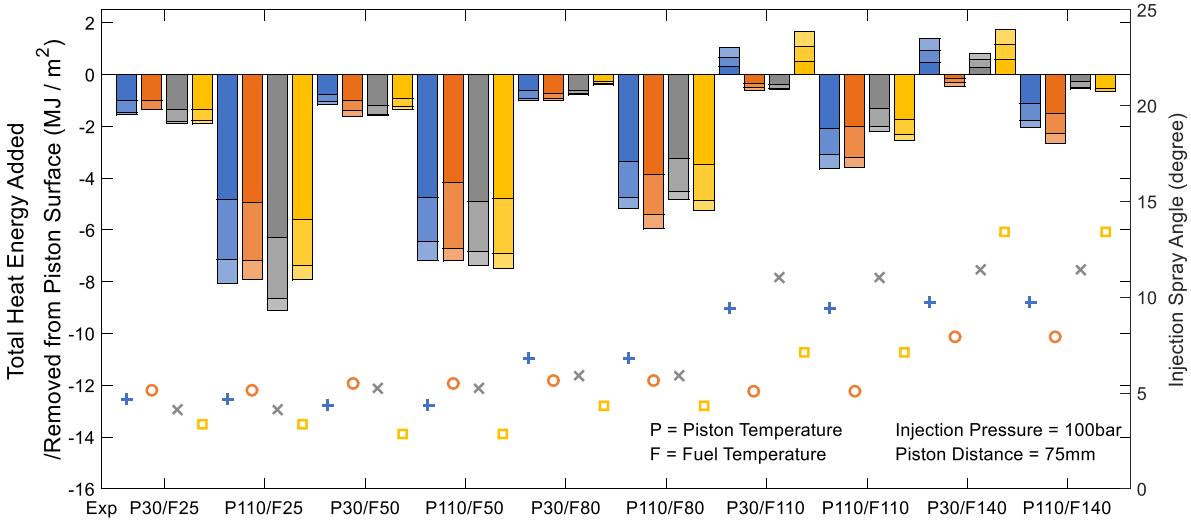


Figure 6.22: Comparisons of total heat energy added or removed from the piston surface when heated to temperatures of 30°C and 110°C during a single jet impingement event. Fuels compared here are Fuel B, Fuel C, Fuel D and Euro 5; injected at pressure of 100 bar and at a distance of 75 mm from the piston surface. The darkest colour gradient represents the nearest thermometer to the centre of the piston while the lightest is the furthest. The markers in the plot show the spray angles of the spray plume at different tested fuel temperatures.

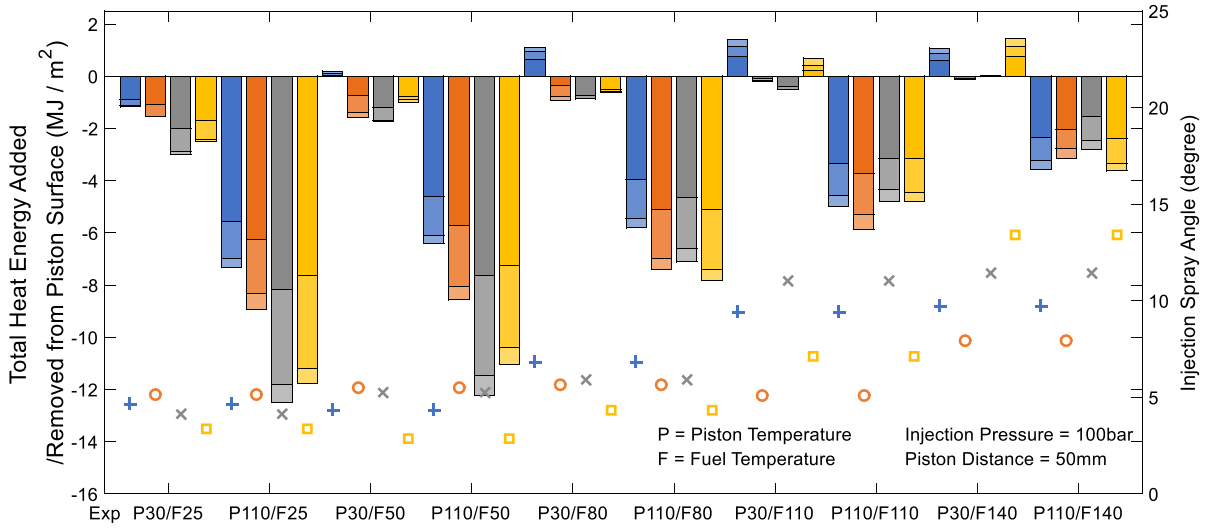


Figure 6.23: Comparisons of total heat energy added or removed from the piston surface when heated to temperatures of 30°C and 110°C during a single jet impingement event. Fuels compared here are Fuel B, Fuel C, Fuel D and Euro 5; injected at pressure of 100 bar and at a distance of 50 mm from the piston surface. The darkest colour gradient represents the nearest thermometer to the centre of the piston while the lightest is the furthest. The markers in the plot show the spray angles of the spray plume at different tested fuel temperatures.

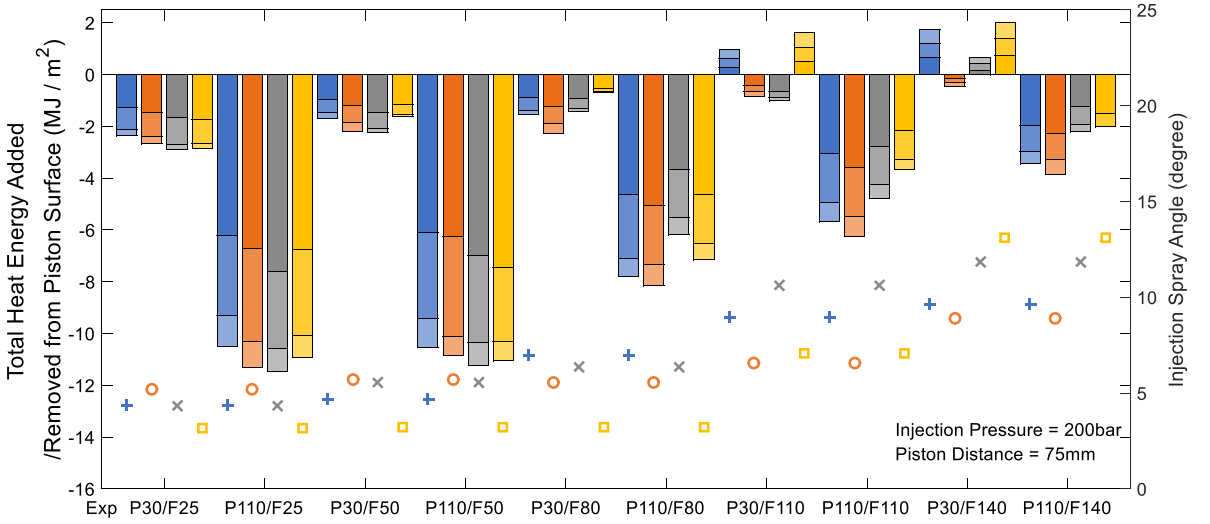


Figure 6.24: Comparisons of total heat energy added or removed from the piston surface when heated to temperatures of 30°C and 110°C during a single jet impingement event. Fuels compared here are Fuel B, Fuel C, Fuel D and Euro 5; injected at pressure of 200 bar and at a distance of 75 mm from the piston surface. The darkest colour gradient represents the nearest thermometer to the centre of the piston while the lightest is the furthest. The markers in the plot show the spray angles of the spray plume at different tested fuel temperatures.

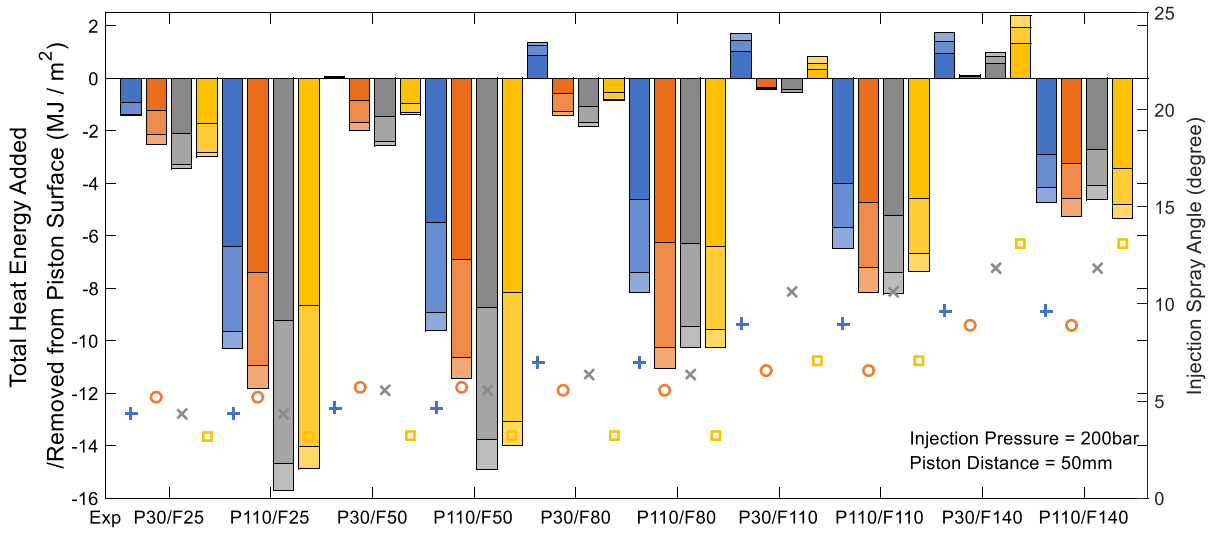


Figure 6.25: Comparisons of total heat energy added or removed from the piston surface when heated to temperatures of 30°C and 110°C during a single jet impingement event. Fuels compared here are Fuel B, Fuel C, Fuel D and Euro 5; injected at pressure of 200 bar and at a distance of 50 mm from the piston surface. The darkest colour gradient represents the nearest thermometer to the centre of the piston while the lightest is the furthest. The markers in the plot show the spray angles of the spray plume at different tested fuel temperatures.

6.5. Chapter summary

This Chapter begins with the objective to investigate a single plume spray impinging on a surrogate piston. Several parameters and fuels have been identified from previous experiments on the optical engine to be used here. The first set of results presented were the high-speed images of the injection together with spray impingement events. This was then followed by 2D heat maps for the piston surface that were calculated using the finite difference method. The heat map results, as well as the high-speed images, give a better visualization of where the spray impact on the TFGs and how different characteristics of the spray geometry output different cooling patterns.

The chapter continues with the findings of latent heat of evaporation of the three modelled fuels which was essential for explaining the results of heat exchange during spray impingement. Using the vapour pressure plot against temperature results obtained using the UNIFAC method, the latent heat of evaporation was derived by using the Clausius-Clapeyron equation.

Following this, the total heat energy calculation method was then explained. This was meant to simplify the data to focus on only during the injection event and not any other period. First, the pure fuel results of methanol and n-pentane were compared. It was found that n-pentane can be ineffective on surface cooling when at superheated conditions, due to the inability of the spray to travel much further to cause impingement while this was not the case for methanol. One of the main finding was that, at cold fuel temperatures (disregarding any changes in spray geometry), methanol was very effective in cooling hot surface during impingement (due to the high latent heat of evaporation) whereas for the cold surface, n-pentane was more effective (due to having a much lower boiling point).

The second part of the experiment covers spray impingement tests using the model fuel mixtures. These experiments were meant to investigate the cooling behaviour of the non-ideal mixtures when subjected to spray impingement. From the results, it was found that certain fuels produced higher surface cooling magnitudes when the piston surface was closer to the injector tip. This however only happens for sub-saturation fuel temperatures. This would suggest that even at the transitional flash boiling, the lighter components evaporate much faster leaving behind only the heavy components for the impingement event. A closer look at this condition shows a very similar heat exchange magnitude for all three fuel mixtures (which were deliberately modelled to have a similar percentage of heavy components).

Upon observation of the results, it was found that flash boiling in mixtures changes significantly the capability of the fuel to be effective in surface cooling due to a number of factors. The findings in this chapter makes the particulate matter results in Chapter 5 much more relevant. However, the element of 'available time to evaporate' when fuel mixing in a GDI engine was not explored and could actually have a much more significant influence.

7. Conclusions and Further Work

7.1. Conclusions

GDI engines are foreseen to dominate the midsize and large gasoline engine market in the near future by replacing the ever popular PFI. The smaller sized gasoline engines will however still be dominated by PFI engines due to its simplicity, that leads to cheaper manufacturing cost. Despite the superiority of the GDI engines with their low fuel consumption as well as low CO2 emissions, this engine emits high levels of particulate matter emissions which can be very harmful to human respiratory system. The current GDI engines that are in use may not have been optimized to emit reduced amounts of particulate matter.

With the enforcement of Euro 6 regulations, manufacturers are looking into many different factors in the combustion system to manage the emissions without compromising other important requirements such as power and thermal efficiency. This includes using oxygenated fuels, which have previously been proven in other engines types, and managed to reduce particulate emissions, due to the availability of additional oxygen molecules which acts as a precursor to combustion. However, without a proper injection strategy, directly injecting oxygenated fuels into a combustion chamber can instead cause more severe particulate emission due to their different thermochemical properties. Air fuel mixing with oxygenated fuels has also become more challenging with the introduction of boosting which increases the air density in the chamber. These issues have been explored in this thesis with the following findings and conclusions.

7.1.1. Oxygenated gasoline mixtures modelling and validation

Oxygenated gasoline can be highly beneficial when used in an ICE due to the availability of oxygen molecules that increase the completeness of combustion. Oxygenated gasoline however has a non-ideal behaviour which may lead to different evaporation characteristics. Vapour pressure modelling, as well as evaporation modelling, using the UNIFAC method were essential and have been used to model various M15 gasolines with independent control on volatility. Validation of the M15 mixtures was done using an RVP type apparatus. Vapour pressure of the mixtures at various temperatures were compared against the model. The results show close agreement of the experimental data to the model, which give confidence to the establishment of the saturation pressure ratio as a tool for correlation in spray characterisation.

7.1.2. Establishment of saturation pressure ratio for flash boiling stage identification

The establishment of saturation pressure ratio in this work, simplifies the identification of a fuel spray at various different conditions (i.e ambient pressure, fuel temperature, fuel volatility), be it for a multi-hole injector or a single jet injector. Due to the usage of multiple apparatus (i.e. optical engine and spray rig) that can operate at different ambient pressures, the saturation pressure ratio was used identify the correct operating temperature for each fuel.

7.1.3. Importance of spray characterisation of model fuels on spray rig

The spray characterisation exercise on the model fuels was conducted on the spray rig to identify different spray geometries at different spray conditions and fuel temperatures.

With the knowledge of saturation pressure ratio for each fuel, it was easy to categorise spray geometries at different saturation pressure ratios regardless of the fuel volatility. The high speed imaging of the spray geometry at various conditions gave an in-depth understanding of how the spray will behave in the engine. From these experiments, the spray geometry change stages (i.e. non-flash boiling, transitional flash boiling and flare flashing) were identified. Other than that, it was found that fuel composition did not have major influence on the spray geometry for fuels compared at the same saturation pressure ratio.

For this work, a 6 hole spray guided injector was used. The measurements of spray tip penetration have shown that flash boiling causes the spray to travel further than when at non-flash boiling, due to the collapse of the multi-hole injector plumes to form a single bulk spray. This contradicts with some of the findings in the literature where normally, flash boiling would reduce the travel of the spray plume. This would only happen if there was no coalescing of the spray plumes. The shortest spray tip penetration was identified when the saturation pressure ratio was at the transitional flash boiling condition. The differences in spray behaviour were significant when correlating the engine particulate matter results.

7.1.4. The impact of in-cylinder pressure on fuel evaporation

The optical engine used in this research is representative of spray-guided GDI engines available in the market. It was used to obtain a good understanding of how in-cylinder pressure might influence the fuel spray behaviour and the evaporation rate at different injection timings. In-cylinder pressure can provide vital information to an engine map calibrator when for example, optimizing particulate matter emissions. As discussed in section 1.2.4.2, flash boiling has been known to be introduced deliberately to obtain good

fuel atomization. Therefore, a comparison of in-cylinder pressure between a boosted engine and a natural aspirated engine was made in this research, to study what the impact would be.

It was found that the boosted conditions would give a narrower window of opportunity than a natural aspirated for flash boiling to occur at injection. This is due to the rapid rise in in-cylinder pressure (high intake air volume) at slightly after the start of the intake valve opening. As a result, injection would have to occur much earlier to be in the sub-atmospheric window but at the expense of very close proximity of the injector tip to the piston surface. Injecting late (or a conventionally adopted timing), gives a greater spray distance but on the other hand would result in the spray experiencing a high back pressure (being above atmospheric pressure) that will reduce the evaporation rate. This problem, coupled with the need to inject more fuel mass for an oxygenated gasoline (due to its lower calorific value) and higher air volume density per cycle leads to a longer injection duration that can cause significant problems such as wall wetting or surface cooling when trying to control particulate matter emissions.

7.1.5. Particulate matter correlation towards different spray characteristics

The use of saturation pressure ratio to characterise spray behaviour has enabled a correlation to be made for particulate matter emissions. With the help of the model fuels, it was found that fuel volatility in itself was more significant in determining the trend for particulate number production. A clear segregation on particulate numbers produced were seen when comparing the model fuels. Another conservative conclusion to this experiment is that the introduction of flash boiling seemed to reduce the size of the particulates produced from the optical engine rather than the particulate numbers. However, in the engine

experiments, it was very difficult to segregate the total effectiveness of flash boiling in promoting evaporation when the spray impinges on the piston surface.

The variations of conditions in the engine, as well as fuel properties, managed to show different particulate matter emissions that can be clearly seen to have been affected by the change in spray characteristics. From these results, the non-flash boiling stage, transitional flash boiling stage and flare flashing stage produced very different particulate mass emissions, which indicates the major influence of spray geometry. It was only the 250°BTDC injection timing that enabled full spray development with minimal impingement. However, at this injection timing, the time left for fuel evaporation had become shorter and would not be directly comparable to the tests at 280°BTDC and 310°BTDC). Regardless of this, at 250°BTDC, there was no sudden significant changes in particulate matter emission when the pressure ratio was at the flash boiling stage. Again, changes in the particulate number emissions were minimal (less than an order of magnitude) between fuels but the particulate mass changes were larger.

Using injection timings of 280°BTDC and 310°BTDC, there were opportunities to investigate the impact of flash boiling occurring together with spray impingement. The results again show significant reductions in particulate mass (but not particulate number) for some fuels when at flash boiling conditions, indicating that flash boiling may have reduced the severity of spray impingement on the piston surface (i.e. surface cooling or fuel film build up) that leads to diffusion flames during combustion.

7.1.6. Spray impingement characteristics of the model fuels

Experiments with spray impingement on a piston surface were conducted on the spray rig using the model fuels. The objective was to find how the surface cooling

effectiveness was influenced by the different volatilities of oxygenated gasolines. Thin film gauges were installed on a surrogate piston and the temperature change on the surface was measured. These experiments were conducted using only a single jet injector to minimize the impact of spray geometry changes when comparing the model fuels at elevated temperatures. Multiple parameters were varied on the spray rig to mimic the conditions on the engine.

The first set of experiments was done using pure n-pentane and methanol which were commonly used in all of the model fuels for lowering boiling points. Despite having about 30K lower boiling point than methanol, the n-pentane spray tip penetration was very poor at superheated temperatures. This was evident from the measured temperature data as well as the high-speed images. At high piston surface temperature, methanol removes heat better than n-pentane due to its high latent heat of evaporation (about 3 times higher). At low piston surface temperatures however, n-pentane was the better performer due to having a much lower boiling point which can expedite evaporative cooling of the surface. Generally, the n-pentane spray structure as well as cooling effectiveness was more dependent on the temperature than methanol. If n-pentane is used to reduce the T50 mixture values, the spray structure could be very hard to predict.

For the experiment using model fuels, the key investigation was to study how gasoline mixtures with different volatilities but with the same T90 (as well as the heavy components) would be effective in surface cooling. From the results, it was clear that the lighter components in model gasolines were only effective (by impinging and cooling piston surface) when the fuel temperature was below its saturation temperature. This was evident when similar heat flows were measured for all model fuels which shared the same content of heavy components, but two of the gasoline model fuels contained methanol while one did not. One of the reasons for poor spray cooling was due to the inability of the lighter

components liquid droplets to travel, and impinge on the piston surface when flash boiling occurs. The other indication that supports this claim was that higher heat flow magnitudes were measured, especially for the more volatile fuels when the piston surface to injector distance was varied. The closer distance enables the lighter components to be within reach of the piston surface without evaporating. The other finding from these experiments was that increasing the injection pressure only increases the magnitude of the heat flow to the piston surface for the different piston surface to injector tip distances.

In general, flash boiling, as a mechanism to help vaporization does not significantly improve total liquid evaporation. Other than changes to the spray geometry, heat addition to the fuel (to introduce flash boiling) reduces the magnitude of heat flow from the piston surface.

7.2. Future work

7.2.1. Methanol gasoline blends

Currently, methanol gasoline usage is on the rise and can pose a threat to the health of the surrounding people. This is further exaggerated by the usage of direct injection engines that have been known to emit fine particulate matter. Other than that, the pursuit of higher thermal efficiency has led to the introduction of forced induction systems that are not necessarily suitable with oxygenated fuels. The M15 fuels have been in the market in China for example, for quite some time now and the next preferred choice of methanol gasoline blend is now the M30. While this does not seem like a major change in fuel composition, the M30 has a lower energy density than the M15. Using this fuel in a forced induction ICE would bring a new challenge in controlling particulate emissions. Further investigation in the usage of the M30 gasoline in a GDI engine is crucial and has to be expedited.

7.2.2. Flash boiling spray characterisation standard

Due to the unique build of every injector design to suit the requirements of a direct injection engine, every investigation of spray behaviour impact would have to start from scratch, which can be time consuming and difficult to find general trends between different engines when undertaking calibration activities. A flash boiling spray foot print (or surface area) correlation might be developed using saturation pressure ratio as a common variable that is shared between different direct injection engines. With this in place, fuel impact investigations can be carried out easily on various different engine systems.

7.2.3. Flash boiling correlation towards P_M emissions on boosted engine

In this research work, a comprehensive study of PN and PM emissions with different saturation pressure ratios was done using a naturally aspirated engine. As elaborated in section 7.1.4, inducing flash boiling using oxygenated fuels in a boosted engine would be a challenge and the expected results may instead be totally different. Further investigation on particulate emissions on a boosted engine using model fuels with varying volatilities would instigate different saturation pressure ratio operating conditions, while varying boost pressure and fuel composition (i.e. oxygenated vs non-oxygenated) would also give a spectrum of different injection durations. As highlighted before in Section 6.4.2.1, high fuel mass (by injection duration or different injection pressure) impingement on the piston surface will lead to high surface cooling that will eventually cause a liquid film build-up. Other than that, it would be interesting to find if a similar trend can be found on the boosted engine.

7.2.4. Inclusion of sub 23 nm P_M legislation size distribution

This work has noted the potential health risk towards human life when breathing ultrafine particulate particles. The current legislation has a 50% cut-off at 23 nm (see Figure 2.28), but particles below 23 nm might be more harmful than the larger size particulates being emitted by engines. In this research work, it has been demonstrated, from the unfiltered data, that particulate numbers were higher for some of the model fuels when injected at superheated conditions than cold for certain engine operating conditions. As flash boiling has the potential to cause spray break-up, in which fuel droplets become smaller and therefore could transform into a semi-volatile component if incomplete oxidation occurs during combustion. The Wiebe filtered results presented in this research did show some

evidence of a mass decrease even without significant changes in particulate number. It is imperative that future investigation on particulate matter from SGDI engine must consist of both particulate number as well as mass and measurements starting below the 23 nm size.

7.2.5. Detail measurement of single plume spray

In Chapter 6, a single plume spray was used for experiments to measure heat flux when a piston is subjected to fuel impingement. In this research, the single plume characteristic measurements were not emphasized due to the fact that the spray was deliberately arranged to be impinge on the piston surface. These data would have been less meaningful to be correlated to the heat flux measurement output. However, currently there are not many publications available on the characteristic measurements of single plume sprays for gasoline fuels (single or multi-component). These spray characteristic data would be useful for spray modellers as a validation exercise. The high-speed image data obtained from this research could still be used and analysed to output important parameters such as spray angle and spray tip penetration at non-flash boiling, transitional flash boiling as well as flare flashing conditions.

7.2.6. Papers published, submitted, and in preparation

Some of the work in this thesis has been published or will be submitted:

- Safwan H Mohd Murad, JD Camm, MH Davy, R Stone, and D Richardson, "Spray Behaviour and Particulate Matter Emissions with M15 Methanol/Gasoline Blends in a GDI Engine," SAE Technical Paper 2016-01-0991, 2016, doi:10.4271/2016-01-0991.
- Zhifu Zhou, SH Mohd Murad, Joseph Camm, R Stone, Jiameng Tian "Experimental investigation on heat transfer dynamics of n-pentane spray impingement on piston surface for GDI engines" International Journal of Heat and Mass Transfer. Manuscript submitted.
- Safwan H Mohd Murad, Joseph Camm, Martin Davy, Richard Stone. "Spray Development with In-Cylinder Pressure and Particulate Matter Measurements in a GDI Engine: Effects of Fuel Volatility". Submitted for THIESEL 2018. Conference on thermal and fluid dynamic processes in direct injection engines.
- Safwan H Mohd Murad, Joseph Camm, Martin Davy, Richard Stone. "The Effect of Fuel Composition and Temperature on the Heat Flux with an Impacting Fuel Spray". Manuscript in progress for submission to the journal Fuel.

8. References

1. Aikawa, K., Sakurai, T. & Jetter, J.J., 2010. Development of a Predictive Model for Gasoline Vehicle Particulate Matter Emissions. , SAE Technical Paper 2010-01-2115 3(2), pp.610–622.

2. Aleiferis, P.G. & Van Romunde, Z.R., 2013. An analysis of spray development with iso-octane, n-pentane, gasoline, ethanol and n-butanol from a multi-hole injector under hot fuel conditions. Fuel, 105, pp.143–168.

3. Alkidas, A.C. & El Tahry, S.H., 2003. Contributors to the Fuel Economy Advantage of DISI Engines Over PFI Engines. SAE Technical Paper, 2003-01–3101.

4. Andersson, J., Giechaskiel, B., Muñoz-bueno, R., Sandbach, E. & Dilara, P., 2007. Particle Measurement Programme (PMP) Light-duty Inter-laboratory Correlation Exercise (ILCE _ LD) Final Report. , (January).

5. Araneo, L. & Donde', R., 2017. Flash boiling in a multihole G-DI injector – Effects of the fuel distillation curve. Fuel, 191, pp.500–510.

6. Araujo, J.A. & Nel, A.E., 2009. Particulate matter and atherosclerosis: role of particle size, composition and oxidative stress. Particle and fibre toxicology.

7. Atkinson, R.W., Fuller, G.W., Anderson, H.R., Harrison, R.M. & Armstrong, B., 2010. Urban Ambient Particle Metrics and Health. Epidemiology, 21(4), pp.501–511.

8. Barone, T.L., Storey, J.M.E., Youngquist, A.D. & Szybist, J.P., 2012a. An analysis of direct-injection spark-ignition (DISI) soot morphology. Atmospheric Environment, 49, pp.268–274.

9. Barone, T.L., Storey, J.M.E., Youngquist, A.D. & Szybist, J.P., 2012b. An analysis of direct-injection spark-ignition (DISI) soot morphology. Atmospheric Environment, 49, pp.268–274.

10. Bayley, F.., Owen, J.. & A.B, T., 1972. Heat Transfer, London: Nelson.

11. Berndorfer, A., Breuer, S., Piock, W. & Von Bacho, P., 2013. Diffusion Combustion Phenomena in GDi Engines caused by Injection Process. In SAE Technical Paper 2013-01-0261.

12. Bielaczyc, P., Szczotka, A. & Woodburn, J., 2017. Investigations into Exhaust Particulate Emissions from Multiple Vehicle Types Running on Two Chassis Dynamometer Driving Cycles. SAE Technical Paper 2017-01-1007.

13. Bielaczyc, P., Woodburn, J. & Szczotka, A., 2014. Particulate Emissions from European Vehicles Featuring Direct Injection Spark Ignition Engines Tested Under Laboratory Conditions. SAE Int. J. Fuels Lubr., 7(2), pp.580–590.

14. Bosteels, D., May, J., Karlsson, H. & de Serves, C., 2006. “Regulated” and “Non-regulated” Emissions from Modern European Passenger Cars. SAE Technical Paper 2006-01-1516.

15. Braisher, M., Stone, R. & Price, P., 2010. Particle Number Emissions from a Range of European Vehicles. SAE Technical Paper 2010-01-0786.

16. Cambustion, DMS500 MkII The Rapid Response Engine Particulate Analyzer. www.cambustion.com, accessed 01/07/2017

17. Camm, J., 2016. Mixture preparation and injection strategy in direct injection spark ignition engines. DPhil Thesis. University of Oxford. Department of Engineering Science

18. Chambliss, S. & Bandivadekar, A., 2015. Accelerating progress from Euro 4 / IV to Euro 6 / VI vehicle emissions standards. The International Council on Clean Transportation.

19. Chan, Q.N., Bao, Y. & Kook, S., 2014. Effects of injection pressure on the structural transformation of flash-boiling sprays of gasoline and ethanol in a spark-ignition direct-injection (SIDI) engine. Fuel, 130, pp.228–240.

20. Chen, H., XU, M., Hung, D.L.S., Yang, J. & Zhuang, H., 2013. Fuel impingement analysis of flash-boiling spray in a spark- ignition direct-injection engine. In 16th Annual Conference on Liquid Atomization and Spray Systems.

21. Chen, L., Stone, R. & Richardson, D., 2012a. A study of mixture preparation and PM emissions using a direct injection engine fuelled with stoichiometric gasoline/ethanol blends. Fuel, 96, pp.120–130.

22. Chen, L., Stone, R. & Richardson, D., 2012b. Effect of the valve timing and the coolant temperature on particulate emissions from a gasoline direct-injection engine fuelled with gasoline and with a gasoline–ethanol blend. Proceedings of the Institution of Mechanical Engineers, Part D: Journal of Automobile Engineering, 226(10), pp.1419–1430.

23. Cheng, W.-L., Chen, H., Hu, L. & Zhang, W.-W., 2015. Effect of droplet flash evaporation on vacuum flash evaporation cooling: Modeling. International Journal of Heat and Mass Transfer, 84, pp.149–157.

24. Cheng, W.-L., Han, F.-Y., Liu, Q.-N. & Zhao, R., 2012. Theoretical investigation on the mechanism of surface temperature non-uniformity formation in spray cooling. International Journal of Heat and Mass Transfer, 55(19–20), pp.5357–5366.

25. Czerwinski, J., Comte, P., Heeb, N., Mayer, A. & Hensel, V., 2017. Nanoparticle Emissions of DI Gasoline Cars with/without GPF. SAE Technical Paper 2017-01-1004.

26. Dardiotis, C. & Martini, G., 2012. Assessment of particle number limits for petrol vehicles, European Commission, JCR Scientific and Policy Reports. Report EUR25592EN.

27. Demuynck, J., Favre, C., Bosteels, D., Hamje, H. & Andersson, J., 2017. Real-World Emissions Measurements of a Gasoline Direct Injection Vehicle without and with a Gasoline Particulate Filter. SAE Technical Paper 2017-01-0985.

28. Dergham, M., Lepers, C., Verdin, A., Cazier, F., Billet, S., Courcot, D., Shirali, P. & Garçon, G., 2015. Temporal–spatial variations of the physicochemical characteristics of air pollution Particulate Matter (PM2.5–0.3) and toxicological effects in human bronchial epithelial cells (BEAS-2B). Environmental Research, 137, pp.256–267.

29. EEA, 2016. Air quality in Europe - 2016 report. European Environment Agency

30. EEA, 2014. Air quality in Europe - 2014 report, European Environment Agency

31. Eichlseder, H., Baumann, E., Müller, P. & Rubbert, S., 2000. Gasoline Direct Injection – A Promising Engine Concept for Future Demands. SAE Technical Paper 2000-01-0248.

32. EPA United States Environmental Protection Agency, 2004. EPA Air Quality Criteria for Particulate Matter Volume I of II,

33. European Environment Agency, 2012. Particulate matter from natural sources and related reporting under the EU Air Quality Directive in 2008 and 2009.

34. Farron, C., Matthias, N., Foster, D.E., Andrie, M., Krieger, R., Najt, P., Narayanaswamy, K., Solomon, A. & Zelenyuk, A., 2011. Particulate Characteristics for Varying Engine Operation in a Gasoline Spark Ignited, Direct Injection Engine. SAE Technical Paper 2011-01-1220.

35. Fredenslund, A., Gmehling, J. & Rasmussen, P., 1978. Vapor-liquid equilibria using UNIFAC, Aage Fredenslund, Jurgen Gmehling and Peter Rasmussen, Elsevier Scientific Publishing Company, Amsterdam and New York, 1977. 380 pages. AIChE Journal, 24(3), pp.558–559.

36. Geng, P., Zhang, H. & Yang, S., 2015. Experimental investigation on the combustion and particulate matter (PM) emissions from a port-fuel injection (PFI) gasoline engine fueled with methanol–ultralow sulfur gasoline blends. Fuel, 145, pp.221–227.

37. George E., T. & Shah, R.J., 2003. Fuels and Lubricants Handbook : Technology, Properties, Performance, and Testing, West Consohocken, United States: American Society for Testing & Materials.

38. Greg Archer, 2013. Without future controls particulate emissions from GDI petrol vehicles will be more than from diesels. In report by Transport and Environment. www.transportandenvironment.org. accessed 01/10/2017.

39. Heinzerling, A., Hsu, J. & Yip, F., 2016. Respiratory Health Effects of Ultrafine Particles in Children: a Literature Review. Water, Air, & Soil Pollution, 227(1), p.32.

40. Honda, T., Kawamoto, M., Katashiba, H. & Sumida, M., 2004. A Study of Mixture Formation and Combustion for Spray Guided DISI. SAE Technical Paper 2004-01-0046.

41. Huang, Y., Alger, T., Matthews, R.D. & Ellzey, J., 2001. The Effects of Fuel Volatility and Structure on HC Emissions from Piston Wetting in DISI Engines. SAE Technical Paper 2001-01-1205.

42. Hung, D.L.S., Harrington, D.L., Gandhi, A.H., Markle, L.E., Parrish, S.E., Shakal, J.S., Sayar, H., Cummings, S.D. & Kramer, J.L., 2008. Gasoline Fuel Injector Spray Measurement and Characterization - A New SAE J2715 Recommended Practice. SAE International Journal of Fuels and Lubricants, 1(1), pp.2008-01–1068.

43. Johansson, C., Norman, M. & Gidhagen, L., 2007. Spatial & temporal variations of PM10 and particle number concentrations in urban air. Environmental Monitoring and Assessment, 127(1–3), pp.477–487.

44. Johnson, T. & Joshi, A., 2017. Review of Vehicle Engine Efficiency and Emissions. SAE Technical Paper 2017-01-0907.

45. Kar, K., Last, T., Haywood, C. & Raine, R., 2008. Measurement of Vapor Pressures and Enthalpies of Vaporization of Gasoline and Ethanol Blends and Their Effects on Mixture Preparation in an SI Engine. SAE Technical Paper 2008-01-0317.

46. Karavalakis, G., Short, D., Vu, D., Russell, R.L., Asa-Awuku, A., Jung, H., Johnson, K.C. & Durbin, T.D., 2015. The impact of ethanol and iso-butanol blends on gaseous and particulate emissions from two passenger cars equipped with spray-guided and wall-guided direct injection SI (spark ignition) engines. Energy, 82, pp.168–179.

47. Kasseris, E. & Heywood, J., 2012. Charge Cooling Effects on Knock Limits in SI DI Engines Using Gasoline/Ethanol Blends: Part 1-Quantifying Charge Cooling. SAE Int. J. Fuels Lubr., 5(2), pp.844–854.

48. Katashiba, H., Honda, T., Kawamoto, M., Sumida, M., Fukutomi, N. & Kawajiri, K., 2006. Improvement of Center Injection Spray Guided DISI Performance. SAE Technical Paper 2006-01-1001.

49. Kawano, D., Senda, J. & Kawakami, K., 2001. Fuel Design Concept for Low Emission in Engine Systems 2nd Report : Analysis of Combustion Characteristics for the Mixed Fuels on Exhaust Concentrations in Diesel Engine. SAE Technical Paper 2003-01-1038.

50. Kim, K., Kabir, E. & Kabir, S., 2015. A review on the human health impact of airborne particulate matter. Environment International, 74, pp.136–143.

51. Kim, K.H., Jahan, S.A. & Kabir, E., 2013. A review on human health perspective of air pollution with respect to allergies and asthma. Environment International, 59, pp.41–52.

52. Kittelson, D., 2016. Particle number measurements : How small should we go? Solid particle number emissions. In Cambridge Particle Meeting.

53. Kittelson, D.B., 1998. Engines and nanoparticles: A review. Journal of Aerosol Science, 29(5–6), pp.575–588.

54. Ko, K. & Arai, M., 2002. Diesel Spray and Adhering Fuel on an Impingement Wall. SAE Technical Paper 2002-01-1628.

55. de Kok, T.M.C.M., Driece, H.A.L., Hogervorst, J.G.F. & Briedé, J.J., 2006. Toxicological assessment of ambient and traffic-related particulate matter: A review of recent studies. Mutation Research - Reviews in Mutation Research, 613(2–3), pp.103–122.

56. Leach, F., 2014. Particulate Emissions from Gasoline Direct Injection Engines. DPhil Thesis. University of Oxford. Department of Engineering Science.

57. Leach, F., Stone, R. & Richardson, D., 2013. The Influence of Fuel Properties on Particulate Number Emissions from a Direct Injection Spark Ignition Engine. SAE Technical Paper 2013-01-1558.

58. Liang, B., Ge, Y., Tan, J., Han, X., Gao, L., Hao, L., Ye, W. & Dai, P., 2013. Comparison of PM emissions from a gasoline direct injected (GDI) vehicle and a port fuel injected (PFI) vehicle measured by electrical low pressure impactor (ELPI) with two fuels: Gasoline and M15 methanol gasoline. Journal of Aerosol Science, 57, pp.22–31.

59. Löndahl, J., Massling, A., Pagels, J., Swietlicki, E., Vaclavik, E. & Loft, S., 2007. Size-Resolved Respiratory-Tract Deposition of Fine and Ultrafine Hydrophobic and Hygroscopic Aerosol Particles During Rest and Exercise. Inhalation Toxicology, 19(2), pp.109–116.

60. Löndahl, J., Pagels, J., Swietlicki, E., Zhou, J., Ketzel, M., Massling, A. & Bohgard, M., 2006. A set-up for field studies of respiratory tract deposition of fine and ultrafine particles in humans. Journal of Aerosol Science, 37(9), pp.1152–1163.

61. Marotta, A., Pavlovic, J., Ciu, B., Serra, S. & Fontaras, G., 2015. Gaseous Emissions from Light-Duty Vehicles : Moving from NEDC to the New WLTP Test Procedure. Environmental Science & Technology. 49 (14), pp.8315-8322

62. Marques, O., 2010. Practical image and video processing using Matlab, Oxford : Wiley-Blackwell.

63. McArragher, S., Thompson, N., Bazzani, R., Aarnink, T. & KwonYeong, 2004. CONCAWE/GFC Study on Gasoline Volatility and Ethanol Effects on Hot and Cold

Weather Driveability of Modern European Vehicles. SAE Technical Paper 2004-01-2002.

64. Mojtabi, M., Chadwick, N., Wigley, G. & Helie, J., 2008. The Effect of Flash Boiling on Break Up and Atomization in GDI Sprays. In ILASS Institute for Liquid Atomization and Spray Systems.

65. Moreira, A.L.N., Moita, A.S. & Panao, M.R., 2010. Advances and challenges in explaining fuel spray impingement: How much of single droplet impact research is useful? Progress in Energy and Combustion Science, 36(5), pp.554–580.

66. Morikawa, K. & Kaneko, M., 2005. A Study on New Combustion Method of High Compression Ratio Spark Reprinted From : SI Combustion and Direct Injection SI Engine Technology. SAE Technical Paper. 2005-01-0106.

67. Natti, K., Sinha, A., Hoerter, C., Andersson, P., Andersson, J., Lohmann, C., Schultz, D., Cho, N.H. & Winsor, R., 2013. Studies on the Impact of 300 MPa Injection Pressure on Engine Performance, Gaseous and Particulate Emissions. SAE International Journal of Engines, 6(1), pp.2013-01–0897.

68. Neroorkar, K. & Schmidt, D., 2011. Modeling of vapor-liquid equilibrium of gasoline-ethanol blended fuels for flash boiling simulations. Fuel. 90(2), pp.665-673

69. Ntziachristos, L., Mamakos, A., Samaras, Z., Mathis, U., Mohr, M., Thompson, N., Stradling, R., Forti, L. & de Serves, C., 2004. Overview of the European "Particulates" Project on the Characterization of Exhaust Particulate Emissions From Road Vehicles: Results for Light-Duty Vehicles. SAE Technical Paper 2004-01-1985.

70. Oberdörster, G., Oberdörster, E. & Oberdörster, J., 2005. Nanotoxicology: An emerging discipline evolving from studies of ultrafine particles. Environmental Health Perspectives, 113(7), pp.823–839.

71. Oh, H., Bae, C., Park, J. & Jeon, J., 2011. Effect of the Multiple Injection on Stratified Combustion Characteristics in a Spray-Guided DISI Engine. SAE Technical Paper 2011-24-0059.

72. Otsu, N., 1979. A Threshold Selection Method from Gray-Level Histograms. IEEE Transactions on Systems, Man, and Cybernetics, 9(1), pp.62–66.

73. Oudenijeweme, D., Freeland, P., Behringer, M. & Aleiferis, P.G., 2015. Developing Low Gasoline Particulate Emission Engines Through Improved Fuel Delivery. SAE Technical Paper 2014-01-2843.

74. Owen, K. & Coley, T., 1995. Automotive Fuels Reference Book Second., Society of Automotive Engineers.

75. Parrish, S.E., Zink, R.J., Sivathanu, Y. & Lim, J., 2010. Spray patternation of a multi-hole injector utilizing planar line-of-sight extinction tomography. ILASS Americas, 22nd Annual Conference on Liquid Atomization and Spray Systems.

76. Perez, L., Tobías, A., Querol, X., Pey, J., Alastuey, A., Díaz, J. & Sunyer, J., 2012. Saharan dust, particulate matter and cause-specific mortality: A case-crossover study in Barcelona (Spain). Environment International, 48, pp.150–155.

77. Piock, W.F., Berndorfer, A., Hoffmann, G., Salemi, P. & Fusshoeller, B., 2011. Strategies Towards Meeting Future Particulate Matter Emission Requirements in Homogeneous Gasoline Direct Injection Engines. SAE International Journal of Engines, 4(1), pp.1455–1468.

78. Poling, B.E., Prausnitz, J.M. & O'Connell, J.P., 2001. The Properties of Gases and Liquids, McGraw-Hill.

79. Price, C., Hamzehloo, A., Aleiferis, P. & Richardson, D., 2015. Aspects of Numerical Modelling of Flash-Boiling Fuel Sprays Flash-Boiling Atomization. SAE Technical Paper 2015-24-2463.

80. Price, P., Twiney, B., Stone, R., Kar, K. & Walmsley, H., 2007. Particulate and Hydrocarbon Emissions from a Spray Guided Direct Injection Spark Ignition Engine with Oxygenate Fuel Blends Reprinted From : SI Combustion. SAE Technical Paper 2007-01-0472, (724), pp.776–790.

81. Rappazzo, K.M., Daniels, J.L., Messer, L.C., Poole, C. & Lobdell, D.T., 2014. Exposure to Fine Particulate Matter during Pregnancy and Risk of Preterm Birth among Women in New Jersey, Ohio, and Pennsylvania, 2000-2005. Environmental Health Perspectives, 122(9), pp.992–997.

82. Samenfink, W., Elsäßer, A., Dullenkopf, K. & Wittig, S., 1999. Droplet interaction with shear-driven liquid films: Analysis of deposition and secondary droplet characteristics. International Journal of Heat and Fluid Flow, 20(5), pp.462–469.

83. Sandford, M., Page, G. & Crawford, P., 2009. The All New AJV8. SAE Technical Paper 2009-01-1060.

84. Schoenhaber, J., Kuehn, N., Bradler, B., Richter, J.M., Ag, U., Kg, C., Bauer, S., Lenzen, B., Beidl, C. & Darmstadt, T.U., 2017. Impact of European Real-Driving-Emissions Legislation on Exhaust Gas Aftertreatment Systems of Turbocharged Direct Injected Gasoline Vehicles. SAE Technical Paper 2017-01-0924.

85. Schwarz, C., Schünemann, E., Durst, B., Fischer, J. & Witt, A., 2006. Potentials of the Spray-Guided BMW DI Combustion System. SAE Technical Paper 2006-01-1265.

86. Serras-pereira, J., Aleiferis, P., Richardson, D. & Wallace, S., 2007. Spray Development in a Direct-Injection Spark-Ignition Engine. SAE Technical Paper, 2007-01–2712.

87. Serras-Pereira, J., Aleiferis, P.G., Walmsley, H.L., Davies, T.J. & Cracknell, R.F., 2013. Heat flux characteristics of spray wall impingement with ethanol, butanol, iso-octane, gasoline and E10 fuels. International Journal of Heat and Fluid Flow, 44, pp.662–683.

88. Serras-Pereira, J., Van Romunde, Z., Aleiferis, P.G., Richardson, D., Wallace, S. & Cracknell, R.F., 2010. Cavitation, primary break-up and flash boiling of gasoline, iso-octane and n-pentane with a real-size optical direct-injection nozzle. Fuel, 89(9), pp.2592–2607.

89. Shen, S., Che, Z., Wang, T., Jia, M. & Sun, K., 2017. Numerical Study on Flash Boiling Spray of Multi-Hole Injector. SAE International Journal of Fuels and Lubricants: 10(2): 2017

90. Shigeo Yamamoto, D.T. and K.S., 2009. Keys to Understanding Spray-guided Combustion of a Narrow-spacing Gasoline Direct Injection SI Engine with a Centrally Mounted Multi-hole Injector. SAE Technical Paper, 2009-01-1497.

91. Silva, R.A., West, J.J., Zhang, Y., Anenberg, S.C., Lamarque, J.-F., Shindell, D.T., Collins, W.J., Dalsoren, S., Faluvegi, G., Folberth, G., Horowitz, L.W., Nagashima, T., Naik, V., Rumbold, S., Skeie, R., Sudo, K., Takemura, T., Bergmann, D., Cameron-Smith, P., Cionni, I., Doherty, R.M., Eyring, V., Josse, B., MacKenzie, I.A., Plummer, D., Righi, M., Stevenson, D.S., Strode, S., Szopa, S. & Zeng, G., 2013. Global premature mortality due to anthropogenic outdoor air pollution and the contribution of past climate change. Environmental Research Letters, 8(3), p.34005.

92. Sobotowski, R. a., Butler, A.D. & Guerra, Z., 2015. A Pilot Study of Fuel Impacts on PM Emissions from Light-Duty Gasoline Vehicles. SAE International Journal of Fuels and Lubricants, 8(1), pp.2015-01–9071.

93. Stevens, E. & Steeper, R., 2001. Piston Wetting in an Optical DISI Engine: Fuel Films, Pool Fires, and Soot Generation. SAE Technical Paper 2001-01-1203

94. Stradling, R., Antunez, J., Bellier, A., Elliott, N., Bomholt, C., Kiiski, U. & Gomez-Acebo, P., 2012. Gasoline volatility and vehicle performance, Conservation of Water and Clean Air in Europe, Brussels.

95. Symonds, J.P.R., Price, P., Williams, P.I. & Stone, R., 2008. Density of particles emitted from a gasoline direct injection engine . 12th ETH Conference on Combustion Generated Nanoparticles, p.2008.

96. Tamir, A., 1982. Prediction of latent heat of vaporization of multicomponent mixtures. Fluid Phase Equilibria, 8(2), pp.131–147.

97. Taylor, P., Zheng, Z., Durbin, T.D., Karavalakis, G., Johnson, K.C., Iii, D.R.C., Herner, J.D., Robertson, W.H., Huai, T., Ayala, A., Kittelson, D.B., Jung, H.S., Zheng, Z., Durbin, T.D., Karavalakis, G., Kent, C., Chaudhary, A., Iii, D.R.C., Herner, J.D., William, H., Huai, T., Ayala, A., Kittelson, D.B. & Jung, H.S., 2012. Nature of Sub-23-nm Particles Downstream of the European Particle Measurement Programme (PMP) - Compliant System : A Real-Time Data Perspective. Aerosol Science and Technology, (June), pp.37–41.

98. Trasande, L., Malecha, P. & Attina, T.M., 2016. Particulate matter exposure and preterm birth: Estimates of U.S. attributable burden and economic costs. Environmental Health Perspectives, 124(12), pp.1913–1918.

99. U.S. Environmental Protection Agency, 2013. EPAct/V2/E-89: Assessing the Effect of Five Gasoline Properties on Exhaust Emissions from Light-Duty Vehicles Certified to Tier 2 Standards.

100. Vanderwege, B.A., Han, Z., Iyer, C.O., Muñoz, R.H. & Yi, J., 2003. Development and Analysis of a Spray-Guided DISI Combustion System Concept. SAE Technical Paper 2003-01-3105.

101. Velji, A., Yeom, K., Wagner, U., Spicher, U., Rossbach, M., Suntz, R. & Bockhorn, H., 2010. Investigations of the Formation and Oxidation of Soot Inside a Direct Injection Spark Ignition Engine Using Advanced Laser-Techniques. SAE Technical Paper 2010-01-0352.

102. Vladimír, M. & Svoboda, V., 1985. Enthalpies of vaporization of organic compounds : a critical review and data compilation I. U. of P. and A. Chemistry, ed., Oxford: Oxford : Blackwell Scientific.

103. Vuk, C. & Vander Griend, S.J., 2013. Fuel Property Effects on Particulates In Spark Ignition Engines. SAE Technical Paper 2013-01-1124.

104. Wang, X., 2008. Instantaneous In-cylinder Heat Transfer and Combustion Analysis in Spark Ignition Engines. DPhil Thesis. University of Oxford. Engineering Science Department.

105. Warey, A., Huang, Y., Matthews, R.D., Hall, M. & Ng, H., 2002. Effects of Piston Wetting on Size and Mass of Particulate Matter Emissions in a DISI Engine. SAE Technical Paper 2002-01-1140.

106. Whitaker, P., Kapus, P., Ogris, M. & Hollerer, P., 2011. Measures to Reduce Particulate Emissions from Gasoline DI engines. SAE Technical Paper, 1(4), pp.1498–1512.

107. Wirth, M., Zimmermann, D., Friedfeldt, R., Caine, J., Schamel, A., Davies, M., Peirce, G., Storch, A., Ries-Muller, K Gansert, K.P Pilgram, G., Ortmann, R., Wurfel, G. & Gerhardt, J., 2004. A Cost Optimised Gasoline Spray Guided Direct Injection System for Improved Fuel Economy. In Proceedings of the Seminar on Fuel economy and engine downsizing, London, May 2004, Paper No. 10 (Professional Engineering Publishing Limited, Bury St Edmunds and London).

108. World Health Organization, 2013. Health Effects of Particulate Matter: Policy implications for countries in eastern Europe, Caucasus and central Asia. Journal of the Korean Medical Association, 50(2), p.20.

109. Xu, M., Zhang, Y., Zeng, W., Zhang, G. & Zhang, M., 2013. Flash Boiling: Easy and Better Way to Generate Ideal Sprays than the High Injection Pressure. SAE International Journal of Fuels and Lubricants, 6(1), pp.2013-01–1614.

110. Zeng, W., Xu, M., Zhang, G., Zhang, Y. & Cleary, D.J., 2012. Atomization and vaporization for flash-boiling multi-hole sprays with alcohol fuels. Fuel, 95, pp.287–297.

111. Zervas-Renault, E., 2004. Repeatability of fine particle measurement of diesel and gasoline vehicles exhaust gas. SAE Technical Paper 2004-01-1983.

112. Zhang, G., Xu, M., Zhang, Y. & Hung, D.L.S., 2013. Characteristics of Flash Boiling Fuel Sprays from Three Types of Injector for Spark Ignition Direct Injection (SIDI) Engines. In Automotive Concept Modelling: Optimization of the Vehicle NVH Performance. pp. 443–454.